LIÈGE université
Sciences Appliquées

On the fully-elliptic representation of convective instabilities in streamwise shear flows

Thesis submitted in partial fulfillment of the requirements for the degree of Doctor of Philosophy (PhD) in Engineering Science

by

Sébastien E. M. Niessen

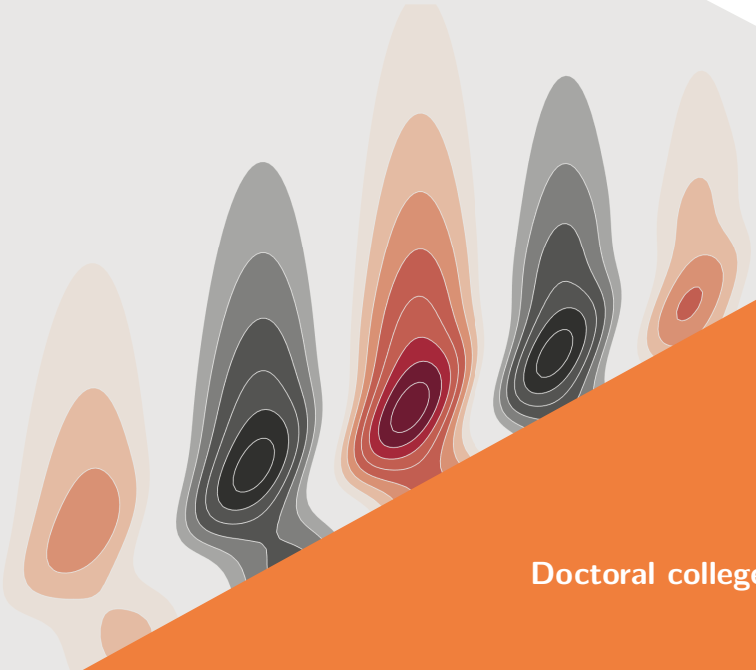

Supervisor: Vincent E. Terrapon

Co-supervisor: Grigorios Dimitriadis

Advisors: Koen J. Groot
Stefan Hickel

Doctoral college in Aerospace and Mechanics

December 2023

LIÈGE université
Sciences Appliquées

On the fully-elliptic representation of convective instabilities in streamwise shear flows

Thesis submitted in partial fulfillment of the requirements for the degree of Doctor of Philosophy (PhD) in Engineering Science

by

Sébastien E. M. Niessen

Supervisor:	Vincent E. Terrapon
Co-supervisor:	Grigorios Dimitriadis
Advisors:	Koen J. Groot Stefan Hickel

Doctoral college in Aerospace and Mechanics

December 2023

Jury:

President:	Prof. dr. V. Denoël,	University of Liège (Belgium)
Supervisor:	Prof. dr. V. E. Terrapon,	University of Liège (Belgium)
Co-supervisor:	Prof. dr. G. Dimitriadis,	University of Liège (Belgium)
Advisors:	Dr. K. J. Groot,	Texas A&M University (USA)
	Prof. dr. S. Hickel,	Technische Universiteit Delft (The Netherlands)
Members:	Prof. dr. K. Hillewaert,	University of Liège (Belgium)
	Prof. dr. P. Schmid,	King Abdullah University of Science and Technology (Saudi Arabia)

This thesis was funded by the Fonds National de la Recherche Scientifique de Belgique (F.R.S.-FNRS) under the FRIA grant No. FC27285.

Computational resources have been provided by the Consortium des Équipements de Calcul Intensif (CÉCI), funded by the Fonds de la Recherche Scientifique de Belgique (F.R.S.-FNRS) under Grant No. 2.5020.11 and by the Walloon Region.

Keywords: Laminar-turbulent transition, Convective instabilities, BiGlobal stability, Streamwise flows, Shock-wave/boundary-layer interaction...

An electronic version of this dissertation is available at
https://orbi.uliege.be/handle/2268/306857.

Summary

Laminar-turbulent transition is ubiquitous in viscous fluid flows and is critical in many engineering applications. While it can be beneficial to enhance mixing, increase heat transfer or avoid flow separation, it also increases the skin friction that, for instance, drastically increases the fuel consumption of aircraft. Understanding the laminar-turbulent transition is thus key to devising control strategies that can promote or delay the onset of turbulence. In many cases, the laminar-turbulent transition originates from external disturbances that enter the flow field and are amplified by instability mechanisms. Among all types of instability, linear convective instability mechanisms are usually the most dominant in flows that evolve from a laminar to a turbulent regime in space. These mechanisms amplify and propagate the disturbances in a preferential direction, away from the source. Once the amplified disturbances have reached a threshold amplitude, nonlinear interactions rapidly break them down into large-scale turbulent motions. By using linear stability equations, the instability mechanisms supported in a flow field can be studied before the nonlinear breakdown. However, existing numerical methods are not suitable for describing convective instability mechanisms in real flow applications. Traditional one-dimensional equations can only tackle flows that slowly develop towards the propagation direction of the disturbances and, if more dimensions are included in the equations, the results become sensitive to the numerical domain boundaries. The description of convective instabilities in complex flows is thus always compromised by insufficient result accuracy. The objective of this work is to propose a methodology that enables a fully-elliptic representation of convective instability mechanisms in two-dimensional flows. The proposed approach solves the stability equations formulated as an eigenvalue problem in a moving frame of reference to obtain eigenfunctions that decay towards the truncation boundaries, i.e., remain localized within the computational domain. Hence, the corresponding solutions are independent of the numerical domain length and boundary conditions. The eigenfunctions are then introduced into the stationary-frame flow field and integrated in time to obtain the finite-time dynamics of the instability mechanisms. After decomposing the resulting time-dependent wave packets into their individual frequencies, the traditional N-factor and neutral curves are reconstructed. The approach is validated by considering the incompressible flat-plate boundary layer. Whereas the traditional one-dimensional stability equations are acknowledged for delivering valid results for this slowly developing flow, two-dimensional stability analyses in the stationary frame of reference are notoriously tainted by the sensitivity of the results to the domain length. By using the proposed moving-frame approach, this sensitivity issue is eliminated and the resulting N-factor and neutral curves are shown to be in excellent agreement with one-dimensional methods. The moving-frame approach is then used to study the linear stability of a laminar shock-wave/boundary-layer interaction. Because this flow case supports strong in-plane gradients, it provides the opportunity to demonstrate the effectiveness of the moving-frame methodology for capturing convective instability mechanisms in highly two-dimensional flows. The dominant spanwise wavenumber and frequency yielding the largest amplification of perturbations in the present shock-induced recirculation bubble are identified. The convective instability mechanisms are then characterized by decomposing the growth rates of both localized eigenfunctions and time-dependent wave packets into their physical energy-production processes. Finally, a remarkably good agreement is found between the time-dependent wave packets and frame-speed-dependent eigensolutions.

Resumé

La transition laminaire-turbulent est un phénomène omniprésent dans les écoulements et a un rôle critique dans beaucoup d'applications d'ingénierie. Alors que la turbulence peut être bénéfique pour améliorer le mélange de composants, les transferts de chaleur ou éviter la séparation d'un écoulement, elle augmente également la friction sur les surfaces qui, par exemple, accroît la consommation de carburant des avions. Il est donc essentiel de comprendre les mécanismes de la transition laminaire-turbulent pour développer des stratégies de contrôle permettant, soit de promouvoir, soit de retarder l'apparition de la turbulence. Dans la majorité des cas, la transition est causée par des perturbations extérieures qui entrent dans l'écoulement et sont ensuite amplifiées par des mécanismes d'instabilité. Parmi les différents types de mécanisme, les instabilités convectives linéaires sont les plus présentes dans les écoulements dont le régime varie spatialement de laminaire à turbulent. Ces instabilités amplifient et propagent les perturbations dans une direction préférentielle. Une fois que l'amplitude des perturbations atteint un certain seuil, les interactions non linéaires prennent le dessus et l'écoulement devient turbulent. Les mécanismes d'instabilité peuvent être étudiés avant l'apparition des interactions non linéaires avec les equations linéaires de stabilité. Cependant, les méthodes numériques existantes ne sont pas adaptées aux instabilités convectives pour des écoulements réels. Les traditionnelles équations unidimensionnelles ne fournissent des résultats précis que pour les écoulements évoluant lentement dans la direction de propagation des perturbations. Si plus d'une dimension spatiale est considérée dans les équations, les résultats sont inévitablement dépendants du domaine numérique. La représentation des instabilités convectives dans des écoulements complexes est donc compromise par des résultats peu fidèles à la réalité. L'objectif de cette thèse est de proposer une méthodologie permettant de résoudre les équations elliptiques de stabilité pour des écoulements avec des gradients importants dans deux dimensions. L'approche proposée consiste à résoudre un problème aux valeurs propres formulé dans un référentiel mobile afin d'obtenir des fonctions propres qui décroissent vers les limites du domaine numérique. Cela permet aux solutions d'être indépendantes de la longueur du domaine et des conditions aux limites. Les fonctions propres sont ensuite introduites dans l'écoulement en référentiel stationnaire et intégrée dans le temps afin d'obtenir la dynamique temporelle des perturbations. En décomposant ces paquets d'onde temporels avec une transformée de Fourier, les courbes de stabilité neutre et d'amplification sont calculées. Pour valider l'approche, une couche limite incompressible se développant lentement sur une plaque plane est considérée. Alors que les équations unidimensionnelles fournissent des résultats précis, les équations bidimensionnelles formulées dans un référentiel fixe délivrent des résultats qui dépendent de la longueur du domaine. En éliminant cette dépendance avec l'approche du référentiel mobile, les courbes de stabilité neutre et d'amplification de la couche limite sont en parfait accords avec celles des méthodes unidimensionnelles. La présente méthode est ensuite appliquée à une interaction onde de choc / couche limite laminaire. Caractérisé par de forts gradients dans deux dimensions, cet écoulement permet de valider la méthode. Les longueurs d'onde et les fréquences des perturbations les plus amplifiées sont dès lors identifiées. En décomposant l'énergie de perturbations associée aux solutions propres et aux paquets d'onde temporels en des contributions individuelles, les mécanismes d'instabilité convective sont caractérisés. Finalement, les similarités entre les mécanismes liés aux fonctions propres obtenues à différentes vitesses de référentiel et aux paquets d'onde à différents temps sont mises en avant.

Acknowledgements

All the work accomplished during my PhD, including the completion of this final manuscript, would not have been possible without the support of several people.

I would like to thank my promotor, Vincent Terrapon, who gave me the opportunity to dive into this research topic on which I started working during my Master's thesis. I am very grateful for your continuous support and the trust you put in my project. I highly appreciated all your excellent feedback and the pleasant discussions we had about fluid mechanics, laminar-turbulent transition and flow stability. Finally, I would like to thank you for all the support you provided to help me delivering this final manuscript.

I am very grateful to Stefan Hickel who gave me the opportunity to join the Aerodynamics group of TU Delft, first as a Master's student, and then as a guest researcher to continue the present research topic. Stefan, I appreciate your trust since we started working together and I would like to thank you for having introduced me to academic research, stability analyses and shock-wave/boundary-layer interactions. Thank you for your contribution and for all the clever advice that made me understand many things about science, research and fluid mechanics and that helped me approach problems from different angles.

I would like to give very special thanks to Koen Groot, who supervised me on a daily basis without any compromise on the time and the quality of the advice/work. Your passion and devotion to teaching and research really inspired me to pursue this PhD. I highly enjoyed the work we did together in the (almost) unique goal of making global stability analyses work for convective instabilities. I cannot count all the discussions we had about stability analyses, fluid mechanics and science in general, sometimes from philosophical points of view to very precise details. I think I will miss our many sessions of intense collaborative work, despite some included endless nights. Koen, thank you for your unconditional trust and for having been so dedicated to my PhD.

I am immensely grateful to Adeline, who supported me, my work, my mood, and my ups and downs over all these years. Your support was key to the accomplishment of my PhD and this final manuscript. I could not have made it to the end without you; I am very grateful for your support that helped me go through the difficulties of this journey. Thank you for having unconditionally been there.

I would like to thank my parents for having let me pursue my ambitions in the exact way I wanted and for having supported me to reach my goals. Finally, I want to thank Jérôme, my brother, who is always curious about my admittedly barely understandable engineering topics. I highly appreciate that you are always open to a discussion, some beers or go cycling together to release the pressure of everyday life.

Contents

1

Introduction

The aviation industry faces new technological challenges to decrease fuel consumption and greenhouse-gas emissions. In this context, a significant lever to achieve higher efficiency is to reduce drag, that opposes the motion of an object in a fluid. For commercial aircraft, the skin-friction drag contributes to 40-50% of the total drag and is mostly influenced by the regime of the fluid flow over the surface. The skin-friction drag is much lower when the flow is quiet and orderly, i.e., laminar, than when it is turbulent. Usually, the flow over the foremost part of the aerodynamic surface is in a laminar regime while the rest of the flow is turbulent. In commercial aircraft, the transition from laminar to turbulent flow occurs early on the wings and fuselage such that 80% of the total skin-friction drag is due to the turbulent regime. There is thus a need to devise surfaces that can support a longer laminar region by delaying or even completely suppressing the transition from a laminar to a turbulent flow. For instance, achieving 50% of laminar flow over the upper surface of a commercial aircraft could reduce the total drag by 6.4%, which in turn would reduce the fuel consumption by 7.8% (Tucker *et al.*, 2014). It is thus important to consider the impact of laminar-turbulent transition on aerodynamic surfaces when targeting effective drag reduction strategies.

The laminar-turbulent transition can play a significant role in many other engineering applications and is not always detrimental. For instance, turbulent flows can be sought in chemical reactors to increase the mixing between different species. In low-speed regimes, such as wind turbines, having a turbulent flow allows reducing or even avoiding flow separation that tends to massively increase the pressure drag. In high-speed aerospace applications, the presence of shock waves in a laminar flow can yield large separation bubbles that can drastically decrease the flow rate in engine inlets. This effect can be mitigated by forcing an earlier transition to a turbulent flow that naturally supports smaller separation regions. In contrast, during the reentry phase of spacecraft in the atmosphere, the heat transfer from the high-temperature flow to the vehicle surfaces must be mitigated by delaying the laminar-turbulent transition. All in all, considering its ubiquitous presence in fluid flows and its notable impact on the performance of many engineering applications, the laminar-turbulent transition remains a critical research topic nowadays.

1.1. Laminar-turbulent transition

The study of the laminar-turbulent transition has been initiated by Reynolds (1883) with experiments on the water flow in a pipe. After introducing a dye at the inlet of the pipe, the

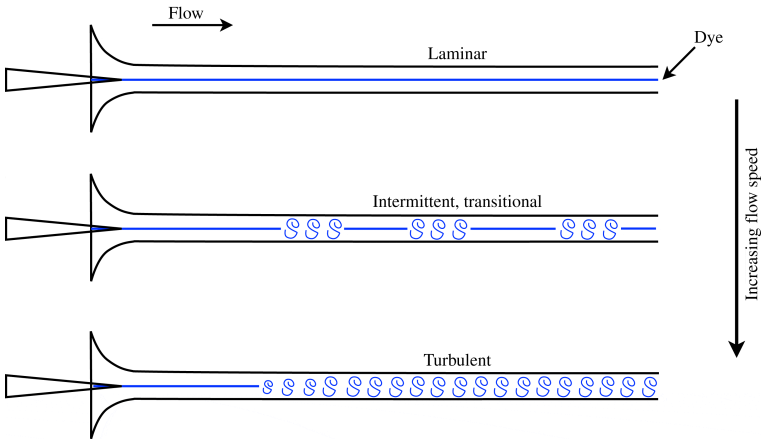

Figure 1.1: Sketch by Barkley (2016) of the flow regimes modeled after the experimental observations of Reynolds (1883) in a pipe flow.

fluid motion was monitored and different regimes have thus been identified. A sketch of the setup and of the regimes is proposed in figure 1.1. At low speeds, the regime is laminar and the dye smoothly follows the water flow. Because the molecular diffusion is very weak, there is almost no mixing and the dye filament remains well defined. When increasing the speed, a swirling, and even chaotic, motion of the dye and a rapid mixing are observed; the flow is considered as being turbulent. A major finding of Reynolds (1883) was that a higher velocity induces an earlier onset of the turbulent regime. This onset is the laminar-turbulent transition. Although the transition does not occur spontaneously, neither in space nor in time, its intermittent character makes it perceived as a sudden emergence of turbulence. According to these observations, Reynolds proposed a single non-dimensional number

$$\mathrm{Re}_{\mathfrak{L}} = \frac{U\mathfrak{L}}{\nu}, \tag{1.1}$$

to assess the regime of a fluid flow by considering only three quantities, namely a characteristic velocity U, a characteristic length $\mathfrak{L}$ and the kinematic viscosity ν of the fluid. The underlying concept of the Reynolds number is to compare the ratio of the inertial forces (i.e., shear rate $U/\mathfrak{L}$) over the viscous forces (i.e., dissipation rate $\nu/\mathfrak{L}^2$). In practice, it allows determining if the flow is laminar or turbulent by assessing whether the shear rate is weak or strong with respect to the dissipation rate, respectively. Finally, this implies that the Reynolds number can be used to predict under which conditions the laminar-turbulent transition occurs.

The mechanisms yielding the imbalance between inertial and viscous forces can be fundamentally different from one flow configuration to another. In this thesis, only external wall-bounded flows, in particular flat-plate boundary layers, are considered. The boundary layer is one of the most fundamental and ubiquitous flows since it develops over any solid surface with a velocity different from the fluid. The fluid viscosity enforces the flow to have the same velocity as the surface and, in turn, it leads to the emergence of a velocity gradient from the surface to the surrounding flow in a direction perpendicular to the sur-

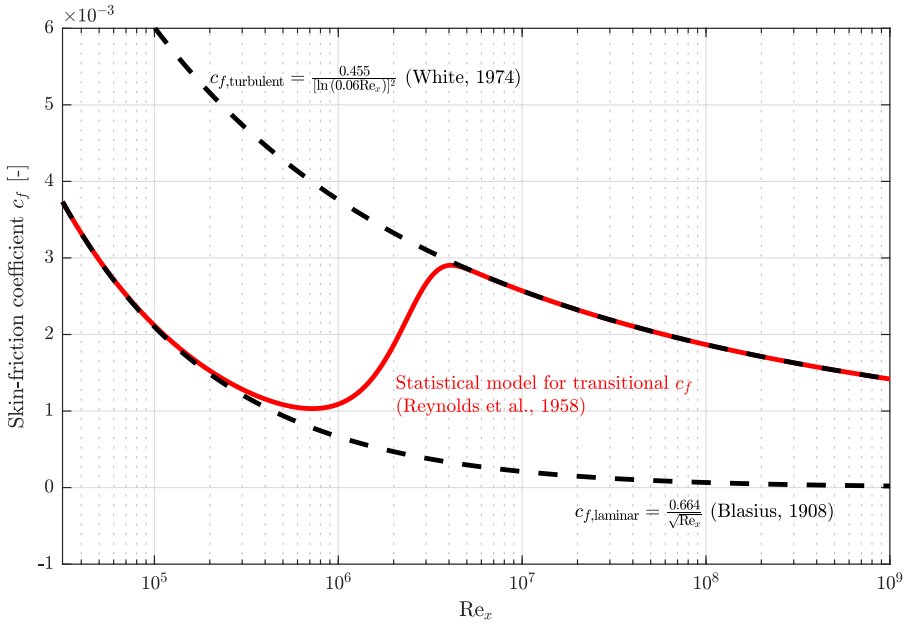

Figure 1.2: Skin-friction coefficient c_f as a function of the Reynolds number Re_x for laminar (Blasius, 1908) and turbulent (White, 1974) flat-plate boundary-layers. A typical transitional c_f from laminar to turbulent flows is indicated by the red curve.

face. The resulting thin shear layer is the so-called boundary layer. It is associated with viscous mechanisms and thus energy dissipation, which are responsible for the skin friction on aerodynamic surfaces.

As the boundary layer develops along the solid surface, the amount of fluid that is entrained into it continuously increases. The velocity gradient perpendicular to the surface decreases and the inertial forces become more dominant as the boundary layer grows downstream. This evolution thus promotes the laminar-turbulent transition and can be thoroughly characterized by a Reynolds number defined as a function of the streamwise coordinate x, starting from the onset of the boundary layer:

$$\text{Re}_x = \frac{u_e x}{\nu}. \tag{1.2}$$

The characteristic velocity is the streamwise velocity u_e at the edge of the boundary layer. This is equivalent to a velocity evaluated in the freestream, away from the solid wall. According to this definition, the Reynolds number can be interpreted as a non-dimensional measure of the streamwise location from the leading edge. The laminar-turbulent transition in boundary layers can be noticed through the evolution of the skin-friction coefficient that drastically increases (red curve in figure 1.2) and achieves a local maximum when the highly energetic turbulent state takes over downstream of the smooth, ordered laminar state at large Reynolds numbers. In view of the dramatic changes in the flow behavior after transition, it is crucial to identify and understand the mechanisms underlying this phenomenon.

1.1.1. Transition in boundary layers

In boundary-layer flows, different routes to turbulence exist that mostly depend on the disturbance level of the environment. On the one hand, if the environment contains only low-

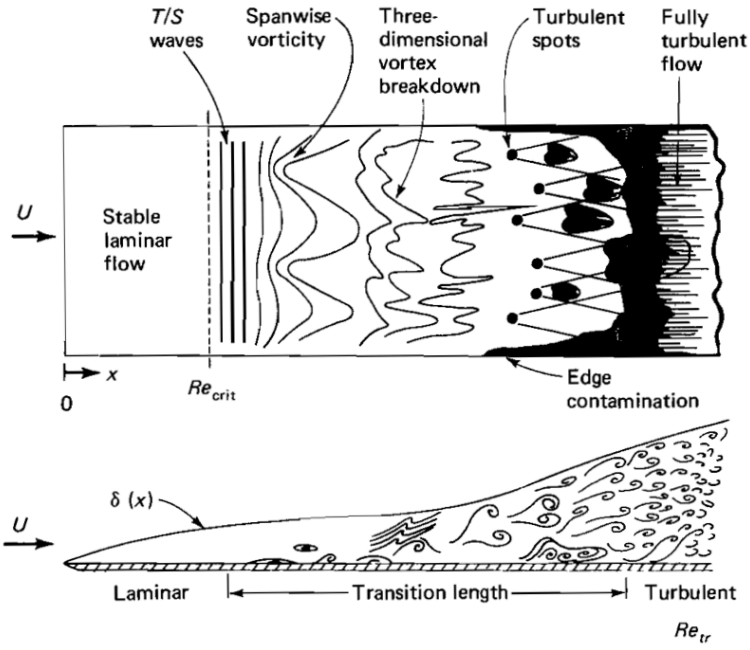

Figure 1.3: Representation of the natural laminar-turbulent transition for a flat-plate boundary layer, taken from White (1974).

amplitude disturbances, the laminar-turbulent transition is said to be natural (Tani, 1969; Reshotko, 1976; Kachanov, 1994; Saric *et al.*, 2003) and follows several stages from the linear growth of the disturbances to the turbulent breakdown. The different stages are depicted in figure 1.3 for a flat-plate boundary layer. This type of transition is the focus of the present work. On the other hand, for large disturbances in the surrounding environment (e.g., large surface roughness, intense freestream turbulence,...), the linear-growth mechanisms are bypassed (Morkovin, 1969, 1994; Andersson *et al.*, 1999; Reshotko, 2001) and the breakdown to turbulence occurs very rapidly. In order to give an overview of the underlying mechanisms, the routes to turbulence are presented in the following by considering the incompressible flat-plate boundary layer with zero-pressure gradient.

In natural laminar-turbulent transition, the first stage prior to the perturbation-growth process corresponds to the receptivity, that is the mechanism allowing an external disturbance to enter the boundary layer (Morkovin, 1969; Reshotko, 1984; Goldstein & Hultgren, 1989; Saric *et al.*, 2002). For instance, the receptivity mechanisms transfer freestream disturbances, that usually contain a broad range of frequencies and wavelengths, into particular waves that can intrinsically exist in the boundary layer. The nature of the external disturbances can be acoustic, kinematic or entropic depending on whether they are pressure waves, vortices or temperature variations, respectively. Note that surface irregularities are not disturbances to the boundary layer per se but can be part of the receptivity process by altering how external disturbances are transferred into the boundary layer. Once entered in the boundary layer through receptivity, the external disturbances can essentially be viewed as initial conditions of the process governing the evolution of the perturbations. Depending on the flow configuration, the amplitude, the frequency or the phase of the initial perturba-

tions, different types of instability mechanisms can be triggered.

The second stage of transition corresponds to the amplification and propagation of two-dimensional waves in the flow field in the streamwise direction (i.e., for increasing x, from left to right in figure 1.3) through a primary instability mechanism. Note that, depending on the flow configuration, an instability mechanism can attenuate or amplify perturbations while also being responsible for their spatial propagation. In this regard, the critical Reynolds number $\mathrm{Re}_{\mathrm{crit}}$ is defined so as to characterize the flow conditions under which at least one frequency is amplified in space and time. For the boundary layer, only one type of unstable primary mechanism exists and causes the growth of the so-called Tollmien-Schlichting waves, depending on their location and their spectral content (Tollmien, 1928; Schlichting, 1933; Schubauer & Skramstad, 1948; Mack, 1984). The process governing the amplification of the primary waves is linear and occurs over a slow viscous time scale $t_\nu = \mathfrak{L}^2/\nu$ while traveling downstream at a phase speed c_{TS}, that is a fraction of the characteristic speed u_e, i.e., $c_{\mathrm{TS}} \approx 0.4u_e$. Hence, the perturbations grow under the linear regime over an extensive region of the flow before they reach large amplitudes.

The nonlinear breakdown yielding turbulence does not result immediately from the amplification of *primary* Tollmien-Schlichting instability waves but, instead, emerges from the growth of linear *secondary* instability waves. This is the third stage of the natural laminar-turbulent transition and, similarly to the primary-instability stage, it can be analyzed using linear stability theory (Herbert, 1988). The secondary instabilities are three-dimensional waves and are a consequence of the slight distortion of the flow by the primary instability waves. Usually, the secondary instabilities emerge when the amplitude of the primary instabilities produce significantly strong inflection points in the distorted flow field. These secondary instabilities have a typical growth rate that is much larger than that of primary waves. This third stage of the transition thus results in a rapid amplification of the disturbances, that scales with the convective time $t_U = \mathfrak{L}/U$, over a relatively short streamwise extent before the nonlinear breakdown. In other words, once secondary instability waves set in, the laminar flow rapidly breaks down to a turbulent flow. This breakdown corresponds to the actual point where large macroscopic changes are observed in the flow. The transition Reynolds number $\mathrm{Re}_{\mathrm{tr}}$ is used to denote the spatial location for this onset of turbulence.

Two different scenarios are usually observed when the amplitude of the primary and secondary waves is large enough to allow nonlinear interaction. These scenarios are denoted as K-type and H-type transitions after Klebanoff *et al.* (1962) and Herbert (1988), respectively. The interaction between the primary and secondary waves yields Λ-vortices that are either aligned in rows (K-type) or arranged in a staggered pattern (H-type). On the one hand, the K-type scenario occurs when the Tollmien-Schlichting and secondary waves have the same frequency. This justifies that the K-type scenario is often referred to as the fundamental transition. On the other hand, the H-type transition is observed when secondary waves oscillate at half the frequency of the primary waves. H-type transition is thus often classified as a subharmonic transition. Since H-type transition requires a lower amplitude of the initial disturbance to set in and has a higher growth rate than K-type, it is theoretically more likely to emerge than K-type transition. In practice, however, the presence of low-amplitude streamwise vorticity in the freestream can favor the formation of K-type transition whereas H-type would have been theoretically expected (Herbert, 1988). Finally, although the breakdown of Λ-vortices to a fully turbulent flow occurs very quickly for both K- and H-type scenarios, a slight difference is observed between the two types of transition. The aligned Λ-vortices in K-type transition first form localized regions of turbulence (turbulent spots) before the flow becomes fully turbulent. In contrast, the formation of turbulent spots is not achievable in the H-type transition because of the staggered arrangement of Λ-vortices and, instead, the

vortices spontaneously break down to a chaotic flow. An extensive review of the different types of nonlinear breakdown is proposed by Kachanov (1994).

Depending on the disturbance level in the environment, the paths of laminar-turbulent transition can be inherently different. The above discussion focused on low-disturbance environments that allow for the sequential growth of linear waves. This scenario can be characterized by the growth of individual eigenmodes at a time (i.e., modal growth). However, increasing the disturbance level can (partially) bypass these mechanisms (Morkovin, 1969). In extreme cases, the laminar-turbulent transition can be solely triggered by disturbances with an amplitude that is large enough to generate turbulence as soon as they enter the boundary layer. This particular scenario is the actual *bypass* transition (Morkovin, 1994) and is usually triggered by intense freestream turbulence or large surface roughness. If only moderate disturbance levels are present in the surrounding environment, the linear stage of the evolution of the perturbations still occurs but eigenmode types combine. This can result in an overall growth that prevails over that of any stable or unstable individual modes. This intermediate scenario is referred to as transient growth (Landahl, 1980; Hultgren & Gustavsson, 1981; Andersson *et al.*, 1999; Reshotko, 2001) and is a consequence of the eigenmodes of the disturbance flow field being non-orthogonal (Schmid *et al.*, 1993; Trefethen *et al.*, 1993). In-depth discussions of the differences between modal and non-modal evolution of disturbances are proposed by Schmid & Henningson (2001).

The main interest of the present work is to describe the dynamics of the inherent flow field perturbations, that are given by the individual eigenmodes. This justifies considering only the evolution of instabilities in a low-disturbance environment. The transient-growth and bypass scenarios, which are triggered by moderate to high disturbance levels, are thus presently left out. In this context, different approaches are usually considered to model and predict the natural transition in boundary layers.

1.1.2. Laminar-turbulent transition in computational fluid dynamics

Depending on the application, numerical modeling of fluid flows is based on different levels of fidelity that can have an impact on the representation of the laminar-turbulent transition. On the one hand, high-fidelity approaches such as Direct Numerical Simulation (DNS) and Large-eddy Simulation (LES) can represent the different stages of the transition from the disturbance growth to the turbulent breakdown without requiring any supplementary closure model for the transition process. Hence, these approaches can be used to study the fundamental aspects of the turbulence breakdown. On the other hand, lower fidelity approaches, based on Reynolds-Averaged Navier-Stokes (RANS) equations for instance, cannot represent the actual transition process. The RANS-based simulations tend to eliminate any linear growth of disturbances present in the early stages of the transition. Since the linear evolution spans most of the streamwise extent of the natural transition process, the RANS approaches are inherently unsuitable to represent the laminar-turbulent transition without considering an additional model dedicated to the prediction of the laminar-turbulent transition. These transition models can either be theoretical or empirical. In both cases, this requires a-priori high-fidelity representations of the laminar-turbulent transition, through numerical simulations or experiments, to first study and then model the transition process. This work tackles the numerical aspects for studying instabilities in a low-disturbance environment in order to ultimately improve the engineering tools for the prediction of the laminar-turbulent transition.

A Direct Numerical Simulation solves the nonlinear Navier-Stokes equations by resolving all scales present in the flows and can thus represent the flow physics with the highest

fidelity. In the context of laminar-turbulent transition, DNS can be used to assess the complete development of perturbations, from receptivity to turbulence breakdown, for any flow configuration. The different stages of the transition for a flat-plate boundary layer have, for instance, been studied with DNS by Rai & Moin (1993) and Rist & Fasel (1995). These studies corroborated the observations made in experiments, especially regarding the different types of nonlinear breakdown (e.g., K- and H-type transition) by having a precise control on the parameters influencing the laminar-turbulent transition. However, since all details of the fluid flow are targeted with DNS, the approach is computationally expensive and, in practice, only a few canonical cases can be accurately resolved in a reasonable amount of time. Hence, DNS is usually not adapted to represent the laminar-turbulent transition for real engineering applications and can only be used as a substitute of experiments in order to, for instance, calibrate transition models to be used in RANS approaches (Menter *et al.*, 2006).

Large-eddy simulations offer better flexibility than DNS regarding the complexity of the flow configurations since they require fewer computational resources. However, because the smallest scales of the turbulence are modeled in LES, the solution suffers from a lower level of fidelity than DNS. These so-called subgrid-scale (SGS) models determine thus the fidelity of the laminar-turbulent transition representation. On the one hand, if the subgrid model is too dissipative, the disturbance growth taking place in the transition process cannot be captured. With such SGS models, an additional modeling of the early stage of transition is required and LES are thus not adapted anymore to study the fundamental aspects of the laminar-turbulent transition. On the other hand, for SGS models with non-constant coefficients, both linear and nonlinear stages of the laminar-turbulent transition can be relatively accurately represented (Sayadi & Moin, 2012) and LES can be used to build lower-fidelity models of the transition.

The DNS and LES approaches inherently rely on solving the nonlinear Navier-Stokes equations and thus require a judicious choice of initial conditions or forcing, especially in terms of amplitude, to disturb the flow. The choice of initial conditions or forcing can be made according to the expected response of the flow to the disturbance. However, if the flow physics is not well known, the choice is most likely arbitrary. In both cases, prescribing an initial condition or forcing can occult (part of) the response of the flow to the disturbance if the relevant instability mechanisms are not triggered. Although this argument holds for all initial-value problems, the choice of initial conditions or forcing becomes even more complicated when solving nonlinear equations because the solutions do not only depend on the type or shape of an initial condition but also on the amplitude. Furthermore, each individual disturbance introduced in the flow requires conducting an entire DNS or LES to analyze the response of the system. Because studying the overall stability of flows genuinely requires considering a large parameter space of disturbances, the computational cost of DNS and LES makes them unsuitable for stability analyses. In order to tackle the stability of fluid flows, another method than DNS and LES is presently necessary. For that purpose, linear stability methods are more suitable since they can provide information about the disturbance growth in a way that is independent of the type and amplitude of initial conditions or forcing.

1.1.3. Predicting transition with linear stability theory

Linear stability methods allow targeting the perturbation dynamics of a flow at a low computational cost while avoiding the difficulties associated with the initial disturbance or forcing. Since the first successful application of linear stability analyses to the boundary layer

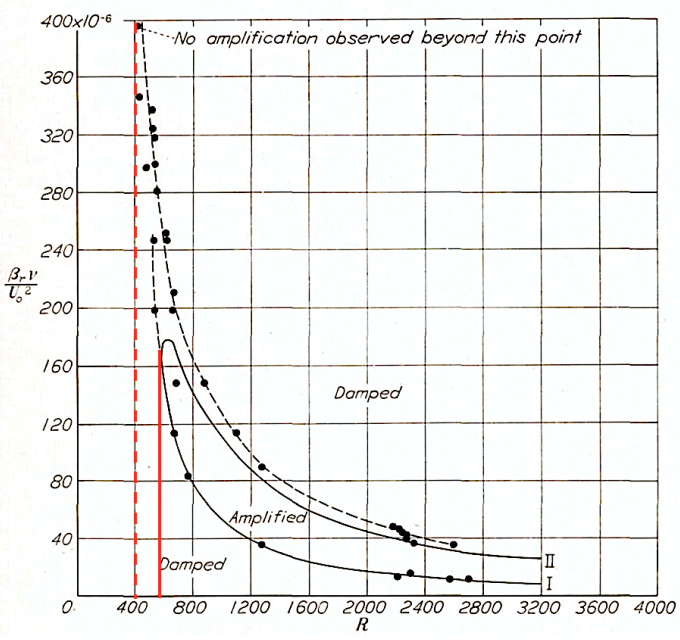

Figure 1.4: Theoretical (solid line, Tollmien (1928)) and experimental (dots and dashed line, Schubauer & Skramstad (1948)) neutral curves of an incompressible flat-plate boundary layer for non-dimensional frequencies (vertical axis) and Reynolds number based on displacement thickness (horizontal axis). Red lines for the theoretical (solid) and experimental (dashed) critical Reynolds numbers. Figure adapted from Schubauer & Skramstad (1948).

by Tollmien (1928) and Schlichting (1933), these methods have been extensively applied to a large variety of flows and remain nowadays an important tool to predict laminar-turbulent transition and, in a general sense, identify flow instabilities.

Since the first experiments of Reynolds (1883), there has been a need for a mathematical framework that could precisely quantify both the onset of instabilities in fluid flows and the breakdown to turbulence (Reynolds, 1895). Although the derivation of the boundary layer equations by Prandtl (1905) led Orr (1907) and Sommerfeld (1909) to elaborate the corresponding stability equation (namely the Orr-Sommerfeld equation), the first unstable solutions have only been found twenty years later by Prandtl's disciples Tollmien (1928) and Schlichting (1933). In particular, they identified two-dimensional waves whose wavelength and (un)stable character vary with the Reynolds number. This eventually led them to compute a critical value of the Reynolds number, $\mathrm{Re}_{\mathrm{crit}}$, that can be used to determine the onset of instabilities in the boundary layer. Hence, their work provides the first theoretical evidence of instability waves in the boundary layer. However, because of the technical difficulties in obtaining a low-disturbance environment in wind tunnels, the existence of Tollmien-Schlichting waves has only been confirmed a decade later by the experiments of Schubauer & Skramstad (1948). Based on these aforementioned studies, a stability diagram, namely the neutral curve, can be obtained for identifying the frequencies and Reynolds numbers for which small-amplitude disturbances in the boundary layer are amplified or damped. The neutral curve obtained from the measurements of Schubauer & Skramstad (1948) and the results from stability theory (Schlichting, 1933) are depicted in figure 1.4.

The experiments prove that linear instability waves are present in the boundary layer and that they can be obtained by solving the linear stability problem. However, the onset of

linear instability growth in the boundary layer does not correspond to the turbulence breakdown. In other words, the left branch (branch I) of the neutral curve (see figure 1.4) does not represent the location where the turbulence emerges but instead gives the point where small-amplitude instability waves start to grow (until reaching the right branch, i.e., branch II). As described earlier, the natural laminar-turbulent transition follows from perturbations being amplified by primary and then secondary linear instability mechanisms before attaining a sufficiently large amplitude to yield the breakdown to turbulence at $\mathrm{Re}_{\mathrm{tr}}$. Hence, there is a significant gap between the onset of the primary instability growth as given by the neutral curve and the turbulence breakdown. This thus led van Ingen (1956) and Smith & Gamberoni (1956) to elaborate a semi-empirical method, namely the e^N-method, that only uses the spatial amplification of primary instabilities to predict the onset of turbulence. The major assumption behind the N-factor method is supported by the fact that the growth of primary instabilities occurs over a much longer streamwise extent than that of the subsequent stages of the transition. However, this method remains semi-empirical in the sense that the threshold value N, that defines the maximum amplification of the instability waves over all frequencies, must be a-priori chosen and is based on the experimental assessment of the turbulence onset. Usually set to $N = 9$ for quiet flight conditions, the value N can also be chosen as a function of the turbulence intensity in the freestream (White, 1974). Finally, given the effectiveness and simplicity of the e^N-method, it is still a widely used engineering tool to predict transition.

This bridge between linear stability analyses and the onset of turbulence reveals the importance of considering the linear regime. With the advent of the computer age, the stability equations gained interest for the study of other flow configurations. A comprehensive review of the stability of the incompressible boundary layer for various conditions, such as with pressure gradient, blowing/suction or non-constant temperature field, has been proposed by Schlichting (1979). Furthermore, with the increasing interest in high-speed flights, Mack (1984) extended the boundary-layer stability analyses by deriving the (in)compressible Linear Stability Theory (LST) equations as a more general formulation than the Orr-Sommerfeld equation, which was limited to the incompressible regime only. Note that, in its incompressible formulation, the LST equations are equivalent to the Orr-Sommerfeld equation and are also cast as an eigenvalue problem.

An essential aspect of the Orr-Sommerfeld and LST equations is that they are devised to assess the linear stability of individual one-dimensional profiles of the flow. In other words, these equations assume that the flow does not evolve in more than one direction. This is the so-called parallel-flow assumption. In the case of the boundary layer, which slowly evolves in the streamwise direction and has a much stronger gradient in the wall-normal direction than in the streamwise direction, accounting for the variation of the velocity profile in the wall-normal direction only is reasonable. This is illustrated in figure 1.4 by the good agreement between experiments and theory for most of the neutral curve. However, the parallel-flow assumption reduces the accuracy of the stability analysis when the flow field features a larger gradient in the streamwise direction. A typical example of the parallel-flow assumption being too strong is the deviation of the LST neutral curve from the experimental measurements at low Reynolds numbers. In fact, in the vicinity of the flat-plate leading edge, the boundary-layer profiles rapidly evolve in the streamwise direction and, by discarding additional destabilizing effects induced by the streamwise gradient, the LST predicts a critical Reynolds number that is larger by 30% than the one observed in experiments. Considering the two dimensionality of the boundary layer is thus essential close to the leading edge. Given that linear stability methods go beyond the study of transition on the flat-plate boundary layer and can actually be used to study the linear regime of instability mechanisms

in highly-dimensional fluid flows, there is a need for more elaborate methods.

1.2. Stability of streamwise flows

Most real applications cannot be reduced to one-dimensional problems, especially if the flow experiences rapid variations in more than one direction. Typical aeronautic applications are, for instance, wings, curved fuselage surfaces or surface roughness caused by joints. Furthermore, in high-speed flows, shock waves introduce discontinuities or very rapid variations of the flow in a short region. This thesis focuses on the stability of flows that have large in-plane gradients in the sense that they rapidly evolve in both the streamwise and wall-normal directions with only weak to no variation in the third, i.e., spanwise, direction. These flows are here referred to as streamwise flows. As already suggested by the low-Reynolds-number boundary layer, stability analysis methods that account for the higher flow dimensionality are essential to accurately resolve all stabilizing and destabilizing effects of streamwise flows. Additionally, the spatial evolution of the flow also impacts how an instability mechanism propagates a disturbance introduced in the flow field.

1.2.1. Instability mechanisms

Disturbances introduced in a flow field vary simultaneously in space and time, but the way they vary depends on the nature of the instability mechanism. The mechanism can be convective, absolute or global. While the first two can be found in both parallel and spatially-developing flows, a global mechanism only exists if the flow is at least two-dimensional. The concept of convective and absolute instabilities was initially developed for plasma physics by Briggs (1964) and Bers (1984) and then extended to fluid flows by Huerre & Monkewitz (1985). It aims to describe how a disturbance initially introduced at $t = 0$ and $x = 0$ behaves in space and time when $t \to \infty$. A convective instability mechanism carries the disturbance such that the flow at $x = 0$ returns back to its initial unperturbed state for $t \to \infty$. Hence, a flow that supports a mechanism that amplifies and transports a perturbation away from its initial position is convectively unstable. In contrast, an absolute instability mechanism supports a disturbance growth for all x-locations, such that an absolutely unstable flow never returns back to its initial, undisturbed state. An illustration of the two instability mechanisms is proposed in figure 1.5. Usually, one flow configuration is not strictly convectively or absolutely unstable and a threshold from one (un)stable to another (un)stable state often exists. A spatially-developing flow can have regions that are locally stable, convectively or absolutely unstable. For example, a boundary layer is stable upstream of the critical Reynolds number and, for more downstream locations, is convectively unstable. The convective instability mechanisms give rise to the Tollmien-Schlichting waves that travel and grow in the downstream direction with a positive speed. A boundary layer is thus either stable or convectively unstable. In contrast, bluff-body wakes can be stable, convectively or absolutely unstable, depending on threshold Reynolds numbers. For a two-dimensional cylinder, the lower limit sets the boundary between a stable and convectively unstable flow while the upper limit defines the transition from a convective to an absolute instability mechanism.

In some spatially-evolving flows, a confined spatial region that is absolutely unstable can trigger a resonant and self-sustained amplification of the perturbation (Pierrehumbert, 1984; Koch, 1985). Chomaz *et al.* (1988), Huerre & Monkewitz (1990), Chomaz *et al.* (1991) and Monkewitz *et al.* (1993) classified this mechanism as a global instability. This can only be observed if a large enough region of the flow that is absolutely unstable is surrounded by stable or convectively unstable regions. If these two conditions are met, any infinitesimal perturbation entering the absolutely unstable region can indefinitely grow within the con-

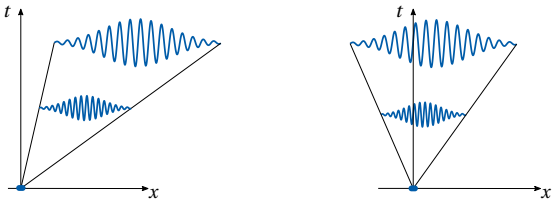

Figure 1.5: Schematic representation of convective (left) and absolute (right) instabilities for an initial disturbance (blue dot) introduced at $t = 0$ and $x = 0$.

fined region of space through feedback mechanisms. Global instability mechanisms thus contrast with convective or absolute instabilities that either leave the flow in its initial unperturbed state or propagate everywhere in space with theoretically infinite-amplitude disturbance when $t \to \infty$. A global instability typically arises in the wake of two-dimensional cylinders for a sufficiently high Reynolds number, i.e., when the pocket of absolutely unstable flow is large enough. Because of the need for a confined region in space, the concept of global instability only applies to spatially evolving flows.

For any type of mechanism, the emergence of unstable regions correlates with regions of the flow where high gradients exist, i.e., in the shear layer. A shear layer can be confined or not in space, although no universal criterion exists to make a clear distinction. On the one hand, a confined shear layer, e.g., in the near-wake of a cylinder (Casacuberta *et al.*, 2018), a roughness element (Loiseau *et al.*, 2014) or in a laminar separation bubble (Theofilis & Rodríguez, 2010), can provide the necessary condition for the emergence of a global (in)stability mechanism. On the other hand, if the shear layer is technically (semi-)infinitely long, such as in a boundary layer, no instability mechanism can be confined in space and the flow is ineluctably globally stable. In other words, the localized character of the instability mechanism is mostly governed by the advection of the flow that redistributes the perturbations in space (Groot, 2018). Hence, if feedback mechanisms are such that the disturbance remains contained in a finite region of the flow, a global (in)stability mechanism can emerge. These feedback mechanisms can be caused by (upstream) advection of perturbations or acoustic waves. A (semi-)infinite boundary layer has a dominant advection component that reaches from upstream to downstream without finite limit. Accordingly, any disturbance that is introduced into the flow is convected away in the direction of the dominant advection component. Note that advection can have the same role in absolutely unstable flows in the sense that it indefinitely carries the disturbances in both upstream and downstream directions. The fact that a shear layer is confined or not has not only a physical consequence on the types of instability that can take place but also on the numerical representation of these instabilities.

1.2.2. Stability analyses

Linear modal stability analysis can identify the different types of instabilities, provided that the underlying assumptions are in agreement with the spatial evolution of the flow. In the following, only modal methods are considered since they provide information about the general perturbation dynamics. The solutions from these methods are (based on) eigensolutions that can actually represent the individual convective, absolute or global instability mechanisms that inherently exist in the flow field. The most well-known methods are the LST equations, the Parabolized Stability Equations (PSE) and the BiGlobal stability equa-

tions.

The LST equations were the first equations derived to study the stability of flows and were used to build the neutral curve of the boundary layer. Since each streamwise location is treated independently from the rest of the flow, the LST method is a local stability method. Hence, by neglecting any interaction between (un)stable regions of the flow, the LST method can only identify absolute and convective instabilities. Furthermore, the parallel-flow assumption in LST completely neglects the streamwise gradients, which, by continuity, implies that no velocity in the wall-normal direction is included in the stability equations. For instance, the slow evolution of the boundary layer in the streamwise direction induces a wall-normal velocity component that scales with $1/\sqrt{\mathrm{Re}_x}$. The non-parallel effects thus become important when approaching the leading edge, i.e., when $\mathrm{Re}_x \to 0$. Since this aspect is neglected in LST, discrepancies between the theoretical and experimental neutral curves of the boundary layer were found at low Reynolds numbers. If accurate solutions are sought in regions of large in-plane gradients, all flow variations must thus be accounted for in the stability equations.

In order to improve upon LST, the parallel-flow assumption must be relaxed and this led to the development of nonlocal methods. These approaches include the contribution of the slow streamwise evolution of the flow by applying a correction onto the local, zeroth-order stability solutions, i.e., the LST solutions. The correction is based on a streamwise integral of the first-order contributions that stem from the in-plane gradients. Because of the integral-based correction, these methods are referred to as nonlocal methods. In practice, boundary-value problems based on multiple-scale and Wentzel–Kramers–Brillouin-Jeffreys (WKBJ) methods were first proposed by Bouthier (1973), Gaster (1974) and Saric & Nayfeh (1975) to include weak streamwise variations in stability analyses. Later, Herbert & Bertolotti (1987) and Bertolotti *et al.* (1992) improved upon the WKBJ approach by introducing the Parabolized Stability Equations (PSE) that are formulated as an initial-value problem. When applied to the boundary layer, all above nonlocal methods can predict a critical Reynolds number that is in excellent agreement with experiments. Nevertheless, the advantage of the PSE method is that it allows tackling slowly-evolving flows in a computationally efficient way. This computational superiority over the other non-parallel methods comes from the parabolization of the stability equations. Note that the equations do not represent a boundary-value problem (or an eigenvalue problem) anymore but, instead, an initial-value problem in space. Hence, the solutions of the PSE are obtained through a spatial integration that is initialized from one LST solution obtained at a given upstream location. Strictly speaking, the PSE is thus not a modal approach since it does not solve an actual eigenvalue problem. However, it still tracks modal solutions in the sense that it only applies a correction to the LST eigensolutions to take into account the history of the streamwise evolution of the flow. Since the advent of the PSE method, it has been applied to a wide variety of flows and good agreement is usually found with experiments or DNS. However, since the PSE method is devised to account for *slowly* evolving flows only, its accuracy decreases when strong in-plane gradients are involved. Furthermore, the PSE method is inherently parabolic in the streamwise direction and can only capture an instability wave that travels downstream (Towne *et al.*, 2019). In order to effectively track this wave, the PSE approach relies on damping all other upstream traveling waves, that are often acoustic waves, and that would destabilize the spatial integration. The damping introduced by the PSE can, however, affect the accuracy of the tracked downstream-traveling wave. In order to overcome this aspect, Towne & Colonius (2015) and Rigas *et al.* (2017) introduced the One-Way Euler (ONE) and Navier-Stokes (OWNS) equations as alternative approaches to PSE that both rely on finding approximate solutions of the exact wave equations. The motivation behind the

one-way approaches is to perform stability analyses of flows that support multiple traveling waves with similar growth rates. Nevertheless, these approaches have a higher computational cost than the PSE approach that usually provides reasonably accurate results for flows dominated by one downstream-traveling convective instability. Finally, since convective instabilities are not the only type of instability mechanisms that can be encountered in fluid flows, the applicability of the PSE and ONE/OWNS methods is limited.

Absolute and global instabilities are elliptic mechanisms, in the sense that they can propagate both upstream and downstream without any preferential direction, and, thus, they cannot be captured by the PSE method. Instead, they require solving actual elliptic stability equations. Although some ellipticity in the streamwise direction can be introduced into the nonlocal stability equations by considering the WKBJ method (Monkewitz *et al.*, 1993), this type of approach is not suitable for highly two-dimensional flows. In order to circumvent these limitations, two-dimensional stability equations have been introduced by Pierrehumbert & Widnall (1982), Pierrehumbert (1986), Theofilis (2003) and Theofilis (2011). The eigenvalue problem formulation of the two-dimensional stability equations is referred to as the streamwise BiGlobal stability problem. Being fully elliptic and accounting for all in-plane gradients, the BiGlobal stability equations aim to improve upon the (non)local approaches. However, the elliptic representation of convective instabilities provided by the BiGlobal method suffers from critical numerical sensitivities. This aspect is the main motivation of the present work.

1.3. Elliptic description of convective instabilities

The streamwise BiGlobal equations have been applied to numerous flow types and enabled accurate numerical representations of global instability mechanisms. However, when applied to represent convective instability mechanisms in the streamwise direction, the results suffer from a notorious sensitivity to the computational setup. This sensitivity is associated with the truncation of the numerical domain in the streamwise direction (Ehrenstein & Gallaire, 2005; Alizard & Robinet, 2007; Rodríguez *et al.*, 2011; Cerqueira & Sipp, 2014; Garnaud *et al.*, 2013). TriGlobal stability analyses (Brynjell-Rahkola *et al.*, 2017) also face the same limitation. The results of Alizard & Robinet (2007, §IV.B.2) suggest that the part of the eigenvalue spectrum that is of interest tends to a continuum as the streamwise domain length tends to infinity. The reason behind this behavior of the solution stems from the very nature of the convective instabilities and the unconfined character of the corresponding shear layer.

Only a finite region of space can be tackled in a numerical context and it thus requires to truncate the flow field at given locations. These locations define the computational domain. If the shear layer is confined, the boundaries can be placed sufficiently far away from the region of interest and thus the limits of the domain do not interact with the physical mechanisms taking place in the interior of the domain. However, for unconfined shear layers, the boundaries necessarily truncate the shear layer that evolves from the inlet to the outlet of the domain. It implies that the behavior enforced at (one of) these two streamwise boundaries influences the interior dynamics (Groot *et al.*, 2015). Hence, since a convective instability is carried along with the shear layer, it inevitably interacts with the domain limits.

When eigenfunctions are pinned to the domain boundaries, a continuous branch of eigenvalues forms in the spectrum. This branch includes all eigenvalues associated with eigenfunctions that fit in the domain; the minimal wavenumber of the eigenfunctions is fixed by the imposed domain length. Increasing the domain length decreases the minimal wavenumber that can be resolved and thus more eigenvalues can be contained in the branch

of the spectrum. For an infinite domain length, a continuum of eigenvalues eventually forms in the spectrum. Continuous branches can, for instance, be observed in LST solutions that are dominated by wall-normal advection or in streamwise BiGlobal stability analyses of flows with streamwise advection. In the regard of the formation of a continuous spectrum as the streamwise domain length is increased towards infinity, Theofilis (2011) states that: "the discretized approximation of the continuous spectrum will always be under-resolved". More generally, the numerical description of convective instabilities with the streamwise BiGlobal equations is conditioned by the mathematical treatment at the truncation boundaries. For this reason, the literature counts many applications of the BiGlobal method whose results depend significantly on the computational setup. This aspect motivated the use of alternative methodologies to tackle convective instabilities in two-dimensional flows.

1.3.1. Alternative methods and their limitations

Alternative approaches accounting for elliptic effects are usually considered to study linear convective instability mechanisms in two- or three-dimensional flows. First, resolvent and optimal-perturbation analyses (Farrell, 1988; Trefethen *et al.*, 1993; Schmid & Henningson, 2001; Sipp *et al.*, 2010; Taira *et al.*, 2017; Bugeat *et al.*, 2022) depart from the eigenvalue-problem formulation by considering a Singular Value Decomposition (SVD) instead. The SVD methods optimize the growth over all possible input perturbations by evaluating the temporal evolution of an arbitrary a-priori-chosen energy norm. By definition, the SVD methods thus restrict the evolution of the perturbations to an optimal scenario only. The resulting optimal solution represents one non-modal perturbation evolution that stems from a very specific combination of modal solutions. In resolvent analysis, the disturbance shape corresponding to a given forcing frequency is sought to maximize the amplification. This approach, therefore, follows a particular forced dynamics; it asks what disturbance is the most amplified upon imposing a forcing at a constant frequency to the flow. In optimal perturbation analysis, initial conditions are sought to optimize the amplification of a perturbation norm after a fixed elapsed time. Although the flow is disturbed in an instantaneous sense rather than being continuously forced, the optimal solutions are particular, because they are specific to the prescribed elapsed time. To summarize, the elliptic effects are taken into account by SVD methods at the cost of restricting the solutions to the non-modal perturbation dynamics instead of the more universal modal perturbation dynamics that was given by the eigensolutions. The results obtained from the SVD methods are actually so particular that, in practice, these disturbance dynamics usually cannot be reproduced in an experimental context. For this reason, White (2002) emphasized the importance of studying non-optimal perturbation growth instead.

Recent work by Huang & Wu (2017), Zhao *et al.* (2019), Hildebrand *et al.* (2020) and Appel (2020) considered the Harmonic Linearized Navier-Stokes (HLNS) method to study linear convective instability mechanisms while accounting for elliptic effects. This method evaluates the perturbation problem as a signaling problem; it studies the response of the flow to a continuous forcing usually applied at the inlet of the domain. In contrast to SVD methods, the HLNS approach relies on an a-priori chosen particular forcing function and does not seek any optimal perturbation growth. For a known incoming disturbance environment or for targeting a specific instability, the HLNS are thus a very reasonable approach for structuring the perturbation dynamics. Nevertheless, the continuous forcing at the inlet of the domain can occult the inherent dynamics of the flow.

All in all, although the SVD and HLNS methods improve upon the LST or PSE methods by accounting for elliptic effects, they only provide information about specific dynamics

of the perturbation. In the present work, the focus is put on finding convective instability mechanisms that are not associated with particular evolution of the perturbations.

1.4. Thesis motivation and objective

On the one hand, the modal stability equations provide (eigen)solutions that represent the general perturbation dynamics of a flow field. This, however, comes at the cost of either neglecting elliptical effects or having the interior dynamics that is influenced by the truncation boundaries. On the other hand, SVD and HLNS methods account for all elliptical effects but only seek particular solutions that do not necessarily represent the general perturbation dynamics. These limitations of SVD, HLNS and BiGlobal methods motivate the development of a novel approach.

The objective of the present work is thus to describe accurately convective instabilities in highly two-dimensional flows by devising a numerical methodology that can:

- represent convective instabilities with linear, fully-elliptic equations that account for all gradients of the flow,
- represent the inherent perturbation dynamics of the flow by avoiding any particular scenario of the perturbation evolution,
- provide solutions forming a basis that can be used to represent the perturbation evolution by projecting any arbitrary disturbance onto it.

All above requirements point toward the eigenvalue-problem formulation of the stability problem. The solutions of an eigenvalue problem (in a stationary frame of reference) are not restricted to any particular frequency or elapsed time; they are valid for (A1)[1] all time and cover (A2) all relevant frequencies for the flow of interest. In this framework, (A3) any perturbation can be reconstructed using a particular superposition of eigenmodes (Schmid & Henningson, 2002; Ehrenstein & Gallaire, 2005; Åkervik *et al.*, 2007, 2008), that actually form a physical basis. This basis allows reconstructing the response of the flow to a particular disturbance *a-posteriori*. Furthermore, it also enables performing receptivity analysis that describes how arbitrary disturbances in the surrounding environment are entrained into a particular flowfield (Saric *et al.*, 2002). Finally, if the eigenmodes dominantly contributing to the amplification of disturbances are known, (A4) the scope of the eigenfunction superposition can be reduced to that particular subset of modes. The degrees of freedom of the problem are thus significantly reduced by focusing on the physically relevant dynamics only, which, in turn, decreases the computational cost. In virtue of these properties, the present thesis builds upon the BiGlobal approach to tackle the fully-elliptic representation of convective instabilities with setup-independent solutions. For that purpose, a framework based on the formulation of the two-dimensional stability problem in a moving frame of reference is proposed.

An additional objective of the thesis is to demonstrate the advantage of this new framework by applying it to perform stability analyses of an incompressible flat-plate boundary layer and a laminar shock-wave/boundary-layer interaction (SWBLI). While the incompressible boundary layer case allows validating the method by comparing it against LST and PSE methods, the SWBLI case is a flow configuration that needs to be tackled with the

[1] In this paragraph, the main advantages of an eigenvalue problem formulation in the stationary frame of reference are labeled (A1) through (A4) for later reference.

present methodology because it is a highly two-dimensional flow with strong in-plane gradients caused by the shock waves. Studying the SWBLI thus allows demonstrating the effectiveness of the method in complex flows and gaining insight into the SWBLI stability. In particular, the present work aims to determine the convective instability mechanisms at the origin of the amplification of perturbations propagating across the shock-induced separation bubble.

1.5. Stability analyses in a moving frame of reference: contribution to the state of the art

The main contributions of this work are twofold. First, the mathematical formulation of the moving-frame methodology is proposed for the two-dimensional stability equations and is compared against the traditional stationary-frame approach. This first contribution includes the validation of the moving-frame approach with stability analyses of an incompressible flat-plate boundary layer. Secondly, the moving-frame methodology is applied to a laminar SWBLI for which traditional stability techniques, i.e., LST and PSE methods, cannot appropriately represent convective instabilities.

1.5.1. Novel formulation of the two-dimensional stability problem

An extensive theoretical motivation for formulating the eigenvalue problem in a moving frame of reference is presented by Groot (2018) and Groot & Schuttelaars (2020). The streamwise two-dimensional stability problem has already been considered in a moving-reference frame before (Mittal & Kumar, 2007; Mittal *et al.*, 2008; Kumar & Mittal, 2012), but only to specifically target convective instability mechanisms in the wake of a cylinder. By building upon the work of Groot (2018) and Groot & Schuttelaars (2020), the present thesis goes beyond a specific application by providing a complete framework with methodological, physical and mathematical insight into two-dimensional stability analyses using a moving frame of reference. A particular emphasis is placed on the fact that using a moving reference frame allows obtaining *localized* eigenfunctions that do not depend on the truncation boundary position or conditions.

By using a moving frame of reference, the eigensolutions solve the linearized Navier-Stokes equations in an instantaneous sense. This implies that the property of being valid for all time, i.e., property (A1) of the eigenvalue problem in the stationary reference frame is lost. Nevertheless, properties (A2), (A3), and (A4) are preserved. In other words, the eigensolutions' validity for all times is sacrificed for a localized, computational-setup-independent nature and to avoid the restriction associated with optimal-growth scenarios. Due to their instantaneous validity, these eigensolutions actually represent perfect initial conditions that can be introduced into the linearized Navier-Stokes equations. The present method thus proposes to integrate these initial conditions in time in order to assess the temporal evolution of the perturbations in the flow. This approach is similar to the PSE methodology but improves upon it in the sense that there is no assumption on the flow evolution or on the type of instability mechanisms that can be resolved. With the moving-frame approach, the perturbation characteristics that are important for practical purposes (such as amplification and neutral curves) are recoverable with all elliptic effects being taken into account. Furthermore, it improves upon traditional time-marching approaches (Rist & Fasel, 1995; Hader & Fasel, 2019; Browne *et al.*, 2019) in the sense that the present results are independent of the choice of the initial conditions and of the speed of the reference frame (as long as localized solutions are obtained). To demonstrate the working principles of the method,

the methodology is applied to convectively unstable wall-bounded shear flows.

1.5.2. Applications of the methods

Two streamwise developing flows are presently considered to demonstrate the effectiveness of the moving-frame approach: the classical incompressible boundary layer over a flat plate and the laminar shock-wave/boundary layer interaction. In both cases, the main goals are, first, to obtain localized eigenfunctions that are independent of the numerical setup and, second, to use these solutions as the initial condition of the temporal perturbation problem to reconstruct the traditional amplification curves.

Incompressible flat-plate boundary layer

The incompressible flat-plate boundary layer is the archetype of convectively unstable non-parallel, wall-bounded shear flows. Furthermore, since the boundary layer is only slowly developing in the streamwise direction, LST and PSE methods can provide relatively accurate stability results. Although the boundary layer is a relatively simple shear flow, it reaches from the inlet to the outlet of the numerical domain and, thus, stability analyses of the boundary layer with the BiGlobal method are untractable. In this regard, Alizard & Robinet (2007) could not obtain converged, setup-independent solutions. Furthermore, comparisons with (non)local methods can only rely on prescribing setup-dependent eigenvalues of the BiGlobal spectrum as (complex) forcing frequencies of the spatial LST and PSE methods. In this sense, the BiGlobal results of the incompressible boundary layer in a stationary frame of reference are actually solutions particularized to specific domain size and truncation boundaries. Hence, these solutions cannot describe the general perturbation dynamics of the boundary layer and do not allow reconstructing the neutral curve (Alizard & Robinet, 2007; Niessen, 2017). The importance of considering non-optimal growth in the boundary layer has also been identified by Sipp & Marquet (2012), who could not recover the sub-optimal, i.e., traditional, neutral curve with the optimal forcing approach, especially branch II.

For these reasons, the boundary layer is an ideal case to demonstrate the principles of the moving-frame method and, most importantly, to compare the two-dimensional localized perturbations with the results traditionally obtained with LST and PSE methods by reconstructing neutral and amplification curves.

Shock-wave/boundary-layer interaction

The second flow configuration is a SWBLI that is a ubiquitous phenomenon in high-speed aerodynamics. The SWBLI significantly impacts aircraft performance and can, for instance, promote laminar-turbulent transition, cause excessive heating of aerodynamics surface, generate pressure losses in engine intakes or even induce local fatigue of structures (Délery & Dussauge, 2009). Since the first discoveries of SWBLI, it has been extensively studied over numerous configurations; reviews of the work accomplished over the past decades have been proposed by Délery *et al.* (1986); Dolling (2001); Babinsky & Harvey (2011) and Gaitonde (2015). Considerable efforts have also been invested to reveal the mechanisms governing the breathing of the recirculation bubble, the oscillations of the shock system or the laminar-turbulent transition. However, comprehensive research work is still required to understand these unsteady phenomena. Since no study converged to a consensus regarding the origin of the unsteadiness, there is a need for an appropriate method to identify and distinguish the governing mechanisms supported by SWBLI configurations. This thesis contributes to that aspect by considering two-dimensional linear stability analyses of a laminar

SWBLI case with the moving-frame approach. The main results are summarized in an article published in Physics of Fluids (Niessen *et al.*, 2023).

Considering the case of a SWBLI first aims to demonstrate the effectiveness of the moving-frame method for a more complex, highly two-dimensional flow that inherently requires a two-dimensional formulation of the stability equations. Second, since the LST and PSE methods are not strictly applicable in two-dimensional flows, convective instability mechanisms could not be accurately captured in SWBLI (Sansica *et al.*, 2013, 2016). Although elliptic methods were considered in past studies, only optimal perturbation growth (Dwivedi *et al.*, 2020) or domain-dependent BiGlobal results (Guiho *et al.*, 2016) could be obtained. A novel perspective on convective instabilities in SWBLI is proposed by considering the moving-frame approach. The characteristics of the most amplified perturbations in SWBLI are identified and, using the perturbation energy equation, the three-dimensional mechanisms responsible for the perturbation growth across the shock-induced bubble are characterized.

1.6. Thesis outline

The present thesis is structured in six chapters as follows. After this introduction, Chapter 2 builds upon the state-of-the-art of linear stability theory to present the mathematical formulation of the two-dimensional stability equations in both stationary and moving frames of reference. This chapter also discusses the consequences of using a moving frame of reference and proposes a framework for the corresponding stability analyses. Furthermore, the perturbation energy equation is presented in order to decompose the growth rate into its individual contributions.

Chapter 3 discusses the numerical strategies to solve the stability problem. First, the mathematical aspects of pseudospectral and finite-difference discretization approaches are presented. Secondly, the methodologies to solve both the initial- and boundary-value problems are discussed.

By considering the incompressible flat-plate boundary layer as a first application of the methodology, Chapter 4:

- verifies that using a moving frame of reference eliminates the numerical sensitivity due to truncation boundaries when targeting convective instability mechanisms,
- demonstrates that eigensolutions obtained in a moving frame of reference are instantaneously valid in the stationary frame of reference,
- reconstructs the traditional neutral and N-factor curves that are independent of the moving-frame eigensolutions.

In particular, it is demonstrated that using a moving frame of reference is arguably necessary to tackle convective instabilities from the perspective of the two-dimensional stability problem and that the numerical representation of convective instabilities with the stationary-frame eigenvalue problem is not reasonable.

The above points are also addressed for the stability analyses of the shock-wave/boundary-layer interaction in Chapter 5. In addition, the novel description of convective instabilities in shock-wave/boundary-layer interaction allows identifying:

- the critical frequency and spanwise wavenumber that yield the largest amplification through the shock-induced bubble,

- the inherent mechanisms that destabilize the flow and produce the perturbation energy.

Finally, Chapter 6 concludes this work by discussing, on the one hand, different perspectives regarding the moving-frame approach and, on the other hand, how future work could build upon the present methodology to carry stability analyses of complex flow fields.

References

ÅKERVIK, E., EHRENSTEIN, U., GALLAIRE, F. & HENNINGSON, D. S. 2008 Global two-dimensional stability measures of the flat plate boundary-layer flow. *European Journal of Mechanics - B/Fluids* **27** (5), 501–513.

ÅKERVIK, E., HŒPFFNER, J., EHRENSTEIN, U. & HENNINGSON, D. S. 2007 Optimal growth, model reduction and control in a separated boundary-layer flow using global eigenmodes. *Journal of Fluid Mechanics* **579**, 305–314.

ALIZARD, F. & ROBINET, J.-C. 2007 Spatially convective global modes in a boundary layer. *Physics of Fluids* **19** (11), 114105.

ANDERSSON, P., BERGGREN, M. & HENNINGSON, D. S. 1999 Optimal disturbances and bypass transition in boundary layers. *Physics of Fluids* **11** (1), 134–150.

APPEL, T. 2020 Boundary layer instabilities due to surface irregularities: a harmonic navier-stokes approach. PhD thesis, Imperial College London.

BABINSKY, H. & HARVEY, J. 2011 *Shock wave–boundary-layer interactions*. Cambridge: Cambridge University Press.

BARKLEY, D. 2016 Theoretical perspective on the route to turbulence in a pipe. *Journal of Fluid Mechanics* **803**, P1.

BERS, A. 1984 Linear waves and instabilities. In *Physique des Plasmas* (ed. C. DeWitt & J. Peyraud), pp. 117–213. New York: Gordon and Breach.

BERTOLOTTI, F. P., HERBERT, T. & SPALART, P. 1992 Linear and nonlinear stability of the Blasius boundary layer. *Journal of Fluid Mechanics* **242**, 441–474.

BLASIUS, H. 1908 Grenzschichten in flüssigkeiten mit kleiner reibung. *Zeitschrift für angewandte Mathematik und Physik* **56**, 1–37.

BOUTHIER, M. 1973 Stabilité linéaire des écoulements presque parallèles. ii. la couche limite de blasius. *Journal de Mécanique* **12**.

BRIGGS, R. J. 1964 *Electron-stream interaction with plasmas. M.I.T. Press research monographs* . M.I.T. Press.

BROWNE, O. M. F., HAAS, A. P., FASEL, H. F. & BREHM, C. 2019 An efficient linear wavepacket tracking method for hypersonic boundary-layer stability prediction. *Journal of Computational Physics* **380**, 243–268.

BRYNJELL-RAHKOLA, M., SHAHRIARI, N., SCHLATTER, P., HANIFI, A. & HENNINGSON, D. S. 2017 Stability and sensitivity of a cross-flow-dominated Falkner–Skan–Cooke boundary layer with discrete surface roughness. *Journal of Fluid Mechanics* **826**, 830–850.

BUGEAT, B., ROBINET, J.-C., CHASSAING, J.-C. & SAGAUT, P. 2022 Low-frequency resolvent analysis of the laminar oblique shock wave/boundary layer interaction. *Journal of Fluid Mechanics* **942**.

CASACUBERTA, J., GROOT, K. J., TOL, H. J. & HICKEL, S. 2018 Effectivity and efficiency of selective frequency damping for the computation of unstable steady-state solutions. *Journal of Computational Physics* **375**, 481–497.

CERQUEIRA, S. & SIPP, D. 2014 Eigenvalue sensitivity, singular values and discrete frequency selection mechanism in noise amplifiers: The case of flow induced by radial wall injection. *Journal of Fluid Mechanics* **757** (6), 770–799.

CHOMAZ, J.-M., HUERRE, P. & REDEKOPP, L. G. 1988 Bifurcations to Local and Global Modes in Spatially Developing Flows . *Physical Review Letters* **60** (1), 25–28.

CHOMAZ, J.-M., HUERRE, P. & REDEKOPP, L. G. 1991 A frequency selection criterion in spatially developing flows . *Studies in applied mathematics* **84**, 119–144.

DÉLERY, J. & DUSSAUGE, J.-P. 2009 Some physical aspects of shock wave/boundary layer interactions. *Shock Waves* **19** (6), 453–468.

DÉLERY, J., MARVIN, J. G. & RESHOTKO, E. 1986 Shock-wave boundary layer interactions. *Tech. Rep.* ADA171302. Advisory Group for Aerospace Research and Development.

DOLLING, D. S. 2001 Fifty years of shock-wave/boundary-layer interaction research: what next? *AIAA Journal* **39** (8), 1517–1531.

DWIVEDI, A., HILDEBRAND, N., NICHOLS, J. W., CANDLER, G. V. & JOVANOVIĆ, M. R. 2020 Transient growth analysis of oblique shock-wave/boundary-layer interactions at Mach 5.92. *Physical Review Fluids* **5** (1), 063904.

EHRENSTEIN, U. & GALLAIRE, F. 2005 On two-dimensional temporal modes in spatially evolving open flows: the flat-plate boundary layer. *Journal of Fluid Mechanics* **536**, 209–218.

FARRELL, B. F. 1988 Optimal excitation of perturbations in viscous shear flow. *Physics of Fluids* **31** (8), 2093–2102.

GAITONDE, D. V. 2015 Progress in shock wave/boundary layer interactions. *Progress in Aerospace Sciences* **72**, 80–99.

GARNAUD, X., LESSHAFFT, L., SCHMID, P. J. & HUERRE, P. 2013 Modal and transient dynamics of jet flows. *Physics of Fluids* **25** (4), 044103.

GASTER, M. 1974 On the effects of boundary-layer growth on flow stability. *Journal of Fluid Mechanics* **66** (3), 465–480.

GOLDSTEIN, M. E. & HULTGREN, L. S. 1989 Boundary-layer receptivity to long-wave free-stream disturbances. *Annual Review of Fluid Mechanics* **21** (1), 137–166.

GROOT, K. J. 2018 BiGlobal Stability of shear flows spanwise & streamwise Analyses. PhD thesis, TU Delft and von Karman Institute for Fluid Dynamics.

GROOT, K. J., PINNA, F. & VAN OUDHEUSDEN, B. W. 2015 On closing the streamwise BiGlobal stability problem: the effect of boundary conditions. *Procedia IUTAM* **14**, 459–468.

GROOT, K. J. & SCHUTTELAARS, H. M. 2020 Accurate numerical approximation of the absolute stability of unbounded flows. *Physica D: Nonlinear Phenomena* **402**, 132224.

GUIHO, F., ALIZARD, F. & ROBINET, J. C. 2016 Instabilities in oblique shock wave/laminar boundary-layer interactions . *Journal of Fluid Mechanics* **789**, 1–35.

HADER, C. & FASEL, H. F. 2019 Three-dimensional wave packet in a Mach 6 boundary layer on a flared cone. *Journal of Fluid Mechanics* **885**, R3.

HERBERT, T. 1988 Secondary Instability of Boundary Layers. *Annual Review of Fluid Mechanics* **20** (1), 487–526.

HERBERT, T. & BERTOLOTTI, F. 1987 Stability analysis of nonparallel boundary layers. *Bulletin of the American Physical Society* **32** (2079), 590.

HILDEBRAND, N., CHOUDHARI, M. M. & PAREDES, P. 2020 Predicting boundary-layer transition over backward-facing steps via linear stability analysis. *AIAA Journal* **58** (9), 3728–3734.

HUANG, Z. & WU, X. 2017 A local scattering approach for the effects of abrupt changes on boundary-layer instability and transition: a finite-reynolds-number formulation for isolated distortions. *Journal of Fluid Mechanics* **822**, 444–483.

HUERRE, P. & MONKEWITZ, P. A. 1985 Absolute and convective instabilities in free shear layers. *Journal of Fluid Mechanics* **159**, 151–168.

HUERRE, P. & MONKEWITZ, P. A. 1990 Local and Global Instabilities in Spatially Developing Flows. *Annual Review of Fluid Mechanics* **22**, 473–537.

HULTGREN, L. S. & GUSTAVSSON, L. H. 1981 Algebraic growth of disturbances in a laminar boundary layer. *Physics of Fluids* **24** (6), 1000–1004.

VAN INGEN, J. 1956 A suggested semi-empirical method for the calculation of the boundary layer transition region. *Tech. Rep.* VTH-74. Delft University of Technology.

KACHANOV, Y. S. 1994 Physical mechanisms of laminar boundary-layer transition. *Annual Review of Fluid Mechanics* **26**, 411–482.

KLEBANOFF, P. S., TIDSTROM, K. D. & SARGENT, L. M. 1962 The three-dimensional nature of boundary layer instability. *Journal of Fluid Mechanics* **12** (1), 1–34.

KOCH, W. 1985 Local instability characteristics and frequency determination of self-excited wake flows. *Journal of Sound and Vibration* **99** (1), 53–83.

KUMAR, B. & MITTAL, S. 2012 On the origin of the secondary vortex street. *Journal of Fluid Mechanics* **711**, 641–666.

LANDAHL, M. T. 1980 A note on an algebraic instability of inviscid parallel shear flows. *Journal of Fluid Mechanics* **98** (2), 243–251.

LOISEAU, J.-C., ROBINET, J.-C., CHERUBINI, S. & LERICHE, E. 2014 Investigation of the roughness-induced transition: global stability analyses and direct numerical simulations. *Journal of Fluid Mechanics* **760**, 175–211.

MACK, L. M. 1984 Boundary-layer linear stability theorys. In *AGARD 709, Special Course of Stability and Transition of Laminar Flows*. North Atlantic Treaty Organization.

MENTER, F. R., LANGTRY, R. & VÖLKER, S. 2006 Transition Modelling for General Purpose CFD Codes. *Flow, Turbulence and Combustion* **77** (1-4), 277–303.

MITTAL, S., KOTTARAM, J. J. & KUMAR, B. 2008 Onset of shear layer instability in flow past a cylinder. *Physics of Fluids* **20** (5), 054102.

MITTAL, S. & KUMAR, B. 2007 A stabilized finite element method for global analysis of convective instabilities in nonparallel flows. *Physics of Fluids* **19** (8), 088105.

MONKEWITZ, P. A., HUERRE, P. & CHOMAZ, J.-M. 1993 Global linear stability analysis of weakly non-parallel shear flows. *Journal of Fluid Mechanics* **251**, 1–20.

MORKOVIN, M. 1994 Transition in open flow systems-a reassessment. *Bulletin of the American Physical Society* **39**, 1882.

MORKOVIN, M. V. 1969 On the many faces of transition. In *Viscous Drag Reduction* (ed. C. S. Wells), pp. 1–31. Boston, MA: Springer US.

NIESSEN, S. E. M. 2017 BiGlobal stability analysis: laminar shock-wave/boundary-layer interactions. Master's thesis, University of Liège, Faculty of Applied Sciences.

NIESSEN, S. E. M., GROOT, K. J., HICKEL, S. & TERRAPON, V. E. 2023 Convective instabilities in a laminar shock-wave/boundary-layer interaction. *Physics of Fluids* **35** (2).

ORR, W. M. 1907 The Stability or Instability of the Steady Motions of a Perfect Liquid and of a Viscous Liquid. *Proceedings of the Royal Irish Academy. Section A: Mathematical and Physical Sciences* **27**, 69–138.

PIERREHUMBERT, R. T. 1984 Local and global baroclinic instability of zonally varying flow. *Journal of the Atmospheric Sciences* **41** (14), 2141–2162.

PIERREHUMBERT, R. T. 1986 Universal short-wave instability of two-dimensional eddies in an inviscid fluid. *Physical Review Letters* **57** (17), 2157–2159.

PIERREHUMBERT, R. T. & WIDNALL, S. E. 1982 The two- and three-dimensional instabilities of a spatially periodic shear layer. *Journal of Fluid Mechanics* **114**, 59–82.

PRANDTL, L. 1905 Über flüssigkeitsbewegung bei sehr kleiner reibung. In *Verhandlungen des dritten Internationalen mathematikerkongresses in Heidelberg: vom 8. bis 13. august 1904*, pp. 485–491. BG Teubner.

RAI, M. M. & MOIN, P. 1993 Direct numerical simulation of transition and turbulence in a spatially evolving boundary layer. *Journal of Computational Physics* **109** (2), 169–192.

RESHOTKO, E. 1976 Boundary-layer stability and transition. *Annual Review of Fluid Mechanics* **8** (1), 311–349.

RESHOTKO, E. 1984 Environment and receptivity. In *AGARD 709, Special Course of Stability and Transition of Laminar Flows.*

RESHOTKO, E. 2001 Transient growth: A factor in bypass transition. *Physics of Fluids* **13** (5), 1067–1075.

REYNOLDS, O. 1883 An experimental investigation of the circumstances which determine whether the motion of water shall be direct or sinuous, and of the law of resistance in parallel channels. *Philosophical Transactions of the Royal Society of London* **174**, 935–982.

REYNOLDS, O. 1895 On the dynamical theory of incompressible viscous fluids and the determination of the criterion. *Philosophical Transactions of the Royal Society of London. A* **186**, 123–164.

REYNOLDS, W. C., KAYS, W. M. & KLINE, S. J. 1958 Heat transfer in the turbulent incompressible boundary layer. *Tech. Rep.* NASA-MEMO-12-3-58W.

RIGAS, G., COLONIUS, T. & BEYAR, M. 2017 *Stability of wall-bounded fows using one-way spatial integration of Navier-Stokes equations*, arXiv: https://arc.aiaa.org/doi/pdf/10.2514/6.2017-1881.

RIST, U. & FASEL, H. F. 1995 Direct numerical simulation of controlled transition in a flat-plate boundary layer. *Journal of Fluid Mechanics* **298**, 211–248.

RODRÍGUEZ, D. A., TUMIN, A. & THEOFILIS, V. 2011 Towards the foundation of a global modes concept. In *6th AIAA Theoretical Fluid Mechanics Conference*.

SANSICA, A., SANDHAM, N. & HU, Z. 2013 Stability and unsteadiness in a 2D laminar shock-induced separation bubble. In *43rd AIAA Fluid Dynamics Conference*.

SANSICA, A., SANDHAM, N. D. & HU, Z. 2016 Instability and low-frequency unsteadiness in a shock-induced laminar separation bubble. *Journal of Fluid Mechanics* **798**, 5–26.

SARIC, W. S. & NAYFEH, A. H. 1975 Nonparallel stability of boundary-layer flows. *Physics of Fluids* **18** (8), 945–952.

SARIC, W. S., REED, H. L. & KERSCHEN, E. J. 2002 Boundary-layer receptivity to freestream disturbances. *Annual Review of Fluid Mechanics* **34** (3), 291–319.

SARIC, W. S., REED, H. L. & WHITE, E. B. 2003 Stability and transition of three-dimensional boundary layers. *Annual Review of Fluid Mechanics* **35** (1), 413–440.

SAYADI, T. & MOIN, P. 2012 Large eddy simulation of controlled transition to turbulence. *Physics of Fluids* **24** (11), 114103.

SCHLICHTING, H. 1933 Zur enstehung der turbulenz bei der plattenströmung. *Nachrichten von der Gesellschaft der Wissenschaften zu Göttingen, Mathematisch-Physikalische Klasse* **1933**, 181–208.

SCHLICHTING, H. 1979 *Boundary-Layer Theory*, 1st edn. McGraw-Hill.

SCHMID, P. J. & HENNINGSON, D. S. 2001 *Stability and transition in shear flows*. Springer.

SCHMID, P. J. & HENNINGSON, D. S. 2002 On the stability of a falling liquid curtain. *Journal of Fluid Mechanics* **463**, 163–171.

SCHMID, P. J., HENNINGSON, D. S., KHORRAMI, M. R. & MALIK, M. R. 1993 A study of eigenvalue sensitivity for hydrodynamic stability operators. *Theoretical and Computational Fluid Dynamics* **4** (5), 227–240.

SCHUBAUER, G. B. & SKRAMSTAD, H. K. 1948 Laminar-Boundary-Layer Oscillations and Transition on a Flat Plate. *Tech. Rep.* NACA-TR-909. NACA.

SIPP, D. & MARQUET, O. 2012 Characterization of noise amplifiers with global singular modes: the case of the leading-edge flat-plate boundary layer. *Theoretical and Computational Fluid Dynamics* **27** (5), 617–635.

SIPP, D., MARQUET, O., MELIGA, P. & BARBAGALLO, A. 2010 Dynamics and control of global instabilities in open-flows: a linearized approach. *Applied Mechanics Reviews* **63** (3), 389–26.

SMITH, A. M. O. & GAMBERONI, N. 1956 Transition, Pressure Gradient and Stability Theory. *Tech. Rep.* ES-26388. Douglas Aircraft Company, El Segundo, California.

SOMMERFELD, A. 1909 Ein Beitrag zur hydrodynamischen Erklärung der turbulenten Flüssigkeitsbewegungen. In *Proceedings of the 4th International Mathematical Congress*, pp. 116–124. Rome.

TAIRA, K., BRUNTON, S. L., DAWSON, S. T. M., ROWLEY, C. W., COLONIUS, T., MCKEON, B. J., SCHMIDT, O. T., GORDEYEV, S., THEOFILIS, V. & UKEILEY, L. S. 2017 Modal analysis of fluid flows: an overview. *AIAA Journal* **55** (12), 4013–4041.

TANI, I. 1969 Boundary-layer transition. *Annual Review of Fluid Mechanics* **1** (1), 169–196.

THEOFILIS, V. 2003 Advances in global linear instability analysis of nonparallel and three-dimensional flows. *Progress in Aerospace Sciences* **39** (4), 249–315.

THEOFILIS, V. 2011 Global linear instability. *Annual Review of Fluid Mechanics* **43** (1), 319–352.

THEOFILIS, V. & RODRÍGUEZ, D. 2010 Structural changes of laminar separation bubbles induced by global linear instability. *Journal of Fluid Mechanics* **655**, 280–305.

TOLLMIEN, W. 1928 Über die entstehung der turbulenz. 1. mitteilung. *Nachrichten von der Gesellschaft der Wissenschaften zu Göttingen, Mathematisch-Physikalische Klasse* **1929**, 21–44.

TOWNE, A. & COLONIUS, T. 2015 One-way spatial integration of hyperbolic equations. *Journal of Computational Physics* **300**, 844–861.

TOWNE, A., RIGAS, G. & COLONIUS, T. 2019 A critical assessment of the parabolized stability equations. *Theoretical and Computational Fluid Dynamics* **33** (3), 359–382.

TREFETHEN, L. N., TREFETHEN, A. E., REDDY, S. C. & DRISCOLL, T. A. 1993 Hydrodynamic stability without eigenvalues. *Science* **261** (5121), 578–584.

TUCKER, A. A., SARIC, W. S. & REED, H. L. 2014 Laminar flow control flight experiment design and execution. In *52nd Aerospace Sciences Meeting*. National Harbor, Maryland.

WHITE, E. B. 2002 Transient growth of stationary disturbances in a flat plate boundary layer. *Physics of Fluids* **14** (12), 4429–4439.

WHITE, F. 1974 *Viscous fluid flow*. McGraw-Hill, New York.

ZHAO, L., DONG, M. & YANG, Y. 2019 Harmonic linearized Navier-Stokes equation on describing the effect of surface roughness on hypersonic boundary-layer transition. *Physics of Fluids* **31** (3), 034108.

2

Stability theory for fluid flows

This chapter presents the mathematical foundations of the linear stability theory for ideal-gas flows. The governing equations for both compressible and incompressible flows are first derived in §2.1 and are thereafter linearized in §2.2 to obtain the system of equations that govern the evolution of linear disturbances in a fluid flow. Based on these equations, the direct stability problem formulated in the traditional stationary frame of reference is derived in §2.3 by considering a two-dimensional modal ansatz. For the sake of completeness, this section also discusses the traditional perturbations ansatzes yielding the Linear Stability Theory (LST) and Parabolized Stability Equations (PSE) problems. The continuous adjoint stability problem is then derived in §2.4 and the different types of boundary conditions used to close the perturbation and stability equations are presented in §2.5.

The motivation to depart from the traditional stationary frame of reference when tackling two-dimensional convective instabilities is discussed in §2.6, and a formulation of the two-dimensional stability problem in a moving frame of reference is proposed. Several fundamental concepts regarding this novel formulation are elaborated and comparisons are made against the fixed-frame stability problem. In order to provide a more practical perspective on the moving-frame method, §2.7 presents various approaches to characterize and interpret the solutions. In particular, it shows how the traditional stationary-frame N-factor curves, that are widely used to predict the laminar-turbulent transition through the e^N-method, can be built. Finally, §2.8 provides the tools to decompose the instability mechanisms into their individual contributions. The theoretical development of this last section provides a useful framework to gain an in-depth insight into the most critical mechanisms at the origin of the convective instabilities in a flow field.

2.1. Navier-Stokes equations

The physical problem for compressible flows is governed by the non-dimensional Navier-Stokes equations

$$\frac{\partial \rho}{\partial t_\mathrm{f}} + u_j \frac{\partial \rho}{\partial x_{\mathrm{f},j}} + \rho \frac{\partial u_j}{\partial x_{\mathrm{f},j}} = 0\,, \tag{2.1a}$$

$$\rho \frac{\partial u_i}{\partial t_\mathrm{f}} + \rho u_j \frac{\partial u_i}{\partial x_{\mathrm{f},j}} = -\frac{\partial p}{\partial x_{\mathrm{f},i}} + \frac{1}{\mathrm{Re}} \frac{\partial \tau_{ij}}{\partial x_{\mathrm{f},j}}\,, \tag{2.1b}$$

$$\rho\frac{\partial T}{\partial t_\mathrm{f}}+\rho u_j\frac{\partial T}{\partial x_{\mathrm{f},j}}=-\gamma\mathrm{Ec}\frac{\partial u_j}{\partial x_{\mathrm{f},j}}p+\frac{\gamma\mathrm{Ec}}{\mathrm{Re}}\boldsymbol{\phi}+\frac{\gamma}{\mathrm{Re}\,\mathrm{Pr}}\frac{\partial q_j}{\partial x_{\mathrm{f},j}}\,, \tag{2.1c}$$

with ρ the density, p the pressure, and u_i the velocity components in the x_f-, y- and z-directions for indices $i=1,2,3$, respectively. The subscript 'f' indicates that the frame of reference is stationary and, since only convective frames in the streamwise direction will be considered later, this notation only strictly applies to the x-coordinate and does not affect the y- and z-directions that are always stationary. The energy equation (2.1c) is based on the internal energy $e=c_v T$ (with the isochoric heat capacity c_v) and provides a transport equation for the temperature only. If based on the enthalpy $h=c_p T$ (with the isobaric heat capacity c_p), the energy equation would involve an additional temporal derivative of the pressure acting as source term to the temperature-transport equation. Being more cumbersome, especially when considering stability analyses, this latter formulation is not retained in the present work. Considering Newtonian fluids only, i.e., fluids for which dissipation depends linearly on the strain rate, the viscous stress tensor τ_{ij} is given by the constitutive law

$$\tau_{ij}=\mu\left(\frac{\partial u_i}{\partial x_{\mathrm{f},j}}+\frac{\partial u_j}{\partial x_{\mathrm{f},i}}\right)+\lambda\frac{\partial u_k}{\partial x_{\mathrm{f},k}}\delta_{ij}\,, \tag{2.2}$$

with the first and second viscosity coefficients, $\mu=\mu(T)$ and $\lambda=\lambda(T)$, respectively, that depend only on the temperature. Furthermore, the Stokes' hypothesis is presently used such that $\lambda=-2/3\mu$. The dissipation function $\boldsymbol{\phi}$ represents the conversion of viscous-stress dissipation into heat and is given by

$$\boldsymbol{\phi}=\tau_{ij}\frac{\partial u_i}{\partial x_{\mathrm{f},j}}\,. \tag{2.3}$$

Finally, the contribution of heat flux in the energy equation is governed by Fourier's law

$$q_j=-\kappa\frac{\partial T}{\partial x_{\mathrm{f},j}}\,, \tag{2.4}$$

where the thermal conductivity $\kappa=\kappa(T)$ is function of the temperature only. Assuming calorically perfect gases with a constant heat capacity ratio $\gamma=c_p/c_v=1.4$, the dimensionless ideal-gas equation

$$p=\frac{\rho T}{\gamma M^2}\,, \tag{2.5}$$

is used. Substituting the equation of state (2.5) into the Navier-Stokes equations (2.1) allows eliminating the pressure (or density) from the system. The formulation of the Navier-Stokes equations (2.1) and ideal-gas law (2.5) is based on the non-dimensional Eckert, Mach, Reynolds and Prandtl numbers that are given by

$$\mathrm{Ec}\overset{(a)}{=}\frac{u_e^2}{c_p T_e}\,,\quad \mathrm{M}\overset{(b)}{=}\frac{u_e}{a_e}\,,\quad \mathrm{Re}_{\mathfrak{L}}\overset{(c)}{=}\rho_e\frac{u_e\mathfrak{L}}{\mu_e}\,,\quad \mathrm{Pr}\overset{(d)}{=}\frac{c_p\mu_e}{\kappa_e}\,, \tag{2.6}$$

respectively, with freestream quantities indicated by subscript 'e' and with the length $\mathfrak{L}$ denoting a generic length scale. The global length scale ℓ is introduced so that $\mathrm{Re}=\mathrm{Re}_\ell=\rho_e u_e\ell/\mu_e=1$. For ideal gases, the speed of sound a, that is used in the definition of the Mach number, is defined by $\sqrt{\gamma\mathrm{R}T}$ with the perfect-gas constant $\mathrm{R}=287\,\mathrm{J/(kg\cdot K)}$. Finally, the fact that only calorically perfect gases are considered allows establishing a relation between the fluid viscosity and the conductivity as follows

$$\kappa(T)=\frac{\gamma\mathrm{R}}{(\gamma-1)\mathrm{Pr}}\mu(T)\,. \tag{2.7}$$

The Sutherland's law is used to determine the temperature dependency of both the viscosity and conductivity coefficients through

$$\mu(T) = \mu_{\text{ref}} \left(\frac{T}{T_{\text{ref}}} \right)^{\frac{3}{2}} \frac{T_{\text{ref}} + T_s}{T + T_s}, \tag{2.8}$$

with constant parameters $\mu_{\text{ref}} = 1.716 \times 10^{-5}$ kg/(m·s), $T_s = 110.4$ K, $T_{\text{ref}} = 273.15$ K and Pr = 0.72.

Since incompressible flows are also considered in the present work, the Navier-Stokes equations (2.1) can be simplified accordingly. The incompressibility hypothesis for homogeneous and isotropic flows considers that density remains constant under any circumstance, i.e., the total derivative of the density $D\rho/Dt = \partial\rho/\partial t + u_i \partial\rho/\partial x_i = 0$. This implies that the density ρ is no longer an unknown of the problem and can thus be fixed to a constant value (here $\rho = 1$). Furthermore, the present incompressible flows are assumed isothermal. The temperature T thus does not need to be considered anymore and the energy equation (2.1c) becomes superfluous. Under these hypotheses, the system of equations (2.1) reduces to the Navier-Stokes equations for incompressible flows

$$\frac{\partial u_j}{\partial x_{\text{f},j}} = 0, \tag{2.9a}$$

$$\frac{\partial u_i}{\partial t_{\text{f}}} + u_j \frac{\partial u_i}{\partial x_{\text{f},j}} = -\frac{\partial p}{\partial x_{\text{f},i}} + \frac{1}{\text{Re}} \frac{\partial^2 u_i}{\partial x_{\text{f},j} \partial x_{\text{f},j}}. \tag{2.9b}$$

The divergence-free condition, introduced by the continuity equation (2.9a), enforces the isochoric character of the flow and allows simplifying the viscous stress tensor (2.2) in the incompressible momentum equations (2.9b).

Casting all equations together, the Navier-Stokes equations for both compressible and incompressible flows in a fixed frame of reference can be written in the abbreviated form

$$\mathscr{B}\left(\boldsymbol{q}_{\text{f}}\right) \frac{\partial \boldsymbol{q}_{\text{f}}}{\partial t_{\text{f}}} = \mathscr{N}\{\boldsymbol{q}_{\text{f}}\} \tag{2.10}$$

with $\mathscr{B}$ a real-valued operator and $\mathscr{N}\{\bullet\}$ the nonlinear Navier-Stokes operator. Note that the formulation of the energy equation with the internal energy makes $\mathscr{B}$ diagonal while an enthalpy-based formulation would introduce one or two off-diagonal components depending on whether p or ρ is eliminated from the system of equations through the equation of state. The primitive variables, that represent the instantaneous flow field, are given by $\boldsymbol{q}_{\text{f}}(x_{\text{f}}, y, z, t) = [u, v, w, T, \rho]_{\text{f}}^{\text{T}}$ or $\boldsymbol{q}_{\text{f}}(x_{\text{f}}, y, z, t) = [u, v, w, p]_{\text{f}}^{\text{T}}$ for compressible or incompressible flows, respectively. The superscript 'T' indicates the real transpose operator. Note that, for the incompressible-flow formulation, there is no temporal derivative for the pressure and thus the row corresponding to the continuity equation in the operator $\mathscr{B}$ only contains zeroes; $\mathscr{B}$ is singular in the incompressible case. Considering the Navier-Stokes equations allows now formulating the perturbation equations that govern the evolution of disturbances in a flow field.

2.2. Perturbation equations

The disturbances in a flow field are studied by expanding the instantaneous flow $\boldsymbol{q}_{\text{f}}$ variables into a base-flow component $\overline{\boldsymbol{Q}}$, that satisfies the stationary Navier-Stokes equations $\partial\overline{\boldsymbol{Q}}/\partial t = \mathscr{N}\left\{\overline{\boldsymbol{Q}}\right\} = 0$, and a perturbation field $\boldsymbol{q}'_{\text{f}}$ such that

$$\boldsymbol{q}_{\text{f}}(x_{\text{f}}, y, z, t) = \overline{\boldsymbol{Q}}(x_{\text{f}}, y, z) + \epsilon \boldsymbol{q}'_{\text{f},r}(x_{\text{f}}, y, z, t), \quad \text{for } \epsilon \ll 1, \tag{2.11}$$

where the subscript 'r' indicates taking the real part of a complex variable. Because perturbations are usually interpreted as waves in the frequency domain through Fourier transformations, the perturbation component $\boldsymbol{q}'_{\mathrm{f}}$ is represented by a complex variable. Nevertheless, the physical representation of the instantaneous flow $\boldsymbol{q}_{\mathrm{f}}$ cannot be complex and the decomposition (2.11) thus only includes the real part of the perturbation field. To obtain the perturbation equations, the expansion (2.11) is introduced into the Navier-Stokes equations (2.10) that are then expanded around the base-flow solution

$$\mathscr{B}(\overline{\boldsymbol{Q}})\left[\epsilon\frac{\partial \boldsymbol{q}'_{\mathrm{f}}}{\partial t_{\mathrm{f}}}+\mathscr{O}(\epsilon^2)\right]=\mathscr{N}\left\{\overline{\boldsymbol{Q}}+\epsilon\boldsymbol{q}'_{\mathrm{f}}\right\}=\underbrace{\mathscr{N}\left\{\overline{\boldsymbol{Q}}\right\}}_{=0}+\epsilon\underbrace{\frac{\partial\mathscr{N}}{\partial\epsilon}\boldsymbol{q}'_{\mathrm{f}}}_{\mathscr{L}(\overline{\boldsymbol{Q}})\boldsymbol{q}'_{\mathrm{f}}}+\mathscr{O}(\epsilon^2)\,. \tag{2.12}$$

Since all operators are real-valued, the subscript 'r' is omitted on the perturbation variables. Upon neglecting the higher-order terms $\mathscr{O}(\epsilon^2)$, the perturbation equations are finally given by

$$\mathscr{B}(\overline{\boldsymbol{Q}})\frac{\partial \boldsymbol{q}'_{\mathrm{f}}}{\partial t_{\mathrm{f}}}=\mathscr{L}(\overline{\boldsymbol{Q}})\boldsymbol{q}'_{\mathrm{f}}, \tag{2.13}$$

with $\mathscr{L}$ the linearized Navier-Stokes operator, that is a function of base-flow variables only. Similarly to the nonlinear Navier-Stokes equations (2.1), the linearized equations (2.13) represents an initial-value problem. It is important to notice that a base flow $\overline{\boldsymbol{Q}}$ is not equivalent to a mean flow; the former is a solution of the steady Navier-Stokes equations, while the second is a statistically time averaged flow that does not satisfy the steady equations. Mean flows are used, for instance, in Reynolds Averaged Navier-Stokes (RANS) approaches, whereas base flows are sought for the present linearized Navier-Stokes approach. The base flow is computed a-priori so as to satisfy $\mathscr{N}\left\{\overline{\boldsymbol{Q}}\right\}=0$ and is then considered as a parameter in the perturbation equations that is independent of the perturbation field.

2.2.1. A note on perturbed variables in compressible flows

For incompressible flows, the derivation of the linearized operator is relatively straightforward and follows from the system of equations (2.9) in which u_i and p are the only instantaneous variables. However, the derivation of the operator for compressible flows is more cumbersome since it involves more variables and equations. First, it is important to consider the additional primitive flow variables T and ρ that are tied together through the equation of state for the perturbation variables. The relation between T', ρ' and p' can be derived by introducing the expansion equation (2.11) for the instantaneous T, ρ and p into the ideal-gas equation (2.5) as follows

$$\begin{aligned} p=\overline{p}+\epsilon p'_{\mathrm{f}}&=\frac{1}{\gamma M^2}(\overline{\rho}+\rho'_{\mathrm{f}})(\overline{T}+T'_{\mathrm{f}})\\ &=\frac{1}{\gamma M^2}(\overline{\rho}\,\overline{T}+\epsilon\overline{\rho}T'_{\mathrm{f}}+\epsilon\overline{T}\rho'_{\mathrm{f}}+\epsilon^2\rho'_{\mathrm{f}}T'_{\mathrm{f}})\,. \end{aligned} \tag{2.14}$$

Upon neglecting the high-order terms, the zeroth- and first-order equations are given by

$$\mathscr{O}(\epsilon^0):\quad \overline{p}=\frac{\overline{\rho}\,\overline{T}}{\gamma M^2}\,, \tag{2.15a}$$

$$\mathscr{O}(\epsilon^1):\quad p'_{\mathrm{f}}=\frac{\overline{\rho}T'_{\mathrm{f}}+\overline{T}\rho'_{\mathrm{f}}}{\gamma M^2}=\overline{P}\left(\frac{T'_{\mathrm{f}}}{\overline{T}}+\frac{\rho'_{\mathrm{f}}}{\overline{\rho}}\right), \tag{2.15b}$$

and represent the equations of state for the base flow and perturbations, respectively. Second, since the coefficients μ, λ and κ depend on the temperature field and thus vary in space, they must also be decomposed into base-flow and perturbation components. However, instead of considering these perturbation components as additional unknowns of the perturbation equations, the three instantaneous coefficients, that depend only on the temperature field, are expanded in a Taylor series around the base-flow temperature $\overline{T}$. For μ'_f, this gives

$$\mu(\overline{T}+\epsilon T'_\mathrm{f}) = \overline{\mu}(\overline{T}) + \epsilon \underbrace{\frac{\partial \overline{\mu}}{\partial \overline{T}}}_{\mu'(\overline{T})} T'_\mathrm{f} \quad + \mathscr{O}(\epsilon^2)\,. \tag{2.16}$$

Hence, all three perturbations μ', λ' and κ' can be replaced by the temperature perturbation T'_f, up to coefficients depending only on the base-flow variables, and are thus not unknowns of the perturbation equations anymore. To simplify further the final equations, the spatial derivatives of both the base-flow μ, λ and κ and the perturbations μ', λ' and κ' involved in the momentum and energy equations (2.1b) can be replaced using the chain rule by

$$\frac{\partial \overline{\mu}}{\partial x_{\mathrm{f},i}} = \frac{\mathrm{d}\overline{\mu}}{\mathrm{d}\overline{T}} \frac{\partial \overline{T}}{\partial x_{\mathrm{f},i}}\,, \tag{2.17a}$$

$$\frac{\partial \mu'_\mathrm{f}}{\partial x_{\mathrm{f},i}} = \frac{\mathrm{d}\overline{\mu}}{\mathrm{d}\overline{T}} \frac{\partial T'_\mathrm{f}}{\partial x_{\mathrm{f},i}} + \frac{\mathrm{d}^2\overline{\mu}}{\mathrm{d}\overline{T}^2} \frac{\partial \overline{T}}{\partial x_{\mathrm{f},i}} T'_\mathrm{f}\,, \tag{2.17b}$$

which hold for λ and κ too. Hence, introducing the equations (2.15), (2.16) and (2.17) into the compressible linearized operator allows reducing the perturbation variables to either $\boldsymbol{q}'_\mathrm{f} = [u'\,, v'\,, w'\,, T'\,, \rho']^\mathrm{T}_\mathrm{f}$ or $\boldsymbol{q}'_\mathrm{f} = [u'\,, v'\,, w'\,, T'\,, p']^\mathrm{T}_\mathrm{f}$, as usually considered in the literature.

2.2.2. Finding solutions of the initial-value perturbation problem

The perturbation equations (2.13) represent an initial-value problem that can be solved by an integration in time and, since $\mathscr{B}(\overline{\boldsymbol{Q}})$ and $\mathscr{L}(\overline{\boldsymbol{Q}})$ are constant over time, the solutions of (2.13) can be written in the exponential matrix form

$$\boldsymbol{q}_\mathrm{f}(x_\mathrm{f}, y, z, t_\mathrm{f}) = \mathrm{e}^{\mathscr{B}^{-1}\mathscr{L}\, t_\mathrm{f}} \boldsymbol{q}_{\mathrm{f},0}(x_\mathrm{f}, y, z)\,, \tag{2.18}$$

which links the initial condition $\boldsymbol{q}_{\mathrm{f},0}$ to its next state $\boldsymbol{q}_\mathrm{f}$ at time t. This is, however, conditioned by $\mathscr{B}$ that must be invertible. While it is often the case in the compressible-flow formulation of the perturbation equations (2.13), the operator $\mathscr{B}$ becomes singular in the incompressible-flow formulation because the continuity equation has no temporal derivative. Nevertheless, the exponential matrix is often barely tractable numerically for real flow configurations with many degrees of freedom and only model problems can be solved. Hence, it is necessary to rely on numerical strategies in order to perform the temporal integration of the perturbation equations (2.13). This is discussed in Chapter 3.

Besides the capability of solving the perturbation equations (2.13), there is a need for an appropriate initial condition. The main interest behind the introduction of disturbances in a flow field lies in finding the mechanisms that lead to rapid and large amplifications of the perturbations, i.e., the mechanisms that are at the origin of large-scale phenomena such as laminar-turbulent transition, shock-induced bubble breathing, vortex street behing a cylinder and so on. It is therefore of paramount importance to select initial conditions $\boldsymbol{q}_0$ that can trigger these mechanisms. Otherwise, if the initial condition is not appropriately chosen, the instability mechanisms might not be revealed and the conclusion about the flow

stability could be biased. Hence, different strategies exist to target the relevant solutions of the perturbation problem and can be classified into three main categories (Schmid & Henningson, 2001; Schmid, 2007; Schmid & Brandt, 2014; Taira *et al.*, 2017) that are discussed in what follows. As pointed out in the introduction, the forcing problem (see the HLNS method for two-dimensional flows, Huang & Wu (2017); Zhao *et al.* (2019); Hildebrand *et al.* (2020); Appel (2020)) is not further discussed since the forcing can occult the inherent perturbation dynamics.

Relevant solutions to the initial-value problem can be found by considering the optimal-growth approach (Schmid & Henningson, 2001; Schmid, 2007) that searches for the initial condition to the perturbation equations (2.13) that maximizes an energy norm at each time instant. In this approach, the problem is cast in a Singular Value Decomposition (SVD) problem and restricts the perturbation dynamics to particular solutions. These solutions are so particular that they have never been observed in experiments and thus do not provide information about the general perturbation dynamics. Hence, White (1974) argued that considering sub-optimal-growth scenarios is just as important as optimal solutions. For these reasons, the optimal perturbation approach is not considered.

Another approach consists in introducing wave packets into the perturbation equations (Gaster, 1967; Hader & Fasel, 2019). The temporal evolution of the wave packets is then sought by numerically evaluating equation (2.18). However, the spatio-temporal character of wave packets makes them less intuitive to interpret than wave trains and the resulting temporal signal is often decomposed into individual wave-train-type frequencies. These frequencies can then be studied independently from each other in order to determine which ones are associated with the most critical instability mechanisms (see §2.7). However, a careful choice of the initial condition, e.g., wave-packet location, size or frequency content, is required in order to trigger all relevant mechanisms. The present thesis aims to tackle this aspect by proposing a new type of initial conditions that contain all necessary frequency content and that avoid any inadvertent transient behavior arising from arbitrarily chosen initial conditions that do not satisfy the governing equations at the initial time. These ideal initial perturbations are given by the moving-frame linear stability problem. Before presenting this problem, the linear stability equations in the stationary frame of reference are first derived.

2.3. Linear stability problem

The linear stability problem relies on casting the perturbation equations into an eigenvalue problem. It thus provides solutions that are building blocks of the perturbation dynamics instead of solutions that emerge from a response to an initial value. In a fixed-frame of reference, the resulting modal solutions are used to assess the long-time stability of flows. For instance, the modal stability equations have yielded the local stability methods, i.e., LST and Orr-Sommerfeld methods (Orr, 1907; Sommerfeld, 1909; Mack, 1984), that are formally applicable to parallel flows only. When extended to nonparallel, slowly-evolving flows, the linear stability problem can be cast into the PSE (Bertolotti *et al.*, 1992) or, for two-dimensional problems, into the BiGlobal stability equations (Theofilis, 2003). In a moving-frame of reference, it is later shown that the results from the linear stability problem are only valid at $t = 0$ but then form ideal candidates for initializing the initial-value perturbation problem. Hence, the solutions to the stability problem are either valid for long- or initial-time behavior. To obtain finite-time solutions without being restricted to the optimal growth scenario, the present method is based on both perturbation and stability problems. The mathematical formalism of the latter is given in the present section.

The formulation of the stability problem relies on prescribing a harmonic behavior of the perturbations in the spatial direction(s) where the base flow is homogeneous, i.e., direction(s) where the base flow has strictly no dependency. Hence, a spatial variation of the base flow in one direction must reflect into the perturbation field. In linear stability problems, the temporal evolution of the perturbations is also assumed harmonic in time.

2.3.1. Two-dimensional stability equations

Many base-flow configurations are laminar flows that evolve essentially in two spatial directions and, although the actual physical space is three-dimensional, it is often sufficient to consider the two-dimensional stability equations with two inhomonegenous and one homogeneous direction to capture the essential perturbation dynamics. When considering wall-bounded flows, the monochromatic character of the perturbations is imposed either in the spanwise z- or streamwise x-direction whereas the wall-normal direction is always kept inhomogeneous because of the strong wall-normal gradient imposed by the boundary layer. In the present work, only streamwise developing flows are considered and thus the spanwise direction is assumed homogeneous. The modal, two-dimensional perturbation ansatz is thus written

$$\boldsymbol{q}'_{\mathrm{f}}(x_{\mathrm{f}}, y, z, t) = \tilde{\boldsymbol{q}}_{\mathrm{f}}(x_{\mathrm{f}}, y)\mathrm{e}^{\mathrm{i}(\beta z - \omega_{\mathrm{f}} t_{\mathrm{f}})}\,, \tag{2.19}$$

where $\tilde{\boldsymbol{q}}_{\mathrm{f}}$ is the vector of amplitude functions and ω_{f} is the angular frequency. These newly introduced variables are all complex in general and, for this reason, taking the real part of the perturbation in the expansion (2.11) is necessary to guarantee that the perturbation vector $\boldsymbol{q}'_{\mathrm{f}}$ is a real-valued quantity in the physical space. The real-valued β parameter is the wavenumber in the spanwise direction and is a-priori prescribed to enforce the monochromatic character of the perturbations in this direction. Upon introducing ansatz (2.19) into the linearized Navier-Stokes equations (2.13), the linear stability problem forms the so-called streamwise BiGlobal stability equations

$$\mathscr{A}(\overline{\boldsymbol{Q}};\beta)\tilde{\boldsymbol{q}}_{\mathrm{f}} = -\mathrm{i}\omega_{\mathrm{f}}\mathscr{B}(\overline{\boldsymbol{Q}})\tilde{\boldsymbol{q}}_{\mathrm{f}}\,, \tag{2.20}$$

that are written in the form of a complex-valued generalized eigenvalue problem with ω_{f} the eigenvalue and $\tilde{\boldsymbol{q}}_{\mathrm{f}}$ the eigenvector. The operators $\mathscr{B}(\overline{\boldsymbol{Q}})$ and $\mathscr{A}(\overline{\boldsymbol{Q}};\beta)$ are real- and complex-valued, respectively. $\mathscr{A}(\overline{\boldsymbol{Q}};\beta)$ contains all partial derivatives in space and depends on the a-priori prescribed spanwise wavenumber. The eigenvalue problem is homogeneous and requires spatial, homogeneous boundary conditions to close the system (see details in §2.5). When deriving the operator $\mathscr{A}(\overline{\boldsymbol{Q}};\beta)$ from the linearized perturbation operator $\mathscr{L}$, the first and second order derivatives in the spanwise direction of the perturbations are replaced by

$$\frac{\partial\,\cdot}{\partial z} = \mathrm{i}\beta\,\cdot\,, \qquad \frac{\partial^2\,\cdot}{\partial z^2} = -\beta^2\,\cdot\,, \tag{2.21}$$

respectively. In contrast, the spanwise derivatives of the base-flow variables $\partial\overline{\boldsymbol{Q}}/\partial z$ vanish since the base flow is assumed homogeneous in the z-direction. Small variations $\partial\overline{\boldsymbol{Q}}/\partial z \ll \partial\overline{\boldsymbol{Q}}/\partial x_{\mathrm{f}}$ and $\partial\overline{\boldsymbol{Q}}/\partial z \ll \partial\overline{\boldsymbol{Q}}/\partial y$ would be acceptable if a three-dimensional base flow is considered, and could be included into the BiGlobal stability problem without introducing significant distortion of the solutions. Nevertheless, in this thesis, only strictly two-dimensional flows are considered and spanwise variations of the base flow are not included in the equations. The complete set of equations can be found in Appendix A and the numerical strategy to solve the problem is discussed in Chapter 3.

2.3.2. One-dimensional stability equations

In some particular configurations, the base flow has no or a very limited spatial evolution in one of the two dimensions. In the case of open flows bounded by a solid wall, the largest gradients are often in the wall-normal direction y and this can thus be assumed as the only inhomogeneous direction. In those cases, the stability problem can be reduced to a (quasi-)one-dimensional problem. The first formulation of the stability equations for boundary layers was proposed by Orr (1907) and Sommerfeld (1909) and involves the parallel flow assumption that neglects any spatial variation in both x- and z-directions. The equations were later extended by Mack (1984) as the Linear Stability Equations (LST) to be valid for both compressible and incompressible parallel flows. The modal ansatz of the LST is given by

$$\boldsymbol{q}'_{\mathrm{f}}(x_{\mathrm{f}}, y, z, t) = \tilde{\boldsymbol{q}}_{\mathrm{f}}(y)\mathrm{e}^{\mathrm{i}(\alpha x_{\mathrm{f}}+\beta z-\omega_{\mathrm{f}} t_{\mathrm{f}})}, \tag{2.22}$$

with α the real-valued wavenumber in the streamwise direction. Note that the mode shape $\tilde{\boldsymbol{q}}_{\mathrm{f}}$ depends only on the wall-normal direction. Assuming that the spanwise wavenumber β is a-priori imposed as for the streamwise BiGlobal approach, introducing ansatz (2.22) into the linearized Navier-Stokes equations (2.13) yields the temporal or spatial LST eigenvalue problem depending on whether temporal or spatial solutions are sought. When seeking temporal solutions, the streamwise wavenumber α is prescribed and the linearized Navier-Stokes equations (2.13) reduce to the temporal LST eigenvalue problem

$$\mathscr{A}(\overline{\boldsymbol{Q}}; \alpha, \beta)\tilde{\boldsymbol{q}}_{\mathrm{f}} = -\mathrm{i}\omega_{\mathrm{f}}\mathscr{B}(\overline{\boldsymbol{Q}})\tilde{\boldsymbol{q}}_{\mathrm{f}}. \tag{2.23a}$$

Instead, if spatial solutions are sought, the frequency ω is imposed and the spatial LST eigenvalue problem

$$\mathscr{A}_\alpha(\overline{\boldsymbol{Q}}; \omega, \beta)\tilde{\boldsymbol{q}}_{\mathrm{f}} = -\mathrm{i}\alpha\mathscr{B}_\alpha(\overline{\boldsymbol{Q}})\tilde{\boldsymbol{q}}_{\mathrm{f}} + \alpha^2\mathscr{C}_\alpha(\overline{\boldsymbol{Q}})\tilde{\boldsymbol{q}}_{\mathrm{f}}, \tag{2.23b}$$

is to be solved. In this latter formulation, the operators $\mathscr{B}_\alpha$ and $\mathscr{C}_\alpha$ include all terms related to the first and second streamwise derivatives of the perturbation field, respectively, and $\mathscr{A}_\alpha$ including all remaining terms. In spatial and temporal analyses, the prescribed values ω or α are real numbers. However, when considering spatio-temporal analysis, complex values for ω or α are prescribed. This third type of analysis is particularly useful to determine the convective or absolute character of instabilities (Briggs, 1964; Bers, 1984; Monkewitz *et al.*, 1993; Delbende *et al.*, 1998; Huerre & Rossi, 2009). Finally, it is important to emphasize that the LST equations are devised for *local* stability analysis and are strictly applicable to parallel flows only; the LST method is thus barely suitable for real flow applications. If it is nonetheless applied to more complex flows, solutions can be contaminated by relatively large model errors depending on the actual spatial evolution of the flow. In order to (partly) overcome this restriction, Bertolotti *et al.* (1992) introduced the Parabolized Stability Equations (PSE) that can account for the slow variation of the flow in the streamwise direction.

2.3.3. Nonlocal and parabolized stability equations

The PSE approach is based on a Wentzel–Kramers–Brillouin-Jeffreys (WKBJ) approximation in the streamwise direction in which the ansatz for the perturbation is given by

$$\boldsymbol{q}'_{\mathrm{f}} = \tilde{\boldsymbol{q}}_{\mathrm{f}}(\epsilon_p x_{\mathrm{f}}, y)\ \mathrm{e}^{\mathrm{i}(\int_{x_{\mathrm{f}}}\alpha(\epsilon_p\bar{x}_{\mathrm{f}})\mathrm{d}\bar{x}_{\mathrm{f}}+\beta z-\omega_{\mathrm{f}} t_{\mathrm{f}})}, \tag{2.24}$$

where ϵ_p is a small number that allows for the slow evolution of both $\tilde{\boldsymbol{q}}_\mathrm{f}$ and α in the streamwise direction. This implies that the first and second derivatives take the form

$$\frac{\partial \boldsymbol{q}'_\mathrm{f}}{\partial x_\mathrm{f}} = \left(\epsilon_p \frac{\partial \tilde{\boldsymbol{q}}_\mathrm{f}}{\partial x_\mathrm{f}} + \mathrm{i}\alpha \tilde{\boldsymbol{q}}_\mathrm{f}\right) \mathrm{e}^{\mathrm{i}\left(\int^{x_\mathrm{f}} \alpha(\epsilon_p \bar{x}_\mathrm{f})\mathrm{d}\bar{x}_\mathrm{f} - \omega_\mathrm{f} t_\mathrm{f}\right)}, \tag{2.25a}$$

$$\frac{\partial^2 \boldsymbol{q}'_\mathrm{f}}{\partial x_\mathrm{f}^2} = \left(\cancel{\epsilon_p^2 \frac{\partial^2 \tilde{\boldsymbol{q}}_\mathrm{f}}{\partial x_\mathrm{f}^2}} + \epsilon_p \left(2\mathrm{i}\alpha \frac{\partial \tilde{\boldsymbol{q}}_\mathrm{f}}{\partial x_\mathrm{f}} + \mathrm{i}\frac{\mathrm{d}\alpha}{\mathrm{d}x_\mathrm{f}} \tilde{\boldsymbol{q}}_\mathrm{f}\right) - \alpha^2 \tilde{\boldsymbol{q}}_\mathrm{f}\right) \mathrm{e}^{\mathrm{i}\left(\int^{x_\mathrm{f}} \alpha(\epsilon_p \bar{x}_\mathrm{f})\mathrm{d}\bar{x}_\mathrm{f} - \omega_\mathrm{f} t_\mathrm{f}\right)}, \tag{2.25b}$$

where high-order terms in ϵ_p can be neglected. Introducing the ansatz (2.24) into the perturbation equation (2.13) hence yields the nonlocal perturbation equation that can be written in the general form

$$(\mathscr{A}_\alpha + \epsilon_p \mathscr{A}_{\alpha,\mathrm{np}})\tilde{\boldsymbol{q}}_\mathrm{f} = \alpha \mathscr{B}_\alpha \tilde{\boldsymbol{q}}_\mathrm{f} + \alpha^2 \mathscr{C}_\alpha \tilde{\boldsymbol{q}}_\mathrm{f} + \epsilon_p \frac{\mathrm{d}\alpha}{\mathrm{d}x_\mathrm{f}} \mathscr{D}_\alpha \tilde{\boldsymbol{q}}_\mathrm{f} + \epsilon_p \alpha \mathscr{E}_\alpha \frac{\partial \tilde{\boldsymbol{q}}_\mathrm{f}}{\partial x_\mathrm{f}} + \epsilon_p \mathscr{F}_\alpha \frac{\partial \tilde{\boldsymbol{q}}_\mathrm{f}}{\partial x_\mathrm{f}}, \tag{2.26}$$

with $\mathscr{A}_\alpha$, $\mathscr{B}_\alpha$ and $\mathscr{C}_\alpha$ being the same as for the spatial LST equations, whereas $\mathscr{D}_\alpha$, $\mathscr{E}_\alpha$ and $\mathscr{F}_\alpha$ are specific operators introduced by the fact that $\tilde{\boldsymbol{q}}_\mathrm{f}$ and α can slowly evolve in the streamwise direction. Furthermore, the operator $\mathscr{A}_{\alpha,\mathrm{np}}$ accounts for all non-parallel-flow effects of the base flow. Equation (2.26) can be solved with a multiple-scale approach (Gaster, 1974), that decomposes the problem into subproblems based on the order of ϵ_p, or with the PSE approach that instead uses the parabolized formulation of equation (2.26). When considering the PSE approach, the solutions are marched in the streamwise direction (Bertolotti *et al.*, 1992) and this thus offers much better performances than a multiple-scale approach. However, as a consequence of the parabolic character of the PSE, the method is strictly limited to flows with instabilities that are convected downstream. If absolute or global instability mechanisms are present somewhere in the flow, the spatial-marching procedure of the PSE method breaks down when approaching these locations. In contrast, the multiple-scale method can still be used (Monkewitz *et al.*, 1993) by analyzing the turning points emerging from the breakdown of the WKBJ approximation.

An important aspect of using equation (2.24) is the ambiguity introduced by the streamwise dependency in *both* $\tilde{\boldsymbol{q}}_\mathrm{f}$ and α in the sense that they can both contain the spatial growth of the perturbation in the streamwise direction. In other words, while the total spatial growth given by the multiplication of $\tilde{\boldsymbol{q}}_\mathrm{f}$ and the exponential factor is constant, the part of growth being included in $\tilde{\boldsymbol{q}}_\mathrm{f}$ and α is not known and is thus ambiguous. In order to eliminate this ambiguity, an auxiliary condition

$$\int_y \tilde{\boldsymbol{q}}_\mathrm{f}^\mathrm{H} \mathscr{M} \frac{\partial \tilde{\boldsymbol{q}}_\mathrm{f}}{\partial x_\mathrm{f}} \mathrm{d}y = 0, \tag{2.27}$$

is used at each step of the spatial integration of PSE and allows transferring the spatial growth rate included in $\tilde{\boldsymbol{q}}_\mathrm{f}$ to the complex wavenumber α. The superscript 'H' denotes the Hermitian transpose and the weight $\mathscr{M}$ can be arbitrarily defined such that it isolates only one or more components of $\tilde{\boldsymbol{q}}_\mathrm{f}$, or such that it is compatible with the definition of a perturbation energy (see §2.7.1). Alternative compatibility conditions exist and, for instance, can be based on the maximum of $\tilde{\boldsymbol{q}}_\mathrm{f}$ at each x-station instead of considering an integral value (Gaster, 1974; Bertolotti *et al.*, 1992). In this work and in recent literature, an integral value is, however, always preferred over a pointwise value because it reduces the impact of the spatial discretization on the results. Finally, it is important to notice that, while the ambiguity is eliminated with equation (2.27), the reduction of the spatial growth rate to an algebraic number remains based on the arbitrarily defined $\mathscr{M}$ weight, especially when it comes to

compressible flows. A thorough discussion about this weight matrix is proposed in §2.7.3. Similarly, the multiple-scale method needs an auxiliary condition as it considers eigenvalue problems for each ϵ_p-scale (Hinch, 1991).

The PSE approach is an initial-value problem in space, which contrasts with LST and BiGlobal approaches that are boundary-value problems, and it thus requires selecting an appropriate initial condition. In practice, this initial condition is a solution of the LST equations but this implies that the initial condition is not an exact solution of the PSE equation and thus transient solutions exist over few streamwise stations downstream of the initial location. Hence, in order to avoid contaminating the actual PSE solution by any transient, it is often preferred to initialize the PSE far upstream of the region of interest. However, for a boundary layer for instance, the flow becomes less and less parallel when decreasing the Reynolds number, i.e., approaching the leading edge. This means that, at more upstream stations, the LST solution carries a larger model error and thus generates a stronger transient when introduced into the PSE. Hence, initializing the marching method to solve the PSE approach can be a tedious task for some flow cases. It is shown in the following that the present moving-frame approach for the two-dimensional stability equations avoids this transient behavior since it uses an initial condition that satisfies the initial-value problem.

Although strictly applicable to a limited number of flow configurations, the LST and PSE methods are still relevant for the present work. In fact, the LST and PSE methods were at the premise of flow stability analyses and remain widely used in the literature for many flow configurations that are not strictly one-dimensional or slowly evolving. These methods are used in the present work to provide a comparison basis for the incompressible boundary layer (see Chapter 4) to compare with the results from the two-dimensional perturbation problem.

2.4. Adjoint linear stability problem

The adjoint formulation of the stability eigenvalue problem can be required for various reasons. First, the adjoint eigenfunctions can be used to identify the regions of the flow that are most sensitive to disturbance growth (Giannetti & Luchini, 2007; Brandt *et al.*, 2011), which is highly valuable from both a numerical and physical point of view. Second, the sensitivity problem based on the adjoint and direct eigensolutions allows performing analytic derivation, i.e., without resorting to any type of numerical differentiation (Schmid & Brandt, 2014; Alves *et al.*, 2019). Third, the adjoint eigensolutions combined to their direct counterparts can be used to reconstruct any arbitrary disturbance field by projecting it onto the eigenbasis (Schmid & Henningson, 2002; Ehrenstein & Gallaire, 2005; Åkervik *et al.*, 2007, 2008).

An essential ingredient for deriving the adjoint problem is the definition of the inner product between two arbitrary vectors $\boldsymbol{f}_1(x,y)$ and $\boldsymbol{f}_2(x,y)$ that is given by

$$\langle \boldsymbol{f}_1, \boldsymbol{f}_2 \rangle = \iint \boldsymbol{f}_1^{\mathrm{H}} \boldsymbol{f}_2 \, \mathrm{d}x_{\mathrm{f}} \mathrm{d}y \,, \tag{2.28}$$

in its continuous formulation. Using the inner product to multiply the direct eigenvalue problem (2.20) by an arbitrary vector $\tilde{\boldsymbol{f}}_{\mathrm{f}}^{\dagger}$ allows writing

$$\left\langle \tilde{\boldsymbol{f}}_{\mathrm{f}}^{\dagger}, (\mathscr{A} + \mathrm{i}\mathscr{B}\omega_{\mathrm{f}})\, \tilde{\boldsymbol{q}}_{\mathrm{f}} \right\rangle = 0 \,. \tag{2.29}$$

The relationship given by equation (2.29) is at the core of the derivation of the adjoint equation. Keeping the continuous formulation throughout the rest of the derivation results in the so-called *continuous* adjoint equations, that can be subsequently discretized. In contrast, if

the direct problem (2.20) is first discretized, the discrete inner product is then required and the final equation corresponds to the so-called *discrete* adjoint equation. Since the derivation of the continuous and discrete adjoint problems slightly differs from this point of the derivation onward, only the continuous form is kept for sake of conciseness throughout the present Chapter 2. The discretized formulation and the differences with its continuous equivalent are discussed in Chapter 3, which focuses on numerical aspects.

In the continuous formulation, the adjoint eigenvector $\tilde{\boldsymbol{q}}_{\mathrm{f}}^{\dagger}$ is defined after integrating the orthogonality relationship (2.29) by parts such that

$$\left\langle \left(\mathscr{A}^{\dagger} - \mathrm{i}\omega_{\mathrm{f}}^{*} \mathscr{B}^{\dagger} \right) \tilde{\boldsymbol{q}}_{\mathrm{f}}^{\dagger}, \tilde{\boldsymbol{f}}_{\mathrm{f}} \right\rangle = b\,, \tag{2.30}$$

must valid for all $\tilde{\boldsymbol{f}}_{\mathrm{f}}$. The operators $\mathscr{A}^{\dagger} = \mathscr{A}^{\mathrm{H}}$ and $\mathscr{B}^{\dagger} = \mathscr{B}^{\mathrm{H}}$ are defined as the continuous adjoint operators and the superscript '$*$' denotes the complex conjugate. The continuous formulation of the adjoint operators uses the superscript '†' in order to distinguish it from the discrete formulation, that will be derived in Chapter 3. The term b represents the boundary term that appears from the integration by parts and is set to zero, i.e., $b = 0$, in what follows. In practice, this is conditioned by a careful selection of homogeneous boundary conditions. After requiring that equation (2.30) is satisfied for any arbitrary vector $\tilde{\boldsymbol{q}}_{\mathrm{f}}$, the continuous adjoint equations can be written as

$$\mathscr{A}^{\dagger} \tilde{\boldsymbol{q}}_{\mathrm{f}}^{\dagger} = \mathrm{i}\omega_{\mathrm{f}}^{*} \mathscr{B}^{\dagger} \tilde{\boldsymbol{q}}_{\mathrm{f}}^{\dagger}\,, \tag{2.31}$$

where the vector $\tilde{\boldsymbol{q}}_{\mathrm{f}}^{\dagger}$ is the adjoint eigenvector. The complete set of equations can be found in Appendix A. The fact that the eigenvalue problem is a generalized eigenvalue problem implies that the adjoint and direct eigenvectors are not orthogonal, but satisfy a bi-orthogonality relationship,

$$\begin{aligned} 0 &= \left\langle \tilde{\boldsymbol{q}}_{\mathrm{f},j}^{\dagger}, \mathscr{A} \tilde{\boldsymbol{q}}_{\mathrm{f},k} \right\rangle - \left\langle \tilde{\boldsymbol{q}}_{\mathrm{f},j}^{\dagger}, \mathscr{A} \tilde{\boldsymbol{q}}_{\mathrm{f},k} \right\rangle \\ &= \left\langle \mathscr{A}^{\dagger} \tilde{\boldsymbol{q}}_{\mathrm{f},j}^{\dagger}, \tilde{\boldsymbol{q}}_{\mathrm{f},k} \right\rangle - \left\langle \tilde{\boldsymbol{q}}_{\mathrm{f},j}^{\dagger}, \mathscr{A} \tilde{\boldsymbol{q}}_{\mathrm{f},k} \right\rangle \\ &= \left\langle \mathrm{i}\omega_{\mathrm{f},j}^{*} \mathscr{B}^{\dagger} \tilde{\boldsymbol{q}}_{\mathrm{f},j}^{\dagger}, \tilde{\boldsymbol{q}}_{k} \right\rangle - \left\langle \tilde{\boldsymbol{q}}_{\mathrm{f},j}^{\dagger}, -\mathrm{i}\omega_{\mathrm{f},k} \mathscr{B} \tilde{\boldsymbol{q}}_{\mathrm{f},k} \right\rangle \\ &= -\mathrm{i}(\omega_{\mathrm{f},j} - \omega_{\mathrm{f},k}) \left\langle \tilde{\boldsymbol{q}}_{\mathrm{f},j}^{\dagger}, \mathscr{B} \tilde{\boldsymbol{q}}_{\mathrm{f},k} \right\rangle\,, \end{aligned} \tag{2.32}$$

with indices j and k for the j^{th} and k^{th} eigenvalue/-vector. This implies that $\langle \tilde{\boldsymbol{q}}_{\mathrm{f},j}^{\dagger}, \mathscr{B} \tilde{\boldsymbol{q}}_{\mathrm{f},k} \rangle = 0$, if the corresponding eigenvalues $\omega_{\mathrm{f},j}$ and $\omega_{\mathrm{f},k}$ are not equal. The functions $\tilde{\boldsymbol{q}}_{\mathrm{f},j}^{\dagger}$ and $\tilde{\boldsymbol{q}}_{\mathrm{f},k}$ are said to be orthogonal with respect to the inner product with weight $\mathscr{B}$. As a result, direct and adjoint eigenfunctions can be normalized such that

$$\left\langle \tilde{\boldsymbol{q}}_{\mathrm{f},j}^{\dagger}, \mathscr{B} \tilde{\boldsymbol{q}}_{\mathrm{f},k} \right\rangle = \delta_{jk} = \begin{cases} 1 & \text{for} \quad j = k\,, \\ 0 & \text{for} \quad j \neq k\,. \end{cases} \tag{2.33}$$

Usually, the stability problems are highly non-normal in the sense that the operator $\mathscr{A}$ is not self-adjoint. The resulting eigenfunctions are thus not orthogonal, i.e., $\langle \tilde{\boldsymbol{q}}_{\mathrm{f},j}, \tilde{\boldsymbol{q}}_{\mathrm{f},k} \rangle \neq \delta_{jk}$, and rather satisfy the bi-orthogonality relationship (2.32). This implies that adjoint eigenfunctions do not correspond to the Hermitian transpose of the direct eigenfunctions and vice-versa. An important source of non-normality in stability problems stems from the first-derivative terms that must take opposite signs in the direct and adjoint formulations

of the equations. This is a consequence of the integration by parts to obtain equation (2.30). Hence, flows supporting a strong advection of the perturbation are often highly non-normal (Schmid & Henningson, 2001; Schmid, 2007; Bagheri *et al.*, 2009; Schmid & Brandt, 2014). This type of non-normal operator reflects into direct and adjoint eigenfunctions that are spatially disjoint in the directions where the advection component is large (Åkervik *et al.*, 2008; Marquet *et al.*, 2009). This is illustrated in Chapters 4 and 5.

2.4.1. Eigenfunction expansion

The eigenvectors are the building blocks of the perturbation dynamics since they can form a basis for projecting any disturbance field onto it. Hence, the two-dimensional perturbation field $\boldsymbol{q}'_{\mathrm{f}}(x_{\mathrm{f}}, y, t)$ can be written as a linear combination of the two-dimensional eigenvectors

$$\boldsymbol{q}'_{\mathrm{f}}(x_{\mathrm{f}}, y, t) = \sum_{k=1}^{\infty} a_k \tilde{\boldsymbol{q}}_{\mathrm{f},k}(x, y) \mathrm{e}^{-\mathrm{i}\omega_{\mathrm{f},k} t_{\mathrm{f}}}, \tag{2.34}$$

with a_k the complex-valued expansion coefficients that need to be determined. Note that the homogeneous direction, that has no impact on the final result, is omitted in the present derivation for sake of conciseness. Considering the initial conditions $\boldsymbol{q}'_{\mathrm{f},0} = \boldsymbol{q}'_{\mathrm{f}}(x_{\mathrm{f}}, y, t_{\mathrm{f}} = 0)$, the expansion at $t_{\mathrm{f}} = 0$ is given by

$$\boldsymbol{q}'_{\mathrm{f},0} = \sum_{k=1}^{\infty} a_k \tilde{\boldsymbol{q}}_{\mathrm{f},k}(x, y). \tag{2.35}$$

Using the weighted inner product (2.33) allows writing

$$\left\langle \tilde{\boldsymbol{q}}^{\dagger}_{\mathrm{f},l}, \mathscr{B} \boldsymbol{q}'_{\mathrm{f},0} \right\rangle = \left\langle \tilde{\boldsymbol{q}}^{\dagger}_{\mathrm{f},l}, \mathscr{B} \sum_{k=1}^{\infty} a_k \tilde{\boldsymbol{q}}_{\mathrm{f},k}(x_{\mathrm{f}}, y) \right\rangle = \delta_{lk} a_k, \tag{2.36}$$

that finally provides an expression for the expansion coefficients

$$a_l = \left\langle \tilde{\boldsymbol{q}}^{\dagger}_{\mathrm{f},l}, \mathscr{B} \boldsymbol{q}'_{\mathrm{f},0} \right\rangle. \tag{2.37}$$

This shows that, once the solutions of both adjoint and direct eigenvalue problems are computed, the temporal evolution of an arbitrary perturbation can be obtained at all times by projecting it onto the eigenbasis. Although the series is supposed to include an infinite number of terms, a finite number N of terms can be used in practice but it requires to evaluate the convergence of the series with respect to N. This approach was used for reduced-order modeling by Ehrenstein & Gallaire (2005), Åkervik *et al.* (2007) and Garnaud *et al.* (2013) to study the stability of boundary layers, separation bubbles and jet flows, respectively.

2.5. Boundary conditions

In order to leverage the benefit of linear stability methods, that is to form a basis for the perturbation dynamics, the solutions are presently required to be independent of the truncation boundary positions and conditions. Satisfying this requirement for arbitrary homogeneous truncation boundary conditions is possible only if the eigensolution naturally decays to arbitrarily small amplitudes when approaching the truncation boundaries. This behavior is defined as "being localized" in the interior of the domain. While two-dimensional global instability mechanisms are, by definition, represented by localized eigenfunctions (Giannetti & Luchini, 2007; Robinet, 2007; Groot *et al.*, 2018), it is later demonstrated that the formulation of the two-dimensional stability problem in a moving frame of reference, derived

in the next section, enables the spatial localization of convective instability mechanisms. Such requirement implies that the boundary conditions have no influence on the solution and, thus, the truncation boundaries do not force the interior perturbation dynamics. Sensitivity studies are performed in Chapters 4 and 5 to evaluate the impact of the different types of boundary conditions on the results.

The two main types of boundary conditions applied to the perturbation variables are the traditional Dirichlet and Neumann conditions. The former, that imposes a vanishing perturbation at the boundary, is particularly suitable for the solid wall ($y = 0$) where perturbations of the velocity components and temperature are supposed to be physically zero. Furthermore, since all sought solutions are required to be localized in space, their decay in the two x- and y-directions towards the truncation boundary allows imposing the Dirichlet boundary condition at the freestream and in-/outlet streamwise boundaries. The Neumann condition imposes that the derivative of the perturbations is zero at the boundary. Because all boundary conditions must be homogeneous, a Neumann condition is often imposed when the actual behavior at the truncation boundaries is not known a-priori. In other words, a Neumann condition is typically imposed at locations where no strict physical constraints exist, in contrast to solid walls for instance. Hence, it is traditionally used for all variables in the wall-normal direction for the freestream truncation boundary and, for the streamwise BiGlobal stability equations, in the streamwise direction. Although it is well established (Malik, 1990; Pinna, 2012; Groot, 2013; Niessen, 2017) that using Neumann conditions in the freestream allows obtaining a converged solution in wall-bounded flows, imposing such behavior in the streamwise direction for convective instabilities leads to setup-dependent solutions (Theofilis, 2003).

At the solid boundary, there is a need to prescribe physically relevant conditions, that actually enforce zero amplitude for the velocity and temperature perturbations. However, no physical boundary condition exists for the pressure perturbation. In incompressible flows, the pressure is not a thermodynamic quantity but instead only acts as a Lagrange multiplier to ensure that the divergence of the velocity field remains zero. Although the pressure field can be defined up to an arbitrary constant, prescribing the pressure at the boundaries is not trivial and different methods have been proposed. A procedure that is often followed in stability analyses is to impose the pressure compatibility condition at the solid wall (Theofilis, 2003; Pinna, 2012). This condition is obtained by evaluating the y-momentum equation at the wall while assuming that all other perturbations vanish. This leads to the simple relation

$$\frac{\partial p'_\mathrm{f}}{\partial y} = \frac{1}{\mathrm{Re}} \frac{\partial^2 v'_\mathrm{f}}{\partial y^2}, \tag{2.38}$$

in incompressible flows, while the compressible compatibility equations is given by

$$\frac{\partial p'_\mathrm{f}}{\partial y} = \frac{1}{\mathrm{Re}} \left[\left(2\frac{\partial \overline{\mu}}{\partial \overline{T}} + \frac{\partial \overline{\lambda}}{\partial \overline{T}} \right) \frac{\partial \overline{T}}{\partial y} + (2\overline{\mu} + \overline{\lambda}) \frac{\partial}{\partial y} \right] \frac{\partial v'_\mathrm{f}}{\partial y} + \frac{1}{\mathrm{Re}} \left(2\frac{\partial \overline{\mu}}{\partial \overline{T}} + \frac{\partial \overline{\lambda}}{\partial \overline{T}} \right) \frac{\partial \overline{V}}{\partial y} \frac{\partial T'_\mathrm{f}}{\partial y}. \tag{2.39}$$

Although it is a widely used approach, an important flaw of the compatibility condition is that it does not bring any new information at the boundary because it re-uses a field equation, i.e., the y-momentum equation as defined in the rest of the domain, nor ensure that the velocity field is divergence free in the incompressible limit. Hence, by not enforcing explicitly a divergence-free velocity field at the boundary with equation (2.38), spurious pressure modes are found to contaminate the physical solution. Evaluating the effect of these spurious modes is important to ensure accurate results and, in some cases, this can require

changing the numerical setup such that they are not in the vicinity of the modes of interest (Niessen, 2017).

In order to improve the traditional compatibility condition, Theofilis (2017) proposes to use, at the boundary, the Linearized Pressure Poisson Equation (LPPE). By incorporating both the momentum and continuity equations, the LPPE does not represent a physical boundary condition for the pressure per se but instead acts as means to enforce the pressure such that the velocity field is divergence-free at the boundaries. Furthermore, since the pressure is defined up to an arbitrary constant, a fixed value is prescribed at one single point of the domain. The rest of the pressure field is governed by the field equations in the domain interior and the LPPE at the boundaries. Doing so, the LPPE allows removing the pressure spurious modes without affecting the physical modes. For isothermal flows in the incompressible limit, the LPPE at the solid wall can be written

$$\left(\frac{\partial^2}{\partial x_\mathrm{f}^2}+\frac{\partial^2}{\partial y^2}+\frac{\partial^2}{\partial z^2}\right)p'_\mathrm{f}=-2\frac{\partial\overline{V}}{\partial y}\frac{\partial v'_\mathrm{f}}{\partial y}\,. \tag{2.40}$$

Although Niessen (2017) considered the LPPE for compressible flows by assuming that the Mach number tends to zero at the solid wall, the equations did not account for the temperature dependence of the viscosity and conduction coefficients. The resulting equations are thus not strictly applicable. However, it was shown that this incomplete formulation allowed removing the spurious modes without affecting the physical modes. An improvement to this compressible formulation of the LPPE would actually rely on having a pressure condition at the wall in the form of a Poisson equation for compressible flows. Such formulation has actually been derived by Toutant (2017) in the form of an anisothermal low-Mach Poisson equation. As a final remark regarding the boundary conditions, another possible approach is to use a staggered grid (Robinet, 2007; Pinna, 2012) for the pressure variable such that it allows virtually avoiding to prescribe any pressure boundary condition. To avoid using a staggered grid, all flow cases considered in the present work make use of the LPPE condition at the wall whereas the traditional compatibility condition is used for the freestream truncation boundary.

2.6. Linear stability analysis in a moving frame of reference

The use of a moving frame of reference to resolve two-dimensional convective instabilities is motivated by the fact that the base-flow advection of perturbations in the streamwise direction introduces a streamwise exponential growth of the eigenfunctions (Groot & Schuttelaars, 2020) when solving the eigenvalue problem (2.20) in the fixed frame of reference. By considering a moving frame of reference instead, the advection imposed by the base flow can be largely mitigated. The advection-induced growth is thus reduced and the eigenfunctions can be localized in the streamwise direction, which is essential to obtain setup-independent solutions.

In order to derive the present method, the perturbation equations (2.13) are first formulated in a moving frame of reference. Second, the two-dimensional stability equations are derived. Since only applications with convective instabilities traveling in the streamwise direction are targeted, a moving frame of reference that travels at a constant speed c_f in the streamwise direction is considered ($c_\mathrm{f}>0$ for downstream displacement). The spatial coordinate x and the time t in the Galilean moving frame of reference are related to the x_f and t_f of the fixed frame of reference according to

$$x=x_\mathrm{f}-c_\mathrm{f}t_\mathrm{f},\qquad t=t_\mathrm{f}\,, \tag{2.41}$$

respectively. Note that the wall-normal and spanwise directions are not affected by the change of streamwise reference frame. The derivatives with respect to x_f and t_f can then be transformed into derivatives with respect to x and t as

$$\begin{cases} \dfrac{\partial \cdot}{\partial x_\mathrm{f}} = \quad 0 \quad + \dfrac{\partial \cdot}{\partial x}\dfrac{\partial x}{\partial x_\mathrm{f}} = \dfrac{\partial \cdot}{\partial x}, \\ \dfrac{\partial \cdot}{\partial t_\mathrm{f}} = \dfrac{\partial \cdot}{\partial t}\dfrac{\partial t}{\partial t_\mathrm{f}} + \dfrac{\partial \cdot}{\partial x}\dfrac{\partial x}{\partial t_\mathrm{f}} = \dfrac{\partial \cdot}{\partial t} - c_\mathrm{f}\dfrac{\partial \cdot}{\partial x}. \end{cases} \tag{2.42}$$

Inserting the expression for the derivatives (2.42) into the linearized Navier-Stokes equations, the perturbation equations (2.13) in the moving frame of reference can be written

$$\mathscr{B}\frac{\partial \boldsymbol{q}'}{\partial t_\mathrm{f}} = \mathscr{B}\left(\frac{\partial \boldsymbol{q}'}{\partial t} - c_\mathrm{f}\frac{\partial \boldsymbol{q}'}{\partial x}\right) = \mathscr{L}(\overline{\boldsymbol{Q}})\boldsymbol{q}', \tag{2.43}$$

which introduces an additional term incorporating the effect of the moving frame. Note that, regarding the element-wise structure of equations (2.13), the newly introduced c_f-term always occurs in pairs with the streamwise advection term $-\overline{U}\mathscr{B}\partial\boldsymbol{q}'/\partial x$ in $\mathscr{L}(\overline{\boldsymbol{Q}})\boldsymbol{q}'$.

In order to derive the stability equations in the moving frame of reference, the ansatz

$$\boldsymbol{q}'(x,y,z,t) = \tilde{\boldsymbol{q}}(x,y)\mathrm{e}^{\mathrm{i}(\beta z-\omega t)}, \tag{2.44}$$

is used. Note that the ansatz (2.44) now prescribes a fixed shape function in the *moving* frame of reference and thus slightly differs from the ansatz (2.19) that assumes a constant shape function in the *stationary* frame of reference. Since the perturbation shape of convective instabilities is not constant in space over time in a fixed frame of reference, it is thus more reasonable to prescribe ansatz (2.44) than the traditional ansatz (2.19). Upon imposing ansatzes (2.19) and (2.44), i.e., respectively looking for constant-frequency disturbances in the fixed or moving frame of reference, different shape functions will result. These shape functions can be transferred from one frame to the other through the relationship $\boldsymbol{q}'_\mathrm{f}(x_\mathrm{f},y,z,t_\mathrm{f}) = \boldsymbol{q}'(x,y,z,t)$. However, the shape function obtained through the moving-frame ansatz (2.44) will not 'fit' in the fixed-frame ansatz (2.19) for non-zero t_f if ω and ω_f are both required to be constant. In §2.6.2, this point is further addressed by generalizing ansatz (2.19).

Inserting the modal ansatz (2.44) into the linearized Navier-Stokes equations (2.43) yields the direct eigenvalue problem

$$\left(\mathscr{A}\left(\overline{\boldsymbol{Q}}(x+c_\mathrm{f}t,y);\beta\right) + c_\mathrm{f}\mathscr{B}\frac{\partial}{\partial x}\right)\tilde{\boldsymbol{q}}(x,y) = -\mathrm{i}\omega\mathscr{B}\tilde{\boldsymbol{q}}(x,y), \tag{2.45a}$$

in the moving frame of reference. Considering the inner product (2.28), the adjoint eigenvalue problem in the moving frame is then given by

$$\mathscr{A}^\dagger\left(\overline{\boldsymbol{Q}}(x+c_\mathrm{f}t,y);\beta\right)\tilde{\boldsymbol{q}}^\dagger(x,y) - c_\mathrm{f}\frac{\partial}{\partial x}\left(\mathscr{B}^\dagger\tilde{\boldsymbol{q}}^\dagger(x,y)\right) = \mathrm{i}\omega^*\mathscr{B}^\dagger\tilde{\boldsymbol{q}}^\dagger(x,y). \tag{2.45b}$$

Note that these problems also need to be closed with boundary conditions, that are exactly the same as for the stationary frame of reference. Hence, the discussions in §2.5 still hold for equations (2.45). Considering a moving frame of reference thus introduces an additional parameter c_f in the system of equations. This frame speed must be adequately selected in order to find converged eigensolutions that have localized eigenfunctions in the streamwise

direction. An initial choice for the frame speed can be the group speed of the sought instability since, as later demonstrated in §2.7.3, both speeds are closely related. If the group speed is not known a-priori, the phase speed can be used as a first estimate, as it is often close to the group speed for convective instabilities. In practice, both phase and group speeds can be approximated with LST calculations at few streamwise stations. The Gaster's transformation (Gaster, 1962), that relates the group speed with the wavenumber and the frequency of spatial and temporal analyses, respectively, could even be considered to obtain a first guess for the frame speed. In any case, a parametric analysis on the frame speed must be conducted to assess the effectiveness of the method and identify the frame speeds of interest. This will be illustrated with practical use of the moving frame of reference in Chapters 4 and 5. In order to clarify the consequences of using a moving frame of reference for stability analyses, several aspects of the moving-frame eigensolutions are tackled in the next subsections, especially regarding their interpretation and their relation with the fixed-frame solutions.

2.6.1. Obtaining time-dependent solutions without model errors

In the moving frame of reference, the base flow depends on t, while it was independent of t_f in the stationary frame of reference. To evaluate this effect, the base-flow quantities are expanded in a Taylor series in t with respect to $t = 0$,

$$\overline{\boldsymbol{Q}}(x + c_\mathrm{f} t, y) = \overline{\boldsymbol{Q}}(x, y) + c_\mathrm{f} t \frac{\partial \overline{\boldsymbol{Q}}}{\partial x_\mathrm{f}}(x, y) + \mathscr{O}\left(\frac{(c_\mathrm{f} t)^2}{2!} \frac{\partial^2 \overline{\boldsymbol{Q}}}{\partial x_\mathrm{f}^2}(x, y) \right), \tag{2.46}$$

where t is to be interpreted as an elapsed time. This reveals that the base flow can be assumed to be constant in t when permitting an error of $\mathscr{O}\left(c_\mathrm{f} t \, \partial \overline{\boldsymbol{Q}} / \partial \bar{x}\right)$, which is small when c_f, t or $\partial \overline{\boldsymbol{Q}} / \partial \bar{x}$ is small. By evaluating the eigenvalue problem (2.45a) for the base flow at $t = 0$, the eigensolutions are exact solutions of the linearized Navier-Stokes equations. Hence, the eigensolutions satisfying (2.45a) must be interpreted in an instantaneous sense at $t = 0$ only. Note that the fact that the solutions are exact at $t = 0$ contrasts with LST and PSE for which the model error exists for all time and streamwise locations.

For non-zero t, the eigensolutions satisfying equation (2.45a) can be integrated in time to account for *all* unsteady effects due to the moving reference frame. That is, the linearized Navier-Stokes equations (2.13), i.e., the *fixed*-reference-frame initial-value problem, are solved while specifying eigensolutions to (2.45a) as the initial condition. In particular, solutions will be sought as

$$\boldsymbol{q}'_\mathrm{f}(x_\mathrm{f}, y, z = 0, t_\mathrm{f}) = \mathrm{e}^{\mathscr{B}^{-1} \mathscr{L} t_\mathrm{f}} \tilde{\boldsymbol{q}}(x_\mathrm{f}(t_\mathrm{f} = 0), y), \tag{2.47}$$

which is similar to equation (2.18), except that the third dimension is assumed homogeneous in equation (2.47). This formulation allows both reducing the computational cost and avoiding to prescribe a domain width in the third dimension that must be imposed such as to fit the spanwise modulation of the wave packet. Note that this approach is consistent with the two-dimensional base flows that are considered in the present work.

The initial-value-problem formulation is very similar to the spatial marching approach used in PSE analyses. However, the model error induced by the spatial parabolization in PSE does not exist in the proposed time-marching approach since the equations are fully elliptic in space and no high-order term is discarded. Hence, the time-marched solutions will not be subject to any model error for $t \geq 0$, up to the chosen numerical strategy, which is discussed in Chapter 3.

2.6.2. Relation with the fixed frame of reference: a complex Doppler shift

It has been established that the moving-frame eigensolutions are instantaneously-exact solutions of the linearized Navier-Stokes equations at time $t = 0$. However, a clarification is needed regarding how the eigenvalue ω, in particular its real and imaginary parts, should be interpreted. To this purpose, the *instantaneous behavior* of the moving-frame eigensolution in the fixed frame of reference is analyzed in what follows.

Ansatz (2.19) falls short of representing the behavior of the moving-frame eigensolution, because it does not capture the streamwise translation effect imposed by the moving frame. To include this effect in the fixed frame, it is essential to depart from imposing the same constant ω_f for the entire eigenvector, i.e., all eigenfunctions or the components of the eigenvector $\tilde{\boldsymbol{q}}_\mathrm{f}$, corresponding to the same eigensolution. This leads to the following generalized fixed-frame ansatz

$$\boldsymbol{q}'_\mathrm{f}(x_\mathrm{f}, y, z, t_\mathrm{f}) = \tilde{\boldsymbol{q}}(x_\mathrm{f}, y)\mathrm{e}^{\mathrm{i}(\beta z - \boldsymbol{\Gamma}_\mathrm{f}(x_\mathrm{f}, y, t_\mathrm{f})\, t_\mathrm{f})}, \tag{2.48}$$

where $\tilde{\boldsymbol{q}}$ represents the eigenvector that satisfies the eigenvalue problem in the moving frame of reference, i.e., equation (2.45a), and

$$\boldsymbol{\Gamma}_\mathrm{f}(x_\mathrm{f}, y, t_\mathrm{f}) = \begin{bmatrix} \omega_{\mathrm{f},\tilde{u}} & 0 & \cdots & 0 \\ 0 & \omega_{\mathrm{f},\tilde{v}} & & 0 \\ \vdots & & \ddots & \vdots \\ 0 & 0 & \cdots & \omega_{\mathrm{f},\tilde{p}} \end{bmatrix} \tag{2.49}$$

is assumed to depend on x_f, y, and t_f. This generalized ansatz poses the question how the individual components evolve in time if the moving-frame eigenvector, $\tilde{\boldsymbol{q}}(x_\mathrm{f}, y)$, is imposed in the fixed frame of reference; hence it is evaluated for x_f, not x. To this end, the way in which each of the components $(\tilde{u}, \tilde{v}, \ldots, \tilde{p})$ can behave is left as general as possible by introducing an $\omega_{\mathrm{f},\tilde{q}}$ per component $\tilde{q}$ of $\tilde{\boldsymbol{q}}$ and allowing each of these functions to depend on the independent variables x_f, y, and t_f.

After substituting ansatz (2.48) into the linearized Navier-Stokes equations, partial derivatives have to be evaluated as follows

$$\left.\begin{aligned} \frac{\partial \boldsymbol{q}'_\mathrm{f}}{\partial t_\mathrm{f}} &\overset{\text{(a)}}{=} \left(-\mathrm{i}\boldsymbol{\Gamma}_\mathrm{f}\tilde{\boldsymbol{q}} - \mathrm{i}t_\mathrm{f}\frac{\partial \boldsymbol{\Gamma}_\mathrm{f}}{\partial t_\mathrm{f}}\tilde{\boldsymbol{q}}\right) \times \mathrm{e}^{\mathrm{i}\cdots}, \qquad \frac{\partial \boldsymbol{q}'_\mathrm{f}}{\partial x_\mathrm{f}} \overset{\text{(b)}}{=} \left(\frac{\partial \tilde{\boldsymbol{q}}}{\partial x_\mathrm{f}} - \mathrm{i}t_\mathrm{f}\frac{\partial \boldsymbol{\Gamma}_\mathrm{f}}{\partial x_\mathrm{f}}\tilde{\boldsymbol{q}}\right) \times \mathrm{e}^{\mathrm{i}\cdots}; \\ \frac{\partial^2 \boldsymbol{q}'_\mathrm{f}}{\partial x_\mathrm{f}^2} &\overset{\text{(c)}}{=} \left(\frac{\partial^2 \tilde{\boldsymbol{q}}}{\partial x_\mathrm{f}^2} - 2\mathrm{i}t_\mathrm{f}\frac{\partial \boldsymbol{\Gamma}_\mathrm{f}}{\partial x_\mathrm{f}}\frac{\partial \tilde{\boldsymbol{q}}}{\partial x_\mathrm{f}} - t_\mathrm{f}^2\left(\frac{\partial \boldsymbol{\Gamma}_\mathrm{f}}{\partial x_\mathrm{f}}\right)^2\tilde{\boldsymbol{q}} - \mathrm{i}t_\mathrm{f}\frac{\partial^2 \boldsymbol{\Gamma}_\mathrm{f}}{\partial x_\mathrm{f}^2}\tilde{\boldsymbol{q}}\right) \times \mathrm{e}^{\mathrm{i}\cdots}. \end{aligned}\right\} \tag{2.50}$$

The partial y- (and cross) derivatives yield very similar results. Since the instantaneous behavior is targeted, the time is set to $t_\mathrm{f} = 0$, which reduces the right-hand side of all derivatives to the first terms. This assumption is also necessary in order to allow 'factoring' the exponential from the equations after substituting the ansatz. Finally, introducing the ansatz into the fixed-frame linearized Navier-Stokes equations yields

$$\mathscr{L}\left(\overline{\boldsymbol{Q}}(x_\mathrm{f}, y)\right)\tilde{\boldsymbol{q}}(x_\mathrm{f}, y) = -\mathrm{i}\mathscr{B}\boldsymbol{\Gamma}_\mathrm{f}(x_\mathrm{f}, y, t_\mathrm{f})\,\tilde{\boldsymbol{q}}(x_\mathrm{f}, y), \qquad \text{for } t_\mathrm{f} = 0. \tag{2.51}$$

This formulation is much more complicated than an eigenvalue problem and is not meant to be solved directly. Instead, its (instantaneous) solutions are obtained by solving the moving-frame eigenvalue problem (2.45a); equation (2.51) is only a tool that helps the physical interpretation of the solutions to (2.45a) at $t_\mathrm{f} = t = 0$ in the fixed frame of reference.

By comparing problem (2.51) against (2.45a), upon moving the term with c_f to the right-hand side in equation (2.45a), it follows the relation

$$-\mathrm{i}\mathscr{B}\boldsymbol{\Gamma}_\mathrm{f}\tilde{\boldsymbol{q}} = -\mathrm{i}\mathscr{B}\begin{bmatrix} \omega_{\mathrm{f},\tilde{u}}\,\tilde{u} \\ \omega_{\mathrm{f},\tilde{v}}\,\tilde{v} \\ \vdots \\ \omega_{\mathrm{f},\tilde{p}}\,\tilde{p} \end{bmatrix} = -\mathrm{i}\omega\mathscr{B}\tilde{\boldsymbol{q}} - c_\mathrm{f}\mathscr{B}\frac{\partial\tilde{\boldsymbol{q}}}{\partial x}. \tag{2.52}$$

The intended relationship between $\omega_{\mathrm{f},\tilde{q}}$ and ω can be directly inferred by realizing that this system of equations is satisfied if the component-wise relationship

$$\omega_{\mathrm{f},\tilde{q}}(x,y) = \omega - \mathrm{i}\frac{c_\mathrm{f}}{\tilde{q}}\frac{\partial\tilde{q}}{\partial x}(x,y) \tag{2.53}$$

holds for all individual components $\tilde{q}$ of the complex $\tilde{\boldsymbol{q}}$. Considering that equation (2.45a) is solved as an eigenvalue problem, ω is constant in that case. The presence of $\tilde{q}$ in equation (2.53), however, renders $\omega_{\mathrm{f},\tilde{q}}$ dependent on x, y and this dependency changes per eigenfunction $\tilde{q}$. This is why it is necessary to generalize ansatz (2.19). The fact that the growth rate and frequency/wavenumber associated with different eigenfunctions (e.g., $\tilde{u}$ versus $\tilde{v}$) in the same eigenvector are different is not new (Alizard & Robinet, 2007; Ehrenstein & Gallaire, 2005) and also arises when describing perturbations with other approaches that account for non-parallel effects (Gaster, 1974; Saric & Nayfeh, 1975; Bertolotti *et al.*, 1992).

From a physical point of view, equation (2.53) can be understood as a complex Doppler shift. First, express $\tilde{q}$ as $|\tilde{q}(x,y)|\mathrm{e}^{\mathrm{i}\theta(x,y)}$ where θ is real, so that both the streamwise wavenumber $\alpha_{\tilde{q},r}(x,y) = \partial\theta/\partial x$ and the corresponding streamwise wavelength $\lambda = 2\pi/\alpha_{\tilde{q},r}$ are real as well. Further expanding the right-hand side of (2.53) then yields

$$\omega_{\mathrm{f},\tilde{q}}(x,y) = \omega - \mathrm{i}c_\mathrm{f}\frac{\partial}{\partial x}\left(\ln|\tilde{q}| + \mathrm{i}\theta\right) = \omega_r + \alpha_{\tilde{q},r}\,c_\mathrm{f} + \mathrm{i}\left(\omega_i - c_\mathrm{f}\frac{\partial\ln|\tilde{q}|}{\partial x}\right). \tag{2.54}$$

The real part of equation (2.54) represents the change in frequency according to the streamwise wavelength of the perturbation and the frame speed as attributed to the Doppler effect. Next to the temporal growth imposed by ω_i, the imaginary part of equation (2.54) represents a translation effect of the disturbance in x_f with time due to the moving frame. This can be observed by recognizing that the term $-c_\mathrm{f}\partial\ln|\tilde{q}|/\partial x$ reduces (increases) the perturbation magnitude wherever the magnitude is locally increasing (decreasing) in the streamwise direction. Figure 2.1 illustrates this by considering the absolute value of ansatz (2.48), after having substituted equation (2.54), and choosing an arbitrary functions f, a substitute for one component of $\tilde{q}$, to be Gaussian in x_f and setting $\omega_i = 0$ to isolate the translation effect. For small times, the function $f(x_\mathrm{f} - c_\mathrm{f}t_\mathrm{f}, 0)$, which represents the translated version of the function $f(x_\mathrm{f}, 0)$, is approximated by

$$f(x_\mathrm{f},0)\exp\left(-c_\mathrm{f}t_\mathrm{f}\frac{\partial\ln|f|}{\partial x}(x_\mathrm{f} - c_\mathrm{f}t_\mathrm{f}, 0)\right), \tag{2.55}$$

where the argument in the exponential represents the effect of the term $-c_\mathrm{f}\partial\ln|\tilde{q}|/\partial x$ in equation (2.54). The second argument of the partial x-derivative of $\ln|f|$ is set to zero, because ansatz (2.44) imposes the assumption that f is independent of time. It will be verified in Chapters 4 and 5, that if eigensolutions are specified as the initial condition for equation (2.13), this results in a time-dependent solution that instantaneously translates in x_f with the speed c_f.

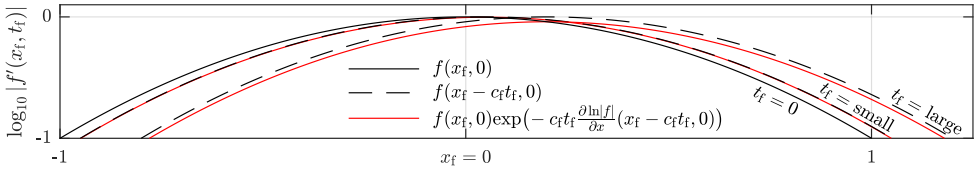

Figure 2.1: Streamwise magnitude evolution of a perturbation f' with $\omega_i = 0$ as represented with the moving-frame modal ansatz (2.44, solid black) at $t = 0$, the moving-frame modal ansatz (2.44, dashed black line), and the generalized fixed-frame ansatz (2.19, solid red) using the Doppler shift (2.54), where $f = f(x, t)$ represents the eigenfunction in the moving reference frame.

2.7. Characterizing the spatio-temporal evolution of instabilities

This section proposes several concepts to characterize the evolution of two-dimensional wave-packet instabilities. Building upon the concept of perturbation energy, this section further establishes the relation between perturbation growth and eigengrowth when moving-frame eigensolutions are used as initial condition of the perturbation equations. Furthermore, a method based on the Fourier transform of the two-dimensional spatio-temporal wave packets is introduced in order to reconstruct amplification curves. These curves represent a practical tool for stability analysis of flows with convective instabilities and, in particular, are key for the e^N method, one of the most useful engineering tools for the prediction of laminar-turbulent transition.

2.7.1. Perturbation energy

The perturbation energy E is a scalar quantity that allows casting the perturbation field $\boldsymbol{q}'$, made of several components that do not necessarily evolve the same way, into one representative variable. Hence, on the one hand, the perturbation energy provides a simple measure of the overall amplification of a disturbance in a flow field and, on the other hand, it allows deriving a balance equation (see §2.8) that can be used to determine what mechanisms produce perturbation energy and how the energy transfers between perturbation components. The perturbation energy includes all variables that are governed by a transport equation and is given as the integral

$$E(t_\mathrm{f}) = \frac{1}{2}\int_{\mathcal{V}_\mathrm{f}} \boldsymbol{q}_\mathrm{f}'^\mathrm{H}\mathcal{M}\boldsymbol{q}_\mathrm{f}'\,\mathrm{d}\mathcal{V}_\mathrm{f}, \tag{2.56}$$

over a generic, finite volume $\mathcal{V}_\mathrm{f}$ with infinitesimal volume elements $\mathrm{d}\mathcal{V}_\mathrm{f} = \mathrm{d}x_\mathrm{f}\,\mathrm{d}y\,\mathrm{d}z$. For compressible flows, the energy weight $\mathcal{M}$ is given by

$$\mathcal{M} = \mathcal{M}(x_\mathrm{f}, y, z) = \mathrm{diag}\left(\overline{\rho}, \overline{\rho}, \overline{\rho}, \frac{\overline{\rho}}{\gamma \mathrm{Ec}\,\overline{T}}, \frac{\overline{T}}{\gamma M^2 \overline{\rho}}\right), \tag{2.57}$$

as originally formulated by Chu (1965) for the perturbation field $\boldsymbol{q}_\mathrm{f}' = [u', v', w', , T', \rho']_\mathrm{f}^\mathrm{T}$, i.e. density formulation of the equations. Instead, if the perturbation equations are formulated with the pressure perturbation (Groot, 2013), i.e., using $\boldsymbol{q}_\mathrm{f}' = [u', v', w', T', p']_\mathrm{f}^\mathrm{T}$, the energy-

weight $\mathscr{M}$ is given by

$$\mathscr{M} = \mathscr{M}(x_\mathrm{f}, y, z) = \begin{bmatrix} \overline{\rho} & 0 & 0 & 0 & 0 \\ 0 & \overline{\rho} & 0 & 0 & 0 \\ 0 & 0 & \overline{\rho} & 0 & 0 \\ 0 & 0 & 0 & \frac{\overline{\rho}}{\mathrm{Ec}\,\overline{T}} & -\frac{1}{\overline{T}} \\ 0 & 0 & 0 & -\frac{1}{\overline{T}} & \frac{1}{\overline{P}} \end{bmatrix}, \tag{2.58}$$

and is not diagonal anymore. The two energy norms are nevertheless equivalent (see Appendix A). With the weight $\mathscr{M}$, the perturbation energy E is essentially made of two different components such that $E = E_k + E_p$ (Chu, 1965). The first component is the kinetic energy E_k that only involves the velocity components (first three rows of $\mathscr{M}$) and the second is the generalized potential energy E_p that only considers the thermodynamic variables (last two rows of $\mathscr{M}$).

In incompressible flows, only transport equations for the velocity components are considered and this implies that, in the absence of pressure imposed at boundaries, the pressure work is conservative and only bridges the energy transfer between velocity components via the continuity equation. Hence, the pressure perturbation does not have a net contribution to the perturbation energy and, as originally suggested by Reynolds (1895), the perturbation energy in incompressible flows reduces to the perturbation kinetic energy

$$E_i(t) = \int_{\mathscr{V}_\mathrm{f}} \left(|u'_\mathrm{f}|^2 + |v'_\mathrm{f}|^2 + |w'_\mathrm{f}|^2 \right) \mathrm{d}\mathscr{V}_\mathrm{f}. \tag{2.59}$$

This is equivalent to considering $\mathscr{M} = \mathrm{diag}(1,1,1,0)$, which has constant coefficients in space, in contrast to the compressible formulations.

For both compressible and incompressible flows, the perturbation energy is based on the definition of a matrix containing multiplicative coefficients that can be arbitrarily defined as long as the resulting quantity is positive definite and a monotone, non-increasing function in time if no external source is involved (Chu, 1965; Hanifi *et al.*, 1996; Padilla Montero & Pinna, 2021). Hence, the energy computed in different systems, i.e., computed with different energy weight matrices $\mathscr{M}$, is often inconsistent from one system of equations to another and quantitative comparisons are often not possible. In the context of perturbation energy in perfect-gas flows, the spatially-dependent matrix (2.57) that was originally defined by (Chu, 1965) is, however, the most used in the literature.

If the modal ansatz (2.19) in the stationary frame of reference is considered, the perturbation energy corresponding to a single eigensolution can be expanded as

$$E(t_\mathrm{f}) = \frac{2\pi}{\beta} \mathrm{e}^{(2\omega_{\mathrm{f},i}\, t_\mathrm{f})} \iint \tilde{\boldsymbol{q}}_\mathrm{f}^\mathrm{H} \mathscr{M} \tilde{\boldsymbol{q}}_\mathrm{f} \mathrm{d}x_\mathrm{f} \mathrm{d}y = \frac{4\pi}{\beta} \mathrm{e}^{(2\omega_{\mathrm{f},i}\, t_\mathrm{f})} \tilde{E}_\mathrm{f}, \tag{2.60}$$

where the integration in the spanwise direction yields a constant contribution of spanwise wavelength β to the perturbation energy. It is therefore more appropriate to omit the spanwise direction and restrict the attention to the in-plane energy only. The absolute measure of energy as given by equation (2.60) is, however, often not of interest since the perturbation problems are linear, i.e., independent of the magnitude of the perturbation. Instead, it is much more relevant to consider the evolution of the perturbation energy, i.e., to consider an energy-based temporal growth rate as introduced in the next section.

2.7.2. Perturbation energy growth and eigengrowth

In order to obtain a global measure of the temporal growth rate in the stationary frame of reference, the temporal derivative of the energy is considered,

$$\frac{\mathrm{d}E}{\mathrm{d}t_\mathrm{f}}(t_\mathrm{f}) = \mathscr{R}\left\{\int_{\mathcal{V}_\mathrm{f}} \boldsymbol{q}_\mathrm{f}'^\mathrm{H} \mathscr{M} \frac{\partial \boldsymbol{q}_\mathrm{f}'}{\partial t_\mathrm{f}} \mathrm{d}\mathcal{V}_\mathrm{f}\right\} = \mathscr{R}\left\{\int_{\mathcal{V}} \boldsymbol{q}'^\mathrm{H} \mathscr{M} \left(\frac{\partial \boldsymbol{q}'}{\partial t} - c_\mathrm{f}\frac{\partial \boldsymbol{q}'}{\partial x}\right) \mathrm{d}\mathcal{V}\right\}, \tag{2.61}$$

where $\mathscr{R}\{\cdot\}$ represents taking the real part. This equation holds for all times. Considering $t_\mathrm{f} = 0$ and the moving-frame modal ansatz (2.44) for $\boldsymbol{q}'$ in equation (2.56), the initial energy growth rate can be written as

$$\sigma(t_\mathrm{f}=0) = \frac{1}{2E}\frac{\mathrm{d}E}{\mathrm{d}t_\mathrm{f}}(t_\mathrm{f}=0) = \omega_i - \frac{1}{2\tilde{E}}\mathscr{R}\left\{c_\mathrm{f}\iint \tilde{\boldsymbol{q}}^\mathrm{H}\mathscr{M}\frac{\partial\tilde{\boldsymbol{q}}}{\partial x}\mathrm{d}x\,\mathrm{d}y\right\}, \tag{2.62}$$

with $\tilde{E} = 1/2\iint \tilde{\boldsymbol{q}}^\mathrm{H}\mathscr{M}\tilde{\boldsymbol{q}}\,\mathrm{d}x\,\mathrm{d}y$ the perturbation energy of a single eigensolution in the moving frame. The presence of the c_f-term in equation (2.62), but also in the imaginary part of the Doppler shift equation (2.54), begs the question of an artificial contribution of the moving frame to the net energy growth when introducing a moving-frame eigenfunction in the stationary frame of reference. In order to assess the impact of the second right-hand-side term in equation (2.62) on the energy growth, this term is divided into boundary and interior contributions through integration by parts in the streamwise direction:

$$\begin{aligned} I := \iint \tilde{\boldsymbol{q}}^\mathrm{H}\mathscr{M}\frac{\partial\tilde{\boldsymbol{q}}}{\partial x}\mathrm{d}x\,\mathrm{d}y &= \int_y \tilde{\boldsymbol{q}}^\mathrm{H}\mathscr{M}\tilde{\boldsymbol{q}}\,\mathrm{d}y\Big|_{x_\mathrm{in}}^{x_\mathrm{out}} - \iint \tilde{\boldsymbol{q}}^\mathrm{H}\frac{\partial\mathscr{M}}{\partial x}\tilde{\boldsymbol{q}}\,\mathrm{d}x\,\mathrm{d}y - \iint \frac{\partial\tilde{\boldsymbol{q}}}{\partial x}^\mathrm{H}\mathscr{M}\tilde{\boldsymbol{q}}\,\mathrm{d}x\,\mathrm{d}y \\ &= \int_y \tilde{\boldsymbol{q}}^\mathrm{H}\mathscr{M}\tilde{\boldsymbol{q}}\,\mathrm{d}y\Big|_{x_\mathrm{in}}^{x_\mathrm{out}} - \iint \tilde{\boldsymbol{q}}^\mathrm{H}\frac{\partial\mathscr{M}}{\partial x}\tilde{\boldsymbol{q}}\,\mathrm{d}x\,\mathrm{d}y - I^*. \end{aligned} \tag{2.63}$$

Inserting the above relation back into equation (2.62), the relationship between the instantaneous perturbation growth and eigengrowth can be obtained as follows

$$\begin{aligned} \sigma(t_\mathrm{f}=0) &= \omega_i - \frac{c_\mathrm{f}}{4\tilde{E}}(I + I^*) \\ &= \omega_i + \frac{c_\mathrm{f}}{4\tilde{E}}\iint \tilde{\boldsymbol{q}}^\mathrm{H}\frac{\partial\mathscr{M}}{\partial x_\mathrm{f}}\tilde{\boldsymbol{q}}\,\mathrm{d}x_\mathrm{f}\,\mathrm{d}y \underbrace{- \frac{c_\mathrm{f}}{4\tilde{E}}\int_y \tilde{\boldsymbol{q}}^\mathrm{H}\mathscr{M}\tilde{\boldsymbol{q}}\,\mathrm{d}y\Big|_{x_\mathrm{in}}^{x_\mathrm{out}}}_{\text{Boundary term } \omega_{i,\mathrm{io}}}. \end{aligned} \tag{2.64}$$

If all eigenfunctions are small at the in-/outflow boundaries, i.e., if eigenfunctions are localized in the streamwise direction, the boundary term $\omega_{i,\mathrm{io}}$ vanishes and the growth of the eigensolutions obtained in the moving frame of reference corresponds to the instantaneous growth of the perturbation in the fixed frame of reference, up to a corrective factor induced by a streamwise variation of the $\mathscr{M}$-matrix. According to equation (2.64), the corrected eigengrowth rate can be defined as

$$\omega_{i,c} = \omega_i + \frac{c_\mathrm{f}}{4\tilde{E}}\iint \tilde{\boldsymbol{q}}^\mathrm{H}\frac{\partial\mathscr{M}}{\partial x_\mathrm{f}}\tilde{\boldsymbol{q}}\,\mathrm{d}x_\mathrm{f}\,\mathrm{d}y, \tag{2.65}$$

and is only different from ω_i if the $\mathscr{M}$-matrix has x-dependent coefficients.

A necessary condition to ensure domain-independence of an eigensolution from a computational perspective is to be able to make all components of $\tilde{\boldsymbol{q}}$ arbitrarily small at the truncation boundaries, by placing the truncation boundaries far enough away from the region of interest for example. The boundary term in equation (2.64) is a relevant measure of the

amplitude of the eigenfunctions at the boundaries. Since the choice of $\mathscr{M}$ is arbitrary in the previous development, it can be chosen such that it selects individual eigenfunctions from $\tilde{\boldsymbol{q}}$. If all eigenfunctions in $\tilde{\boldsymbol{q}}$ are negligibly small at the boundaries, i.e., if they are all localized in the interior of the domain, the boundary term in equation (2.64) is always inactive. In that case, the instantaneous perturbation growth at $t_\mathrm{f} = 0$ equals ω_i for all eigenfunctions corresponding to that solution when $\mathscr{M}$ is constant. If $\mathscr{M}$ depends on the streamwise coordinate, a constant correction (see equation (2.65)) must be taken into account such that the instantaneous perturbation growth at $t_\mathrm{f} = 0$ equals $\omega_{i,c}$. The two cases, i.e., with constant and non-constant $\mathscr{M}$ matrices, will be considered in practical applications in Chapters 4 and 5, respectively.

2.7.3. Spatial amplification and N-factor curves

With the present formulation of the problem, the solutions take the form of two-dimensional wave packets having characteristics distributed in space, which can be inconvenient to analyze. In order to ease the representation of these wave packets, the perturbation energy (2.56) is now associated with the spatial coordinates

$$x_E(t_\mathrm{f}) \overset{\text{(a)}}{=} \frac{\int_{\mathcal{V}_\mathrm{f}} x_\mathrm{f}\, \boldsymbol{q}_\mathrm{f}'^\mathrm{H} \mathscr{M} \boldsymbol{q}_\mathrm{f}' \,\mathrm{d}\mathcal{V}_\mathrm{f}}{\int_{\mathcal{V}_\mathrm{f}} \boldsymbol{q}_\mathrm{f}'^\mathrm{H} \mathscr{M} \boldsymbol{q}_\mathrm{f}' \,\mathrm{d}\mathcal{V}_\mathrm{f}} \qquad y_E(t_\mathrm{f}) \overset{\text{(b)}}{=} \frac{\int_{\mathcal{V}_\mathrm{f}} y\, \boldsymbol{q}_\mathrm{f}'^\mathrm{H} \mathscr{M} \boldsymbol{q}_\mathrm{f}' \,\mathrm{d}\mathcal{V}_\mathrm{f}}{\int_{\mathcal{V}_\mathrm{f}} \boldsymbol{q}_\mathrm{f}'^\mathrm{H} \mathscr{M} \boldsymbol{q}_\mathrm{f}' \,\mathrm{d}\mathcal{V}_\mathrm{f}}, \tag{2.66}$$

that are defined, respectively, as the $x_{(\mathrm{f})}$- and y-energy centroids of the wave packet, in the fixed frame of reference. Hence, the temporal evolution of the perturbation energy can be translated into a spatial evolution and the characteristics of a temporal wave packet, such as its energy growth rate, can be easily analyzed in space. In order to quantify the instantaneous velocity with which the wave packets propagate in the streamwise direction, the group speed c_g is defined as

$$c_\mathrm{g}(t_\mathrm{f}) = \frac{\mathrm{d}x_E}{\mathrm{d}t_\mathrm{f}}. \tag{2.67}$$

As later illustrated in Chapter 4 (§4.3), if the eigenfunctions corresponding to a given eigensolution are localized, then $c_\mathrm{g}(t_\mathrm{f}) \to c_\mathrm{f}$ as $t_\mathrm{f} \to 0$.

In addition to the energy centroids, the streamwise and wall-normal extrema are considered to assess the spatial extent of the wave packets. These locations are determined by the locations where the spatial distribution of energy has decayed by a factor 10^{-3} away from the maximum. This corresponds to the x_f and y-locations where the criteria

$$\frac{\int \tilde{\boldsymbol{q}}^\mathrm{H} \mathscr{M} \tilde{\boldsymbol{q}} \,\mathrm{d}y}{\left(\int \tilde{\boldsymbol{q}}^\mathrm{H} \mathscr{M} \tilde{\boldsymbol{q}} \,\mathrm{d}y\right)_\mathrm{max}} \overset{\text{(a)}}{=} 10^{-3} \quad \text{and} \quad \frac{\int \tilde{\boldsymbol{q}}^\mathrm{H} \mathscr{M} \tilde{\boldsymbol{q}} \,\mathrm{d}x}{\left(\int \tilde{\boldsymbol{q}}^\mathrm{H} \mathscr{M} \tilde{\boldsymbol{q}} \,\mathrm{d}x\right)_\mathrm{max}} \overset{\text{(b)}}{=} 10^{-3}, \tag{2.68}$$

are satisfied, respectively. In this work, the upstream and downstream extrema are denoted by x_u and x_d, respectively, while the near-wall and freestream bounds of the wave packet are labeled y_w and y_e, respectively.

While the perturbation energy, spatial centroids and extrema provide information regarding the global evolution of the wave packet, each single frequency constituting the wave packet can possibly be amplified differently in space and time. Therefore, when it comes to identifying the most amplified (range of) frequencies, it is relevant to decompose the wave packet into its individual frequency components. Considering individual frequencies is equivalent to PSE and LST, which focus on wave-train-type instabilities only, but now with

the superior elliptic representation that is inherently provided by the two-dimensional perturbation problem (2.13). In order to decompose the wave packet, the perturbation energy per individual frequency Ω_f is defined as

$$\hat{E}(x_\mathrm{f};\Omega_\mathrm{f}) = \frac{1}{2}\int \hat{\boldsymbol{q}}(x_\mathrm{f},y;\Omega_\mathrm{f})^\mathrm{H}\mathscr{M}(x_\mathrm{f},y)\,\hat{\boldsymbol{q}}(x_\mathrm{f},y;\Omega_\mathrm{f})\,\mathrm{d}y\,, \tag{2.69}$$

where the variables with hats, $\hat{\boldsymbol{q}}$, correspond to the Fourier transform of the reconstructed perturbation variables, $\boldsymbol{q}'$,

$$\hat{\boldsymbol{q}}(x_\mathrm{f},y;\Omega_\mathrm{f}) = \int_0^{T_s} \boldsymbol{q}'_\mathrm{f}(x_\mathrm{f},y,z=0,t_\mathrm{f})\,\mathrm{e}^{+\mathrm{i}\Omega_\mathrm{f}t_\mathrm{f}}\,\mathrm{d}t_\mathrm{f}, \qquad \Omega_\mathrm{f}\in\mathbb{R}, \tag{2.70}$$

with the sampling period T_s. The real-valued angular frequency Ω_f is introduced in order to distinguish the Fourier-transform frequency from the eigenvalues. The spatial evolution of the Fourier coefficients can be assessed by reconstructing the individual amplification ΔN-factor curves and the streamwise wavenumber α based on $\hat{E}(x_\mathrm{f};\Omega_\mathrm{f})$:

$$\Delta N(x_\mathrm{f},\Omega_\mathrm{f}) = \frac{1}{2}\ln\frac{\hat{E}(x_\mathrm{f};\Omega_\mathrm{f})}{\hat{E}_0(x_{\mathrm{f},0};\Omega_\mathrm{f})}, \qquad \alpha(x_\mathrm{f},\Omega_\mathrm{f}) = -\frac{\mathrm{i}}{2}\frac{\partial\ln\hat{E}(x_\mathrm{f};\Omega_\mathrm{f})}{\partial x_\mathrm{f}}\,, \tag{2.71}$$

with $x_{\mathrm{f},0}(\Omega_\mathrm{f})$ a streamwise *reference* location. Preferably, the reference location $x_{\mathrm{f},0}(\Omega_\mathrm{f})$ is the location where the spatial growth rate α_i is zero. In order to determine the maximum amplification at each streamwise location, the envelope

$$\Delta N_\mathrm{max}(x_\mathrm{f}) = \max_{\Omega_\mathrm{f}}\left(\Delta N(x_\mathrm{f},\Omega_\mathrm{f})\right), \tag{2.72}$$

is evaluated. Note that an amplification ΔN-curve that is normalized based on its corresponding neutral-growth location is a so-called N-factor curve. If all curves are normalized this way, their envelope can be directly used in the e^N method. With the tools presented above, the moving-frame approach can be applied to various flow configurations and provides practical flow-stability information that can be interpreted in a similar manner as with the traditional LST and PSE methods.

2.8. Physical mechanisms with growth-rate decomposition

The underlying mechanisms of an instability can be identified by decomposing the growth rate into its individual contributions. In particular, Chu (1965) derived an equation that describes the (temporal) evolution of the perturbation energy and each term of this equation can be used to assess its contribution to the overall growth of the perturbation energy. Later, Padilla Montero & Pinna (2021) extended the work of Chu (1965) to three-dimensional perturbations in a two-dimensional base flow in the yz-plane. One particular aspect of this extended equation is that it accounts for boundary terms that are non-zero if the perturbations are not localized in the domain. In this thesis, the perturbation energy equation is formulated in the xy-plane and, although only localized solutions are presently sought and so the contributions from the boundaries must vanish, these boundary terms are kept in the equation for sake of completeness.

Following Chu (1965), the perturbation energy equation can be obtained by considering the temporal derivative of the energy (2.61) alongside the linearized Navier-Stokes equations (2.13). Note that, while the scaling of each individual equations of the system, i.e., momentum, energy and continuity equations, can be arbitrary in the perturbation equations (2.13), the equations must be scaled appropriately when deriving the energy equation

in order to ensure that the energy fluctuations from one equation to another are compatible. In order to be consistent with the definition of the perturbation energy, the linearized Navier-Stokes equations are scaled such that $\mathscr{B} = \mathscr{M}$ and the perturbation energy equation in the stationary frame of reference is thus given by

$$\frac{\mathrm{d}E}{\mathrm{d}t_\mathrm{f}} = \mathscr{R}\left\{\int_{\mathcal{V}_\mathrm{f}} \boldsymbol{q}_\mathrm{f}'^\mathrm{H} \mathscr{M} \frac{\partial \boldsymbol{q}_\mathrm{f}'}{\partial t_\mathrm{f}} \mathrm{d}\mathcal{V}_\mathrm{f}\right\} = \mathscr{R}\left\{\int_{\mathcal{V}_\mathrm{f}} \boldsymbol{q}_\mathrm{f}'^\mathrm{H} \mathscr{L} \boldsymbol{q}_\mathrm{f}' \mathrm{d}\mathcal{V}_\mathrm{f}\right\}. \tag{2.73}$$

Upon assuming the spanwise direction as homogeneous and factoring out the temporal growth rate $\sigma(t_\mathrm{f})$ from the stationary-frame perturbation, the temporal evolution of the perturbation energy in the xy-plane is given by

$$\sigma(t_\mathrm{f}) = \frac{1}{2E}\frac{\mathrm{d}E}{\mathrm{d}t_\mathrm{f}} = \frac{1}{2\check{E}} \iint \check{\boldsymbol{q}}_\mathrm{f}^\mathrm{H} \mathscr{A} \check{\boldsymbol{q}}_\mathrm{f} \mathrm{d}x_\mathrm{f} \mathrm{d}y, \tag{2.74}$$

with $\mathscr{A}$ from the stability equation (2.20), $\check{\boldsymbol{q}}_\mathrm{f}(x_\mathrm{f}, y, t_\mathrm{f}) = \mathscr{R}\left\{\boldsymbol{q}_\mathrm{f}'(x_\mathrm{f}, y, z=0, t_\mathrm{f})\right\} \mathrm{e}^{(-\sigma(t_\mathrm{f})\, t_\mathrm{f})}$ and $\check{E} = 1/2 \iint \check{\boldsymbol{q}}_\mathrm{f}^\mathrm{H} \mathscr{M} \check{\boldsymbol{q}}_\mathrm{f} \mathrm{d}x_\mathrm{f} \mathrm{d}y$. The right-hand-side term of equation (2.74) allows decomposing the temporal growth rate into its individual contributing terms. Following the same procedure for the perturbation energy of moving-frame eigensolutions, the temporal eigengrowth ω_i can be decomposed as follows

$$\omega_i = \frac{1}{2E}\frac{\mathrm{d}E}{\mathrm{d}t} = \frac{1}{2\tilde{E}} \mathscr{R}\left\{\iint \tilde{\boldsymbol{q}}^\mathrm{H} \mathscr{A} \tilde{\boldsymbol{q}} \mathrm{d}x\, \mathrm{d}y + c_\mathrm{f} \iint \tilde{\boldsymbol{q}}^\mathrm{H} \mathscr{M} \frac{\partial \tilde{\boldsymbol{q}}}{\partial x} \mathrm{d}x\, \mathrm{d}y\right\}, \quad \text{for} \quad t \to 0, \tag{2.75}$$

which, up to the contribution of the moving-frame advection, is similar to equation (2.74). In order to interpret the individual terms that are gathered in the right-hand side of equations (2.74) and (2.75), the contribution to the temporal growth rate is decomposed into different categories

$$\sigma(t_\mathrm{f}) = \underbrace{R_\mathrm{stress}}_{\substack{\text{Reynolds}\\ \text{stress}}} + \underbrace{R_\mathrm{heat}}_{\substack{\text{Reynolds}\\ \text{heat flux}}} + \underbrace{A_{\overline{U}} + A_{\overline{V}} + A_{\overline{W}}}_{\text{Advection}} + \underbrace{D_\mathrm{frict.} + D_\mathrm{cond.}}_{\text{Dissipation}} + P + F_\mathrm{b} \overset{t_\mathrm{f}=0}{=} \omega_i - A_{c_\mathrm{f}}, \tag{2.76}$$

where the Reynolds-stress and Reynolds-heat-flux production (R), the advection (A) and the dissipation (D) terms usually have the largest contribution to the perturbation growth. The terms included in F_b are boundary-forcing terms, that must vanish in the context of the present work, and the contribution P includes all the remaining production terms that contribute to a much smaller extent (by at least one order of magnitude) to the perturbation energy than the other terms explicitly written in equation (2.76). This has been observed by Chu (1965), Weder *et al.* (2015) and Padilla Montero & Pinna (2021), as well as in this thesis, for all considered flow applications. Note that, the temporal eigengrowth can be decomposed in a similar manner such that, when $t_\mathrm{f} = 0$, $\omega_i = \sigma(0) + A_{c_\mathrm{f}}$.

The Reynolds-stress term, denoted by R_stress, is commonly interpreted as producing a velocity perturbation through the advection of the base-flow velocity by the velocity perturbations. The Reynolds-stress term includes the following contributions

$$R_\mathrm{stress} \overset{(a)}{=} R_{\check{u}^*\check{v}} + R_{|\check{u}|^2} + R_{\check{v}^*\check{u}} + R_{|\check{v}|^2} + R_{\check{w}^*\check{u}} + R_{\check{w}^*\check{v}}, \tag{2.77}$$

$$R_{\check{u}^*\check{v}} \overset{(b)}{=} -\mathscr{R}\left\{\iint \check{u}^*\check{v}\overline{\rho}\frac{\partial\overline{U}}{\partial y}\frac{\mathrm{d}x_\mathrm{f}\mathrm{d}y}{\check{E}}\right\}, \qquad R_{|\check{u}|^2} \overset{(c)}{=} -\mathscr{R}\left\{\iint |\check{u}|^2\overline{\rho}\frac{\partial\overline{U}}{\partial x_\mathrm{f}}\frac{\mathrm{d}x_\mathrm{f}\mathrm{d}y}{\check{E}}\right\},$$
$$R_{\check{v}^*\check{u}} \overset{(d)}{=} -\mathscr{R}\left\{\iint \check{v}^*\check{u}\overline{\rho}\frac{\partial\overline{V}}{\partial x_\mathrm{f}}\frac{\mathrm{d}x_\mathrm{f}\mathrm{d}y}{\check{E}}\right\}, \qquad R_{|\check{v}|^2} \overset{(e)}{=} -\mathscr{R}\left\{\iint |\check{v}|^2\overline{\rho}\frac{\partial\overline{V}}{\partial x_\mathrm{f}}\frac{\mathrm{d}x_\mathrm{f}\mathrm{d}y}{\check{E}}\right\},$$
$$R_{\check{w}^*\check{u}} \overset{(f)}{=} -\mathscr{R}\left\{\iint \check{w}^*\check{u}\overline{\rho}\frac{\partial\overline{W}}{\partial x_\mathrm{f}}\frac{\mathrm{d}x_\mathrm{f}\mathrm{d}y}{\check{E}}\right\}, \qquad R_{\check{w}^*\check{v}} \overset{(g)}{=} -\mathscr{R}\left\{\iint \check{w}^*\check{v}\overline{\rho}\frac{\partial\overline{W}}{\partial y}\frac{\mathrm{d}x_\mathrm{f}\mathrm{d}y}{\check{E}}\right\}.$$

A similar interpretation can be made for the Reynolds-heat-flux production terms, denoted by R_heat, that produce a specific disturbance entropy

$$\gamma\mathrm{M}^2\check{s} = \frac{\gamma}{\gamma-1}\frac{\check{T}}{\overline{T}} - \frac{\check{p}}{\overline{P}} = \frac{1}{\gamma-1}\frac{\check{T}}{\overline{T}} - \frac{\check{\rho}}{\overline{\rho}}, \tag{2.78}$$

by in-plane advection effects of the base-flow temperature layer. The Reynolds-heat-flux production terms can be decomposed into

$$R_\mathrm{heat} \overset{(a)}{=} R_{\check{s}^*\check{u}} + R_{\check{s}^*\check{v}}, \tag{2.79}$$
$$R_{\check{s}^*\check{u}} \overset{(b)}{=} -\mathscr{R}\left\{\iint \check{s}^*\check{u}\overline{\rho}\frac{\partial\overline{T}}{\partial x_\mathrm{f}}\frac{\mathrm{d}x_\mathrm{f}\mathrm{d}y}{\check{E}}\right\}, \qquad R_{\check{s}^*\check{v}} \overset{(c)}{=} -\mathscr{R}\left\{\iint \check{s}^*\check{v}\overline{\rho}\frac{\partial\overline{T}}{\partial y}\frac{\mathrm{d}x_\mathrm{f}\mathrm{d}y}{\check{E}}\right\}.$$

Since the perturbations are mostly confined in the shear-layer, which has a much smaller characteristic length scale in the wall-normal direction than in the streamwise direction, the quantities involving the wall-normal derivatives are often much larger than the streamwise-derivative terms. Hence, the Reynolds-stress and Reynolds-heat-flux terms that involve the wall-normal derivative of the base-flow quantities often prevail over the terms involving the derivative in the x-direction. The wall-normal Reynolds stress and heat-flux originate in the linearization of the advection terms of the Navier-Stokes equations and they involve the wall-normal velocity perturbation component, that thus moves (infinitesimally) the base-flow quantities upward, away from the wall. For this reason, each of these wall-normal-based Reynolds production terms are related to the so-called lift-up effect that is a convective-like mechanism often observed in non-modal perturbation analysis (Schmid & Henningson, 2001).

The terms denoted by A contribute to the energy growth through the advection of the perturbations by one of the base-flow velocity components (or by the moving frame of reference) and are given by

$$A_{\overline{U}} \overset{(a)}{=} -\mathscr{R}\left\{\iint \overline{U}\check{\boldsymbol{q}}^\mathrm{H}\mathscr{M}\frac{\partial\check{\boldsymbol{q}}}{\partial x_\mathrm{f}}\frac{\mathrm{d}x_\mathrm{f}\mathrm{d}y}{\check{E}}\right\}, \qquad A_{\overline{V}} \overset{(b)}{=} -\mathscr{R}\left\{\iint \overline{V}\check{\boldsymbol{q}}^\mathrm{H}\mathscr{M}\frac{\partial\check{\boldsymbol{q}}}{\partial y}\frac{\mathrm{d}x_\mathrm{f}\mathrm{d}y}{\check{E}}\right\},$$
$$A_{\overline{W}} \overset{(c)}{=} -\mathscr{R}\left\{\iint \beta\overline{W}\check{\boldsymbol{q}}^\mathrm{H}\mathscr{M}\check{\boldsymbol{q}}\frac{\mathrm{d}x_\mathrm{f}\mathrm{d}y}{\check{E}}\right\}, \qquad A_{c_\mathrm{f}} \overset{(d)}{=} +\mathscr{R}\left\{\iint c_\mathrm{f}\check{\boldsymbol{q}}^\mathrm{H}\mathscr{M}\frac{\partial\check{\boldsymbol{q}}}{\partial x_\mathrm{f}}\frac{\mathrm{d}x_\mathrm{f}\mathrm{d}y}{\check{E}}\right\}. \tag{2.80}$$

For the integrands of these contributions to be locally positive, the projection of the vector $-\check{\boldsymbol{q}}^\mathrm{H}\mathscr{M}\,\partial\check{\boldsymbol{q}}/\partial x_{\mathrm{f},j}$ onto the base-flow velocity vector $[\overline{U},\overline{V},\overline{W}]^\mathrm{T}$ must be positive. A positive value can be interpreted as that the base-flow velocity field stretches the perturbation in space. The moving-frame advection term, equation (2.80d), vanishes for the perturbations $\check{q}$ because they are only evaluated in the stationary frame of reference ($c_\mathrm{f} = 0$). However, when considering the moving-frame eigenfunctions, i.e., $\check{q} = \tilde{q}$ for $t_\mathrm{f} = 0$ in equation (2.76), the moving-frame advection term can be non-zero if the $\mathscr{M}$-matrix is not constant in the x-direction.

The energy growth can be attenuated through the dissipation by friction ($D_{\text{frict.}}$) or conduction ($D_{\text{cond.}}$), which are both characterized by terms involving the second derivatives of the velocity or temperature perturbations, respectively. Following Chu (1965), these terms are hereafter integrated by parts in order to introduce boundary terms and simplify their interpretation. This can be exemplified by considering the streamwise velocity perturbation component of the x-momentum perturbation equation

$$\iint \breve{u}^* \left(\overline{\mu} \frac{\partial^2 \breve{u}}{\partial y^2} + \frac{\mathrm{d}\overline{\mu}}{\mathrm{d}\overline{T}} \frac{\partial \overline{T}}{\partial y} \frac{\partial \breve{u}}{\partial y} \right) \frac{\mathrm{d}x_\mathrm{f}\mathrm{d}y}{\breve{E}} = \underbrace{\left[\int \overline{\mu} \breve{u}^* \frac{\partial \breve{u}}{\partial y} \frac{\mathrm{d}x_\mathrm{f}}{\breve{E}} \right]_0^{y_e}}_{\text{part of } F_\mathrm{b}} - \underbrace{\iint \overline{\mu} \left| \frac{\partial \breve{u}}{\partial y} \right|^2 \frac{\mathrm{d}x_\mathrm{f}\mathrm{d}y}{\breve{E}}}_{\text{part of } D_{\text{frict.}}} . \tag{2.81}$$

The first right-hand-side term is a boundary term that belongs to F_b, and thus vanishes for localized perturbations, while the second term is part of the internal friction. The above example of integration by parts holds for all second derivative terms of the momentum and energy equations. This comes from the fact that each single term with a second derivative of the velocity or temperature perturbations always appears in combination with a term involving the first derivative of the viscosity or conductivity coefficients. Applying the integration by parts allows decomposing, on the one hand, the friction-induced dissipation into different contributions as

$$D_{\text{frict.}} \overset{\text{(a)}}{=} D_{\text{frict.},x} + D_{\text{frict.},y} + D_{\text{frict.},z} + D_{\text{frict.,cross}} , \tag{2.82}$$

$$\begin{aligned}
D_{\text{frict.},x} &\overset{\text{(b)}}{=} -\frac{1}{\mathrm{Re}} \iint \left[(2\overline{\mu} + \overline{\lambda}) \left| \frac{\partial \breve{u}}{\partial x_\mathrm{f}} \right|^2 + \overline{\mu} \left(\left| \frac{\partial \breve{v}}{\partial x_\mathrm{f}} \right|^2 + \left| \frac{\partial \breve{w}}{\partial x_\mathrm{f}} \right|^2 \right) \right] \frac{\mathrm{d}x_\mathrm{f}\mathrm{d}y}{\breve{E}} , \\
D_{\text{frict.},y} &\overset{\text{(c)}}{=} -\frac{1}{\mathrm{Re}} \iint \left[(2\overline{\mu} + \overline{\lambda}) \left| \frac{\partial \breve{v}}{\partial y} \right|^2 + \overline{\mu} \left(\left| \frac{\partial \breve{u}}{\partial y} \right|^2 + \left| \frac{\partial \breve{w}}{\partial y} \right|^2 \right) \right] \frac{\mathrm{d}x_\mathrm{f}\mathrm{d}y}{\breve{E}} , \\
D_{\text{frict.},z} &\overset{\text{(d)}}{=} -\frac{\beta^2}{\mathrm{Re}} \iint \left[(2\overline{\mu} + \overline{\lambda}) |\breve{w}|^2 + \overline{\mu} (|\breve{u}|^2 + |\breve{v}|^2) \right] \frac{\mathrm{d}x_\mathrm{f}\mathrm{d}y}{\breve{E}} , \\
D_{\text{frict.,cross}} &\overset{\text{(e)}}{=} -\frac{1}{\mathrm{Re}} \mathscr{R} \left\{ \iint \overline{\lambda} \left[\frac{\partial \breve{u}^*}{\partial x_\mathrm{f}} \left(\frac{\partial \breve{v}}{\partial y} + \frac{\partial \breve{w}}{\partial z} \right) + \frac{\partial \breve{v}^*}{\partial y} \left(\frac{\partial \breve{u}}{\partial x_\mathrm{f}} + \frac{\partial \breve{w}}{\partial z} \right) + \mathrm{i}\beta \breve{w}^* \left(\frac{\partial \breve{u}}{\partial x_\mathrm{f}} + \frac{\partial \breve{v}}{\partial y} \right) \right] \frac{\mathrm{d}x_\mathrm{f}\mathrm{d}y}{\breve{E}} \right\} ,
\end{aligned}$$

and, on the other hand, the dissipation of the perturbation energy by conductive heat transfer as

$$D_{\text{cond.}} = -\frac{1}{\mathrm{Ec}\,\mathrm{Pr}\,\mathrm{Re}} \iint \left[\left| \frac{\partial \breve{T}}{\partial x_\mathrm{f}} \right|^2 + \left| \frac{\partial \breve{T}}{\partial y} \right|^2 + \beta^2 |\breve{T}|^2 \right] \frac{\mathrm{d}x_\mathrm{f}\mathrm{d}y}{\breve{E}} . \tag{2.83}$$

Based on the same argument as for the Reynolds-stress and Reynolds-heat-flux terms, the dissipation terms involving the second derivative of the perturbations in the wall-normal direction, i.e., the $|\partial \cdot / \partial y|^2$-terms, are usually the most stabilizing contributions in wall-bounded flows. For this reason, the analysis of the heat-conduction-induced dissipation can often be reduced to

$$D_{\tilde{T},y} = -\frac{1}{\mathrm{Ec}\,\mathrm{Pr}\,\mathrm{Re}} \iint \left| \frac{\partial \breve{T}}{\partial y} \right|^2 \frac{\mathrm{d}x_\mathrm{f}\mathrm{d}y}{\breve{E}} , \tag{2.84}$$

that is usually the largest contribution to equation (2.83). Similarly, equation (2.82c) is also found to be the largest contribution to equation (2.82a) for all flow cases considered in the

present work. Hence, considering the individual contributions

$$\begin{aligned} D_{\breve{u},y} &\overset{\text{(a)}}{=} -\frac{1}{\mathrm{Re}} \iint \overline{\mu} \left| \frac{\partial \breve{u}}{\partial y} \right|^2 \frac{\mathrm{d}x_\mathrm{f}\mathrm{d}y}{\breve{E}}, \\ D_{\breve{v},y} &\overset{\text{(b)}}{=} -\frac{1}{\mathrm{Re}} \iint (2\overline{\mu}+\overline{\lambda}) \left| \frac{\partial \breve{v}}{\partial y} \right|^2 \frac{\mathrm{d}x_\mathrm{f}\mathrm{d}y}{\breve{E}}, \\ D_{\breve{w},y} &\overset{\text{(c)}}{=} -\frac{1}{\mathrm{Re}} \iint \overline{\mu} \left| \frac{\partial \breve{w}}{\partial y} \right|^2 \frac{\mathrm{d}x_\mathrm{f}\mathrm{d}y}{\breve{E}}, \end{aligned} \tag{2.85}$$

instead of the term (2.82c) as a whole arguably simplifies the physical interpretation of the wall-normal friction-induced dissipation $D_{\mathrm{frict.},y}$. These aspects are clarified in Chapters 4 and 5 where the different contributions to the energy growth are quantified for different flow cases.

Although the P term in equation (2.76) contributes to a much smaller extent to the perturbation energy than most of the terms presented above, the complete expansion of the remaining production term is given in the following for sake of completeness:

$$P \overset{\text{(a)}}{=} P_\mathrm{mom} + P_{\nabla\overline{P}} + P_{s,\overline{T}} + P_\mathrm{dil} + P_{\overline{Q}}, \tag{2.86}$$

$$\begin{aligned} P_\mathrm{mom} &\overset{\text{(b)}}{=} -\mathscr{R}\left\{ \iint \breve{u}^*\breve{\rho}\,\overline{U}\frac{\partial\overline{U}}{\partial x_\mathrm{f}}\frac{\mathrm{d}x_\mathrm{f}\mathrm{d}y}{\breve{E}} + \iint \breve{u}^*\breve{\rho}\,\overline{V}\frac{\partial\overline{U}}{\partial y}\frac{\mathrm{d}x_\mathrm{f}\mathrm{d}y}{\breve{E}} \right\} \\ &\quad -\mathscr{R}\left\{ \iint \breve{v}^*\breve{\rho}\,\overline{U}\frac{\partial\overline{V}}{\partial x_\mathrm{f}}\frac{\mathrm{d}x_\mathrm{f}\mathrm{d}y}{\breve{E}} + \iint \breve{v}^*\breve{\rho}\,\overline{V}\frac{\partial\overline{V}}{\partial y}\frac{\mathrm{d}x_\mathrm{f}\mathrm{d}y}{\breve{E}} \right\} \\ &\quad -\mathscr{R}\left\{ \iint \breve{w}^*\breve{\rho}\,\overline{U}\frac{\partial\overline{W}}{\partial x_\mathrm{f}}\frac{\mathrm{d}x_\mathrm{f}\mathrm{d}y}{\breve{E}} + \iint \breve{w}^*\breve{\rho}\,\overline{V}\frac{\partial\overline{W}}{\partial y}\frac{\mathrm{d}x_\mathrm{f}\mathrm{d}y}{\breve{E}} \right\}, \\ P_{\nabla\overline{P}} &\overset{\text{(c)}}{=} -\mathscr{R}\left\{ \iint \breve{\rho}^*\breve{u}\frac{1}{\overline{\rho}}\frac{\partial\overline{P}}{\partial x_\mathrm{f}}\frac{\mathrm{d}x_\mathrm{f}\mathrm{d}y}{\breve{E}} + \iint \breve{\rho}^*\breve{v}\frac{1}{\overline{\rho}}\frac{\partial\overline{P}}{\partial y}\frac{\mathrm{d}x_\mathrm{f}\mathrm{d}y}{\breve{E}} \right\}, \\ P_{s,\overline{T}} &\overset{\text{(d)}}{=} -\mathscr{R}\left\{ \iint \breve{T}^*\breve{\rho}\frac{\overline{U}}{\gamma\mathrm{Ec}\overline{T}}\frac{\partial\overline{T}}{\partial x_\mathrm{f}}\frac{\mathrm{d}x_\mathrm{f}\mathrm{d}y}{\breve{E}} + \iint \breve{T}^*\breve{\rho}\frac{\overline{V}}{\gamma\mathrm{Ec}\overline{T}}\frac{\partial\overline{T}}{\partial y}\frac{\mathrm{d}x_\mathrm{f}\mathrm{d}y}{\breve{E}} \right\}, \\ P_\mathrm{dil} &\overset{\text{(e)}}{=} -\mathscr{R}\left\{ \iint \breve{T}^*\breve{p}\frac{1}{\overline{T}}\frac{\partial\overline{U}}{\partial x_\mathrm{f}}\frac{\mathrm{d}x_\mathrm{f}\mathrm{d}y}{\breve{E}} + \iint \breve{T}^*\breve{p}\frac{1}{\overline{T}}\frac{\partial\overline{V}}{\partial y}\frac{\mathrm{d}x_\mathrm{f}\mathrm{d}y}{\breve{E}} \right\} \\ &\quad -\mathscr{R}\left\{ \iint |\breve{\rho}|^2\frac{\overline{T}}{\gamma\mathrm{M}^2\overline{P}}\frac{\partial\overline{U}}{\partial x_\mathrm{f}}\frac{\mathrm{d}x_\mathrm{f}\mathrm{d}y}{\breve{E}} + \iint |\breve{\rho}|^2\frac{\overline{T}}{\gamma\mathrm{M}^2\overline{P}}\frac{\partial\overline{V}}{\partial y}\frac{\mathrm{d}x_\mathrm{f}\mathrm{d}y}{\breve{E}} \right\}, \\ P_{\overline{Q}} &\overset{\text{(f)}}{=} -\mathscr{R}\left\{ \iint \frac{\breve{T}^*\breve{Q}}{\overline{T}}\frac{\mathrm{d}x_\mathrm{f}\mathrm{d}y}{\breve{E}} \right\}. \end{aligned}$$

The disturbance heat $\breve{Q}$ per unit volume, defined by Chu (1965) and Padilla Montero & Pinna (2021), includes all contributions involving terms $\mathscr{R}\{\breve{T}^*\breve{u}\}$, $\mathscr{R}\{\breve{T}^*\breve{v}\}$ and $\mathscr{R}\{\breve{T}^*\breve{w}\}$ that multiply (the derivatives of) the viscosity and conductivity coefficients. Hence, the specific dis-

turbance heat $\check{Q}$ writes

$$\begin{aligned}\check{Q} = &\frac{1}{\mathrm{Re}}\left(2\overline{\mu}-\frac{\mathrm{d}\overline{\mu}}{\mathrm{d}\overline{T}}\overline{T}\right)\left(2\frac{\partial\overline{U}}{\partial x_\mathrm{f}}\frac{\partial\check{u}}{\partial x_\mathrm{f}}+\frac{\partial\overline{U}}{\partial y}\left(\frac{\partial\check{u}}{\partial y}+\frac{\partial\check{v}}{\partial x_\mathrm{f}}\right)+\frac{\partial\overline{V}}{\partial x_\mathrm{f}}\left(\frac{\partial\check{u}}{\partial y}+\frac{\partial\check{v}}{\partial x_\mathrm{f}}\right)+2\frac{\partial\check{v}}{\partial y}\frac{\partial\overline{V}}{\partial y}\right.\\ &\left.+\frac{\partial\overline{W}}{\partial x_\mathrm{f}}\left(\mathrm{i}\beta\check{u}+\frac{\partial\check{w}}{\partial x_\mathrm{f}}\right)+\frac{\partial\overline{W}}{\partial y}\left(\mathrm{i}\beta\check{v}+\frac{\partial\check{w}}{\partial y}\right)\right)\\ &+\frac{1}{\mathrm{Re}}\left(2\overline{\lambda}-\frac{\mathrm{d}\overline{\lambda}}{\mathrm{d}\overline{T}}\overline{T}\right)\left(\frac{\partial\overline{U}}{\partial x_\mathrm{f}}+\frac{\partial\overline{V}}{\partial y}\right)\left(\frac{\partial\check{u}}{\partial x_\mathrm{f}}+\frac{\partial\check{v}}{\partial y}+\mathrm{i}\beta\check{w}\right)\\ &+\frac{1}{\mathrm{Re}}\frac{\mathrm{d}\overline{\mu}}{\mathrm{d}\overline{T}}\check{T}\left(2\left(\frac{\partial\overline{U}}{\partial x_\mathrm{f}}\right)^2+\left(\frac{\partial\overline{U}}{\partial y}\right)^2+2\frac{\partial\overline{U}}{\partial y}\frac{\partial\overline{V}}{\partial x_\mathrm{f}}+\left(\frac{\partial\overline{V}}{\partial x_\mathrm{f}}\right)^2+2\left(\frac{\partial\overline{V}}{\partial y}\right)^2+\left(\frac{\partial\overline{W}}{\partial x_\mathrm{f}}\right)^2+\left(\frac{\partial\overline{W}}{\partial y}\right)^2\right)\\ &+\frac{1}{\mathrm{Re}}\frac{\mathrm{d}\overline{\lambda}}{\mathrm{d}\overline{T}}\check{T}\left(\left(\frac{\partial\overline{U}}{\partial x_\mathrm{f}}\right)^2+2\frac{\partial\overline{U}}{\partial x_\mathrm{f}}\frac{\partial\overline{V}}{\partial y}+\left(\frac{\partial\overline{V}}{\partial y}\right)^2\right)\\ &+\frac{1}{\mathrm{Ec}\,\mathrm{Pr}\,\mathrm{Re}}\left[\frac{\partial}{\partial x_\mathrm{f}}\left(\check{T}\frac{\partial\overline{k}}{\partial T}\frac{\partial\overline{T}}{\partial x_\mathrm{f}}\right)+\frac{\overline{k}}{\overline{T}}\frac{\partial\overline{T}}{\partial x_\mathrm{f}}\frac{\partial\check{T}}{\partial x_\mathrm{f}}+\frac{\partial}{\partial y}\left(\check{T}\frac{\partial\overline{k}}{\partial T}\frac{\partial\overline{T}}{\partial y}\right)+\frac{\overline{k}}{\overline{T}}\frac{\partial\overline{T}}{\partial y}\frac{\partial\check{T}}{\partial y}\right].\end{aligned}\tag{2.87}$$

Since obtaining $\check{Q}$ in this form requires integrating by part several terms, boundary terms emerge that are related to forces, pressure and heat fluxes imposed at the domain boundaries. These boundary terms must all vanish for localized perturbations and are all included into F_b that is given by

$$F_\mathrm{b} \overset{\text{(a)}}{=} \mathscr{R}\{F_\tau\}+\mathscr{R}\{F_p\}+\mathscr{R}\{F_q\}+\mathscr{R}\{F_{\mu_T}\},\tag{2.88}$$

$$\begin{aligned}F_\tau &\overset{\text{(b)}}{=} \int(\check{u}^*\check{\tau}_{xx})\big|_x\frac{\mathrm{d}y}{\check{E}}+\int(\check{v}^*\check{\tau}_{yy})\big|_y\frac{\mathrm{d}x_\mathrm{f}}{\check{E}}+\int(\check{u}^*\check{\tau}_{xy})\big|_y\frac{\mathrm{d}x_\mathrm{f}}{\check{E}}\\ &\quad+\int(\check{v}^*\check{\tau}_{xy})\big|_x\frac{\mathrm{d}y}{\check{E}}+\int(\check{w}^*\check{\tau}_{xz})\big|_y\frac{\mathrm{d}x_\mathrm{f}}{\check{E}}+\int(\check{w}^*\check{\tau}_{yz})\big|_x\frac{\mathrm{d}y}{\check{E}},\\ F_p &\overset{\text{(c)}}{=} \int(\check{p}^*\check{u})\big|_x\frac{\mathrm{d}y}{\check{E}}+\int(\check{p}^*\check{v})\big|_y\frac{\mathrm{d}x_\mathrm{f}}{\check{E}},\\ F_q &\overset{\text{(d)}}{=} \int\frac{1}{\overline{T}}(\check{T}^*\check{q}_x)\big|_x\frac{\mathrm{d}y}{\check{E}}+\int\frac{1}{\overline{T}}(\check{T}^*\check{q}_y)\big|_y\frac{\mathrm{d}x_\mathrm{f}}{\check{E}},\\ F_{\mu_T} &\overset{\text{(e)}}{=} \int\left[\check{T}^*\check{u}\left(2\frac{\mathrm{d}\overline{\mu}}{\mathrm{d}\overline{T}}\frac{\partial\overline{U}}{\partial x_\mathrm{f}}+\frac{\mathrm{d}\overline{\lambda}}{\mathrm{d}\overline{T}}\frac{\partial\overline{U}}{\partial x_\mathrm{f}}+\frac{\mathrm{d}\overline{\lambda}}{\mathrm{d}\overline{T}}\frac{\partial\overline{V}}{\partial y}\right)+\check{T}^*\check{v}\left(\frac{\mathrm{d}\overline{\mu}}{\mathrm{d}\overline{T}}\frac{\partial\overline{U}}{\partial y}+\frac{\mathrm{d}\overline{\mu}}{\mathrm{d}\overline{T}}\frac{\partial\overline{V}}{\partial x_\mathrm{f}}\right)+\check{T}^*\check{w}\left(\frac{\mathrm{d}\overline{\mu}}{\mathrm{d}\overline{T}}\frac{\partial\overline{W}}{\partial x_\mathrm{f}}\right)\right]\right|_x\frac{\mathrm{d}y}{\check{E}}\\ &\quad+\int\left[\check{T}^*\check{u}\left(\frac{\mathrm{d}\overline{\mu}}{\mathrm{d}\overline{T}}\frac{\partial\overline{U}}{\partial y}+\frac{\mathrm{d}\overline{\mu}}{\mathrm{d}\overline{T}}\frac{\partial\overline{V}}{\partial x_\mathrm{f}}\right)+\check{T}^*\check{v}\left(\frac{\mathrm{d}\overline{\lambda}}{\mathrm{d}\overline{T}}\frac{\partial\overline{U}}{\partial x_\mathrm{f}}+2\frac{\mathrm{d}\overline{\mu}}{\mathrm{d}\overline{T}}\frac{\partial\overline{V}}{\partial y}+\frac{\mathrm{d}\overline{\lambda}}{\mathrm{d}\overline{T}}\frac{\partial\overline{V}}{\partial y}\right)+\check{T}^*\check{w}\left(\frac{\mathrm{d}\overline{\mu}}{\mathrm{d}\overline{T}}\frac{\partial\overline{W}}{\partial y}\right)\right]\right|_y\frac{\mathrm{d}x_\mathrm{f}}{\check{E}},\end{aligned}$$

with the disturbance shear stresses

$$\begin{aligned}\check{\tau}_{xx} &\overset{\text{(a)}}{=} \frac{1}{\mathrm{Re}}\left[(2\overline{\mu}+\overline{\lambda})\frac{\partial\check{u}}{\partial x_\mathrm{f}}+\overline{\lambda}\left(\frac{\partial\check{v}}{\partial y}+\mathrm{i}\beta\check{w}\right)\right], &\qquad \check{\tau}_{xy} &\overset{\text{(b)}}{=} \frac{\overline{\mu}}{\mathrm{Re}}\left(\frac{\partial\check{u}}{\partial y}+\frac{\partial\check{v}}{\partial x_\mathrm{f}}\right),\\ \check{\tau}_{yy} &\overset{\text{(c)}}{=} \frac{1}{\mathrm{Re}}\left[(2\overline{\mu}+\overline{\lambda})\frac{\partial\check{v}}{\partial y}+\overline{\lambda}\left(\frac{\partial\check{u}}{\partial x_\mathrm{f}}+\mathrm{i}\beta\check{w}\right)\right], &\qquad \check{\tau}_{xz} &\overset{\text{(d)}}{=} \frac{\overline{\mu}}{\mathrm{Re}}\left(\mathrm{i}\beta\check{u}+\frac{\partial\check{w}}{\partial x_\mathrm{f}}\right),\\ \check{\tau}_{zz} &\overset{\text{(e)}}{=} \frac{1}{\mathrm{Re}}\left[(2\overline{\mu}+\overline{\lambda})\mathrm{i}\beta\check{w}+\overline{\lambda}\left(\frac{\partial\check{u}}{\partial x_\mathrm{f}}+\frac{\partial\check{v}}{\partial y}\right)\right], &\qquad \check{\tau}_{yz} &\overset{\text{(f)}}{=} \frac{\overline{\mu}}{\mathrm{Re}}\left(\mathrm{i}\beta\check{v}+\frac{\partial\check{w}}{\partial y}\right),\end{aligned}\tag{2.89}$$

and the disturbance heat fluxes

$$\check{q}_x \overset{(a)}{=} -\frac{\overline{k}}{\mathrm{Ec}\,\mathrm{Pr}\,\mathrm{Re}}\frac{\partial \check{T}}{\partial x_\mathrm{f}}, \quad \check{q}_y \overset{(b)}{=} -\frac{\overline{k}}{\mathrm{Ec}\,\mathrm{Pr}\,\mathrm{Re}}\frac{\partial \check{T}}{\partial y}, \quad \check{q}_z \overset{(c)}{=} -\mathrm{i}\beta\frac{\overline{k}}{\mathrm{Ec}\,\mathrm{Pr}\,\mathrm{Re}}\check{T}. \tag{2.90}$$

Considering all terms independently allows making an energy budget that can be used to identify the most critical mechanisms that are inherent to an instability. Usually, this translates into focusing on the three contributions R, A and D that are often at least one order of magnitude larger than the other terms. Note that, for incompressible cases, the number of terms can be drastically reduced since all contributions associated with the temperature (or entropy) perturbation vanish. Therefore, only Reynolds-stress R_stress, advection A and friction-induced-dissipation ($D_\mathrm{frict.}$) terms are involved in the instability mechanisms of incompressible flows. A further theoretical discussion regarding the different contributions in incompressible (free-shear-layer) flows was proposed by Groot (2018). In the present context, the perturbation energy budget is considered in Chapters 4 and 5 to determine the underlying mechanisms of convective instabilities in the incompressible boundary layer and the shock-wave/boundary-layer interaction, respectively.

References

ÅKERVIK, E., EHRENSTEIN, U., GALLAIRE, F. & HENNINGSON, D. S. 2008 Global two-dimensional stability measures of the flat plate boundary-layer flow. *European Journal of Mechanics - B/Fluids* **27** (5), 501–513.

ÅKERVIK, E., HŒPFFNER, J., EHRENSTEIN, U. & HENNINGSON, D. S. 2007 Optimal growth, model reduction and control in a separated boundary-layer flow using global eigenmodes. *Journal of Fluid Mechanics* **579**, 305–314.

ALIZARD, F. & ROBINET, J.-C. 2007 Spatially convective global modes in a boundary layer. *Physics of Fluids* **19** (11), 114105.

ALVES, L. S. D. B., HIRATA, S. C., SCHUABB, M. & BARLETTA, A. 2019 Identifying linear absolute instabilities from differential eigenvalue problems using sensitivity analysis. *Journal of Fluid Mechanics* **870**, 941–969.

APPEL, T. 2020 Boundary layer instabilities due to surface irregularities: a harmonic navier-stokes approach. PhD thesis, Imperial College London.

BAGHERI, S., HENNINGSON, D. S., HŒPFFNER, J. & SCHMID, P. J. 2009 Input-Output Analysis and Control Design Applied to a Linear Model of Spatially Developing Flows. *Applied Mechanics Reviews* **62** (2), 020803.

BERS, A. 1984 Linear waves and instabilities. In *Physique des Plasmas* (ed. C. DeWitt & J. Peyraud), pp. 117–213. New York: Gordon and Breach.

BERTOLOTTI, F. P., HERBERT, T. & SPALART, P. 1992 Linear and nonlinear stability of the Blasius boundary layer. *Journal of Fluid Mechanics* **242**, 441–474.

BRANDT, L., SIPP, D., PRALITS, J. O. & MARQUET, O. 2011 Effect of base-flow variation in noise amplifiers: the flat-plate boundary layer. *Journal of Fluid Mechanics* **687**, 503–528.

BRIGGS, R. J. 1964 *Electron-stream interaction with plasmas. M.I.T. Press research monographs* . M.I.T. Press.

CHU, B. T. 1965 On the energy transfer to small disturbances in fluid flow (Part I). *Acta Mechanica* **1** (3), 215–234.

DELBENDE, I., CHOMAZ, J.-M. & HUERRE, P. 1998 Absolute/convective instabilities in the Batchelor vortex: a numerical study of the linear impulse response. *Journal of Fluid Mechanics* **355**, 229–254.

EHRENSTEIN, U. & GALLAIRE, F. 2005 On two-dimensional temporal modes in spatially evolving open flows: the flat-plate boundary layer. *Journal of Fluid Mechanics* **536**, 209–218.

GARNAUD, X., LESSHAFFT, L., SCHMID, P. J. & HUERRE, P. 2013 Modal and transient dynamics of jet flows. *Physics of Fluids* **25** (4), 044103.

GASTER, M. 1962 A note on the relation between temporally-increasing and spatially-increasing disturbances in hydrodynamic stability. *Journal of Fluid Mechanics* **14** (2), 222–224.

GASTER, M. 1967 The development of three-dimensional wave packets in a boundary layer. *Journal of Fluid Mechanics* **32** (1), 173–184.

GASTER, M. 1974 On the effects of boundary-layer growth on flow stability. *Journal of Fluid Mechanics* **66** (3), 465–480.

GIANNETTI, F. & LUCHINI, P. 2007 Structural sensitivity of the first instability of the cylinder wake. *Journal of Fluid Mechanics* **581**, 167–197.

GROOT, K. J. 2013 Derivation of and simulations with BiGlobal stability equations. Master's thesis, Delft University of Technology.

GROOT, K. J. 2018 BiGlobal Stability of shear flows spanwise & streamwise Analyses. PhD thesis, TU Delft and von Karman Institute for Fluid Dynamics.

GROOT, K. J. & SCHUTTELAARS, H. M. 2020 Accurate numerical approximation of the absolute stability of unbounded flows. *Physica D: Nonlinear Phenomena* **402**, 132224.

GROOT, K. J., SERPIERI, J., PINNA, F. & KOTSONIS, M. 2018 Secondary crossflow instability through global analysis of measured base flows. *Journal of Fluid Mechanics* **846**, 605–653.

HADER, C. & FASEL, H. F. 2019 Three-dimensional wave packet in a Mach 6 boundary layer on a flared cone. *Journal of Fluid Mechanics* **885**, R3.

HANIFI, A., SCHMID, P. J. & HENNINGSON, D. S. 1996 Transient growth in compressible boundary layer flow. *Physics of Fluids* **8** (3), 826–837.

HILDEBRAND, N., CHOUDHARI, M. M. & PAREDES, P. 2020 Predicting boundary-layer transition over backward-facing steps via linear stability analysis. *AIAA Journal* **58** (9), 3728–3734.

HINCH, E. J. 1991 *Perturbation Methods*. Cambridge University Press.

HUANG, Z. & WU, X. 2017 A local scattering approach for the effects of abrupt changes on boundary-layer instability and transition: a finite-reynolds-number formulation for isolated distortions. *Journal of Fluid Mechanics* **822**, 444–483.

HUERRE, P. & ROSSI, M. 2009 Hydrodynamic instabilities in open flows. In *Hydrodynamics and Nonlinear Instabilities*, pp. 81–294. Cambridge University Press.

MACK, L. M. 1984 Boundary-layer linear stability theorys. In *AGARD 709, Special Course of Stability and Transition of Laminar Flows*. North Atlantic Treaty Organization.

MALIK, M. 1990 Numerical methods for hypersonic boundary layer stability. *Journal of Computational Physics* **86** (2), 376 – 413.

MARQUET, O., LOMBARDI, M., CHOMAZ, J.-M., SIPP, D. & JACQUIN, L. 2009 Direct and adjoint global modes of a recirculation bubble: lift-up and convective non-normalities. *Journal of Fluid Mechanics* **622**, 1–21.

MONKEWITZ, P. A., HUERRE, P. & CHOMAZ, J.-M. 1993 Global linear stability analysis of weakly non-parallel shear flows. *Journal of Fluid Mechanics* **251**, 1–20.

NIESSEN, S. E. M. 2017 BiGlobal stability analysis: laminar shock-wave/boundary-layer interactions. Master's thesis, University of Liège, Faculty of Applied Sciences.

ORR, W. M. 1907 The Stability or Instability of the Steady Motions of a Perfect Liquid and of a Viscous Liquid. *Proceedings of the Royal Irish Academy. Section A: Mathematical and Physical Sciences* **27**, 69–138.

PADILLA MONTERO, I. & PINNA, F. 2021 Analysis of the instabilities induced by an isolated roughness element in a laminar high-speed boundary layer. *Journal of Fluid Mechanics* **915**, A90.

PINNA, F. 2012 Numerical study of stability and transition of flows from low to high Mach number. PhD thesis, Von Karman Institute for Fluid Dynamics and Universitá "La Sapienza" di Roma.

REYNOLDS, O. 1895 On the dynamical theory of incompressible viscous fluids and the determination of the criterion. *Philosophical Transactions of the Royal Society of London. A* **186**, 123–164.

ROBINET, J. C. 2007 Bifurcations in shock-wave/laminar-boundary-layer interaction: global instability approach. *Journal of Fluid Mechanics* **579**, 85–112.

SARIC, W. S. & NAYFEH, A. H. 1975 Nonparallel stability of boundary-layer flows. *Physics of Fluids* **18** (8), 945–952.

SCHMID, P. J. 2007 Nonmodal Stability Theory. *Annual Review of Fluid Mechanics* **39** (1), 129–162.

SCHMID, P. J. & BRANDT, L. 2014 Analysis of fluid systems: stability, receptivity, sensitivity. *Applied Mechanics Reviews* **66** (2), 24803.

SCHMID, P. J. & HENNINGSON, D. S. 2001 *Stability and transition in shear flows*. Springer.

SCHMID, P. J. & HENNINGSON, D. S. 2002 On the stability of a falling liquid curtain. *Journal of Fluid Mechanics* **463**, 163–171.

SOMMERFELD, A. 1909 Ein Beitrag zur hydrodynamischen Erklärung der turbulenten Flüssigkeitsbewegungen. In *Proceedings of the 4th International Mathematical Congress*, pp. 116–124. Rome.

TAIRA, K., BRUNTON, S. L., DAWSON, S. T. M., ROWLEY, C. W., COLONIUS, T., MCKEON, B. J., SCHMIDT, O. T., GORDEYEV, S., THEOFILIS, V. & UKEILEY, L. S. 2017 Modal analysis of fluid flows: an overview. *AIAA Journal* **55** (12), 4013–4041.

THEOFILIS, V. 2003 Advances in global linear instability analysis of nonparallel and three-dimensional flows. *Progress in Aerospace Sciences* **39** (4), 249–315.

THEOFILIS, V. 2017 The linearized pressure Poisson equation for global instability analysis of incompressible flows. *Theoretical and Computational Fluid Dynamics* **31**, 623–642.

TOUTANT, A. 2017 General and exact pressure evolution equation. *Physics Letters A* **381** (44), 3739–3742.

WEDER, M., GLOOR, M. & KLEISER, L. 2015 Decomposition of the temporal growth rate in linear instability of compressible gas flows. *Journal of Fluid Mechanics* **778**, 120–132.

WHITE, F. 1974 *Viscous fluid flow*. McGraw-Hill, New York.

ZHAO, L., DONG, M. & YANG, Y. 2019 Harmonic linearized Navier-Stokes equation on describing the effect of surface roughness on hypersonic boundary-layer transition. *Physics of Fluids* **31** (3), 034108.

3

Numerical methodology

In this chapter, the numerical methodologies that are used to discretize and solve the eigenvalue and initial-value problems are presented. First, the finite-difference and pseudospectral-collocation methods are detailed for the spatial discretization of the equations and the derivation of the differentiation matrices, that are used to replace the partial derivative operators in the equations, is discussed. Two different mapping formulas are then proposed to map the discrete points to the physical space when using pseudospectral collocation methods. Secondly, the approaches for solving the eigenvalue and initial-value problems are presented and some specific characteristics related to the spatial integration of the Parabolized Stability Equations (PSE) are discussed. Finally, an overview of the practical aspects regarding the implementation of these numerical methodologies is proposed.

3.1. Spatial discretization

The finite-difference and pseudospectral Chebyshev-Gauss-Lobatto methods are used to discretize the partial differential equations in space. The major difference between the two methods is that the former is built on compact support while the latter relies on global functions that span the entire domain. On the one hand, finite-difference approaches provide flexibility regarding the grid geometry and allow managing the computational requirements in a relatively easy way. However, this often comes at the cost of accuracy and undesirable oscillatory behavior close to boundaries (Runge phenomenon). On the other hand, the Chebyshev-Gauss-Lobatto method is computationally more expensive but allows minimizing the discretization error and the Runge phenomenon. Furthermore, while the Chebyshev-Gauss-Lobatto is appropriate to discretize eigenvalue problems, the fact that each individual grid point depends on all other points introduces substantial difficulties when it comes to solving initial-value problems. In this case, it is preferred to use finite-difference methods that evaluate the derivatives at one discrete location by using only a few neighboring points. Therefore, both Chebyshev-Gauss-Lobato and finite-difference methods are considered depending on the application. This section presents the two approaches and their corresponding differentiation matrices.

3.1.1. Polynomial interpolation and differentiation matrices

In its general formulation, a polynomial differentiation approach allows obtaining the coefficients of the differentiation matrices for a discrete grid with N_ξ distinct nodes that are ar-

bitrarily spaced. For the Chebyshev-Gauss-Lobato method, a global span of N_ξ nodes with a specific distribution is considered to minimize the discretization error. For finite-difference approaches, the polynomial differentiation is first considered on a subset of $n_\xi < N_\xi$ arbitrarily spaced nodes and the global differentiation matrix is then constructed after isolating the nodes of interest in each subdomains. This specific aspect will be discussed in §3.1.3. To keep the formulation general, let first represent an arbitrary function $f(\xi)$ on N_ξ distinct discrete nodes ξ_j with the Lagrange interpolating polynomials as

$$f(\xi) \approx f_{N_\xi}(\xi) = \sum_{j=1}^{N_\xi} \psi_j(\xi) f_j \,, \tag{3.1}$$

where $f_j = f(\xi_j)$ is the value taken by the function f at the discrete nodes ξ_j and $f_{N_\xi}(\xi)$ is the interpolated function. The functions $\psi_j(\xi)$ are trial functions and span N_ξ discrete nodes. Considering collocation methods, it is required that $\psi_j(\xi_k) = \delta_{jk}$ and it can be satisfied by considering the basis polynomials of degrees $j-1 = 0, ..., N_\xi - 1$:

$$\psi_j(\xi) = \prod_{\substack{m=1 \\ m\neq j}}^{N_\xi} \left(\frac{\xi - \xi_m}{\xi_j - \xi_m} \right), \quad j = 1, 2, ..., N_\xi \,. \tag{3.2}$$

Evaluating the l-derivative of the interpolant $f_{N_\xi}(\xi)$ with respect to ξ at the discrete point ξ_k yields

$$f^{(l)}_{N_\xi}(\xi_k) = \frac{d^l}{d\xi^l} \left(\sum_{j=1}^{N_\xi} \psi_j(\xi) f_j \right)_{\xi=\xi_k} = \sum_{j=1}^{N_\xi} \left(\frac{d^l}{d\xi^l} \psi_j(\xi) \right)_{\xi=\xi_k} f_j \,, \tag{3.3}$$

or, in matrix form,

$$\mathbf{f}^{(l)} = \mathbf{D}^{(l)}_\xi \mathbf{f}, \tag{3.4}$$

with the coefficients

$$D^{(l)}_{\xi,k,j} = \psi^{(l)}_j(\xi_k) = \frac{d^l}{d\xi^l} \psi_j(\xi_k) \,. \tag{3.5}$$

The matrix elements $D^{(l)}_{\xi,k,j}$ form together the differentiation matrix and are independent of the function f. Note that, in the above developments, the distribution of discrete point ξ_j is arbitrary and their choice become relevant only when selecting a particular spatial discretization scheme. With this general formulation, a differentiation matrix can be built by only knowing the distribution of discrete nodes and the interpolating functions. The differentiation matrix allows obtaining, a posteriori, the derivative of any arbitrary function f on a given grid and can be used in place of (partial) differential operators when discretizing (partial) differential equations.

In order to deal with two-dimensional flows, the polynomial interpolation is extended to a second dimension η, that comprises N_η distinct discrete nodes, and the interpolant (3.1) thus becomes

$$f(\xi,\eta) \approx f_{N_\xi \times N_\eta}(\xi,\eta) = \sum_{j=1}^{N_\xi} \sum_{k=1}^{N_\eta} \psi_j(\xi) \phi_k(\eta) f_{j,k} \,, \tag{3.6}$$

with $f_{j,k} = f(\xi_j, \eta_k)$ and $\phi_k(\eta)$ the interpolating functions in the second dimension. Accordingly, the derivatives in each dimension are given by

$$\frac{\partial f_{N_\xi \times N_\eta}(\xi,\eta)}{\partial \xi} = \sum_{j=1}^{N_\xi} \sum_{k=1}^{N_\eta} f_{k,j} \frac{\partial \psi_j(\xi)}{\partial \xi} \phi_k(\eta) \,, \tag{3.7}$$

$$\frac{\partial f_{N_\xi \times N_\eta}(\xi,\eta)}{\partial \eta} = \sum_{j=1}^{N_\xi} \sum_{k=1}^{N_\eta} f_{k,j} \psi_j(\xi) \frac{\partial \phi_k(\eta)}{\partial \eta}, \tag{3.8}$$

or written in term of the individual differential operators D_ξ or D_η in each dimension

$$\frac{\partial f_{N_\xi \times N_\eta}(\xi,\eta)}{\partial \xi} = \sum_{j=1}^{N_\xi} \sum_{k=1}^{N_\eta} \sum_{m=1}^{N_\xi} f_{k,m} D_{\xi,m,j} \psi_k(\xi) \phi_k(\eta), \tag{3.9}$$

$$\frac{\partial f_{N_\eta \times N_\eta}(\xi,\eta)}{\partial \eta} = \sum_{j=1}^{N_\xi} \sum_{k=1}^{N_\eta} \sum_{m=1}^{N_\eta} D_{\eta,k,m} f_{m,j} \psi_j(\xi) \phi_k(\eta). \tag{3.10}$$

In practice, in order to cast a discretized two-dimensional field $f_{N_\eta \times N_\eta}$ into an actual one-dimensional vector, the following stack-column vector form is used

$$f_{N_\xi \times N_\eta} = \begin{bmatrix} f_{11} & f_{12} & \cdots & f_{1N_\xi} \\ f_{21} & f_{22} & & \vdots \\ \vdots & & \ddots & \vdots \\ f_{N_\eta 1} & \cdots & \cdots & f_{N_\eta N_\xi} \end{bmatrix} \Longrightarrow f_{N_\xi \times N_\eta} = \begin{bmatrix} f_{11} \\ \vdots \\ f_{N_\eta 1} \\ f_{12} \\ \vdots \\ f_{N_\eta 2} \\ \vdots \\ f_{1N_\xi} \\ \vdots \\ f_{N_\eta N_\xi} \end{bmatrix}. \tag{3.11}$$

and according to equations (3.9) and (3.10), the differentiation matrices can be obtained by computing the one-dimensional differentiation matrices individually. In fact, considering the Kronecker product

$$\boldsymbol{A}_{m\times n} \otimes \boldsymbol{B}_{p\times q} = \begin{bmatrix} a_{11}\boldsymbol{B} & \cdots & a_{1n}\boldsymbol{B} \\ \vdots & \ddots & \vdots \\ a_{m1}\boldsymbol{B} & \cdots & a_{mn}\boldsymbol{B} \end{bmatrix} = C_{nq\times mp}, \tag{3.12}$$

for arbitrary matrices $\boldsymbol{A}_{m\times n}$ (with coefficients a_{ij} for $0 < i \leq m$ and $0 < i \leq n$) and $\boldsymbol{B}_{p\times q}$, the first derivative operators (3.9) and (3.10) can be obtained in matrix form as

$${}_2\boldsymbol{D}_\xi = \boldsymbol{D}_\xi \otimes \boldsymbol{I}_{N_\eta}, \qquad {}_2\boldsymbol{D}_\eta = \boldsymbol{I}_{N_\xi} \otimes \boldsymbol{D}_\eta, \tag{3.13}$$

and the second derivative operators as

$${}_2\boldsymbol{D}_{\xi\xi} = \boldsymbol{D}_\xi^2 \otimes \boldsymbol{I}_{N_\eta}, \qquad {}_2\boldsymbol{D}_{\eta\eta} = \boldsymbol{I}_{N_\xi} \otimes \boldsymbol{D}_\eta^2, \qquad {}_2\boldsymbol{D}_{\xi\eta} = \boldsymbol{D}_\xi \otimes \boldsymbol{D}_\eta, \tag{3.14}$$

with ${}_2\boldsymbol{D}$ denoting the two-dimensional differentiation matrices. The matrices $\boldsymbol{I}_{N_\xi}$ and $\boldsymbol{I}_{N_\eta}$ are square identity matrices of sizes N_ξ and N_η, respectively. The differentiation matrices

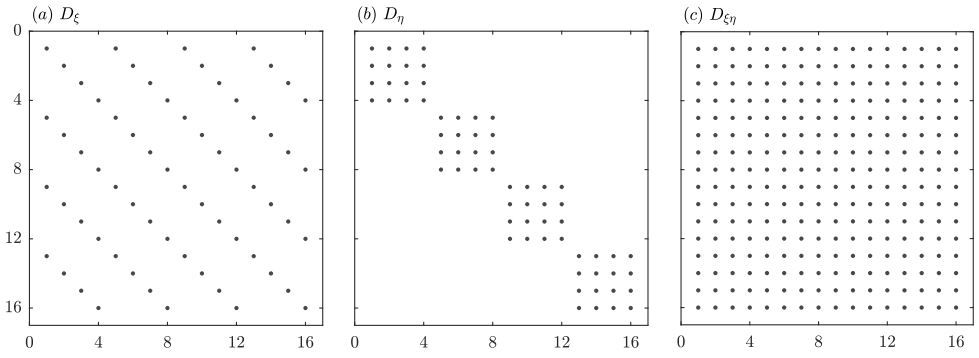

Figure 3.1: Non-zero coefficients of the two-dimensional Chebyshev pseudospectral differentiation matrices for $N_\xi = N_\eta = 4$. See §3.1.2 for detail.

can thus be applied to obtain the spatial derivative of any two-dimensional field $f_{N_\eta \times N_\eta}$ written in the stack-column form (3.11). For sake of visualization, the non-zero elements of the pseudospectral differentiation matrices (see later §3.1.2 for detail) with $N_\xi = N_\eta = 4$ discrete points in each direction are shown in figure 3.1. Finally, note that integration matrices can be obtained by inverting the differentiation matrices after setting appropriate conditions.

3.1.2. Chebyshev-Gauss-Lobatto pseudospectral methods

Stability analyses are highly sensitive to the numerically-computed gradient and, for this reason, the pseudospectral methods are often used in the literature to benefit from their spectral accuracy and thus minimize the impact of the numerical discretization on the results. The Chebyshev-Gauss-Lobatto method (Canuto *et al.*, 2006) is the most used method in the literature when it comes to discretizing stability equations. Since the present work aims to find setup-independent solutions, using the Chebyshev-Gauss-Lobatto approach allows isolating the effectiveness of the moving-frame method from the formulation of the numerical derivatives. The Chebyshev-Gauss-Lobatto approach is based on the Lagrange polynomials distributed on a cosine grid

$$\xi_j = \cos\left(\frac{(j-1)\pi}{N_\xi - 1}\right), \quad j = 1, 2, ..., N_\xi, \tag{3.15}$$

in the interval $[-1, 1]$. Considering the Gauss-Lobatto grid distribution, the Lagrange interpolating polynomials $\psi(\xi)$ can be rewritten with Chebyshev polynomials. These polynomials are solutions of the Sturm-Liouville equation

$$(1-\xi^2)\frac{\partial T^2_{N_\xi-1}}{\partial \xi^2}(\xi) - \xi\frac{\partial T_{N_\xi-1}}{\partial \xi}(\xi) - N_\xi^2 T_{N_\xi-1} = 0, \tag{3.16}$$

that, after the change of variables $\xi = \cos(\theta)$, becomes

$$\frac{d^2 T_{N_\xi-1}}{d\theta^2} + (N_\xi - 1)^2 T_{N_\xi-1} = 0. \tag{3.17}$$

Solving equation (3.17) gives the Chebyshev polynomials of the first and second kind

$$T_{N_\xi-1} = \cos((N_\xi - 1)\theta), \quad U_{N_\xi-1} = \frac{1}{N_\xi - 1}\frac{dT_{N_\xi-1}}{d\theta} = \sin((N_\xi - 1)\theta), \tag{3.18}$$

respectively. Transforming back to the ξ-coordinate system with $\theta = \arccos(\xi)$, the two polynomials finally read

$$T_{k-1} = \cos((k-1)\arccos(\xi)), \qquad U_{k-1} = \frac{\sin((k-1)\arccos(\xi))}{\sin(\arccos(\xi))}, \tag{3.19}$$

in the domain $\xi \in [-1,1]$. To circumvent the restrictions on the domain size and on the cosine node distribution, mappings of the discrete nodes to the physical space are usually considered (see §3.1.4). Finally, the Lagrange polynomials $\psi_i(\xi)$ on the Chebyshev-Gauss-Lobatto nodes become

$$\psi_j(\xi) = \frac{(-1)^j}{c_j(N_\xi-1)^2}\left(\frac{1-\xi^2}{\xi-\xi_j^2}\right)\frac{dT_{N_\xi-1}}{d\xi} = \frac{(-1)^{j+1}}{c_j(N_\xi-1)^2}\left(\frac{\sqrt{1-\xi^2}}{\xi-\xi_j^2}\right)U_{N_\xi-1}, \tag{3.20}$$

$$\text{where} \quad c_j = \begin{cases} 2 & \text{for } j=1 \text{ or } j=N_\xi \\ 1 & \text{for } 2 \le j \le N_\xi - 1 \end{cases},$$

Taking the derivative of ψ_j with respect to ξ at node ξ_k allows obtaining the coefficients

$$D_{\xi,k,j} = \begin{cases} D_{\xi,1,1} = \frac{2(N_\xi-1)^2+1}{6}, & \\ D_{\xi,k,k} = -\frac{\xi_k}{2(1-\xi_k^2)} & \text{for } k = 2,\dots,N_\xi-1, \\ D_{\xi,k,j} = \frac{c_k}{c_j}\frac{(-1)^{k+j}}{\xi_k-\xi_j} & \text{for } k \neq j \quad k,j = 2,\dots,N_\xi-1, \\ D_{\xi,N_\xi,N_\xi} = -\frac{2(N_\xi-1)^2+1}{6}, & \end{cases}. \tag{3.21}$$

such that the Chebyshev pseudospectral differentiation matrix writes

$$\boldsymbol{D}_\xi = \left[\begin{array}{c|ccc|c} \frac{2(N_\xi-1)^2+1}{6} & \dots & 2\frac{(-1)^{1+m}}{1-\xi_m} & \dots & \frac{1}{2}(-1)^{1+N_\xi} \\ \hline \vdots & \ddots & \dots & \frac{(-1)^{k+j}}{\xi_k-\xi_j} & \vdots \\ \frac{1}{2}\frac{(-1)^{k+1}}{\xi_k-1} & \vdots & -\frac{\xi_k}{2(1-\xi_j^2)} & \vdots & \frac{(-1)^{k+N_\xi}}{\xi_k+1} \\ \vdots & \frac{(-1)^{k+j}}{\xi_k-\xi_j} & \dots & \ddots & \vdots \\ \hline -\frac{1}{2}(-1)^{N_\xi+1} & \dots & 2\frac{(-1)^{N_\xi+m}}{1+\xi_m} & \dots & -\frac{2(N_\xi-1)^2+1}{6} \end{array}\right]. \tag{3.22}$$

The matrix (3.22) and its analogue for η can then be used to compute the derivatives of any function $f(\xi,\eta)$ at the collocation nodes. For the two directions, the Chebyshev-Gauss-Lobatto differentiation method relies on a specific grid distribution that cannot be altered. The domain and node distribution can thus be very restrictive for real flow applications. In order to have more flexibility when using pseudospectral differentiations, the method-specific numerical space can be mapped into a more realistic physical space (see §3.1.4).

3.1.3. Finite-difference method

The differentiation matrix for a finite-difference method on arbitrarily spaced nodes can be obtained by considering the polynomial differentiation approach on a stencil with $n_\xi \leq N_\xi$ nodes. Fornberg (1988); Welfert (1997) developed an approach that computes the coefficients of a global differentiation matrix to evaluate the derivative of a function $f(x)$ at discrete, arbitrarily spaced nodes through recursion formulas. Using this approach, the local polynomial differentiation matrices that evaluate the derivative at ξ_k on the stencil $[\bar{\xi}_1,...,\bar{\xi}_i,...,\bar{\xi}_{n_\xi}] = [\xi_{k-n_\mathrm{b}},...,\xi_k,...\xi_{k+n_\mathrm{f}}]$ with $n_\xi = n_\mathrm{b} + n_\mathrm{f} + 1$ are built. The values n_b and n_f indicate the number of nodes to be considered backward and forward with respect to ξ_j, respectively. For a second-order-accuracy finite difference, a central scheme is given for $n_\mathrm{b} = n_\mathrm{f} = 1$ while a backward scheme is given for $n_\mathrm{b} = 2$ and $n_\mathrm{f} = 0$. For each subset, recursion formulas are used to construct the polynomial differentiation matrices in an efficient way. These formulas are obtained by first rewriting the polynomials (3.2) on a subset in the form

$$\bar{\psi}_{n_\xi,i}(\bar{\xi}) = \frac{\bar{\Psi}_{n_\xi}(\bar{\xi})}{\bar{\Psi}^{(1)}_{n_\xi}(\bar{\xi}_i)(\bar{\xi}-\bar{\xi}_i)}, \tag{3.23}$$

with

$$\bar{\Psi}_{n_\xi}(\bar{\xi}) = \prod_{m=0}^{n_\xi} (\bar{\xi}-\bar{\xi}_m). \tag{3.24}$$

The subscript n_ξ indicates the number of points spanned by the polynomials and all functions associated with a stencil, i.e., that do not have a global span N_ξ, are indicated with an overline. Since $\bar{\Psi}_{n_\xi}(\bar{\xi})$ and its first-order derivative $\bar{\Psi}^{(1)}_{n_\xi}(\bar{\xi})$ can be obtained through the recursion formulas

$$\bar{\Psi}_{n_\xi}(\bar{\xi}) = (\bar{\xi}-\bar{\xi}_{n_\xi})\bar{\Psi}_{n_\xi-1}(\bar{\xi}), \tag{3.25a}$$

$$\bar{\Psi}^{(1)}_{n_\xi}(\bar{\xi}) = (\bar{\xi}-\bar{\xi}_{n_\xi})\bar{\Psi}^{(1)}_{n_\xi-1}(\bar{\xi}) + \bar{\Psi}_{n_\xi-1}(\bar{\xi}), \tag{3.25b}$$

the polynomials become

$$\bar{\psi}_{n_\xi,i}(\bar{\xi}) = \frac{\bar{\xi}-\bar{\xi}_{n_\xi}}{\bar{\xi}_i-\bar{\xi}_{n_\xi}}\bar{\psi}_{n_\xi-1,i}(\bar{\xi}), \tag{3.26a}$$

$$\bar{\psi}_{n_\xi,n_\xi}(\bar{\xi}) = \frac{\bar{\Psi}_{n_\xi-2}(\bar{\xi}_{n_\xi-1})}{\bar{\Psi}_{n_\xi-1}(\bar{\xi}_{n_\xi})}(\bar{\xi}-\bar{\xi}_{n_\xi-1})\bar{\psi}_{n_\xi-1,n_\xi-1}(\bar{\xi}). \tag{3.26b}$$

These polynomials can be derived with respect to ξ according to equation (3.3) but Welfert (1997) shows that, when considering an arbitrary node distribution, the diagonal terms cannot be computed recursively. In order to obtain an actual recursion formula for all coefficients of the differentiation matrix, Fornberg (1988) instead expanded the basis polynomials as a Taylor series around $\bar{\xi} = \bar{\xi}_m$ such that

$$\bar{\psi}_{n_\xi,i}(\xi) = \sum_{s=0}^{n_\xi} \frac{(\bar{\xi}-\bar{\xi}_m)^s}{s!}\bar{\psi}^{(s)}_{n_\xi,i}(\bar{\xi}_m) = \sum_{s=0}^{n_\xi} \frac{(\bar{\xi}-\bar{\xi}_m)^s}{s!}\bar{D}^{(s)}_{\bar{\xi},m,i}. \tag{3.27}$$

Introducing equation (3.27) into the recursive relation (3.26), the coefficients for the local polynomial differentiation matrix on the stencil $[\bar{\xi}_1,...,\bar{\xi}_i,...,\bar{\xi}_{n_\xi}]$ are then given by

$$\bar{D}^{(l)}_{\bar{\xi},m,i} = \begin{cases} \frac{1}{\bar{\xi}_{n_\xi}-\bar{\xi}_i}\left((\bar{\xi}_i-\bar{\xi}_m)\bar{D}^{(l)}_{\bar{\xi},m,i} - l\bar{D}^{(l-1)}_{\bar{\xi},m,i}\right) & \text{if } i \neq n_\xi, \\ \frac{\bar{\Psi}_{n_\xi-2}(\bar{\xi}_{n_\xi-1})}{\bar{\Psi}_{n_\xi-1}(\bar{\xi}_{n_\xi})}\left(l\bar{D}^{(l-1)}_{\bar{\xi},m,i-1} - (\bar{\xi}_{n_\xi-1}-\bar{\xi}_m)\bar{D}^{(l-1)}_{\bar{\xi},m,i-1}\right) & \text{if } i = n_\xi. \end{cases} \tag{3.28}$$

The coefficients for the derivative at ξ_k (global grid) correspond to the row $m = (n_\xi + n_\mathrm{b} - n_\mathrm{f})/2$ of the local differentiation matrix $\bar{D}^{(l)}_{\bar{\xi},m,i}$. Hence, the global differentiation matrix can be obtained with

$$D^{(l)}_{\xi,k,j} = \bar{D}^{(l)}_{\bar{\xi},m,i} \quad \text{for} \quad \begin{cases} k = 1,2,...,N_\xi\,, \\ j = k - n_\mathrm{b},...,k,...,k + n_\mathrm{f}\,, \\ m = (n_\xi + n_\mathrm{b} - n_\mathrm{f})/2\,, \\ i = 1,2,...n_\xi\,, \end{cases} \tag{3.29}$$

where the local $\bar{D}^{(l)}_{\bar{\xi},m,i}$ must be computed for each subset $[\bar{\xi}_1,...,\bar{\xi}_i,...,\bar{\xi}_{n_\xi}]$. For the interior of the domain, any value n_b and n_f can be chosen as long as $n_\mathrm{b} + n_\mathrm{b} \leq N_\xi - 1$. Close to the boundaries, the scheme can be adapted in two different ways. The first approach is to maintain the type of the scheme, i.e., central, backward or forward, and then decrease the order of accuracy, i.e., the stencil length, as ξ_k approaches the boundary. The second strategy consists in maintaining the order of the scheme by swapping the central point of the derivatives. Hence, at the inlet and outlet boundaries, the spatial differentiation becomes mostly forward and backward, respectively. This second approach is presently considered when using the finite-difference method. Finally, note that the above development can be extended to the direction η in order to form the two-dimensional differentiation matrices (see §3.1.1). In the present thesis, the `Matlab` suite developed by Weideman & Reddy (2000) has been adapted to generate the finite-difference and Chebyshev differentiation matrices for the discretization of the two-dimensional partial differential operators in rectangular domains.

3.1.4. Mapping to physical space

Although applicable to finite-difference methods, mapping techniques are mostly relevant for the Chebyshev-Gauss-Lobatto method that is restricted to the square domain $[-1,1] \times [-1,1]$ in two-dimensional cases. To improve upon this restrictive aspect, two mapping methods are presently considered. Originally proposed by Malik (1990) and extensively used for one-dimensional stability analyses of wall-bounded flows in the literature, the Malik's mapping relies on a bilinear relationship

$$x = \frac{x_i\, x_\mathrm{max}(1+\xi)}{x_\mathrm{max} - \xi(x_\mathrm{max} - 2x_i)}, \tag{3.30}$$

that maps the streamwise Chebyshev nodes ξ to the physical nodes x defined in the physical space $[0, x_\mathrm{max}]$. In particular, equation (3.30) maps half the collocation nodes in $[0, x_i]$ and the other half in $[x_i, x_\mathrm{max}]$. When mapping the coordinate η in the y-direction, the Malik's mapping is particularly suitable to enforce a high density of nodes close to the wall, in the region of the boundary layer. This mapping becomes, however, less relevant when the dynamics of interest is not in close proximity with a (physical) border of the domain. Instead, in order to reduce the amount of nodes at the domain boundaries and increase the grid density in particular regions of space, a bi-quadratic mapping can be used (Groot *et al.*, 2018).

The formulation of the mapping for the x-direction is given by

$$x = x_{\max}\frac{a\xi^2 + b\xi + c}{d\xi^2 + e\xi + cf}, \qquad \text{with} \begin{cases} a = & (x_{i2} - 3x_{i1}), \\ b = & 1.5(x_{i2} - x_{i1}), \\ c = & 0.5(x_{i2} + 3x_{i1}), \\ d = & 2(2x_{i2} - 2x_{i1} - x_{\max}), \\ e = & 0, \\ f = & 2x_{\max} - x_{i2} + x_{i1}, \end{cases} \tag{3.31}$$

with $0 < x_{i1} < x_{i2} < x_{\max}$, $x_{i2} < 9x_{i1}$ and $9x_{i2} < x_{i1} + x_{\max}$. The bi-quadratic mapping divides the domain into three parts ($[0, x_{i1}]$, $[x_{i1}, x_{i2}]$ and $[x_{i2}, x_{\max}]$), each containing one third of the collocation nodes. This mapping is particularly suitable for the laminar shock-wave/boundary-layer interaction because it allows increasing the grid density around the shock and the bubble in the x-direction. Note that, for the two aforementioned mappings, a distribution similar to the original cosine distribution is kept near the boundaries in order to avoid the Runge phenomenon and maintain the numerical properties of the Chebyshev collocation method.

The mapping functions are applied to the pseudospectral differentiation matrices in order to obtain the spatial derivatives in the physical space. Using the chain rule, the streamwise derivative of an arbitrary function f becomes

$$\frac{\partial f}{\partial x} = \frac{\mathrm{d}\xi}{\mathrm{d}x}\frac{\partial f}{\partial \xi}, \tag{3.32}$$

and the differentiation matrices can thus be mapped by

$$\boldsymbol{D}_x = \boldsymbol{T}_x^{\xi}\,\boldsymbol{D}_{\xi}, \tag{3.33}$$

with $\boldsymbol{T}_x^{\xi}$ the discrete analogue of $\mathrm{d}\xi/\mathrm{d}x$. Hence, the matrix $\boldsymbol{T}_x^{\xi}$ scales the coefficients of the initial differentiation matrix according to the mapping functions. The same applies to the wall-normal direction and higher order differentiation matrices.

3.2. Temporal discretization and integration

After discretization in space, the linearized Navier-Stokes equations (2.13) take the semi-discrete form

$$\boldsymbol{B}\frac{\partial \boldsymbol{q}'_{\mathrm{f}}}{\partial t} = \boldsymbol{L}\boldsymbol{q}'_{\mathrm{f}}, \tag{3.34}$$

with $\boldsymbol{B}(\overline{\boldsymbol{Q}})$ and $\boldsymbol{L}(\overline{\boldsymbol{Q}})$ the matrix equivalent of the operators $\mathscr{B}(\overline{\boldsymbol{Q}})$ and $\mathscr{L}(\overline{\boldsymbol{Q}})$, respectively. The discrete solutions thus read

$$\boldsymbol{q}_{\mathrm{f}}(x_{\mathrm{f}}, y, z, t_{\mathrm{f}}) = \mathrm{e}^{\boldsymbol{B}^{-1}\boldsymbol{L}t_{\mathrm{f}}}\boldsymbol{q}_{\mathrm{f},0}(x_{\mathrm{f}}, y, z), \tag{3.35}$$

and are exact solutions in time. If $\boldsymbol{B}$ can be inverted, the exponential matrix $\mathrm{e}^{\boldsymbol{B}^{-1}\boldsymbol{L}t_{\mathrm{f}}}$ needs to be evaluated only once in order to obtain the exact temporal solutions at any time instant. However, the evaluation of the exponential matrix is numerically intractable for large problems. Although numerical strategies exist to compute the exponential matrix (Ruiz *et al.*, 2016) explicitly, they are often unsatisfactory in terms of performances when high accuracy

is required (Moler & van Loan, 2003), especially regarding memory requirements. Hence, iterative numerical integration methods, that approximate the temporal derivative and advance the initial-value problem (3.34) in time, are preferred.

The temporal perturbation problem is less stiff when formulated for compressible flows than for incompressible flows because the former contains at least one temporal derivative per equation. The compressible-flow perturbation problem can thus be solved with an explicit Runge-Kutta method without any artifact. For an ordinary differential equation with time-independent coefficients, the solutions obtained with a generic explicit p^{th}-order Runge-Kutta method with s steps ($s \geq p$) read

$$\mathbf{q}_{\mathrm{f},n+1} = \mathbf{q}_{\mathrm{f},n} + \Delta t \sum_{i=1}^{i=s} b_i \mathbf{k}_i \,, \tag{3.36}$$

where n is the index corresponding to the discrete time t_n and Δt is the constant time-step size such that $t_{n+1} = t_n + \Delta t$. The intermediate solutions $\mathbf{k}_i$ are given by

$$\mathbf{B}\mathbf{k}_i = \mathbf{L}\left(\mathbf{q}_{\mathrm{f},n} + \Delta t \sum_{j=1}^{j=s-1} a_{ij}\mathbf{k}_j\right). \tag{3.37}$$

where the matrices $\mathbf{B}$ and $\mathbf{L}$ include all boundary conditions. Since the Runge-Kutta method originates from a Taylor expansion of the solutions around time t_n, the weights b_i must be chosen such that $\sum_i b_i = 1$. In contrast, the coefficients a_{ij} do not need to satisfy a particular constraint and can be adapted to obtain variant Runge-Kutta methods. If $s = 1$, the weight $b_1 = 1$ and the method reduces to the simple explicit forward Euler method. However, this method has a limited region of stability and has a slow first-order convergence with respect to the time-step size. To ensure high accuracy at a reasonable computational cost, the traditional four-step Runge-Kutta scheme is presently used. Its coefficients are given by

$$\boldsymbol{a} = \begin{bmatrix} 1/2 & 0 & 0 \\ 0 & 1/2 & 0 \\ 0 & 0 & 1 \end{bmatrix}, \qquad \boldsymbol{b} = \begin{bmatrix} 1/6 \\ 1/3 \\ 1/3 \\ 1/6 \end{bmatrix}. \tag{3.38}$$

Since the matrices $\boldsymbol{B}$ and $\boldsymbol{L}$ have constant coefficients, the resulting matrix $\boldsymbol{B}^{-1}\boldsymbol{L}$ has to be evaluated only once. However, this operation is computationally intractable for large problems and matrix-vector operations must be preferred. In order to optimize the computation of each $\boldsymbol{k}_i$, the matrix $\boldsymbol{B}$ is thus factorized with the LU-decomposition $\boldsymbol{B} = \boldsymbol{L}_{\boldsymbol{B}}\boldsymbol{U}_{\boldsymbol{B}}$. This allows obtaining an optimized Runge-Kutta scheme with the four steps

$$\boldsymbol{k}_1 = \boldsymbol{U}_{\boldsymbol{B}}^{-1}\boldsymbol{L}_{\boldsymbol{B}}^{-1}\boldsymbol{L}\boldsymbol{q}_{\mathrm{f},n} \,, \tag{3.39a}$$

$$\boldsymbol{k}_2 = \boldsymbol{U}_{\boldsymbol{B}}^{-1}\boldsymbol{L}_{\boldsymbol{B}}^{-1}\boldsymbol{L}\left(\boldsymbol{q}_{\mathrm{f},n} + \frac{\Delta t}{2}\boldsymbol{k}_1\right), \tag{3.39b}$$

$$\boldsymbol{k}_3 = \boldsymbol{U}_{\boldsymbol{B}}^{-1}\boldsymbol{L}_{\boldsymbol{B}}^{-1}\boldsymbol{L}\left(\boldsymbol{q}_{\mathrm{f},n} + \frac{\Delta t}{2}\boldsymbol{k}_2\right), \tag{3.39c}$$

$$\boldsymbol{q}_{\mathrm{f},n+1} = \boldsymbol{q}_{\mathrm{f},n} + \Delta t \boldsymbol{k}_3 \,. \tag{3.39d}$$

Note that the boundary conditions are imposed in the $\boldsymbol{B}$ matrix and thus are implicitly enforced for each intermediate solution $\boldsymbol{k}_i$ (Pathria, 1997). This ensures the numerical stability

of the integration. Hence, the temporal integration can be conducted with a larger time-step size than if the boundary conditions were applied only to the last step (3.39d).

On the other hand, the (linearized) Navier-Stokes equations for incompressible flows are stiff; there is no temporal derivative for the pressure term and, thus, the matrix $\boldsymbol{B}$ is singular. Hence, an explicit temporal integration cannot be used without an additional strategy, e.g., a pressure correction method, to circumvent the fact that $\boldsymbol{B}$ cannot be inverted. In contrast, implicit time-marching techniques do not rely on the inversion of the matrix $\boldsymbol{B}$ but of a scheme-dependent operator instead. Although implicit integration techniques are computationally more expensive, they offer a much larger region of numerical stability. Hence, larger time-step sizes can be used with implicit schemes than with explicit schemes. Since only linear problems are presently considered, it is found that implicit schemes are computationally affordable to solve the incompressible-flow perturbation equations. Two different schemes are implemented for the implicit time-marching of the initial-value problem. These are the second-order backward differentiation formula

$$\left(\boldsymbol{B}-\frac{2}{3}\Delta t\boldsymbol{L}\right)\boldsymbol{q}_{\mathrm{f},n+1}=\frac{4}{3}\boldsymbol{q}_{\mathrm{f},n}-\frac{1}{3}\boldsymbol{q}_{\mathrm{f},n-1}\,, \tag{3.40}$$

and the Crank-Nicolson formula

$$\left(\boldsymbol{B}+\frac{1}{2}\Delta t\boldsymbol{L}\right)\boldsymbol{q}_{\mathrm{f},n+1}=\left(\boldsymbol{B}-\Delta t\boldsymbol{L}\right)\boldsymbol{q}_{\mathrm{f},n}\,, \tag{3.41}$$

that both offer second-order accuracy in time. The Crank-Nicolson scheme is a one-step method that requires only the current time step n to compute the next time instant t_{n+1}. In contrast, the second-order backward differentiation approach is a two-step method, i.e., it needs both the previous and current time steps to evaluate the solution at t_{n+1}. To evaluate the first time step (t_1), it is thus required to start the integration with a one-step scheme, e.g., a first-order backward differentiation or the Crank-Nicolson scheme, before continuing with the second-order backward scheme. This lack of consistency during the initial steps justifies considering the Crank-Nicolson scheme when assessing the short-time/instantaneous behavior of a solution. However, the second-order backward differentiation scheme allows prescribing a larger time-step size and is thus chosen to compute long-time solutions. As for the Runge-Kutta approach, the LU decomposition is used at the first time step to inverse the left-hand-side matrix of equations (3.40) and (3.41), after having imposed the boundary conditions. Although the two implicit schemes can also be used to solve the compressible-flow perturbation equations for the shock-wave/boundary-layer interaction, they were found to be computationally more expensive than the explicit Runge-Kutta method. Hence, in the present work, implicit schemes are used for incompressible flows while explicit integration is used to solve the compressible-flow perturbation equations.

3.3. The discretized eigenvalue problem

The two-dimensional stability equations (2.20) can be written in their discrete form as

$$\boldsymbol{A}\tilde{\boldsymbol{q}}_{\mathrm{f}}=-\mathrm{i}\omega_{\mathrm{f}}\boldsymbol{B}\tilde{\boldsymbol{q}}_{\mathrm{f}}\,, \tag{3.42}$$

with the matrices $\boldsymbol{A}$ and $\boldsymbol{B}$ including the spatial discretization of the base-flow components, the spatial differentiation operators and the boundary conditions. The solutions of the eigenvalue problem (3.42) are then determined by finding the roots of

$$\det\left(\boldsymbol{A}+\mathrm{i}\omega_{\mathrm{f}}\boldsymbol{B}\right)=0\,. \tag{3.43}$$

The same applies to the eigenvalue problem formulated in the moving frame of reference with $\tilde{\boldsymbol{q}}$ the moving-frame eigenfunctions. Note that, when considering the one-dimensional *temporal* stability problem (2.23a), the discretized eigenvalue problem takes the same form as equation (3.42). It can thus be solved in the exact same way, after having prescribed a value for the wavenumber α. However, when considering the one-dimensional *spatial* stability problem (2.23b), the (discretized) eigenvalue problem

$$\boldsymbol{A}_\alpha \tilde{\boldsymbol{q}}_\mathrm{f} = -\mathrm{i}\alpha \boldsymbol{B}_\alpha \tilde{\boldsymbol{q}}_\mathrm{f} + \alpha^2 \boldsymbol{C}_\alpha \tilde{\boldsymbol{q}}_\mathrm{f}, \tag{3.44}$$

is quadratic and cannot be solved directly. The companion linearization approach is thus used to rewrite equation (3.44) as a linear generalized eigenvalue problem

$$\underbrace{\begin{bmatrix} \boldsymbol{A}_\alpha & \boldsymbol{B}_\alpha \\ 0 & -\boldsymbol{I} \end{bmatrix}}_{\boldsymbol{A}_{\alpha,c}} \underbrace{\begin{bmatrix} \tilde{\boldsymbol{q}}_\mathrm{f} \\ \mathrm{i}\alpha\tilde{\boldsymbol{q}}_\mathrm{f} \end{bmatrix}}_{\tilde{\boldsymbol{q}}_{\mathrm{f},c}} = -\mathrm{i}\alpha \underbrace{\begin{bmatrix} 0 & \boldsymbol{C}_\alpha \\ \boldsymbol{I} & 0 \end{bmatrix}}_{\boldsymbol{B}_{\alpha,c}} \underbrace{\begin{bmatrix} \tilde{\boldsymbol{q}}_\mathrm{f} \\ \mathrm{i}\alpha\tilde{\boldsymbol{q}}_\mathrm{f} \end{bmatrix}}_{\tilde{\boldsymbol{q}}_{\mathrm{f},c}}, \tag{3.45}$$

with the subscript c denoting the companion vectors and matrices. The companion spatial eigenvalue problem can thus be solved in the exact same way as the temporal problem. Once solutions are found, only the first half of the companion eigenvector $\tilde{\boldsymbol{q}}_{\mathrm{f},c}$ must be taken in order to isolate the sought eigenfunctions $\tilde{\boldsymbol{q}}_\mathrm{f}$.

The temporal and spatial eigenvalue problems have sparse matrices and can thus be solved with the iterative Arnoldi algorithm in a computationally effective way (Saad, 2011). Based on a Krylov projection method, the Arnoldi algorithm computes a subset of eigensolutions in an a-priori-prescribed region of the eigenvalue spectrum. The algorithm is implemented in `Matlab` via the function `eigs` that relies on the `ARPACK` routines (Lehoucq *et al.*, 1998; Wright & Trefethen, 2001). All eigenvalue problems that are considered in the present work are solved with this function.

3.3.1. Discretization of the adjoint eigenvalue problem

While the discretization of the direct eigenvalue problem immediately followed from its continuous formulation, two different approaches exist to obtain the discrete form of the adjoint eigenvalue problem. On the one hand, the adjoint problem can first be derived by starting from the continuous direct problem (see §2.4) and then discretized. This formulation is the so-called continuous adjoint problem. The major difficulties with this formulation are that the problem must be explicitly derived and that appropriate boundary conditions must be specified. Because only homogeneous boundary conditions are presently considered, the latter aspect is, however, not an issue. On the other hand, the adjoint eigenvalue problem can be obtained by Hermitian transposing the discretized direct eigenvalue problem (3.42). This form of the problem is the so-called discrete adjoint problem and is easily implemented in a numerical code. However, in general, it does not ensure that actual adjoint boundary conditions are satisfied. A comparison of the two mathematical formulations is proposed in the following.

The discrete adjoint eigenvalue problem relies on the discretized form of the inner product, given by equation (2.28) in its continuous formulation, that can be written

$$\langle \boldsymbol{f}_1, \boldsymbol{f}_2 \rangle = \boldsymbol{f}_1^\mathrm{H} \boldsymbol{D} \boldsymbol{f}_2, \tag{3.46}$$

with $\boldsymbol{D}$ a real-valued diagonal matrix that accounts for the size of the grid cells. As its continuous equivalent, the discrete adjoint problem relies on the orthogonality relationship be-

tween the direct eigenvalue problem and the vector $\tilde{\boldsymbol{q}}_{\mathrm{f}}^{\dagger}$ such that

$$\left\langle \tilde{\boldsymbol{q}}_{\mathrm{f}}^{\dagger}, (\boldsymbol{A}+\mathrm{i}\boldsymbol{B}\omega_{\mathrm{f}})\,\tilde{\boldsymbol{q}}_{\mathrm{f}} \right\rangle = 0 = \left(\tilde{\boldsymbol{q}}_{\mathrm{f}}^{\dagger}\right)^{\mathrm{H}} \left(\boldsymbol{D}\,(\boldsymbol{A}+\mathrm{i}\boldsymbol{B}\omega_{\mathrm{f}})\,\tilde{\boldsymbol{q}}_{\mathrm{f}}\right) = \left(\left(\boldsymbol{A}^{\mathrm{H}}-\mathrm{i}\boldsymbol{B}^{\mathrm{H}}\omega_{\mathrm{f}}^{*}\right)\boldsymbol{D}^{\mathrm{H}}\tilde{\boldsymbol{q}}_{\mathrm{f}}^{\dagger}\right)^{\mathrm{H}}\tilde{\boldsymbol{q}}_{\mathrm{f}}. \tag{3.47}$$

Because only matrix manipulations are involved, no boundary term appears in the derivation of the discrete adjoint problem. This contrasts with the continuous formulation that requires integrating by parts, and thus, dealing with boundary terms. Finally, because $\boldsymbol{D}$ is diagonal and both $\boldsymbol{B}$ and $\boldsymbol{D}$ are real-valued matrices, equation (3.47) can be written

$$0 = \left(\left(\boldsymbol{A}^{\mathrm{H}}-\mathrm{i}\boldsymbol{B}^{\mathrm{T}}\omega_{\mathrm{f}}^{*}\right)\boldsymbol{D}^{\mathrm{H}}\tilde{\boldsymbol{q}}_{\mathrm{f}}^{\dagger}\right)^{\mathrm{H}}\tilde{\boldsymbol{q}}_{\mathrm{f}} = \left(\left(\boldsymbol{D}^{-1}\boldsymbol{A}^{\mathrm{H}}\boldsymbol{D}^{\mathrm{H}}-\mathrm{i}\boldsymbol{B}^{\mathrm{T}}\omega_{\mathrm{f}}^{*}\right)\tilde{\boldsymbol{q}}_{\mathrm{f}}^{\dagger}\right)^{\mathrm{H}}\tilde{\boldsymbol{q}}_{\mathrm{f}}. \tag{3.48}$$

The discretized continuous (from equation (2.31)) and discrete adjoint eigenvalue problems are thus given by

$$\boldsymbol{A}^{\dagger}\tilde{\boldsymbol{q}}_{\mathrm{f}}^{\dagger} = \mathrm{i}\omega_{\mathrm{f}}^{*}\boldsymbol{B}^{\mathrm{T}}\tilde{\boldsymbol{q}}_{\mathrm{f}}^{\dagger}, \tag{3.49a}$$

$$\boldsymbol{D}^{-1}\boldsymbol{A}^{\mathrm{H}}\boldsymbol{D}\tilde{\boldsymbol{q}}_{\mathrm{f}}^{\dagger} = \mathrm{i}\omega_{\mathrm{f}}^{*}\boldsymbol{B}^{\mathrm{T}}\tilde{\boldsymbol{q}}_{\mathrm{f}}^{\dagger}, \tag{3.49b}$$

respectively. Note that the operator $\mathscr{B}^{\dagger}$ of the continuous formulation is reduced to $\boldsymbol{B}^{\mathrm{T}}$ because it does not involve any spatial derivative nor any complex-valued numbers. For the discretized problems, the bi-orthogonality condition (2.32) becomes

$$\left\langle \tilde{\boldsymbol{q}}_{\mathrm{f},j}^{\dagger}, \boldsymbol{B}\tilde{\boldsymbol{q}}_{\mathrm{f},k} \right\rangle = \delta_{jk} = \begin{cases} 1 & \text{for} \quad j = k, \\ 0 & \text{for} \quad j \neq k. \end{cases} \tag{3.50}$$

and can be verified numerically.

By inspecting equations (3.49a) and (3.49b), the relationship $\boldsymbol{A}^{\dagger} = \boldsymbol{D}^{-1}\boldsymbol{A}^{\mathrm{H}}\boldsymbol{D}$ can be established between the discrete and continuous adjoint problems; the two formulations are mathematically equivalent. However, the conditions at the boundaries need to be explicitly enforced in the continuous formulation while, in the discrete formulation, they are already included in the coefficient matrices of the direct problem. Hence, small discrepancies can be found in the numerical results between the continuous adjoint and discrete adjoint problems. After verifying that the solutions obtained from the continuous and discrete formulations only yielded very minor differences for setup-independent solutions, the discrete formulation is presently chosen to solve the adjoint eigenvalue problems.

3.4. Spatial integration of the Parabolized Stability Equations

The Parabolized Stability Equations (PSE) are formulated as an initial-value problem in space and are then solved through spatial integration in the downstream direction (Bertolotti, 1991). A common way to initialize the integration of the PSE is to consider solutions of the Linear Stability Theory (LST) method at an upstream streamwise station. When applied to wall-bounded flows, the literature often uses the following spatial discretization techniques for the PSE method. The wall-normal discretization usually relies on the Chebyshev-Gauss-Lobato pseudospectral method with Malik's mapping to increase the node density close to the wall. The streamwise direction is discretized with equally spaced nodes and the x-derivative is then formulated with a first-order finite-difference scheme. Finally, because the PSE contain nonlinear terms, each spatial step is solved iteratively. This is usually done with a predictor-corrector method that applies a correction to α until the normalization

condition (2.27) is satisfied up to a prescribed criterion. This ensures that all spatial growth is effectively captured into the streamwise wavenumber α at each x-station and thus that the streamwise variation of the shape function $\tilde{\boldsymbol{q}}$ remains small, as assumed by the WKBJ ansatz (2.24).

Using an implicit spatial integration scheme to discretize the PSE in the streamwise direction is essential to solve the problem. In fact, the PSE are not strictly parabolic equations in nature and still contain some ellipticity that is mostly associated with the streamwise derivative of the pressure term. Hence, while *parabolic* equations only contain solutions that propagate in one direction, the *parabolization* of the linear perturbation equations only eliminates some of the (viscous) upstream-traveling waves by neglecting the second-order terms $\mathcal{O}(\epsilon_p^2)$. The main consequence of the parabolization approach is thus that some upstream-traveling acoustic waves are still present in the system (Li & Malik, 1997; Andersson *et al.*, 1998). To ensure that the problem is well-posed, these waves must be specified at the outlet of the domain. However, the PSE are solved through spatial marching techniques starting from the inlet and the upstream-traveling acoustic waves are thus underspecified. Although these waves should physically decay toward the inlet, numerical instabilities caused by the ill-posedness of the problem can lead to spurious growth in the downstream direction. Spectral analyses of the PSE operator indicate that the numerical problem is unconditionally unstable if an explicit time-marching scheme is used (Andersson *et al.*, 1998). Hence, in order to damp out upstream-traveling waves and only track the relevant downstream-traveling wave, solving the PSE must, at least, rely on an implicit spatial-marching technique.

Considering a first-order implicit scheme makes the system conditionally stable and a relatively restrictive criterion exists on the size of the spatial discretization Δx. According to Andersson *et al.* (1998), the step size Δx must be larger than $1/|\alpha|$ for incompressible flows. Although this criterion allows solving the PSE, it can be too restrictive in some cases, especially when considering flows that do not evolve slowly in the streamwise direction. The criterion also implies that refining the spatial discretization in the streamwise direction unlikely converges for reasonably small step sizes. Nevertheless, although the minimum-step-size criterion can be satisfied in some cases, the problem to be solved is ill-posed. To improve upon this aspect and reduce the minimum step size, two stabilization techniques have been devised. The first approach is a pressure-relaxation method that eliminates the upstream-acoustic waves by removing the term associated with the streamwise gradient of the pressure-perturbation shape function (Chang *et al.*, 1991; Haj-Hariri, 1994). It is an arguably valid approach provided that most of the spatial growth rate is included in the streamwise wavenumber instead of the shape function. Li & Malik (1996) showed that this stabilization technique allows reducing the minimum step size by two orders of magnitude. However, they also observed that neglecting the streamwise pressure term can affect the value of the computed growth rate in some flow cases. A second stabilization technique was later proposed by Andersson *et al.* (1998). Since the second-order terms are eliminated from the original physical equations when deriving the PSE, Andersson *et al.* (1998) argued that the second-order terms that stem from the truncation error of the implicit scheme must also be discarded. Hence, Andersson *et al.* (1998) proposed a new formulation of the PSE by adding a source term to the original equations. The goal is to damp the second-order truncation error and thus prevent the upstream-traveling waves to grow up to the leading order. Doing so, the minimum step size is drastically reduced and the physical problem remains unaltered. For more details about the PSE well-posedness and the stabilization techniques, the reader is referred to the recent work of Towne *et al.* (2019). In the present work, the stabilization technique proposed by Andersson *et al.* (1998) is used to solve the PSE.

3.5. Computational code and practical implementation

The present computational code is built upon the works of Groot (2013); Niessen (2017) and Groot (2018) that use a similar approach for solving flow-stability eigenvalue problems in the stationary frame of reference. The capabilities have nevertheless been extended in order to provide a tool that can solve:

- the Linear Stability Theory equations,
- the Parabolized Stability Equations,
- the two-dimensional streamwise stability problems (direct, discrete and continuous adjoint eigenvalue problems),
- the two-dimensional streamwise perturbation problem (initial-value problem),

for both compressible and incompressible flows. For compressible flows, the problems are solved for the pressure perturbation. However, the density perturbation is always computed a-posteriori to ease the interpretation of the results when considering the perturbation energy equation (see Chapter 2). Since the density formulation offers more meaningful results when it comes to energy transfer, future improvement of the present computational program should focus on implementing the density-based equations for both direct and adjoint problems.

The present tool can solve the initial-value and eigenvalue problems in frames of reference moving in the streamwise direction. When considering the initial-value problem, the two-dimensional temporal wave packets are decomposed into their frequency components by using a `Matlab` built-in Fast Fourier Transform algorithm. The spatial discretizations can be made independently for each direction with the Chebyshev-Gauss-Lobato pseudospectral or finite-difference methods. The differentiation matrix based on a finite-difference scheme can be central, forward or backward at arbitrary degrees of accuracy.

For both initial-value and eigenvalue problems, the core of the computational procedure consists in setting up the matrices $\boldsymbol{A}$, $\boldsymbol{L}$, and $\boldsymbol{B}$ with the appropriate boundary conditions. The different steps to construct these final matrices are:

(a) Build matrices $\boldsymbol{A}$, or $\boldsymbol{L}$, and $\boldsymbol{B}$ without boundary conditions:

  (1) Interpolation of the base-flow variables with `Matlab`'s spline interpolation routine onto the grid used for stability analyses,

  (2) Reshaping the base-flow coefficients in a stack-column vector according to equation (3.11) (two-dimensional problems only),

  (3) Multiplication of the base-flow coefficients with the differentiation matrices according to the linear system of equations to be solved,

(b) Enforce zero at node locations corresponding to boundaries, independently of boundary conditions and without reducing the matrix size,

(c) Impose homogeneous boundary conditions for velocity, temperature and, depending on the case/boundary location, pressure perturbations:

  (1) In matrix $\boldsymbol{A}$ for eigenvalue problems or in the right-hand-side matrix for initial-value problems, the coefficients corresponding to the boundaries are set to one for Dirichlet conditions while the coefficients of the pseudospectral differentiation matrices $\boldsymbol{D}_\xi$ or $\boldsymbol{D}_\eta$ are imposed for the Neumann conditions,

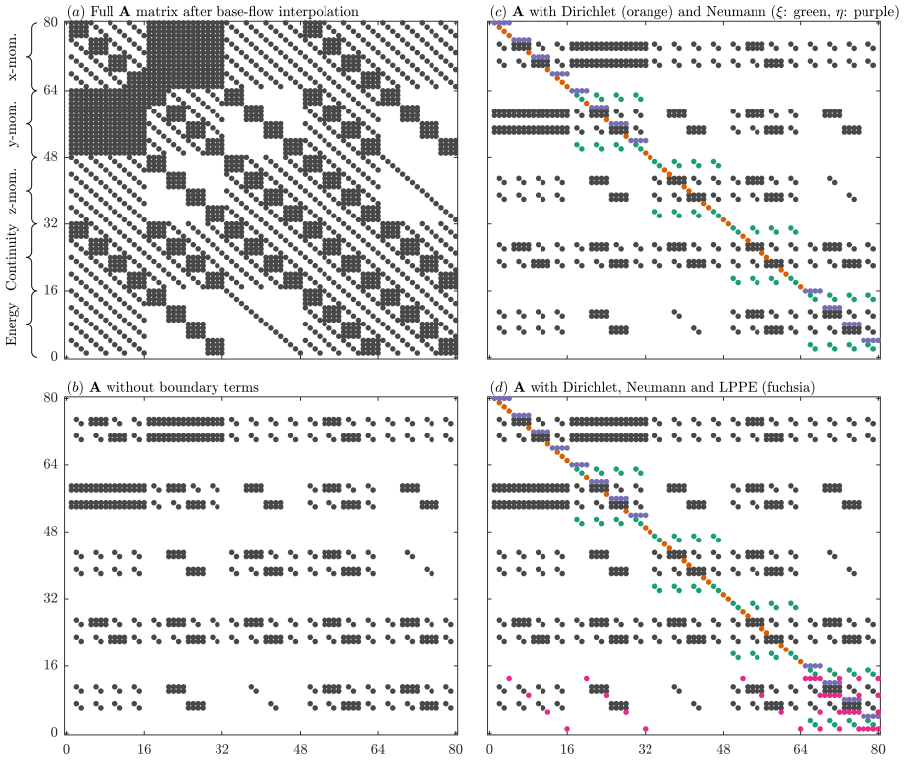

Figure 3.2: Matrix $\boldsymbol{A}$ with $[N_\xi, N_\eta] = [4,4]$ built for the stack-column vector $\tilde{\boldsymbol{q}} = [\tilde{u}, \tilde{v}, \tilde{w}, \tilde{T}, \tilde{p}]^{\mathrm{T}}$ from steps (*a*) to (*d*) described in the main text. Colored dots for Dirichlet (orange), Neumann ($\partial\cdot/\partial\xi = 0$ in green, $\partial\cdot/\partial\eta = 0$ in purple) and LPPE (fuchsia) boundary conditions.

(2) In matrix $\boldsymbol{B}$ for eigenvalue problem or in the left-hand-side matrix for initial-value problems, the coefficients at the boundaries remain zero,

(*d*) At the location where the pressure perturbation is not specified with Dirichlet or Neumann conditions, the compatibility condition (equation (2.38)) or the pressure Poisson equation (equation (2.40)) is imposed.

The aforementioned steps are illustrated in figure 3.2. In this example, various boundary conditions are used in order to illustrate the principle of the matrix construction on the matrix **A** and do not represent an actual physical case. In the wall-normal direction, homogeneous Dirichlet conditions (orange dots) are imposed at the wall for $\tilde{u}$, $\tilde{v}$, $\tilde{w}$ and $\tilde{T}$ and also at the freestream for $\tilde{w}$ and $\tilde{T}$. Wall-normal homogeneous Neumann conditions (purple dots) are imposed in the freestream for $\tilde{u}$, $\tilde{v}$ and $\tilde{p}$. In the streamwise direction, homogeneous Dirichlet boundary conditions are imposed for $\tilde{u}$ at the in-/outlet boundaries whereas streamwise homogeneous Neumann conditions (green dots) are imposed for $\tilde{v}$, $\tilde{w}$, $\tilde{T}$ and $\tilde{p}$. For the generalized eigenvalue problems, the discretized operators can be directly used in the solver. For the initial-value problems, the left-hand-side matrix is first LU-decomposed and the problems are then advanced in time iteratively.

References

ANDERSSON, P., HENNINGSON, D. S. & HANIFI, A. 1998 On a stabilization procedure for the Parabolic Stability Equations . *Journal of Engineering Mathematics* **33**, 311–332.

BERTOLOTTI, F. P. 1991 Linear and nonlinear stability of boundary layers with streamwise varying properties. PhD thesis, The Ohio State University.

CANUTO, C., HUSSAINI, M. Y., QUARTERONI, A. & ZANG, T. A. 2006 *Spectral methods. Fundamentals in single domains* . Springer.

CHANG, C.-L., MALIK, M., ERLEBACHER, G. & HUSSAINI, M. 1991 Compressible stability of growing boundary layers using parabolized stability equations. In *22nd Fluid Dynamics, Plasma Dynamics and Lasers Conference*, p. 1636.

FORNBERG, B. 1988 Generation of finite difference formulas on arbitrarily spaced grids. *Mathematics of computation* **51** (184), 699–706.

GROOT, K. J. 2013 Derivation of and simulations with BiGlobal stability equations. Master's thesis, Delft University of Technology.

GROOT, K. J. 2018 BiGlobal Stability of shear flows spanwise & streamwise Analyses. PhD thesis, TU Delft and von Karman Institute for Fluid Dynamics.

GROOT, K. J., SERPIERI, J., PINNA, F. & KOTSONIS, M. 2018 Secondary crossflow instability through global analysis of measured base flows. *Journal of Fluid Mechanics* **846**, 605–653.

HAJ-HARIRI, H. 1994 Characteristics analysis of the parabolized stability equations. *Studies in Applied Mathematics* **92** (1), 41–53.

LEHOUCQ, R. B., SORENSEN, D. C. & YANG, C. 1998 *ARPACK users' guide: solution of large-scale eigenvalue problems with implicitly restarted Arnoldi methods*. SIAM.

LI, F. & MALIK, M. R. 1996 On the nature of pse approximation. *Theoretical and Computational Fluid Dynamics* **8** (4), 253–273.

LI, F. & MALIK, M. R. 1997 Spectral analysis of parabolized stability equations. *Computers & fluids* **26** (3), 279–297.

MALIK, M. 1990 Numerical methods for hypersonic boundary layer stability. *Journal of Computational Physics* **86** (2), 376 – 413.

MOLER, C. & VAN LOAN, C. 2003 Nineteen dubious ways to compute the exponential of a matrix, twenty-five years later. *SIAM Review* **45**, 3–49.

NIESSEN, S. E. M. 2017 BiGlobal stability analysis: laminar shock-wave/boundary-layer interactions. Master's thesis, University of Liège, Faculty of Applied Sciences.

PATHRIA, D. 1997 The correct formulation of intermediate boundary conditions for runge–kutta time integration of initial boundary value problems. *SIAM Journal on Scientific Computing* **18** (5), 1255–1266.

RUIZ, P., SASTRE, J., IBÁÑEZ, J. & DEFEZ, E. 2016 High performance computing of the matrix exponential. *Journal of Computational and Applied Mathematics* **291**, 370–379.

SAAD, Y. 2011 *Numerical Methods for Large Eigenvalue Problems*. Society for Industrial and Applied Mathematics.

TOWNE, A., RIGAS, G. & COLONIUS, T. 2019 A critical assessment of the parabolized stability equations. *Theoretical and Computational Fluid Dynamics* **33** (3), 359–382.

WEIDEMAN, J. A. C. & REDDY, S. C. 2000 A MATLAB differentiation matrix suite. *ACM Transactions on Mathematical Software* **26** (4), 465–519.

WELFERT, B. D. 1997 Generation of pseudospectral differentiation matrices I. *SIAM Journal on Numerical Analysis* **34** (4), 1640–1657.

WRIGHT, T. G. & TREFETHEN, L. N. 2001 Large-scale computation of pseudospectra using arpack and eigs. *SIAM Journal on Scientific Computing* **23** (2), 591–605.

4

The incompressible flat-plate boundary layer

Laminar boundary layers are classical examples of flows that are slowly developing in the streamwise direction. Traditional methods such as LST and PSE exploit this slowly developing nature in order to chart the stability characteristics of this flow type, while accepting a model error. Even though the model error is small for slowly developing flows, it can be completely removed upon studying the stability of these flows with the BiGlobal approach. As mentioned in the introduction, the notorious domain dependency of the results presented in the literature, however, renders their interpretation questionable. To improve upon this aspect, this chapter applies the moving-frame methodology to the incompressible flat-plate boundary layer. The objective is to illustrate and discuss the underlying principle of the approach and then to demonstrate its effectiveness. In particular, reconstructing the neutral and amplification curves allows comparing the two-dimensional localized perturbations against the solution of the LST and PSE methods.

The present chapter is structured as follows. The base-flow computation and the numerical setup for stabilty analyses are presented in §4.1. The resulting eigensolutions obtained in the moving frame of reference are then studied in §4.2 with a particular focus on obtaining setup-independent, localized eigenfunctions. In this section, the behavior of the solutions as the speed of the reference frame approaches zero is also considered in order to possibly recover stationary-frame solutions. In §4.3, the temporal behavior of the flow disturbed with the moving-frame eigenfunctions is discussed. The amplification and neutral curves for the flat-plate boundary layer are reconstructed and then compared against the results of the LST and PSE methods. In §4.4, a Reynolds-Orr energy-budget analysis is proposed to highlight the main mechanisms characterizing the eigensolutions. To gain further insight into the working principle of the method, the global mode theory is used in §4.5 to reconstruct the moving-frame, two-dimensional global eigensolutions with the WKBJ approach. Finally, an intermediate conclusion is proposed in §4.6.

4.1. Base-flow computation and numerical setup

The most universal boundary layer is the Blasius flow (Blasius, 1908). Although it does not satisfy the incompressible Navier-Stokes equations exactly, it can be obtained to arbitrary precision and is independent of critical parameters of the numerical setup (e.g., streamwise

Table 4.1: Parameters for the flat plate boundary layer reference case (not rounded).

c_f/u_e	N_x	x_{in}/ℓ	x_{i1}/ℓ	x_{i2}/ℓ	x_{out}/ℓ	N_y	y_i/ℓ	y_{max}/ℓ
0.415	300	0.2×10^5	2.8×10^5	5.4×10^5	8.0×10^5	50	4.0×10^3	1.6×10^5

boundary conditions, leading-edge sharpness) that can be encountered when solving the full Navier-Stokes equations. Therefore, by eliminating all uncertainties related to the base flow, all effort can be concentrated on determining the numerical sensitivity associated with the global stability analysis.

The Blasius self-similar boundary-layer solution is computed at Mach number M = 0 with DEKAF (Groot *et al.*, 2018), a software for high-order computation of (in)compressible self-similar and developing boundary layers. The largest residual is related to the term $\partial^2\overline{U}/\partial y^2$ and equals $\mathcal{O}(10^{-15})$. The discretization is based on $N_\eta = 500$ nodes used in the wall-normal direction, yielding at most $\mathcal{O}(10^{-12})$ differences with the solution on a grid with $2N_\eta-1$ nodes. The x-derivatives of the base-flow quantities are determined with the spectral differentiation matrix used to discretize the two-dimensional stability problem.

The eigensolutions to the direct and adjoint stability problems (2.45) are obtained numerically on a domain that is truncated in the up- and downstream directions, at $x = x_{in}$ and $x = x_{out}$, and far from the flat plate at $y = y_{max}$ ($x = 0$ corresponds to the leading edge and $y = 0$ to the wall). At $y = y_{max}$, all perturbation variables are zeroed. The truncation boundaries at $x = x_{in}$ and $x = x_{out}$ are respectively referred to as the in- and outflow boundaries. The streamwise domain length is denoted by $L = x_{out} - x_{in}$. The literature presents several attempts in prescribing reasonable boundary conditions at the in- and outflow boundaries, see for instance Alizard & Robinet (2007), Rodríguez (2010, §5.4.3), Groot (2013, chapter 8) and Groot *et al.* (2015). The present goal is to ensure that the solutions are independent of all truncation boundary conditions through the use of the moving reference frame. Unless stated otherwise, homogeneous Neumann conditions are used at the in- and outflow boundaries. This allows identifying when the solutions become dominant at the boundaries and, as a consequence, when they do become affected by the specific domain choice.

The problem is discretized with Chebyshev collocation in both x and y. The bi-quadratic mapping is used in the x-direction, mapping one-third of the collocation points in-between the points x_{i1} and $x_{i2} > x_{i1}$, each lying within $[x_{in}, x_{out}]$. The values $x_{i1} = x_{in} + \frac{1}{3}(x_{out} - x_{in})$ and $x_{i2} = x_{in} + \frac{2}{3}(x_{out} - x_{in})$ are used for all flat-plate boundary layer results. The Malik mapping is used for the wall-normal direction y, mapping half the collocation nodes above and below y_i. Further details about the theoretical aspects of the numerical strategy can be found in Chapter 3.

Velocity and length scales are respectively made non-dimensional with the freestream speed u_e and the global length ℓ. Table 4.1 summarizes the parameters used for the selected reference case. To demonstrate the principle of the method and reconstruct the traditional neutral curve, considering only the case $\beta = 0$ for all computations is sufficient. However, because of the physical importance of three-dimensional instabilities, non-zero-β cases for the shock-wave/boundary-layer interaction are considered in Chapter 5. Note that having $\beta = 0$ and $\overline{W} = 0$ allows decoupling the z-momentum equation from the rest of the system of equations (2.45).

4.2. Localized eigensolutions in the flat-plate boundary layer

In this section, the direct and adjoint eigenvalue problems (2.45) formulated in the moving frame of reference are solved. The resulting eigenvalue spectra and eigenfunctions are presented in §4.2.1 for the reference case. The sensitivity of the localized solutions with respect to the numerical setup is addressed in §4.2.2 and a specific discussion about the influence of the domain length on the spectrum is proposed in §4.2.3. The effect of the moving-frame speed on the eigensolutions is illustrated in §4.2.4 and the choice for $c_f/u_e = 0.415$ as a reference-case frame speed is justified. Finally, an attempt to recover converged eigensolutions in the stationary frame of reference is presented in §4.2.5.

4.2.1. Spectra and eigenfunctions

The spectrum and several direct $\tilde{u}$ and adjoint $\tilde{u}^\dagger$-eigenfunctions of interest are shown in figure 4.1 for the reference case with $c_f/u_e = 0.415$. As demonstrated later in §4.2.4, the most unstable eigensolution found at this frame speed has the largest growth rate over all localized solutions found in the c_f-parameter space. The spectrum is symmetric about the ω_i-axis, because the eigenvalue problem has real coefficients. The attention is thus restricted to the most unstable eigenvalues with negative ω_r-values (every second one is marked by a red cross in figure 4.1(*b*)). The reference case and eigenmode selection are justified in §4.2.4.

The modes of interest, i.e., the non-spurious modes with the largest ω_i in the boundary layer, form a branch with 3 sub-branches: the top-left 'main' branch, housing modes labeled 1 to 6, the rightward 'side' branch, in which modes 7 and 8 reside, and the 'downward' branch, consisting of the modes with index 9 and greater. The downward branch appears to continue into the stable half-plane indefinitely. The selected direct eigenmodes for the streamwise velocity shown in figure 4.1(*c–h*) represent wave packets: the eigenfunctions decay at least exponentially toward all truncation boundaries. As illustrated in figure 4.2(*a–c*) for the second most unstable mode at $c_f/u_e = 0.415$, this eigenfunction decay is observed for all components, such that $\tilde{u}$, $\tilde{v}$ and $\tilde{p}$ are all wave packets. If the eigensolutions are not localized, they cannot be treated as if they represent wave packets and should rather be considered as wave trains. Modes that belong to none of the three branches are discarded since they are observed to be either dominant outside the boundary layer and are stable (freestream modes) or physically spurious solutions.

The spectrum inevitably contains physically spurious solutions associated with infinite eigenvalues because no temporal derivative acts on the pressure in the incompressible-flow formulation of the eigenvalue problem (Christodoulou & Scriven, 1988). These modes represent the pressure perturbation field that instantaneously reacts to any change in the velocity perturbation field. Nevertheless, these solutions highly depend on the number of grid points and identifying them can be done without effort through sensitivity analyses. Note that the aforementioned *physically* spurious are different from *numerically* spurious modes that, instead, are underresolved solutions because of the spatial discretization. As shown later, the eigensolutions corresponding to side and downward branches depend on both grid density and domain length and, thus, according to the definition of Boyd (2001), could be classified as numerically spurious modes.

The speed at which wave packets propagate downstream is the so-called group speed, denoted c_g, and is defined by equation (2.67). Assuming that the eigensolutions are valid for small, non-zero times, the shape of the perturbation that is represented is exactly preserved as it translates downstream with the frame speed. This was illustrated with an arbitrary function in §2.6.2. Therefore, if this assumption is valid, which is demonstrated in §4.3 for the present boundary layer, the group speed of the represented wave packet is exactly equal

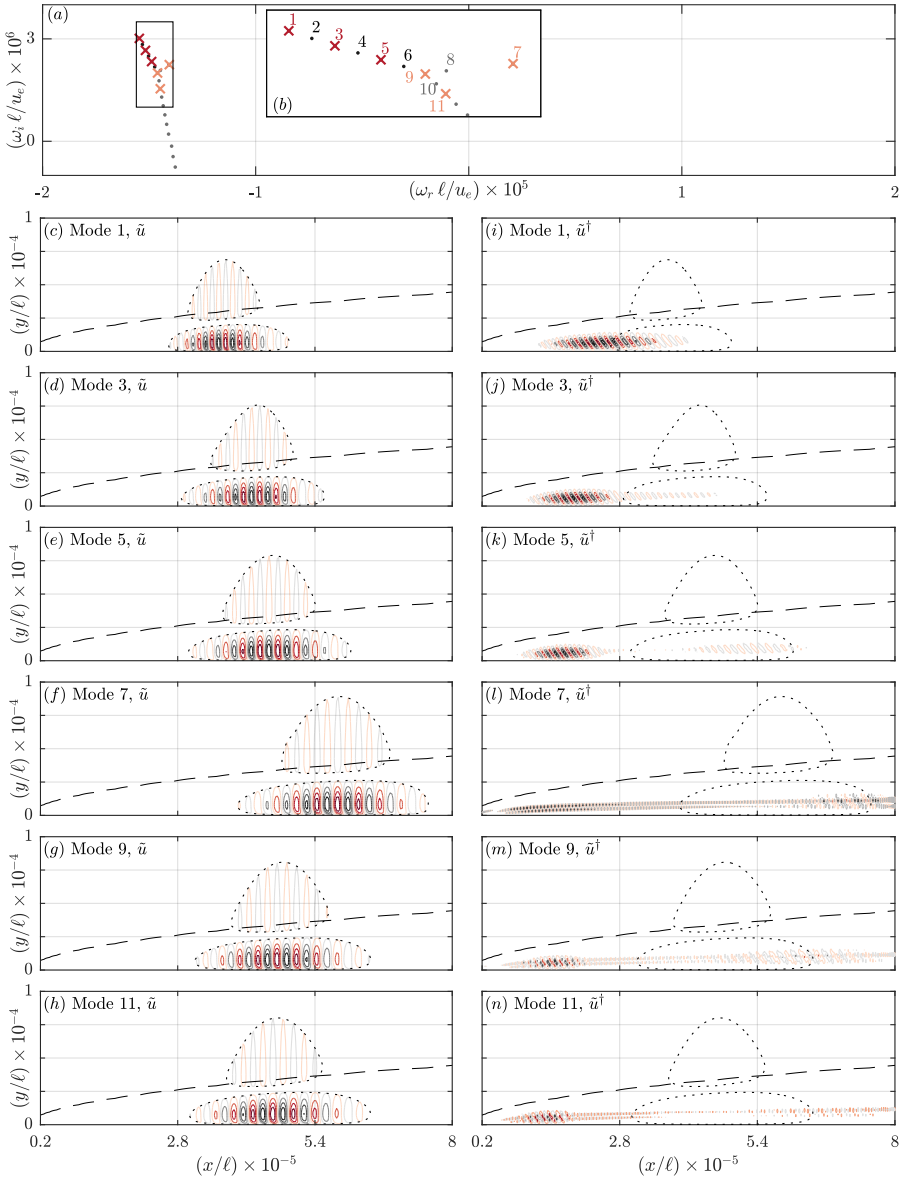

Figure 4.1: (*a*) ω-spectrum for the reference case $c_f/u_e = 0.415$ with (*b*) zoom on the black rectangle in (*a*). Converged and unconverged solutions are indicated by dark and light colors, respectively. (*c–n*) isocontour of $|\tilde{u}|/|\tilde{u}|_{\max}$ (dotted black, level: 1/9), (*c–h*) isocontours of direct eigenfunctions $\mathscr{R}\{\tilde{u}\}/|\tilde{u}|_{\max}$ and (*i–n*) adjoint eigenfunctions $\mathscr{R}\{\tilde{u}^\dagger\}/|\tilde{u}^\dagger|_{\max}$ (colored lines, from minimum (gray) to maximum (red) with $\Delta = 2/9$) corresponding to the eigenvalues identified by crosses in (*a*,*b*) for increasing label index in (*b*) from the top to bottom row. Boundary layer height indicated by $\overline{U} = 0.99u_e$-isocontour (dashed).

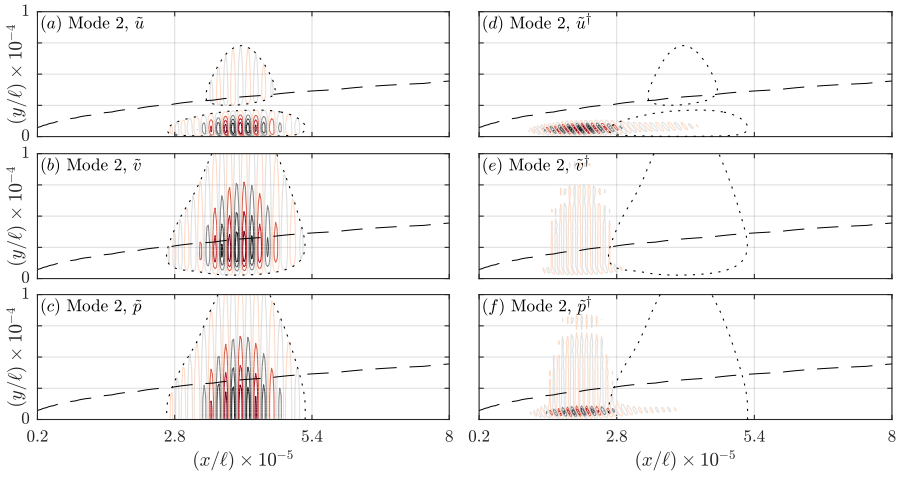

Figure 4.2: (*a–c*) Direct and (*d–f*) adjoint velocity and pressure perturbation fields for the second most unstable mode at $c_f/u_e = 0.415$. Isocontour of (*a*,*d*) $|\tilde{u}|/|\tilde{u}|_{\max}$, (*b*,*e*) $|\tilde{v}|/|\tilde{v}|_{\max}$ and (*c*,*f*) $|\tilde{p}|/|\tilde{p}|_{\max}$ (dotted black, level: 1/9). Isocontours of direct eigenfunctions (*a*) $\mathscr{R}\{\tilde{u}\}/|\tilde{u}|_{\max}$, (*b*) $\mathscr{R}\{\tilde{v}\}/|\tilde{v}|_{\max}$, (*c*) $\mathscr{R}\{\tilde{p}\}/|\tilde{p}|_{\max}$ and adjoint eigenfunctions (*d*) $\mathscr{R}\{\tilde{u}^\dagger\}/|\tilde{u}^\dagger|_{\max}$, (*e*) $\mathscr{R}\{\tilde{v}^\dagger\}/|\tilde{v}^\dagger|_{\max}$ and (*f*) $\mathscr{R}\{\tilde{p}^\dagger\}/|\tilde{p}^\dagger|_{\max}$ (colored lines, from minimum (gray) to maximum (red) with $\Delta = 2/9$). Boundary layer height indicated by $\overline{U} = 0.99u_e$-isocontour (dashed).

to the frame speed. This implies that a guess for the frame speed can be obtained from the knowledge of the typical group speed for the instability mechanism of interest. Gaster & Grant (1975, figure 6) showed that a wave packet initiated by a pulse in a boundary layer has a *group* speed $c_g \approx 0.4u_e$. If no group speed is known, it is usually close to the typical *phase* speed. In particular, for Tollmien-Schlichting waves, it is known that $c_{ph} = \omega_{f,\tilde{q}}/\alpha_{\tilde{q},r} \lesssim 0.4u_e$ White (1991). A further discussion about the phase speed and the critical layer, i.e., the wall-normal locations where the phase speed corresponds to the streamwise base flow velocity, is proposed in §4.2.4 where the influence of the frame speeds on the solution is discussed.

The adjoint eigenfunctions that are associated with localized direct eigenfunctions, shown in figures 4.1(*i–n*) and figure 4.2(*d–f*), do not all decay toward the boundaries, depending on which branch they belong to. In the case of the main branch, all direct and adjoint eigenfunctions display the aforementioned decay toward the boundaries. These solutions are shown to be independent of the numerical setup in §4.2.2. In contrast, the adjoint eigenfunctions corresponding to the side and downward branches always interact with the inlet and outlet boundaries, even though the corresponding direct eigenfunctions exhibit the appropriate decaying behavior. This implies that localized direct eigenfunctions are insufficient indicators for the independence of the numerical setup. It is actually found that the interaction of the adjoint, direct or both types of eigenfunctions with the boundaries always makes the eigensolutions sensitive to the boundary conditions and domain length. Hence, in this flow case, all solutions that belong to the side and downward branches depend on the numerical setup. A further quantification of the numerical sensitivity is proposed in the following section. Note that, although non-localized solutions are not converged and thus do no represent physical solutions, they are included here to provide a complete overview of the eigensolutions obtained with the moving frame of reference.

Table 4.2: Mode properties and relative errors ($\epsilon = |\omega_{\text{ref}} - \omega|/|\omega_{\text{ref}}|$) in the eigenvalue for the reference parameters given in Table 4.1 with respect to the parameter changes: $x_{\text{out}}/\ell = 7.0 \times 10^5$ (fixing the density N_x/L); $N_x = 260$; the use of homogeneous Dirichlet in-/outflow boundary conditions; and $y_{\max}/\ell = 1.4 \times 10^5$ (fixing $N_y = 50$ and $y_i = 4.0 \times 10^3$). Two modes along the main branch for $c_f/u_e = 0.415$, labeled in figure 4.1(*a*) and most unstable mode (main branch) for $c_f/u_e = 0.47$ (figure 4.5(*a*)). The reported digits are truncated (not rounded) and those that are tainted by the largest reported error are underlined.

	c_f/u_e	0.415	0.415	0.470
Mode properties	Mode#	1	5	1
	$\omega_r \ell/u_e$	$-1.54607445982 \times 10^{-5}$	-1.48826×10^{-5}	$-3.84287728 \times 10^{-5}$
	$\omega_i \ell/u_e$	$+3.0143827834 \times 10^{-6}$	$+2.33523 \times 10^{-6}$	$-3.07160739 \times 10^{-7}$
Relative $\lvert\omega\rvert$-errors	ϵ_L	1.4×10^{-4}	5.9×10^{-4}	1.5×10^{-5}
	ϵ_{N_x}	9.3×10^{-11}	2.5×10^{-7}	3.1×10^{-10}
	ϵ_{BC}	1.5×10^{-10}	2.0×10^{-6}	1.5×10^{-9}
	$\epsilon_{y_{\max}}$	2.3×10^{-4}	2.2×10^{-4}	3.7×10^{-4}

4.2.2. Sensitivity to the numerical setup

The numerical dependency on the setup parameters is summarized in table 4.2 for two modes at $c_f/u_e = 0.415$ along the main branch and labeled in figure 4.1(*a*) and for the most unstable mode at $c_f/u_e = 0.47$ (see later figure 4.5(*a*)). The relative error ϵ in the eigenvalue's magnitude is determined by varying the following numerical aspects independently: the streamwise domain length (ϵ_L, fixing the relative resolution N_x/L), the resolution in the streamwise direction (ϵ_{N_x}), the boundary conditions (ϵ_{BC}) and the domain height ($\epsilon_{y_{\max}}$, fixing the resolution in the boundary layer by keeping N_y and y_i constant). Overall, relative errors of $\mathcal{O}(10^{-4})$ are attained. When representing convective instability mechanisms with the streamwise BiGlobal approach, these small errors are unprecedented; spectra computed in the stationary frame of reference presented in the literature experienced $\mathcal{O}(1)$ errors while changing the streamwise domain length. Before elaborating further, it should be mentioned that $\epsilon_{y_{\max}}$ is the largest contributor to the overall eigenvalue error. This suggests that, with the issues related to the streamwise direction being tackled, $\epsilon_{y_{\max}}$ now features the slowest convergence rate. Accordingly, the reference case and the convergence study were selected by reducing $\epsilon_{y_{\max}}$ to a reasonably low level and then by using that level as a target for the other errors.

The error introduced by the finite domain length, ϵ_L, representing a primary source of error in the literature (Ehrenstein & Gallaire, 2005; Alizard & Robinet, 2007; Åkervik *et al.*, 2008), can be made smaller than $\epsilon_{y_{\max}}$ using the moving frame of reference. Altering the resolution in the streamwise direction yields a very small error, ϵ_{N_x}, due to the use of the spectral scheme with $N_x = 260$ to 300 nodes. It should be emphasized that these numbers of nodes are not at all necessary to obtain converging solutions for the reference case; using $N_x = 100$ nodes for mode '1' results in an error comparable to $\epsilon_{y_{\max}}$. The truncation boundary conditions represent the other primary uncertainty throughout the literature. By changing from homogeneous Neumann to homogeneous Dirichlet conditions, a remarkably small ϵ_{BC} is obtained, that is equivalent to ϵ_{N_x}.

These results conclusively demonstrate that the obtained solutions are independent of the numerical setup. The negligible influence of the streamwise domain length and trunca-

tion boundary conditions on the eigensolutions of the main branch is observed to be directly related to the small amplitude of both the direct and adjoint eigenfunctions at the truncation boundaries. The spatial decay of the eigenfunctions within the domain allows placing the truncation boundaries at a *far enough, but finite* distance, so that the eigeninformation is virtually unaffected.

Only the modes along the main branch are found to converge; the side and downward branches persistently depend on the domain length. Although the direct eigenfunction decays toward the boundaries for the side and downward branches, it is observed that the adjoint eigenfunction does not. Figure 4.1(l,m) shows that the adjoint eigenfunctions corresponding to modes 7 and 9 are dominant at the boundary, for example. Therefore, it is suspected that this prevents the solution from converging while increasing L. The dependency of the side and downward branch on the domain length is further illustrated and discussed in subsection §4.2.3. Due to their independence of the computational setup, only the main-branch eigensolutions are considered in §4.3 to obtain the perturbation-amplification information (e.g., amplification or neutral curves) in a given region in space.

The magnitude of the direct and adjoint eigenfunctions at the boundaries is quantified with the c_f-correction term, derived in equation (2.64), and is shown in figure 4.3 for varying frame speeds and two distinct domain lengths. For sake of clarity, only the values at the inlet boundary are shown in figure 4.3 because it is found that the c_f-correction terms at the in- and outlet locations have the same order of magnitude and are highly correlated. The Pearson coefficients are 0.999 for both the short- and long-domain cases. This strong correlation indicates that, as the wave packet interferes with *one* boundary, an artificial structure emerges from the *opposite* boundary. By requiring the c_f-correction term to be several orders of magnitude smaller than ω_i, the main-branch solutions can be uniquely identified from the rest of the (entire) spectrum.

As the frame speed is increased above $c_f/u_e \approx 0.41$, the c_f-correction term for both the direct and adjoint eigenfunctions corresponding to the most unstable solutions strongly diminishes at both the in- and outlet, implying that the eigenfunctions become localized in the interior of the domain. The amplitude of the adjoint eigenfunctions at the truncation boundaries decreases at a slower rate than that of the direct eigenfunctions when frame speed increases, which is likely the consequence of the more upstream location of the former functions. The adjoint solutions are representative of the region where the system is most sensitive to external variations (Schmid & Brandt, 2014). This suggests that the decay of both the direct and adjoint eigenfunctions toward the truncation boundaries is required for the eigensolution to be independent of the numerical setup. Figure 4.3 demonstrates that this can be achieved for a fixed domain length if a large enough frame speed is used. Comparing the short-domain (panels (a,c)) against the long-domain solutions (b,d) also indicates that a lower frame speed can be used if the domain length is increased. However, solutions at high frame speeds require a finer grid in the streamwise direction than at low frame speeds because the wavelength of the eigenfunctions decreases. A compromise must thus be found between grid resolution and domain length. This is further discussed in subsection §4.2.5.

4.2.3. Dependency on the domain length

It has just been shown that, for a fixed long domain, the eigenfunctions corresponding to several eigensolutions can be localized within the domain. These solutions are always found to belong to the main branch, while the side and downward branches persistently depend on the domain length. The displacement of these two branches with respect to the outlet

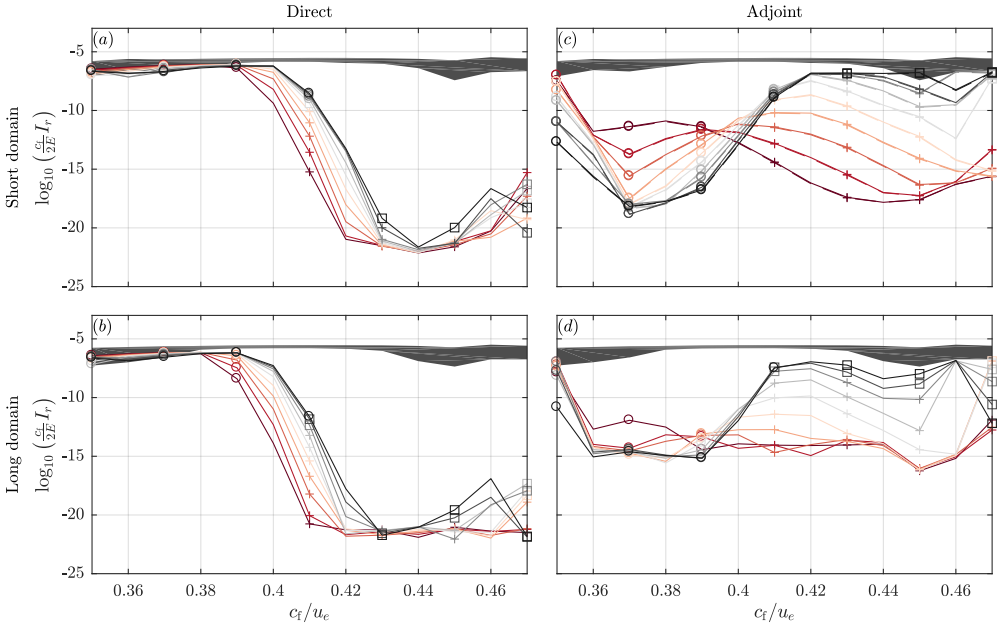

Figure 4.3: Magnitude of the c_f-correction term in equation (2.64) at $x = x_{in}$ for the direct (a,b) and adjoint (c,d) eigenfunctions with domain length (a,c) $L/\ell = 7.8 \times 10^5$ and (b,d) 9.3×10^5. Increasing mode indices, as defined in figure 4.1(a), are indicated with line colors running from red to gray. Modes that are classified as belonging to the main, side and downward branches are indicated with symbols +, □ and ○, respectively. The gray patch indicates $\log_{10}|\omega_i|$ for all considered modes.

location x_{out}, i.e., the domain length, is shown in figure 4.4.

For more downstream location of the outlet boundary x_{out}, i.e., for longer domain, the side branch moves approximately *linearly* down-/rightward, and thus likely never converges. The downward branch has a more complicated pattern, especially at the junction with the two other branches. Figure 4.4 shows that modes, that are originally positioned within the downward branch, merge either with the side or with the main branch. When a mode moves into the main branch, both adjoint and direct eigenfunctions attain a small amplitude at the truncation boundaries and this enables convergence with respect to the domain length. Hence, although the side and downwards branches can be barely distinguished at the junction, the main branch is easily identified since the eigensolutions are independent of the domain length. This behavior of the spectrum suggests that more and more main-branch modes can be resolved by extending the domain. Note that merely translating the domain downstream is not appropriate, because the adjoint eigenfunctions corresponding to these modes reach farther and farther upstream.

From these observations it can be concluded that, although still not corresponding to converged solutions, the side and downward branches could likely be moved to an arbitrarily stable location in the spectrum ($\omega_i < 0$) when using a sufficiently large domain in the streamwise direction. However, using a large domain is computationally expensive and it is shown in §4.3 that practical stability results, i.e., the amplification and neutral curves, can be obtained with only one localized eigensolution, i.e., one eigensolution of the rapidly converging main branch. Hence, in practice, it is not necessary to increase the domain length to resolve stable side and downward branches.

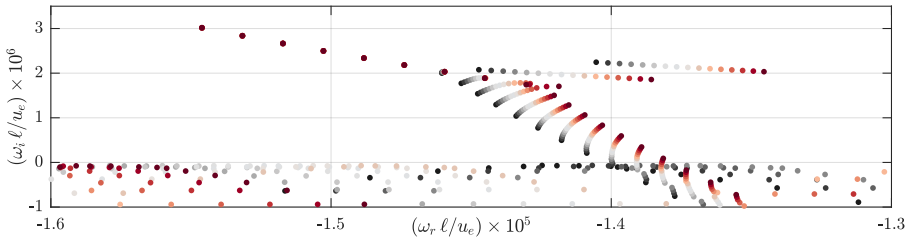

Figure 4.4: ω-spectrum for the reference case $c_f/u_e = 0.415$ for a varying outlet location from $x_{out}/\ell = 8\times10^5$ (black) to 9.5×10^5 (red) with steps of $\Delta x/\ell = 0.1\times10^5$ indicated by color scale and with the streamwise grid density fixed to $N_x/L = 1/2600$.

4.2.4. Dependency on the speed of the moving frame of reference

The frame speed is the unique free parameter to select prior to solving the eigenvalue problems (2.45) and its effect on the spectrum can be estimated through the Doppler formula given by equation (2.54). The Doppler effect dictates that the frequency ω_r should decrease with respect to $\omega_{f,r}$ when c_f increases. This follows from the real part of equation (2.54) by considering the positive values $\omega_{f,r}$ and $\alpha_{\tilde{q},r}$ of solutions in the stationary frame of reference. Note that, since the spectrum is symmetric about the ω_i-axis, the choice of either positive or negative $\omega_{f,r}$ is actually arbitrary and every ω has a counterpart with the eigenvalue $-\omega^*$. Upon substituting either solution back into the perturbation ansatz and taking the real part (see equation (2.11)), they represent the same solution and hence carry an identical physical interpretation. For the sake of consistency with the traditional treatment of stationary-frame eigensolutions, negative ω_r are considered. Figure 4.5 shows that the considered negative-ω_r solutions move to more negative values as the frame speed is increased, in agreement with the Doppler effect. Furthermore, the temporal growth rate ω_i also depends on the frame speed; figure 4.5(*a*) shows an arc-shaped movement of the branches. The maximum ω_i-value is attained at $c_f/u_e = 0.415$ approximately, which motivated the choice of this value as reference case.

By increasing c_f, the direct and adjoint eigenfunctions both move upstream, but at different rates with respect to the frame speed. This is depicted in panels (*b*–*f*) and (*g*–*k*) of figure 4.5, where the dotted lines indicate the 1/9 level of the absolute value of the direct $\tilde{u}$-eigenfunction. The different rate of displacement for the adjoint and direct eigenfunctions cause them to overlap closely for a limited range of frame speeds. Furthermore, while the direct (and adjoint) eigenfunctions move upstream for increasing c_f, the streamwise extent of the eigenfunctions decreases and so does the streamwise wavelength. These variations are expected because the boundary layer becomes thinner when approaching the leading edge. As a consequence of the smaller wavelength, $\alpha_{\tilde{q},r}$ in equation (2.54) increases and the frequency ω_r thus changes faster for larger c_f. This can be observed in figure 4.5(*a*).

Because the frame speed influences $\alpha_{\tilde{q},r}$ and ω_r, it has also an impact on the phase speed $c_{ph} = \omega_{f,\tilde{q}}/\alpha_{\tilde{q},r}$, that can be related to the critical layer. The concept of the critical layer has been detailed by Lin (1944) and is defined as the location where the phase speed corresponds to the streamwise velocity of the base flow. Since the region around the critical layer has a high sensitivity to external forcing (Tissot *et al.*, 2017), convective instability mechanisms receive their perturbation energy in this region. As illustrated in figure 4.5(*c*–*f*), the present results corroborate this behavior because the critical layer lies at the wall-normal maximum of the eigenfunctions. Furthermore, for all cases, the critical layer is always located slightly below the isoline $\overline{U} = c_f$, that separates the moving-frame base flow into an

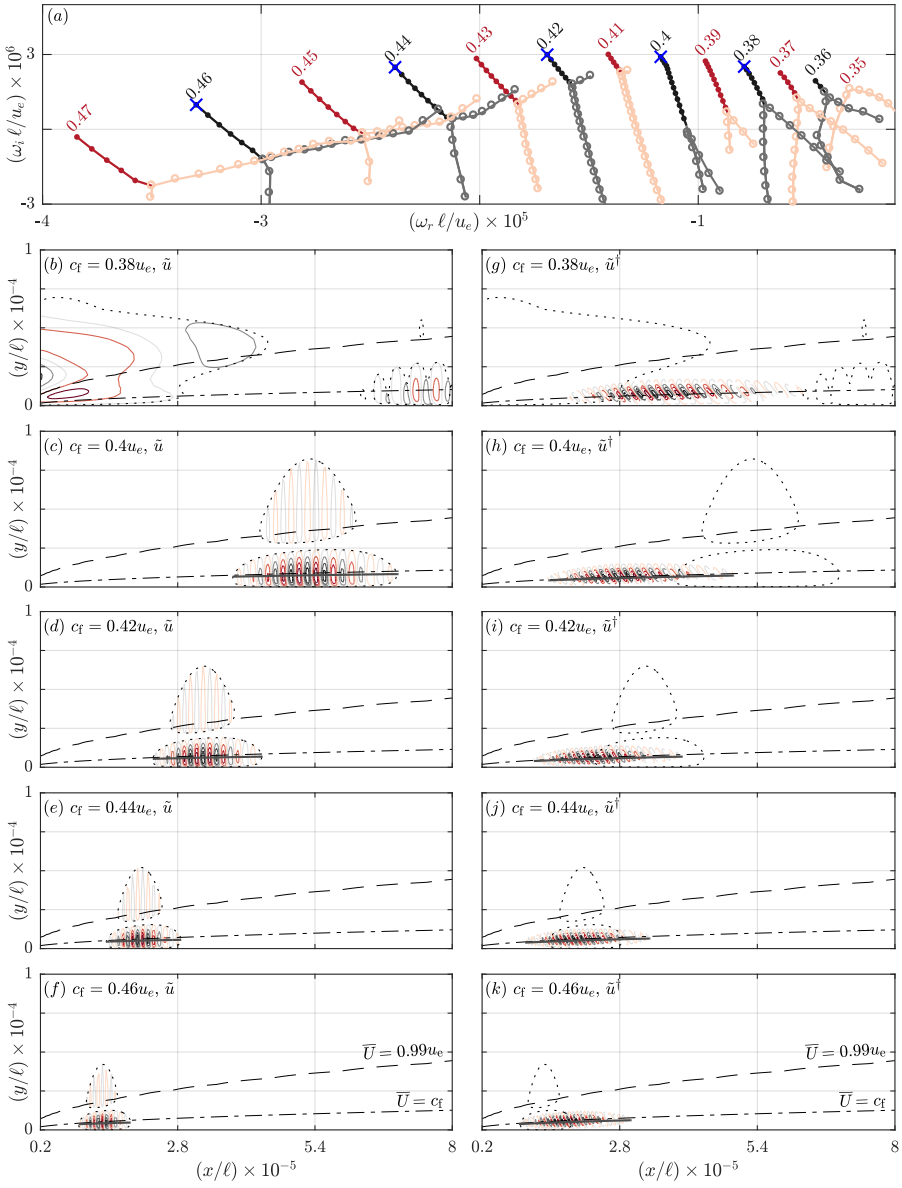

Figure 4.5: (*a*) ω-spectrum for different frame speeds from $c_f/u_e = 0.35$ to 0.47 with $\Delta c_f/u_e = 0.01$. Dots for main branch (converged solutions) and light-colored circles for downward and side branches (unconverged solutions). (*b–k*) isocontour of $|\tilde{u}|/|\tilde{u}|_{\max}$ (dotted black, level: 1/9). (*b–f*) isocontours of $\mathscr{R}\{\tilde{u}\}/|\tilde{u}|_{\max}$ (colored lines, from minimum (gray) to maximum (red) with $\Delta = 2/9$) corresponding to the most unstable eigenvalues, identified by blue crosses in (*a*), for ascending frame speed from the top to bottom row. (*g–k*) isocontours of $\mathscr{R}\{\tilde{u}^\dagger\}/|\tilde{u}^\dagger|_{\max}$(colored lines, from minimum (gray) to maximum (red) with $\Delta = 2/9$) corresponding to direct counterpart (*b–f*, respectively). Boundary layer height indicated by $\overline{U} = 0.99u_e$-isocontour (dashed). Dash-dotted lines and thick gray lines indicate $\overline{U} = c_f$-isocontour and the moving-frame critical layer ($c_{ph} = (\overline{U} - c_f)$), respectively.

upper region of downstream advection and a lower region of upstream advection. Given the location of the critical layer, the perturbation energy of the moving-frame eigenfunctions is thus generated in the region of upstream base-flow advection. This suggests that the localization of the eigenfunctions in the streamwise direction is made possible by having a finite upstream-traveling flow region, which is introduced by the moving frame of reference. Finally, because the critical layer is located slightly below the c_f-isoline, higher frame speeds induce more upstream locations of the eigenfunctions.

While increasing $c_f/u_e \geq 0.415$ results in longer main and side branches, decreasing $c_f u_e < 0.415$ yields the side branch to coalesce with the main branch. The main branch thus includes less eigenvalues when the frame speed decreases such that, when $c_f/u_e \leq 0.4$, the side and main branches completely merge into the downward branch. At this point, only the downward branch exists and splits into two parts further down the spectrum. Simultaneously, the eigenfunctions move downstream, at different rates for the direct and the adjoint, and have a longer spatial extent. When the direct eigenfunction approaches the outflow boundary, i.e., when the level $|\tilde{u}|/|\tilde{u}|_{\max} = \mathcal{O}(10^{-3})$ is attained at the boundary, it suddenly latches onto the outflow boundary. Simultaneously, an artificial structure emerges from the *in*flow boundary. This behavior is quantified with the c_f-correction term from equation (2.64). The magnitude of this correction was given for all considered modes and frame speeds in figure 4.3. Again, it shows that the side and downwards branches are only artifacts of the truncation boundary conditions that could be resolved, i.e., could merge into the main branch (see figure 4.4), by increasing the domain length while maintaining a sufficient resolution. When c_f/u_e approaches 0.35, the splitting point of the downwards branch moves upwards in the spectrum, that ultimately displays an arc-branch shape, as described by Lesshafft (2017). At this point, the latching tail from the inlet reaches the downstream structure, overwhelming the solution throughout the entire domain; all dynamics are then dominated by the artificial truncation boundary conditions. As also encountered in the aforementioned literature, solutions displaying this feature are strongly affected by the artificial boundary conditions, domain size and discretization in the x-direction. Despite changes in the process by which the downward branch splits and how the eigenfunctions interact with the boundary, applying finite-difference schemes in the streamwise direction also results in artificial structures that span the entire domain at $c_f/u_e = 0.35$. The results of Alizard & Robinet (2007, §IV.B.2, for $c_f = 0$, i.e., obtained in the stationary frame of reference) suggest that the arc-shaped spectra presently obtained for too small c_f approach a continuum as the streamwise domain length tends to infinity. Numerous analyses presented in the literature are performed in the stationary reference frame and result in arc-shaped spectra. The present analysis suggests that the domain truncation has a non-negligible artificial impact on these results.

The main-branch adjoint eigenfunctions also move downstream with an increasing spatial extent when the frame speed decreases but do not interact with the truncation boundary as the direct eigenfunctions do. Instead, the adjoint eigenfunctions converge to a fixed location as the frame speed decreases, without actually losing their localized nature. This could at first suggest that the adjoint problem could support domain-independent solutions, while the direct problem does not. This is unfortunately not the case. In particular, although the adjoint solution remains localized for a small enough frame speed, this is not sufficient to ensure a converged spectrum. In fact, an increase (decrease) of the domain length causes the adjoint eigenfunctions to move downstream (upstream), if the domain cannot accommodate the direct eigenfunctions. Note that the reverse situation (direct eigenfunctions decay, adjoint eigenfunctions reach one domain boundary) was observed for the side- and downward-branch solutions. The decay of either the direct or adjoint eigenfunctions

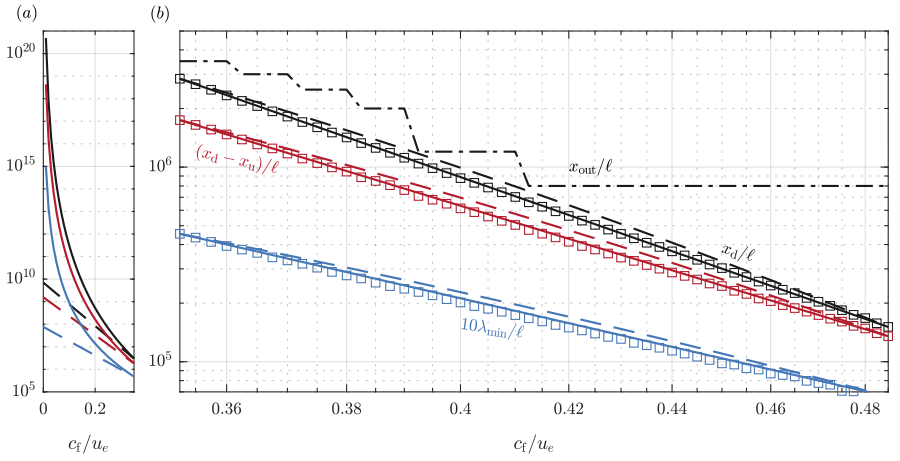

Figure 4.6: For the most unstable $\tilde{u}$-eigenfunction: downstream location (x_d, black), streamwise extent ($x_d - x_u$, red) and minimum wavelength ($10 \times \lambda_{min}$, blue) of the wave packet versus c_f. Measured values (symbols), power (solid lines) and exponential (dashed) fits and outflow boundary x_{out} (dash-dotted). (*a*) Trend-extrapolation as $c_f \to 0$ (minimum: $0.025u_e$) and (*b*) data and fits.

alone is clearly not sufficient to ensure a domain-independent solution; the current observations indicate that both need to decay sufficiently toward the truncation boundaries. To conclude, when keeping the reference domain length fixed, a large enough c_f-value is required to prevent the direct and adjoint eigenfunctions from reaching the outlet truncation boundary and eliminate the unwanted dependency on the numerical setup. Nevertheless, as the wavelength of the eigenfunctions decreases with the frame speeds, a denser grid in the streamwise direction is required to accurately resolve the solutions. This is further discussed in the next subsection.

4.2.5. The frame-speed limit $c_f \to 0$

Previous analyses suggest that the direct eigenfunctions can propagate further downstream if c_f is further decreased while increasing the domain length. Attempting to recover domain-independent solutions for the stationary reference frame thus sounds reasonable. To determine if this is possible, the location of the wave packets with respect to the frame speed is monitored. The boundary-interaction process is from now on identified by the dominant emergence of an artificial structure at the boundary opposite to the boundary with which the wave packet collides. Besides corresponding to a large magnitude of the c_f-correction term with respect to ω_i, from equation (2.64), the boundary-interaction process is observed when the $\tilde{u}$-eigenfunction attains at the outflow boundary an $\mathcal{O}(10^{-3})$ relative magnitude to its absolute maximum value for the reference domain length. Hence, the most up- and downstream position of the wave packet representing the $\tilde{u}$-eigenfunction, x_u and x_d, are respectively defined to be the first and last streamwise positions where this level is measured. It should be noted that the relative $\tilde{u}$-magnitude indicative of boundary-interaction can change significantly for different boundary/flow conditions. Furthermore, the minimum wavelength λ_{min} (represented by the real and imaginary part of $\tilde{u}$) for $x \in [x_u, x_d]$ is measured. The domain length is increased (fixing N_x/L) by displacing, in the downstream direction, the outlet boundary at a faster rate than the inlet boundary in order to capture only the most unstable solution along the main branch. Two different displacement rates of

Table 4.3: Fitting parameters for x_d, $x_d - x_u$ and λ_{min} of the wave packet: p in ac_f^p for the power law, ε in $b10^{\varepsilon c_f}$ for the base-10 exponential law, the Pearson correlation coefficients evaluated for all data points are given in brackets.

	x_d	$x_d - x_u$	λ_{min}
Power law	−9.0 (0.9999)	−7.9 (0.9998)	−5.8 (0.9995)
Exponential law	−9.5 (0.9979)	−8.2 (0.9981)	−6.1 (0.9972)

the in- and outlet boundaries are used to capture both the direct and adjoint eigenfunctions that, as illustrated in figure 4.5, were found to move at two different rates with respect to the frame speed. The measured variation of $x_d - x_u$, x_d and λ_{min} with c_f is shown in figure 4.6(*b*); all increase with decreasing c_f. Their growth rates are quantified by fitting a power law and an exponential law on data points at $c_{f,min}$ and $c_{f,max}$ in figure 4.6. The resulting parameters are reported in Table 4.3. Based on the results that could be obtained with the available computational resources, significantly larger correlations were found for the power law.

These data-driven extrapolations indicate that all quantities become extremely large when $c_f \to 0$, which renders the numerical problem barely tractable in the limit of the stationary frame of reference. This can be explained as follows. As stated by Groot & Schuttelaars (2020), the advection term of the stability equations induces an exponential spatial growth of the direct eigenfunctions. Lowering the frame speed thus increases the contribution of the streamwise advection term in stability equations and the eigenfunctions thus rapidly reach large amplitude at the truncation boundaries. Generally speaking, this advection-induced growth makes the stationary frame problem untractable. Furthermore, λ_{min} increases at a much lower rate than $x_d - x_u$. Therefore, both the number of points in the streamwise direction and the domain length have to be increased as $c_f \to 0$, so that the problem is more computationally demanding when c_f becomes small.

4.3. Finite-time evolution of wave packets

In the following, the main-branch eigensolutions obtained in the moving frame of reference are introduced into the initial-value problem. First, it is verified that they are valid in an instantaneous sense and that they can be used as initial condition. This property of the eigensolutions implies that inadvertent transients are avoided in the initial-value problem. Secondly, upon time-marching for a large enough time and Fourier transforming the wave packets, the most important stability-theory results, i.e., neutral and individual-frequency amplification curves, are recovered. This illustrates how the proposed methodology can be used in practice.

4.3.1. Instantaneous characteristics of wave-packets

In the stationary frame of reference, the eigeninformation is representative of the long-time dynamics. In case convective perturbations are considered, the asymptotically-long-time behavior is arguably irrelevant in describing perturbations. In fact, they will leave the region of interest (Groot & Schuttelaars, 2020, §6.2) and (in reality) attain finite amplitudes after a finitely long time. This justifies the use of a moving frame of reference, which, instead, restricts the interpretation of the eigensolutions to representing the instantaneous dynamics only. According to equation (2.64), the growth indicated by the eigenvalue in the *moving* frame of reference exactly represents, for an incompressible flow, the initial growth of the eigenfunctions introduced in the *stationary* frame of reference. A main objective of this sec-

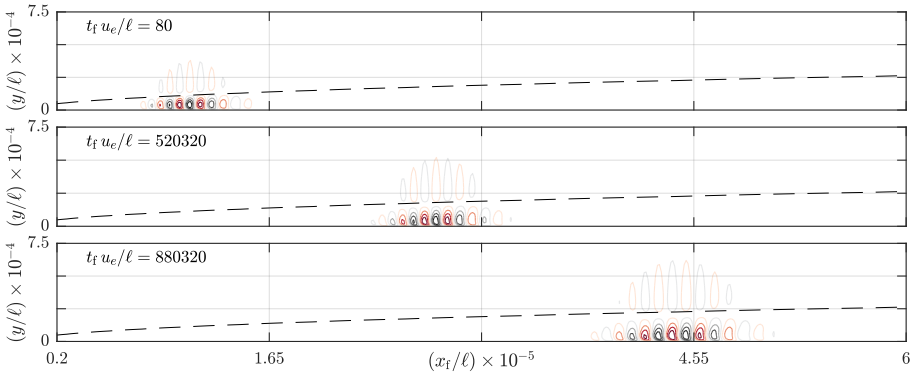

Figure 4.7: Snapshots at different time instants of the temporal evolution of the u'-perturbation (real part in coloured lines, from min- (gray) to maximum (red) with $\Delta = 2/9$, scaling the maximum to unity) initialized with the most least stable eigenfunction for $c_f/u_e = 0.47$. Boundary layer height indicated by $\overline{U} = 0.99u_e$-isocontour (dashed).

tion is to verify this relationship.

To address this particular feature of the solutions in the stationary frame of reference, the eigenfunctions (both the real and imaginary parts) obtained in the moving frame of reference are used as initial conditions for the linearized Navier-Stokes equations (2.13) and integrated in time. This is done with an implicit second-order scheme with step size $\Delta t\,u_e/\ell = 80$. The rest of the numerical setup is exactly the same as for the eigenvalue problem, except the streamwise discretization. For the sake of affordable computational cost, a 16^{th} order central-finite-difference scheme (in the interior of the domain) with 600 uniformly-spaced grid points replaces the streamwise Chebyshev grid. In this configuration, the absolute change in the eigenvalues with respect to the Chebyshev discretization is $\mathcal{O}(10^{-11})$.

For the analysis of the time-evolving perturbations for small times, eigensolutions corresponding to high frame speeds are selected for which the most unstable eigenvalue of the main branch lies close to the real axis ($\omega_i \approx 0$). In particular, two frame speeds, $c_f/u_e = 0.470$ and 0.465, are used, which correspond to a situation where the main branch is completely stable and another with only one unstable mode (see figure 4.5). The spatio-temporal evolution of the least stable eigenfunction as a wave packet for $c_f/u_e = 0.47$ is shown in figure 4.7. When time advances, the wave packet travels downstream and widens. As long as the outflow boundary is not reached, the perturbation is localized within the domain and unaffected by the boundary conditions. The shape of the wave packet is distorted with respect to the initial eigenfunctions as a consequence of the streamwise variation of the base flow. These observations are confirmed by all time-marching simulations in which a moving-frame eigensolution was used as the initial condition.

In figure 4.8(*a*), the growth rates measured for the six least stable time-marched solutions are compared to their respective eigengrowth ω_i, with ω_i the imaginary part of the eigenvalues computed in the moving frame of reference. When approaching the time instances $t \to 0^+$, the measured growth rate in the fixed frame of reference smoothly approaches the eigenvalue in the moving frame of reference. This is observed for all main-branch modes for the two tested frame speeds. Equation (2.64) is thus verified numerically. The comparison between the short-time behavior and the eigensolutions is completed by measuring the wave-packet group speed (see equation (2.67)). In the stationary reference

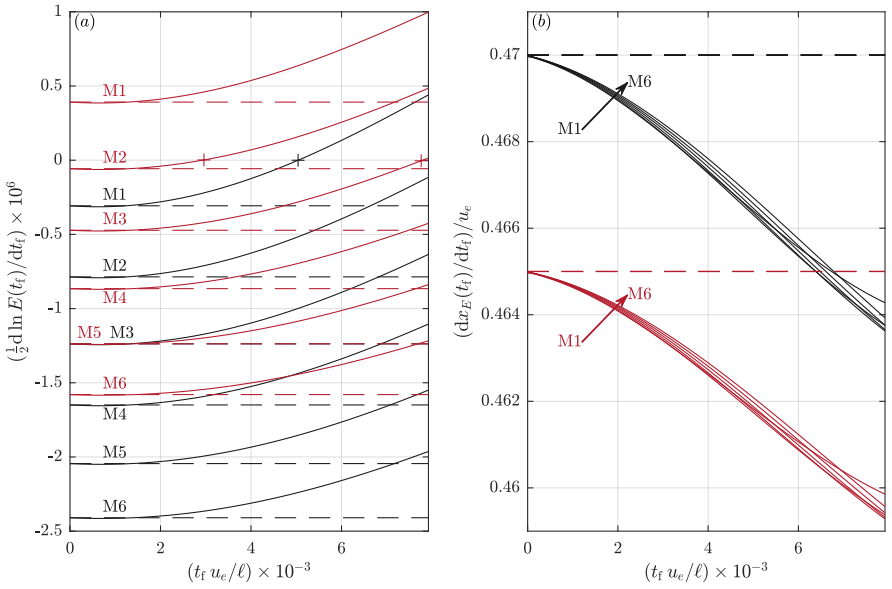

Figure 4.8: (*a*) Temporal growth rate (measured with perturbation kinetic energy) in the stationary reference frame and (*b*) measured speed of the wave packets, initialized from the sixth least stable eigenfunctions (labeled from most unstable M1 to more stable M6) computed in the moving frame of reference at $c_f/u_e = 0.47$ (black) and 0.465 (red). Eigengrowth ω_i in (*a*) and frame speed c_f in (*b*) indicated by dashed lines. Neutral temporal growth indicated by crosses in (*a*).

frame and at $t_f = 0$, the wave packet moves at the speed of the frame of reference in which the eigensolutions are computed figure 4.8(*b*). That is, at $t_f = 0$, the group speed of the solutions is equal to the frame speed. For longer elapsed times, the growth rate and group speed deviate from the values corresponding to the eigensolution as a consequence of the base-flow development. In particular, the *group* speed of the wave packet decreases as the boundary layer grows. Similarly, experiments of Schubauer & Skramstad (1948) showed that the *phase* speed of the Tollmien-Schlicthing waves decreases with the growing boundary layer. All these observations qualitatively agree with the results of §4.2.4; by decreasing the frame speed for the eigenvalue problem, the wave packets move downstream.

The previous observations confirm that the formulation of the eigenvalue problem in a moving frame of reference yields eigensolutions whose characteristics represent the instantaneous perturbation dynamics in the fixed frame of reference, at $t_f = 0$. In this sense, initializing the time-integration with eigensolutions is free from unpredictable transient behavior. As mentioned before, this approach is very similar to the PSE approach, which is initiated from an LST eigenfunction. For that problem, however, there is a short-lived transient for the very first marching steps, because the LST solution does not account for several terms that newly appear in the PSE system. In the case of the time-evolution of the BiGlobal eigenfunctions, no such transient occurs because *the eigensolutions are exact instantaneous solutions of the full, linearized Navier-Stokes equations.*

The usual way to quantify perturbation growth with solutions of the LST and PSE approaches is to consider N-factor *curves*, i.e., the natural logarithm of the amplification of disturbances with a *single* frequency. In the present context, the amplification of wave packets, that contain a band of frequencies, is considered as they travel downstream. Since N-factor curves are targeted, only eigenfunctions with stable eigenvalues are used as initial condi-

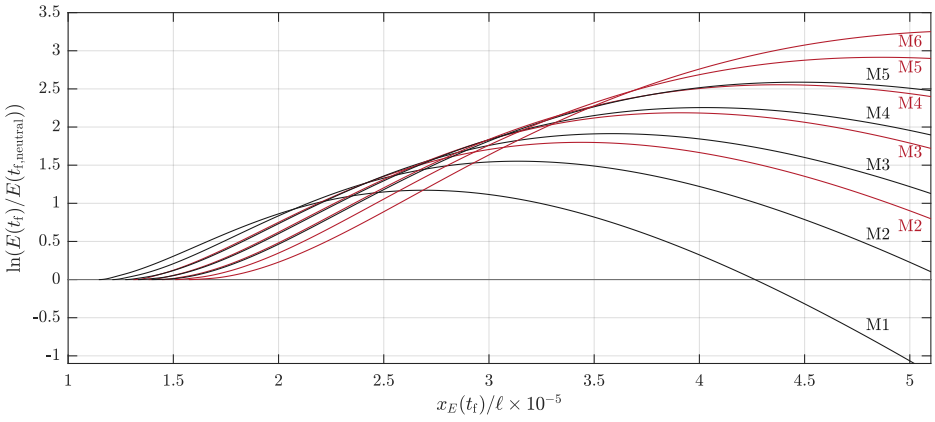

Figure 4.9: Perturbation amplification downstream of the neutral point in the stationary reference frame, initialized from the least stable eigenfunctions belonging to the main branch (labeled from most unstable M1 to more stable M6) as obtained in the moving frame of reference at $c_f/u_e = 0.47$ (black) and 0.465 (red).

tions for the two frame speeds $c_f/u_e = 0.465$ and 0.47. For the former speed, this implies marching the solutions along the branch from the second-most unstable mode onward. Hence, for both considered speeds, all selected wave packets decay initially ($\sigma(0) < 0$), as indicated in figure 4.8(*a*), before reaching a minimum amplitude. At the specific time where the minimum is attained, i.e., when the temporal growth reaches zero (indicated by crosses in figure 4.8(*a*)), the perturbations start growing while still being advected downstream. This point is referred to as a neutral point and is denoted with $t_f = t_{f,neutral}$. All amplification curves $E(t_f)$ are scaled by their respective $E(t_{f,neutral})$ at the neutral point, similarly to LST and PSE, and are shown in figure 4.9.

Taking the envelope of the amplification curves $E(t_f)$ unfortunately does not compare with the actual LST and PSE envelopes because of the very definition of the N-factor curves. From the perspective of the LST and PSE approaches, individual N-factor curves represent a disturbance with a single frequency. By forming the envelope over all relevant frequencies, it can be determined which frequency is amplified most at a certain streamwise location. However, since wave packets containing a narrow band of frequencies are presently considered, they cannot be expected to dictate the entire N-factor envelope. In the following, the N-factor curves are instead reconstructed by considering a Fourier transform of the wave packets to isolate the amplification curves at each frequency. The exact same information as from the PSE and LST approaches can thus be extracted, with all elliptic effects included.

4.3.2. Amplification and neutral curves: a wave-train interpretation

The individual frequency information, i.e., the wave-*train* information, can be obtained from the wave *packets* by performing a Fourier transformation in time. To further ensure consistent and accurate comparisons between the present method and PSE, a measure of the spatial growth has to be chosen. In non-parallel flows, the shape function of the perturbation evolves in the streamwise direction and this must be accounted for when assessing the overall perturbation growth in space. Hence, in contrast to parallel flows (or under the parallel-flow hypothesis), in which the perturbation growth is entirely defined by the complex spatial wavenumber, the perturbation growth in non-parallel flows depends on the choice of the norm and measurement technique used to quantify the spatial evolution of the shape functions. This has been extensively discussed by Gaster (1974); Herbert & Bertolotti

Table 4.4: Properties of the initial conditions (i.e., the moving-frame main-branch eigensolutions) used to construct the N-factor and neutral curves in figure 4.10. The initial-condition number labels all different initial conditions used for reference in the text, while the mode number refers to the place of the eigenvalue in the spectrum for a given frame speed.

Initial condition $\#_{\mathrm{ic}}$	c_{f}/u_e	Mode #	$(\omega\ell/u_e)\times10^{-5}$	$(x_E/\ell)\times10^{-4}$	$(x_d/\ell)\times10^{-5}$
1	0.525	1	$-8.143-1.719\mathrm{i}$	3.912	0.716
2	0.525	2	$-8.015-1.897\mathrm{i}$	4.169	0.756
3	0.500	1	$-5.902-0.732\mathrm{i}$	6.263	1.090

(1987); Bertolotti *et al.* (1992); Govindarajan & Narasimha (1995); Herbert (1997) for PSE and by Fasel & Konzelmann (1990) for DNS. In what follows, the wall-normal integration of the individual-frequency perturbation energy (equation (2.69) with kinetic-energy norm (2.59)) and streamwise perturbation velocity are considered. The latter is given by

$$\hat{E}_u(x_{\mathrm{f}};\Omega_{\mathrm{f}}) = \int |\hat{u}(x_{\mathrm{f}},y;\Omega_{\mathrm{f}})|^2\,\mathrm{d}y. \tag{4.1}$$

Relying on integral measurements allows removing any uncertainty regarding the choice of a wall-normal location where the growth/amplification is measured (Gaster, 1974). The sampling period for the Fourier transform is chosen as $T\approx 2.7\times10^6\ell/u_e$.

To achieve a converged Fourier-transform at a specific fixed streamwise location in the stationary frame of reference, a wave packet needs to be sufficiently far away from this point as time tends both to zero and infinity. In the context of reconstructing the N-factor envelope and the most upstream portion of the neutral curve, it is necessary to disturb the flow with an eigensolution whose eigenfunctions are located relatively far upstream. In fact, the near-neutral solutions obtained for $c_{\mathrm{f}}/u_e=0.47$ and 0.465 are not located far enough upstream to capture the most upstream neutral point, which indicates that neutrally-stable eigensolutions (wave packets) do no imply neutrally-stable wave trains. The entire neutral curve can be reconstructed by selecting the least stable main-branch eigensolution for $c_{\mathrm{f}}/u_e=0.525$, which is located upstream of the kinetic-energy-based critical Reynolds number $\mathrm{Re}_{\mathrm{crit},\hat{E}}\gtrsim 7.23\times10^4$ ($\mathrm{Re}_{\delta^*,\mathrm{crit},\hat{E}}\approx 463$) as predicted by PSE. Figure 4.10(*a*) demonstrates the agreement between the wave-packet and PSE N-factor curves, independently of the measurement method, i.e., using either the kinetic energy or the streamwise velocity. The neutral curve, depicted in figure 4.10(*b*), is also completely recovered by the time-integrated wave-packet for both measurement methods. This shows that, by initializing the time-integration procedure with only one *single eigenfunction*, stability information for *all relevant individual frequencies* is captured. From here onward, the presently used initial condition is indicated with the label $\#_{\mathrm{ic}}=1$.

It should be emphasized that the N-factor and neutral curves can be reconstructed successfully with other initial conditions than just the most unstable eigensolution at $c_{\mathrm{f}}/u_e=0.525$. In fact, these curves are observed to be independent of the choice of the eigensolution, as long as its eigenfunctions are located far enough upstream. This is here demonstrated by initializing the time integration with different eigensolutions. The second-most unstable eigensolution along the main branch at the same frame speed ($c_{\mathrm{f}}/u_e=0.525$), labeled $\#_{\mathrm{ic}}=2$, and the most unstable main-branch solution at a much smaller frame speed ($c_{\mathrm{f}}/u_e=0.5$), $\#_{\mathrm{ic}}=3$, are considered. Further details about these initial conditions are presented in table 4.4. The comparison between the results obtained when using the differ-

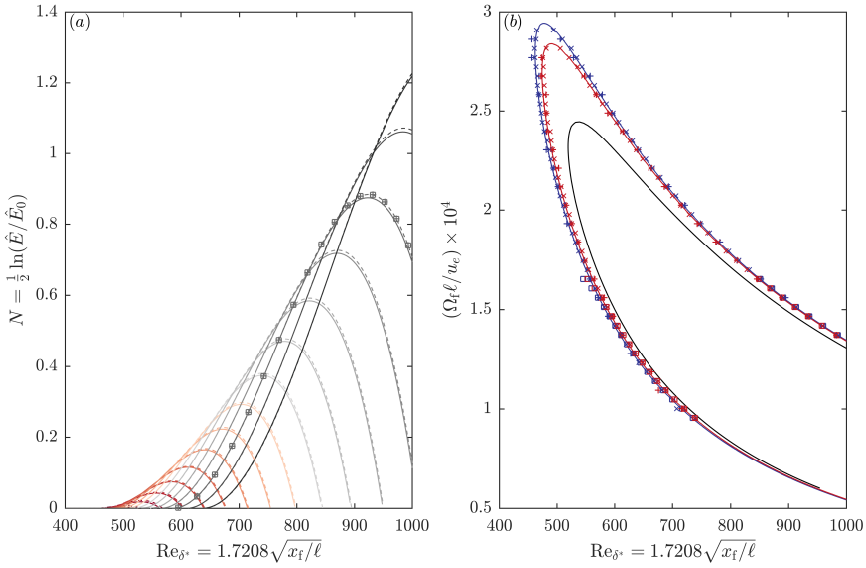

Figure 4.10: (*a*) Individual-frequency N-factor curves for PSE (solid) and the time-dependent wave-packet solutions (dashed and pluses for first and second most unstable modes at $c_f/u_e = 0.525$ ($\#_{ic} = 1$ and 2, respectively), squares for most unstable at $c_f/u_e = 0.5$ ($\#_{ic} = 3$)) with spatial growth based on kinetic energy $\hat{E}$. Angular frequencies indicated by color level from $\Omega_f \ell/u_e = 1.256 \times 10^{-4}$ (gray) to 2.885×10^{-4} (red) with $\Delta\Omega_f \ell/u_e = 1.16 \times 10^{-5}$. (*b*) Neutral curve for LST (black line), PSE (red and blue lines) and the wave packets (crosses and pluses for $\#_{ic} = 1$ and 2, resp., and squares for $\#_{ic} = 3$) with spatial growth based on $\hat{E}$ (blue) and $\hat{E}_u$ (red).

ent initial conditions is illustrated in figure 4.10. Since the eigenfunctions corresponding to initial conditions $\#_{ic} = 2$ and 3 are located downstream with respect to those of $\#_{ic} = 1$, a converged Fourier transform can only be obtained at streamwise stations $\mathrm{Re}_x \gtrsim 0.75 \times 10^5$ ($\mathrm{Re}_{\delta^*} \gtrsim 473$) for initial condition $\#_{ic} = 2$ and $\mathrm{Re}_x \gtrsim 1.09 \times 10^5$ ($\mathrm{Re}_{\delta^*} \gtrsim 568$) for $\#_{ic} = 3$. In the overlapping regions of space where the Fourier transform converges when using the different initial conditions, the information is practically identical ($|\Delta x|/\ell \approx 3 \times 10^2$, $|\Delta N_{\max}| \approx 5 \times 10^{-4}$ at $\Omega_f \ell/u_e = 1.488 \times 10^{-4}$). Hence, this demonstrates that the choice of eigensolution as initial condition does not constrain the physics. It is expected that the independence of the N-factor and neutral curves with respect to the initial condition extends to the use of all other eigensolutions with localized eigenfunctions that are located sufficiently far upstream.

This observation suggests that the N-factor and neutral curves can possibly be reconstructed with *any* initial condition. If the initial condition does not exactly solve the moving-frame eigenvalue problem, the time-integrated solution is, however, highly prone to contamination by inadvertent transients. A similar transient behavior exists in the context of the PSE spatial marching approach, which is initialized with an LST solution that does not exactly satisfy the PSE problem, as mentioned before. In slowly-evolving flows, the transient behavior can be very manageable. However, in arbitrarily more complicated flow fields the contamination by the transient can be very difficult, if not impossible, to eliminate or even identify. Because the presently considered eigensolutions satisfy the full, linearized Navier-Stokes equations instantaneously, transients are identically avoided when using them as initial conditions. Hence, the localized eigenfunctions obtained in a moving frame of reference are arguably the most appropriate choice for the initialization of a wave-packet time-integration approach.

Since the eigenfunctions belonging either 1) to another mode along a branch at the same frame speed or 2) to an eigensolution at another frame speed have different streamwise locations and extent, each corresponding time-integrated wave packet covers a different region in space. The streamwise extent of the spatial region where Fourier coefficients converge depends on the location of the eigenfunctions and on the temporal evolution of the amplitude of the time-integrated wave packet. The latter can be restrictive if the magnitude of the Fourier coefficients reaches a level that is so low that they cannot be accurately captured numerically, i.e., due to arithmetic underflow. Nevertheless, as demonstrated previously, if an overlapping region exists between two time-integrated wave packets, the N-factor curves are identical; the disturbance physics is not affected by which eigensolution is chosen. This degree of freedom allows covering individual spatial regions of the flow, which can be particularly useful for flows that develop quickly in distinct regions separated by a long streamwise extent. In the case of the flat-plate boundary layer, when seeking for N-factor curves in a specific region, it is thus not necessary to integrate wave packets that lie upstream of the entire neutral curve. It is only necessary to ensure that the eigenfunctions lie sufficiently upstream of the relevant region for the frequency of interest. For instance, selecting the most unstable eigenfunction at $c_\mathrm{f}/u_e = 0.45$, which has a downstream magnitude $|\tilde{u}|/|\tilde{u}|_\mathrm{max} < \mathcal{O}(10^{-5})$ for $\mathrm{Re}_x \gtrsim 3.5 \times 10^5$, is suitable if instability information is sought downstream of this location.

As a rule of thumb when applying the present methodology, the time integration should always be initialized with eigenfunctions located far enough upstream of the region of interest. In regard to the observed upstream movement of the eigenfunctions upon increasing the frame speed, it is recommended to consider eigensolutions in the large frame-speed limit. If the growth of perturbations is sought for additional downstream locations, and if that cannot be appropriately captured by the use of the upstream initial condition, a smaller frame speed should be considered.

Obtaining the N-factor curves from the time-integration of moving-frame eigensolutions has many advantages over other approaches, at least as it can be synthesized from the application to the flat-plate boundary layer. Non-elliptic equations like LST and PSE are discarded in the following discussion since the present method targets the application to quickly developing flows, for which these methods are inapplicable. First, in contrast to frequency-forcing approaches, only one wave-packet solution, represented by the eigensolution, is required to excite all relevant frequencies in a given region of interest. Having to repeat monochromatic simulations for a large number of individual frequencies and determining the spatial distribution of the forcing function (Fasel & Konzelmann, 1990) is avoided. Although the latter forcing function could be determined with an optimal-forcing approach, the perturbation-amplification scenario is then restricted to the optimal one and this would obstruct reconstructing the (inherently non-optimal) monochromatic N-factor curves and the corresponding neutral curves. This is reflected by the results of Sipp & Marquet (2012), who argue that branch II is not appropriately captured in the region where the optimal forcing is strong. The same argument likely applies to the use of an initial condition obtained in optimal-perturbation analysis, in the spatial range where the growth is non-modal/transient. Therefore, since non-optimal stability information is presently sought, disturbing a flow with moving-frame eigensolutions is arguably more appropriate than the singular vectors obtained in the optimal-perturbation or in resolvent analysis, or a multitude of monochromatic waves. These analyses close the methodological aspects of the moving-frame approach for stability analysis. In the following, theoretical aspects are discussed in order to better understand the moving-frame eigensolutions.

4.4. Reynolds-Orr energy budget of the moving-frame eigensolutions

It has been established that the eigenmodes in the side and downward branches have the distinguishing property with respect to the main branch that they are domain dependent because the corresponding adjoint eigenfunctions are not localized. It is still unknown, however, whether a specific significance can be assigned to the eigensolutions' specific arrangement in the different branches of the spectrum at a given frame speed, and what mechanisms are involved. The goal of the present section is twofold. First, it aims to determine the distinguishing *physical* mechanisms from mode to mode in the *main* branch. Secondly, other characteristics of the *non-physical* side and downward branches with respect to the main branch are investigated in order to identify them in future studies. These points are addressed by analyzing the wavenumber of the two-dimensional eigensolutions and then applying the Reynolds-Orr energy equation presented in §2.8.

Usually, spectra consist of a fundamental mode and its harmonics. Higher harmonics have a more oscillatory spatial structure, characterized by small wavelengths, and therefore are more strongly damped by viscous dissipation. This explains that these modes should, far enough down the spectrum, become stable. In the present case, however, figure 4.1 suggests that the streamwise wavelength of one eigenfunction with respect to the next along the branch is relatively constant. In fact, the wavelength does not decrease, as would be expected from higher harmonics. In order to quantify this aspect, a mean wavenumber based on the kinetic perturbation energy (see equation (2.59)) is defined as

$$\alpha_{\text{mean}} = -\mathrm{i}\frac{\iint\left(\tilde{u}^*\dfrac{\partial\tilde{u}}{\partial x}+\tilde{v}^*\dfrac{\partial\tilde{v}}{\partial x}\right)\mathrm{d}x\,\mathrm{d}y}{\iint\left(|\tilde{u}|^2+|\tilde{v}|^2\right)\mathrm{d}x\,\mathrm{d}y}, \tag{4.2}$$

which allows reducing the (x, y)-dependent wavenumber into one scalar value. Figure 4.11 shows the real part of α_{mean} for $c_{\text{f}}/u_e = 0.415$ and 0.470 with two different scalings. Figure 4.11(*a*) reveals that, if scaled with ℓ, the wavenumber *decreases* when considering more stable solutions along the main branch, as indicated by the filled circles. The wavelength of the main-branch eigenfunctions appears to increase at approximately the same rate as the length of the wave packets. This is emphasized in figure 4.11(*b*) by the relatively constant number of wavecrests per wave-packet length for the eigenfunctions along the main branch. This clearly suggests that the modes along the main branch are not higher harmonics of the most unstable mode. If scaled with ℓ, the wavenumber of the solutions on the side branch increases. However, when scaled by the wave-packet length, the number of wavecrests per wave packet *decreases* for both the side and downward branches. This again indicates that modes further down these two branches are not higher harmonics. This observation hints that the stabilization of the modes along a branch is unlikely due to viscous dissipation acting on the streamwise wavelength of the eigenfunctions. A mechanism other than dissipation must be causing the greater stability of these modes. To assess which mechanism is responsible, the Reynolds-Orr decomposition of the temporal growth rate is used.

The different terms of the perturbation energy are presented in §2.8 for compressible flows. In particular, the growth-rate decomposition was given by equation (2.76). Considering an incompressible flow drastically reduces the decomposition such that

$$\omega_i = R_{\tilde{u}^*\tilde{v}} + R_{|\tilde{u}|^2} + R_{\tilde{v}^*\tilde{u}} + R_{|\tilde{v}|^2} + D_{\text{frict.}} + A_{\overline{U}} + A_{\overline{V}} + A_{\overline{W}} + A_{c_{\text{f}}} + P_{\tilde{p}}\,. \tag{4.3}$$

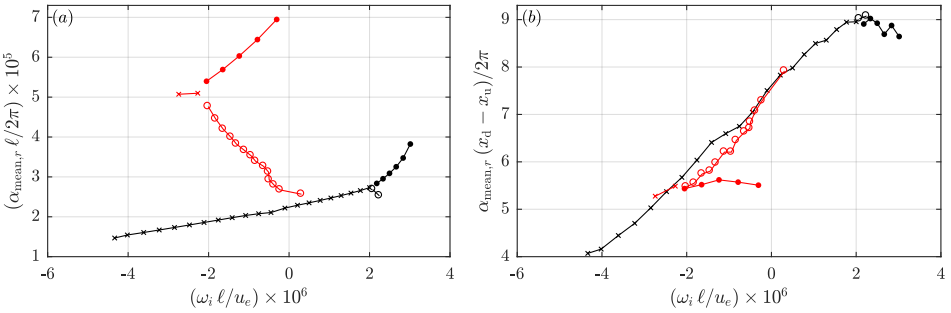

Figure 4.11: Real part of the mean wavenumber (equation (4.2)) for the different modes along the main (filled circles), side (open circles) and downward (crosses) branches for $c_\mathrm{f}/u_e = 0.415$ (black) and $c_\mathrm{f}/u_e = 0.47$ (red). The wavenumber is scaled by (*a*) the Blasius length ℓ and (*b*) the wave packet length $x_d - x_u$, where x_u and x_d are defined as the most up-/downstream locations of the iso-contour at which $|\tilde{u}| = |\tilde{u}|_{\max}/9$. The scaling by 2π converts the angular wavenumbers into "number of waves" per unit of the used length scale.

All terms in equation (4.3) can be obtained from the compressible-flow formulation, provided that $\overline{\rho} = 1$ and that the incompressible-flow energy norm (2.59) is used. The only terms requiring additional manipulation when departing from the compressible-flow formulation are the $P_{\tilde{p}}$ and $D_{\mathrm{frict.}}$ contributions, that are given by

$$\left.\begin{aligned} D_{\mathrm{frict.}} &\overset{(a)}{=} \underbrace{\frac{1}{\mathrm{Re}}\iint\left|\frac{\partial\tilde{u}}{\partial y}\right|^2\frac{\mathrm{d}x\,\mathrm{d}y}{\tilde{E}}}_{D_{\tilde{u},y}} + \frac{1}{\mathrm{Re}}\iint\left|\frac{\partial\tilde{u}}{\partial x}\right|^2 + \left|\frac{\partial\tilde{v}}{\partial x}\right|^2 + \left|\frac{\partial\tilde{v}}{\partial y}\right|^2\frac{\mathrm{d}x\,\mathrm{d}y}{\tilde{E}}, \\ P_{\tilde{p}} &\overset{(b)}{=} -\mathscr{R}\left\{\iint\left(\tilde{u}^*\frac{\partial\tilde{p}}{\partial x} + \tilde{v}^*\frac{\partial\tilde{p}}{\partial y}\right)\frac{\mathrm{d}x\,\mathrm{d}y}{\tilde{E}}\right\}. \end{aligned}\right\} \tag{4.4}$$

The terms that have the largest contribution to the growth rate ω_i for the modes along the three branches are shown in figures 4.12(*a*) and 4.13(*a*) for $c_\mathrm{f}/u_e = 0.415$ and 0.470, respectively. As established before, the stabilization of the modes further down the branch does not appear to relate to the streamwise wavelength of the eigenfunctions. This is further demonstrated by the very small size of the dissipation terms (4.4a) involving the streamwise derivatives of $\tilde{u}$ and $\tilde{v}$, contributing for less than 2% to the growth rate of the most unstable mode. This means that the streamwise wavelength is so large that these streamwise dissipation terms are almost inactive. For this reason, these contributions, along with other insignificant terms, are included in the remainder in figures 4.12(*a*) and 4.13(*a*).

For a more detailed consideration, the main branch is first analyzed by considering both figures 4.12 (mode # 1 through 6) and 4.13 (# 1 – 5). The energy budget reveals that the Reynolds-stress $R_{\tilde{u}^*\tilde{v}}$ is the most destabilizing contribution for all the main-branch modes. More importantly, the variation of ω_i is highly correlated with that of $R_{\tilde{u}^*\tilde{v}}$. The Pearson correlation coefficient is 0.995 for both $c_\mathrm{f}/u_e = 0.415$ and 0.47. This establishes that $R_{\tilde{u}^*\tilde{v}}$ dominantly controls the instantaneous growth rate of the main-branch modes. The imaginary part of $R_{\tilde{u}^*\tilde{v}}$ consists of two main factors: $\mathscr{R}\{\tilde{u}^*\tilde{v}\}$ and $\partial\overline{U}/\partial y$. Figures 4.12(*b*) and 4.13(*b*) show that the overall shape of $\mathscr{R}\{\tilde{u}^*\tilde{v}\}$ is relatively invariant along the main branch. In fact, the decrease of the Reynolds-stress term along the main branch is mostly brought by the downstream displacement of the corresponding eigenfunctions, which causes the wave packets to experience a diminishing shear magnitude, $\partial\overline{U}/\partial y$. This is supported by correlation coefficients of -0.998 and -0.9991 between the position of the wave packet, measured

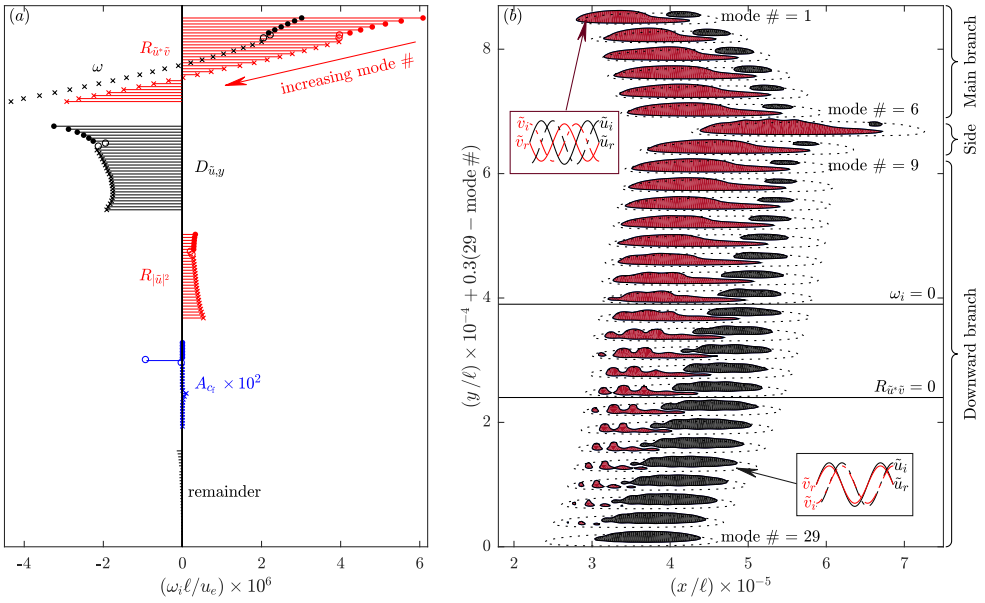

Figure 4.12: Analysis of the solutions for $c_f/u_e = 0.415$. (*a*) Most dominant terms in the ω_i-budget (equation (4.3)) for the different modes along the main (filled circles), side (open circles), and downward (crosses) branches. (*b*) Regions where $\tilde{u}$ and $\tilde{v}$ are locally out of phase (dark red, $\mathscr{R}\{\tilde{u}^*\,\tilde{v}\} < -3 \times 10^{-3}\,\tilde{E}_{\max} < 0$, produces ω_i) and in phase (black, $\mathscr{R}\{\tilde{u}^*\,\tilde{v}\} > 3 \times 10^{-3}\,\tilde{E}_{\max} > 0$, destroys ω_i). Isocontour of $|\tilde{u}|/|\tilde{u}|_{\max}$ (dotted black, level: 6×10^{-2}). Contours are elevated in y based on their mode number. Horizontal lines indicate where the imaginary part of $R_{\tilde{u}^*\,\tilde{v}}$ and ω switch sign. The mode numbers corresponding to the first and last considered modes along the main and downward branch are indicated. The top and bottom insets illustrate the behavior of arbitrary complex-valued waves in the out-of-phase and in-phase regions, respectively.

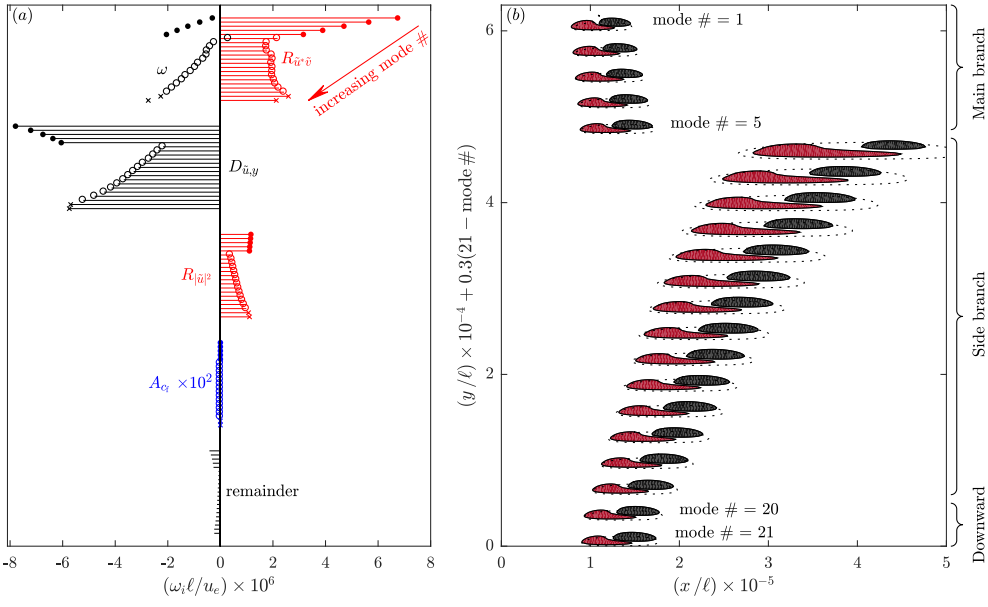

Figure 4.13: Analysis of the solutions for $c_f/u_e = 0.470$, see figure 4.12.

by the streamwise energy centroid x_E, and the imaginary part of $R_{\tilde{u}^*\tilde{v}}$ for the frame speeds $c_f/u_e = 0.415$ and 0.470, respectively. A very similar argument applies to the dissipation term $D_{\tilde{u},y}$. Upon displacing the eigenfunctions downstream, the height of the boundary layer increases as the square root of x and the wall-normal support of the eigenfunctions increases at this rate as well. This means that $\partial^2\tilde{u}/\partial y^2$ is expected to decrease as $1/x$. The correlation coefficients between x_E and the imaginary part of $D_{\tilde{u},y}$ are 0.9993 and 0.996 for $c_f/u_e = 0.415$ and 0.47, respectively.

Second, the downward-branch modes are considered. This is best done with figure 4.12, because at this frame speed the branch has a large number of modes (mode # 9−29). Just like for the main-branch modes, the Reynolds-stress term $R_{\tilde{u}^*\tilde{v}}$ represents the dominant contribution to the growth rate. All other terms are relatively constant in this particular case. The stabilizing effect (imaginary part of $R_{\tilde{u}^*\tilde{v}} < 0$) of the Reynolds-stress term for higher modes deserves some more attention. The shear $\partial\overline{U}/\partial y$ is always positive for the flat-plate boundary layer and thus the Reynolds-stress term can only reduce the growth rate for higher modes if $\mathscr{R}\{\tilde{u}^*\tilde{v}\} = \tilde{u}_r\tilde{v}_r + \tilde{u}_i\tilde{v}_i$ changes sign. If $\mathscr{R}\{\tilde{u}^*\tilde{v}\} > 0$ (< 0) then the two complex-valued streamwise traveling wave-functions $\tilde{u}$ and $\tilde{v}$ are in (out of) phase, as illustrated in the insets of figure 4.12(*b*). Figure 4.12(*b*) also shows that, while the magnitude of $\mathscr{R}\{\tilde{u}^*\tilde{v}\}$ relative to $\tilde{E}_{\max}$ is always approximately the same, the region representing an in-phase correlation between $\tilde{u}$ and $\tilde{v}$ (black) outweighs the out-of-phase region (red) for higher modes on the downward branch. A positive value of $\mathscr{R}\{\tilde{u}^*\tilde{v}\}$ yields a negative $R_{\tilde{u}^*\tilde{v}}$ contribution to ω_i. This therefore implies the more stabilized character of the solutions for modes that are located further along the downward branch.

Finally, side-branch modes are investigated, i.e., mode # 6 − 19 in figure 4.13. The imaginary part of $R_{\tilde{u}^*\tilde{v}}$ is always positive and relatively constant in this case. This is reflected by the weak decrease in the ratio of the size of the out-of-phase region to that of the in-phase region that is compensated by the increase of $\partial\overline{U}/\partial y$ as the side-branch modes move upstream (see figure 4.13(*b*)). For the side branch, the dissipation term $D_{\tilde{u},y}$ represents the largest contribution to the growth rate. As for the main branch, this is related to the streamwise position of the wave packets in the boundary layer. Quantitatively, a correlation coefficient of 0.958 between $D_{\tilde{u},y}$ and x_E is found.

Besides $R_{\tilde{u}^*\tilde{v}}$ and $D_{\tilde{u},y}$, two other terms are considered as well. The longitudinal Reynolds-stress term $R_{|\tilde{u}|^2}$ contribution is observed to always have a small but significant destabilizing effect, which is a consequence of the negative $\partial\overline{U}/\partial x$ in a flat-plate boundary layer. Just like $R_{\tilde{u}^*\tilde{v}}$, the dependence of $R_{|\tilde{u}|^2}$ on $\partial\overline{U}/\partial x$ causes this term to be strongly correlated with the streamwise position of the eigenfunctions (main branch correlation coefficients: −0.990 and −0.998 for $c_f/u_e = 0.415$ and 0.470, respectively; downward branch: −0.9992; side branch: −0.967). The contribution of the other Reynolds-stress terms $R_{\tilde{v}^*\tilde{u}}$ and $R_{|\tilde{v}|^2}$ amounts to about 0.0006% and 1.3% of the total growth rate of the most unstable mode, which justifies their factorization into the remainder term. Lastly, the c_f-correction term, expressed as A_{c_f} in the present context, is always insignificant with respect to the other terms. This is emphasized by the small size of this term as shown in the figure, even after it is amplified by a factor 10^2. This is desired, as it indicates that the deviation of the instantaneous growth of E from the eigenvalue growth ω_i is negligibly small (see equation (2.64)).

The delineation of the terms that contribute to ω_i has revealed the main behavior of the modes along the different branches. The main and side branches represent solutions with similar $\mathscr{R}\{\tilde{u}^*\tilde{v}\}$ shapes that displace in the streamwise direction. The difference in the behavior of the modes along the main and side branch is the direction in which the eigenfunctions are displaced as more stable eigenmodes are considered. The downward branch,

instead, represents solutions that sit at approximately the same x-location, while the solutions' $\mathscr{R}\{\tilde{u}^*\,\tilde{v}\}$ shape deforms significantly, representing relative phase changes of $\tilde{u}$ with respect to $\tilde{v}$.

4.5. Global mode theory in a moving frame of reference

This section uses the global mode theory (Huerre & Monkewitz, 1990; Chomaz *et al.*, 1991; Monkewitz *et al.*, 1993) to illustrate how the two-dimensional eigensolutions can be reconstructed with the WKBJ approach, that allows extending the local LST method to spatially developing flows. Alizard & Robinet (2007) and Rodríguez (2010) have shown the relationship between local and global solutions for the flat-plate boundary-layer case before, by using the complex frequency provided by BiGlobal simulations as input for the LST and PSE approaches. It is presently demonstrated how to *independently* approximate the moving-frame solutions, i.e., without using information from the solution obtained with the BiGlobal approach. This also gives the opportunity to highlight the similarities and differences between the nonlocal and global solutions.

4.5.1. Nonlocal perturbation approach

The WKBJ ansatz has already been introduced in §2.3.3 for the PSE approach and allows accounting for the variation of the perturbations from one streamwise station to another. In contrast to the PSE approach that solves both the zeroth- and first-order ϵ_p equations at once, an actual WKBJ approach separates the zeroth and first-order terms into a set of two equations solved sequentially. At the leading-order, the nonlocal stability equation (2.26) is given by

$$(\mathscr{A}_\alpha + \epsilon_p \mathscr{A}_{\alpha,\mathrm{np}})\tilde{\boldsymbol{q}}_\mathrm{f} = \alpha\mathscr{B}_\alpha\tilde{\boldsymbol{q}}_\mathrm{f} + \alpha^2\mathscr{C}_\alpha\tilde{\boldsymbol{q}}_\mathrm{f}. \tag{4.5}$$

Keeping all non-parallel-flow terms, included in $\mathscr{A}_\mathrm{np}$, at the leading order allows obtaining the local solutions by only solving equation (4.5). This avoids solving the composite, multiple-scale problem to include the non-parallel effects (Siconolfi *et al.*, 2017). If $\mathscr{A}_\mathrm{np}$ is dropped, the parallel assumption on the base-flow evolution is enforced back and the system is thus here referred to as parallel WKBJ. Strictly speaking, the parallel WKBJ is inconsistent since the perturbations would be allowed to evolve while the flow variables are assumed constant in the streamwise direction. However, this approach is useful to illustrate the effect of the non-parallel-flow terms $\mathscr{A}_\mathrm{np}$ on the local perturbation solutions.

To reconstruct 'global' solutions that are similar to the eigensolutions found with the two-dimensional stability equations, equation (4.5) is formulated in the moving frame of reference. Note that, in this case, converting the solution properties between reference frames is relatively simple since the Doppler shift formula (2.54) reduces to the simple algebraic relation $\omega_\mathrm{f} = \omega + \alpha c_\mathrm{f}$. In the past, local analyses have thus been applied in moving frames of reference to study convective or absolute instability mechanisms in various flows (Deissler, 1987; Brevdo, 1988; Wright *et al.*, 2000; Arratia *et al.*, 2018), including the Blasius boundary layer (Brevdo, 1995). The reconstruction of an equivalent global solution in the moving frame of reference has, however, not been attempted.

Unfortunately, the local results of Brevdo (1995) cannot be directly compared to the present two-dimensional global stability results because a manipulation of the local approaches is required to approximate the global solutions. This justifies using the global theory in the present work. The global theory in a stationary frame of reference was presented by Huerre & Monkewitz (1990), Chomaz *et al.* (1991) and thoroughly developed by Monkewitz *et al.* (1993). For a more practical perspective of the global theory, the reader

is referred to the book of Huerre & Rossi (2009). Furthermore, Juniper *et al.* (2011), Juniper & Pier (2015), and Siconolfi *et al.* (2017) have used the approach to compare global modes computed with BiGlobal and (non)local approaches for several flow cases that support global instability mechanisms in the stationary frame of reference. Hence, domain-independent solutions could be obtained for these flow cases without having to resort to a moving-reference-frame formulation.

4.5.2. Approximation of the global eigenvalues

The global theory is applied according to the following steps in order to obtain the global solution frequency ω_g in a moving frame of reference. First, the streamwise spatial distribution of the absolute frequencies ω_0 is sought by finding a solution of equation (4.5) with zero group speed, in a given frame of reference. When such a solution exists at one spatial location, an absolute instability mechanism is supported locally in the flow. Second, the absolute frequencies are used to determine the turning-point frequency ω_s, which provides the lowest-order approximation of the global frequency. Third, the correction ω_ϵ, that accounts for the effects of the streamwise variation of α, is computed in order to evaluate the global frequency $\omega_g = \omega_s + \epsilon_p \omega_\epsilon$.

In order to determine the x-distribution of absolute frequencies, the pair $(\omega_0(x), \alpha_0(x))$ satisfying

$$\left.\frac{\partial \omega}{\partial \alpha}\right|_{(\omega_0,\alpha_0)} = 0\,, \tag{4.6}$$

is sought by solving the eigenvalue problem (4.5). Since the equations are solved in a moving frame of reference, the equation (4.6) is equivalent to finding convective solutions in the stationary reference frame that satisfy $\partial\omega_f/\partial\alpha = c_f$. Finding the pairs satisfying equation (4.6) is done by sequentially solving the temporal and spatial formulations of the eigenvalue problem (4.5), i.e., solving for ω (given α) and then for α (given ω), respectively. Note that another approach based on a sensitivity analysis with the adjoint eigensolutions could also be used (Alves *et al.*, 2019). For the present computations, condition (4.6) is satisfied numerically up to $\mathcal{O}(10^{-8}u_e)$ for each streamwise location along the boundary layer.

The lowest-order approximation of the global eigenvalue is given by the unique frequency $\omega_s = \omega_0(X_s)$, which satisfies $\partial\omega_0/\partial x = 0$. The location $x = X_s$ is referred to as a second-order turning point and is found by continuing analytically the function $\omega_0(x)$ into the complex plane. This is done by using a rational interpolation of the discrete $\omega_0(x)$ (Juniper & Pier, 2015; Siconolfi *et al.*, 2017) with the `Chebfun Matlab` library (Driscoll *et al.*, 2014). The resulting interpolating function of $\omega_0(x)$ is then evaluated in the complex x-plane. The evaluation of $\omega_0(x)$ in the relevant region of the complex x-plane is shown in figure 4.14(*a*) for the incompressible boundary layer in the moving frame of reference with $c_f/u_e = 0.415$. In this reference frame, the flow accommodates a spatial pocket of absolute instabilities for real x (black dotted line in figure 4.14(*a*)). Since $\omega_{s,i}$ can only be positive at $x = X_s$ if there is some local region of the complex x-plane where $\omega_{0,i} > 0$, having an absolutely unstable region is a necessary condition for the emergence of a global instability (Chomaz *et al.*, 1991). The frequencies ω_s computed with both non-parallel (black open circle) and parallel (red open circle) WKBJ are compared against the BiGlobal solution in figure 4.14(*b*). The numerical values of X_s and ω_s are reported in table 4.5. The solution including all non-parallel contributions is more unstable and is thus a better approximation of the most unstable BiGlobal eigenvalue than that excluding the non-parallel effects. This is in agreement with the observation of Gaster (1974) on the incompressible flat-plate boundary layer and, as mentioned in § 1.1.3, this also illustrates why the parallel assumption yields a

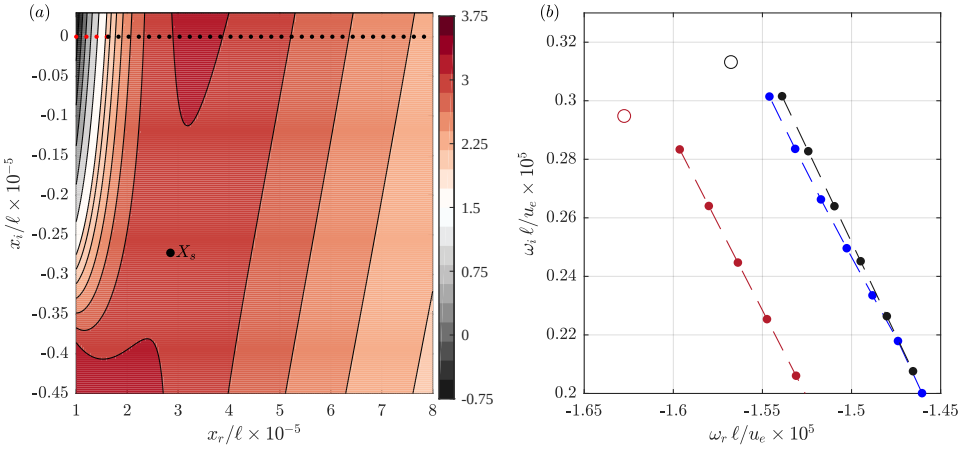

Figure 4.14: (*a*) Contour level of the imaginary part of the analytically continued absolute frequency $\mathscr{I}(\omega_0(X))$ with the non-parallel WKBJ in the complex X-plane. The dotted line highlights the real axis for $\omega_{0,i} < 0$ (red) and $\omega_{0,i} > 0$ (black). X_s is the center of the saddle point in the double turning point region for the non-parallel WKBJ. (*b*) Main branch with $c_f/u_e = 0.415$ for BiGlobal (blue), parallel (ω_g, red) and non-parallel (ω_g, black) WKBJ equations. Open circles indicate the leading-order frequency ω_s for WKBJ.

Table 4.5: Parameters corresponding to the most unstable mode for $c_f/u_e = 0.415$ as approximated using local and global stability approaches. The parameters x_E and α_{mean} are based on the direct $\tilde{v}$-eigenfunction.

	$X_s/\ell \times 10^{-5}$	$\omega_s\,\ell/u_e \times 10^5$	$\omega_g\,\ell/u_e \times 10^5$	$x_E/\ell \times 10^{-5}$
'Parallel' WKBJ	$2.6571 - 0.4564$i	$-1.6269 + 0.2944$i	$-1.596 + 0.2833$i	3.3423
WKBJ	$2.8504 - 0.2726$i	$-1.5670 + 0.3128$i	$-1.538 + 0.3015$i	3.4065
BiGlobal	$--$	$--$	$-1.546 + 0.3014$i	3.4965

more stable neutral curve.

A better approximation than ω_s can be obtained for the global eigenvalues ω_g by considering the first-order correction term ω_ϵ, which also allows obtaining the other global modes along the branch. This correction term follows from a separate analysis in the close vicinity of $x = X_s$, where the WKBJ expansion breaks down, and is given by

$$\omega_\epsilon = -\frac{i}{2}\frac{\partial^2\omega_0}{\partial\alpha^2}\frac{\partial\alpha_0}{\partial x} + \left(n+\frac{1}{2}\right)\sqrt{\frac{\partial^2\omega_0}{\partial x^2}\frac{\partial^2\omega_0}{\partial\alpha^2}}, \quad \forall n = 0,1,2... \tag{4.7}$$

with the partial derivatives being evaluated at $(x,\alpha,\omega) = (X_s,\alpha_0,\omega_0)$. The imaginary part of the square-root term is presently negative, which, as observed by Monkewitz *et al.* (1993), Juniper *et al.* (2011) and Siconolfi *et al.* (2017), is usually the case. Hence, the case $n = 0$ corresponds to the most unstable global mode and $n > 0$ yields more stable modes. Note that the correction term ω_ϵ proposed by Monkewitz *et al.* (1993) includes an additional component $\delta\omega$ that accounts for viscous and first-order base-flow effects. For the present study and following Siconolfi *et al.* (2017), these two contributions are part of the zeroth-order eigenvalue problem (4.5) and thus are already included in both ω_0 and ω_s.

The approximations of the most unstable global eigenvalue (i.e., $n = 0$) obtained for the boundary layer in the moving frame with $c_f/u_e = 0.415$ are given in table 4.5. It shows that

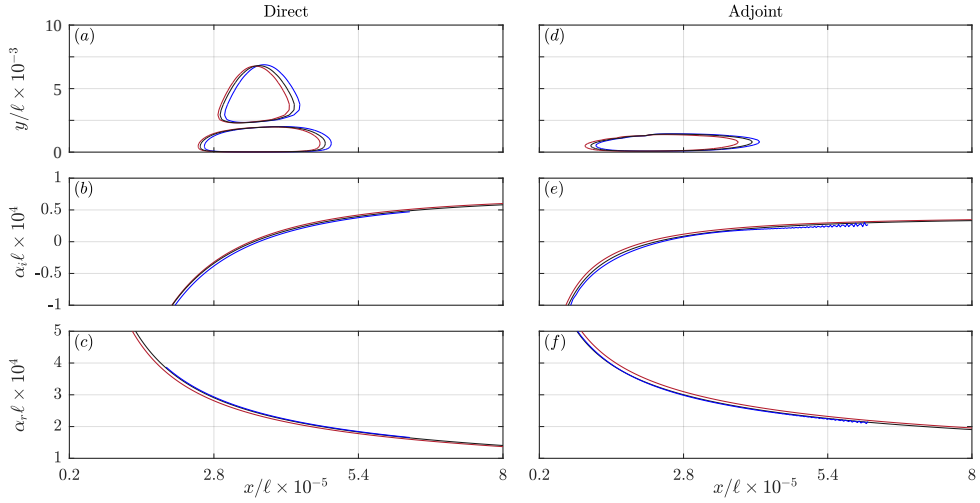

Figure 4.15: (*a*) Direct ($|\tilde{u}| = |\tilde{u}|_{\max}/9$) and (*d*) adjoint ($|\tilde{u}^\dagger| = |\tilde{u}^\dagger|_{\max}/9$) eigenfunctions corresponding to the most unstable global mode at $c_f/u_e = 0.415$ determined by the WKBJ approach excluding (red) or including (black) parallel-flow effects, and the BiGlobal approach (blue). (*b*,*e*) Imaginary and (*c*,*f*) real part of the streamwise wavenumber corresponding to the direct (*b*,*c*) and adjoint (*e*,*f*) eigenfunction for parallel WKBJ (red, $\alpha_g^{(\dagger)}(x)$), non-parallel WKBJ (black, $\alpha_g^{(\dagger)}(x)$), and BiGlobal (blue, $\alpha_{\tilde{v}^{(\dagger)}}$ extracted at constant heights $y/\ell = 1972$ (direct) and 946 (adjoint), cropped for $|\tilde{v}|/|\tilde{v}|_{\max} < 10^{-4}$).

the approximations ω_g with or without the parallel-flow assumption match the most unstable BiGlobal eigenvalue better than ω_s. Accordingly, small relative errors $|\omega - \omega_g|/|\omega| = 3.4\%$ (parallel) and 0.44% (non-parallel) are observed when comparing to the BiGlobal eigenvalue ω. Other BiGlobal eigenvalues on the main branch and the corresponding approximations ω_g for $n = 1, 2, \ldots, 6$ are also shown in figure 4.14(*b*). The overall match between the BiGlobal eigenvalues and the approximation with the WKBJ approach is deemed very good, especially from the perspective of having used an approach that arguably represents a low-order approximation.

4.5.3. Approximation of the global eigenfunctions

The global direct and adjoint eigenfunctions can be reconstructed with the WKBJ approach. In particular, the present work focuses on obtaining a leading-order approximation for the most unstable solution (i.e., $n = 0$). This approximation is obtained by evaluating ansatz (2.24), with the turning-point frequency ω_s and considering x to be real. It relies on the fact that solving the local eigenvalue problem (4.5) for ω_s in the region of X_s yields a double α-solution. When x departs upstream and downstream from X_s, the two $\alpha(\omega_s, x)$ solutions become more distinct, thus forming two branches. The two α-solutions are labeled as follows. One solution, referred to as α^+, has $\alpha_i > 0$ as $|x| \to \infty$ and the other solution α^- is defined for $\alpha_i < 0$ as $|x| \to \infty$. Note that this definition does not imply continuity of the $\alpha^\pm(x)$-branches in x. From now on, referring to an α-branch implies the combination of the function $\alpha(x)$ and the corresponding local shape functions of the perturbation in the wall-normal direction.

Since the global eigenfunctions must be localized solutions, only the α-solutions that decay as $x \to \pm\infty$ are selected. For the direct eigenfunctions, this implies that the α^+-branch ought to be considered as $x \to +\infty$ and α^- as $x \to -\infty$. In practice the α^+-branch is made to

dictate the direct global eigenfunctions' behavior for $x > X_c$ and the α^--branch for $x < X_c$, where X_c is chosen to be the location where $\alpha_i^+ = \alpha_i^-$. Reconstructing the adjoint eigenfunctions is done similarly. The adjoint wavenumber is equal to the complex conjugate of the direct wavenumber (Juniper & Pier, 2015) and the shape function in the wall-normal direction is based on the adjoint equation of the zeroth-order direct problem (4.5) with frequency $\omega_s^\dagger = \omega_s^*$. The local wavenumber of the direct and adjoint global eigenfunctions, $\alpha_g(x)$ and $\alpha_g^\dagger(x)$, are thereby related to the $\alpha^\pm$-branch through

$$\alpha_g(x) = \begin{cases} \alpha^+(x) & \text{for } x > X_c \\ \alpha^-(x) & \text{for } x < X_c \end{cases}, \qquad \alpha_g^\dagger(x) = \begin{cases} (\alpha^-(x))^* & \text{for } x > X_c \\ (\alpha^+(x))^* & \text{for } x < X_c \end{cases}. \tag{4.8}$$

The shape of the global eigenfunctions in the wall-normal direction is governed by the local shape functions corresponding to the α-branches. In practice, these shape functions have an arbitrary phase and amplitude at each individual streamwise location. In order to fit these functions in the WKBJ ansatz (2.24), they are presently normalized by dividing the direct and adjoint functions by their complex value at $y/\ell \approx 1972$ and at 946, respectively. These heights correspond to the collocation nodes for which the shape functions $\tilde{v}$ and $\tilde{v}^\dagger$ are close to attaining their unique maximum value in the wall-normal direction in the domain of interest. The normalization is based on a constant y-value because it ensures that there is no streamwise growth at that height. The choice of the normalization is arbitrary and considering $\tilde{u}$, $\tilde{p}$, or even a different height yields small changes only. The present normalization yields the best match between the solutions corresponding to the different approximation methods. In figure 4.15, the direct (panel (*a*)) and adjoint (panel (*d*)) BiGlobal eigenfunctions corresponding to the most unstable mode are compared against the WKBJ approximations with and without the parallel-flow assumption. The WKBJ and BiGlobal approaches thus yield solutions that have a very similar amplitude distribution and the discrepancies are further reduced when including all non-parallel effects. The streamwise spatial growth rate and wavenumber, shown in figures 4.15(*b*,*e*) and (*c*,*f*), respectively, are also in very good agreement. As indicated in table 4.5 by the location of the streamwise energy centroid, x_E, including all non-parallel effects allows obtaining a solution that lies closer to the BiGlobal eigenfunction. Hence, the WKBJ approach and the global mode theory applied in a moving frame of reference provide a very good approximation of the moving-frame eigensolutions for the flat-plate incompressible boundary layer. Applying the global mode theory to this case demonstrates how the moving frame of reference transforms the fixed-frame problem, that is governed by one downstream-traveling wave, into an elliptic problem for which the leading solution is a combination of downstream- and upstream-traveling waves.

4.6. Intermediate conclusion

This chapter focused on applying the moving-frame methodology on the two-dimensional flat-plate boundary layer. It allowed showing the working principles of the method and how to interpret the moving-reference-frame results, especially by reconstructing the N-factor and neutral curves.

An important aspect was to show that the dependency of the eigenvalue problem on the numerical setup can be eliminated by using a moving frame of reference. In formulating the eigenvalue problem this way, the eigenfunctions describing convective mechanisms become localized in the streamwise direction. That is, the eigenfunction amplitude can be made arbitrarily small at the truncation boundaries by placing those boundaries far enough

from the region of interest. As a consequence, converged solutions can be obtained that are independent of the imposed truncation boundary conditions.

Upon computing the eigenvalue spectrum for the flat-plate boundary-layer case for an appropriate speed of the reference frame, the most unstable solutions arrange themselves in three branches. The modes along all branches are found to represent different configurations of the Reynolds-stress energy production term; they are not higher harmonics of the most unstable mode. Only the main branch contains modes that are independent of the computational setup (resolution, truncation boundary positions and conditions). The effects of the variation of the domain length and frame speed on the two-dimensional eigensolutions have been studied. For a given domain length, localized eigenfunctions can be found if the frame speed and the streamwise discretization are large enough. This is a consequence of the reduced streamwise extent of the eigenfunctions for a larger frame speed. In contrast, in attempting to recover converged solutions for the stationary reference frame, the results suggest that the streamwise domain length and resolution must be considerably extended at a rate that is inversely proportional to the frame speed. This demonstrates that obtaining domain-independent solutions representing convective perturbation mechanisms requires the use of a moving frame of reference and that obtaining such solutions in the stationary reference frame is arguably not possible. Finally, since the flow is only slowly developing in the streamwise direction, a WKBJ method for the nonparallel stability equations formulated in the moving frame of reference was used to confirm the results; the main-branch eigensolutions can be recovered and are in good agreement with the results obtained with the present two-dimensional approach.

A main benefit of the present approach is that the moving-frame eigensolutions solve the stationary-frame linearized Navier-Stokes equations in an instantaneous sense. Hence, in contrast to the situation in the stationary frame of reference, the eigensolutions in the moving frame of reference do not solve the linearized Navier-Stokes equations for all times but only for $t_f = 0$. To obtain the time-dependent solutions, the stationary-frame linearized Navier-Stokes equations are integrated in time with the moving-frame eigenfunctions used as the initial conditions. As demonstrated in Chapter 2, the present analyses showed that the resulting instantaneous growth and movement of the perturbations match the eigeninformation. By using the eigenfunctions of the main branch as initial conditions for the time-integration of the initial-value problem and by performing a Fourier transform of the time-integrated wave-packet, the N-factor and neutral curves are recovered. These curves were shown to be in excellent agreement with PSE results. Importantly, the converged Fourier coefficients are independent of the frame speed and of the choice of the eigenmodes belonging to the main branch. Hence, for the flat-plate boundary layer, time-marching only a single wave packet is sufficient to reconstruct the N-factor and neutral curves for a streamwise region of interest. The only requirement is to find an eigensolution with a spatially-localized eigenfunction that is located sufficiently upstream of the region where converged Fourier coefficients are sought. In practice, obtaining complete N-factor and neutral curves requires finding eigenfunctions located upstream of the neutral point.

A considerable aspect of using the moving-frame eigenfunctions as initial conditions is that transients are avoided when time-marching the solutions. Avoiding transients is essential in obtaining uncontaminated N-factor curves. This contrasts with the usual situation in which the LST solutions are used to initialize the spatial marching of the PSE. The LST solutions do not solve the PSE at a given streamwise station and hence a transient solution behavior is inevitable. No such transient behavior has to be dealt with in the present methodology, because the eigensolutions are instantaneously exact solutions to the linearized Navier-Stokes equations. Furthermore, by having formulated the problem as an eigenvalue prob-

lem and then use the obtained moving-frame eigensolutions as initial conditions, the dynamics has not been restricted to an optimal-growth scenario as would be the case with SVD methods. Instead, the present approach provides a lower bound for the growth, rather than an upper bound. Having access to this lower bound allows reconstructing the traditional N-factor and neutral curves.

References

Åkervik, E., Ehrenstein, U., Gallaire, F. & Henningson, D. S. 2008 Global two-dimensional stability measures of the flat plate boundary-layer flow. *European Journal of Mechanics - B/Fluids* **27** (5), 501–513.

Alizard, F. & Robinet, J.-C. 2007 Spatially convective global modes in a boundary layer. *Physics of Fluids* **19** (11), 114105.

Alves, L. S. d. B., Hirata, S. C., Schuabb, M. & Barletta, A. 2019 Identifying linear absolute instabilities from differential eigenvalue problems using sensitivity analysis. *Journal of Fluid Mechanics* **870**, 941–969.

Arratia, C., Mowlavi, S. & Gallaire, F. 2018 Absolute/convective secondary instabilities and the role of confinement in free shear layers. *Physical Review Fluids* **3** (5), 053901.

Bertolotti, F. P., Herbert, T. & Spalart, P. 1992 Linear and nonlinear stability of the Blasius boundary layer. *Journal of Fluid Mechanics* **242**, 441–474.

Blasius, H. 1908 Grenzschichten in flüssigkeiten mit kleiner reibung. *Zeitschrift für angewandte Mathematik und Physik* **56**, 1–37.

Boyd, J. P. 2001 *Chebyshev and Fourier spectral methods*. Courier Corporation.

Brevdo, L. 1988 A study of absolute and convective instabilities with an application to the Eady model. *Geophysical and Astrophysical Fluid Dynamics* **40** (1-2), 1–92.

Brevdo, L. 1995 Convectively unstable wave packets in the Blasius boundary layer. *Journal of Applied Mathematics and Mechanics* **75** (6), 423–436.

Chomaz, J.-M., Huerre, P. & Redekopp, L. G. 1991 A frequency selection criterion in spatially developing flows . *Studies in applied mathematics* **84**, 119–144.

Christodoulou, K. & Scriven, L. 1988 Finding leading modes of a viscous free surface flow: An asymmetric generalized eigenproblem. *Journal of scientific computing* **3**, 355–406.

Deissler, R. J. 1987 The convective nature of instability in plane Poiseuille flow. *Physics of Fluids* **30** (8), 2303–2305.

Driscoll, T. A., Hale, N. & Trefethen, L. N. 2014 *Chebfun Guide*. Pafnuty Publications.

Ehrenstein, U. & Gallaire, F. 2005 On two-dimensional temporal modes in spatially evolving open flows: the flat-plate boundary layer. *Journal of Fluid Mechanics* **536**, 209–218.

Fasel, H. & Konzelmann, U. 1990 Non-parallel stability of a flat-plate boundary layer using the complete navier-stokes equations. *Journal of Fluid Mechanics* **221**, 311–347.

Gaster, M. 1974 On the effects of boundary-layer growth on flow stability. *Journal of Fluid Mechanics* **66** (3), 465–480.

Gaster, M. & Grant, I. 1975 An experimental investigation of the formation and development of a wave packet in a laminar boundary layer . *Proceedings of the Royal Society A: Mathematical, Physical and Engineering Sciences* **347** (1649), 253–269.

GOVINDARAJAN, R. & NARASIMHA, R. 1995 Stability of spatially developing boundary layers in pressure gradients. *Journal of Fluid Mechanics* **300**, 117–147.

GROOT, K. J. 2013 Derivation of and simulations with BiGlobal stability equations. Master's thesis, Delft University of Technology.

GROOT, K. J., MIRÓ MIRÓ, F., BEYAK, E. S., MOYES, A. J., PINNA, F. & REED, H. L. 2018 DEKAF: spectral multi-regime basic-state solver for boundary layer stability. In *2018 Fluid Dynamics Conference*.

GROOT, K. J., PINNA, F. & VAN OUDHEUSDEN, B. W. 2015 On closing the streamwise BiGlobal stability problem: the effect of boundary conditions. *Procedia IUTAM* **14**, 459–468.

GROOT, K. J. & SCHUTTELAARS, H. M. 2020 Accurate numerical approximation of the absolute stability of unbounded flows. *Physica D: Nonlinear Phenomena* **402**, 132224.

HERBERT, T. 1997 Parabolized stability equations. *Annual Review of Fluid Mechanics* **29**, 245–283.

HERBERT, T. & BERTOLOTTI, F. 1987 Stability analysis of nonparallel boundary layers. *Bulletin of the American Physical Society* **32** (2079), 590.

HUERRE, P. & MONKEWITZ, P. A. 1990 Local and Global Instabilities in Spatially Developing Flows. *Annual Review of Fluid Mechanics* **22**, 473–537.

HUERRE, P. & ROSSI, M. 2009 Hydrodynamic instabilities in open flows. In *Hydrodynamics and Nonlinear Instabilities*, pp. 81–294. Cambridge University Press.

JUNIPER, M. P. & PIER, B. 2015 The structural sensitivity of open shear flows calculated with a local stability analysis. *European Journal of Mechanics - B/Fluids* **49**, 426–437.

JUNIPER, M. P., TAMMISOLA, O. & LUNDELL, F. 2011 The local and global stability of confined planar wakes at intermediate Reynolds number. *Journal of Fluid Mechanics* **686**, 218–238.

LESSHAFFT, L. 2017 Artificial eigenmodes in truncated flow domains. *Theoretical and Computational Fluid Dynamics* **32** (3), 245–262.

LIN, C. 1944 On the stability of two-dimensional parallel flows. *Proceedings of the national academy of sciences* **30** (10), 316–324.

MONKEWITZ, P. A., HUERRE, P. & CHOMAZ, J.-M. 1993 Global linear stability analysis of weakly non-parallel shear flows. *Journal of Fluid Mechanics* **251**, 1–20.

RODRÍGUEZ, D. A. 2010 Global instability of laminar separation bubbles. PhD thesis, Universidad Politécnica de Madrid.

SCHMID, P. J. & BRANDT, L. 2014 Analysis of fluid systems: stability, receptivity, sensitivity. *Applied Mechanics Reviews* **66** (2), 24803.

SCHUBAUER, G. B. & SKRAMSTAD, H. K. 1948 Laminar-Boundary-Layer Oscillations and Transition on a Flat Plate. *Tech. Rep.* NACA-TR-909. NACA.

SICONOLFI, L., CITRO, V., GIANNETTI, F., CAMARRI, S. & LUCHINI, P. 2017 Towards a quantitative comparison between global and local stability analysis. *Journal of Fluid Mechanics* **819**, 147–164.

SIPP, D. & MARQUET, O. 2012 Characterization of noise amplifiers with global singular modes: the case of the leading-edge flat-plate boundary layer. *Theoretical and Computational Fluid Dynamics* **27** (5), 617–635.

TISSOT, G., ZHANG, M., LAJÚS, F. C., CAVALIERI, A. V. G. & JORDAN, P. 2017 Sensitivity of wavepackets in jets to nonlinear effects: the role of the critical layer. *Journal of Fluid Mechanics* **811**, 95–137.

WHITE, F. 1991 *Viscous fluid flow*. McGraw-Hill Professional Publishing.

WRIGHT, A. N., MILLS, K. J., RUDERMAN, M. S. & BREVDO, L. 2000 The absolute and convective instability of the magnetospheric flanks. *Journal of Geophysical Research* **105** (1), 385–393.

5

The laminar shock-wave/boundary-layer interaction

The present chapter considers a laminar shock-wave/boundary-layer interaction (SWBLI) flow and has two main objectives. First, it aims to demonstrate that formulating the two-dimensional streamwise stability equations in a moving frame of reference allows obtaining eigensolutions that are independent of the truncation boundaries. In particular, it extends the verification of Chapter 4 to two- and three-dimensional perturbations in a rapidly evolving flow that inherently necessitates an elliptic formulation of the stability equations to capture all in-plane gradients. The second objective is to identify and characterize the instability mechanisms related to convective instabilities in the laminar SWBLI. In practice, after having reconstructed the individual-frequency amplification curves, the frequencies and spanwise wavenumbers yielding the largest spatial amplification across the shock-induced bubble are identified. The corresponding instability mechanisms are then thoroughly analyzed by decomposing the material derivative of the perturbation energy into its individual physical mechanisms.

To address these two objectives, the present chapter is structured as follows. In §5.1, an overview of the SWBLI physics is proposed. A particular emphasis is put on the instabilities in SWBLI and on the methodologies used in past studies to identify them. Thereafter, §5.2 discusses the flow configuration, the numerical setup and the Selective Frequency Damping (SFD) method used to obtain the steady base-flow solution. In §5.3, the initial conditions, i.e., the moving-frame eigensolutions, used to disturb the flow are presented. This section also proposes an in-depth analysis of the eigengrowth mechanisms. The initial-value problem is then solved in §5.4 to obtain the finite-time evolution of the perturbation wave packets. By applying the Fourier transform on these temporal solutions, the individual-frequency amplification curves are reconstructed. In §5.5, the physical mechanisms responsible for the growth of the most amplified wave packets are characterized. Finally, an intermediate conclusion is proposed in §5.7.

5.1. Context: SWBLI and instabilities

Shock-wave/boundary-layer interaction is a ubiquitous phenomenon in high-speed aerodynamics that significantly impacts aircraft performance by, for instance, promoting laminar-turbulent transition, causing excessive heating of aerodynamic surfaces, creating pressure losses in engine intakes or even local fatigue of the solid structures (Délery & Dussauge, 2009). SWBLI is present in applications ranging from the transonic to hypersonic regime and a comprehensive understanding of its physics is required to devise effective and efficient high-speed vehicles. The first observations of SWBLI were made on airfoils by Ferri (1939) and, shortly later, thorough experimental studies have been published with normal (Donaldson, 1944), compression ramp (Liepmann, 1946; Ackeret *et al.*, 1947) and normal/oblique (Fage & Sargent, 1947) shock waves. Since then, SWBLI has been extensively studied over numerous flow configurations; the progress accomplished over the past decades have been reviewed by, e.g., Délery *et al.* (1986), Dolling (2001),Babinsky & Harvey (2011), Gaitonde (2015) and Gaitonde & Adler (2023). Considerable efforts have been invested to reveal the mechanisms governing the unsteadiness of the SWBLI, such as breathing of the recirculation bubble, oscillations of the shock system, or laminar-turbulent transition, but comprehensive research is still required to better understand these phenomena.

The unsteadiness of the SWBLI often refers to low-frequency oscillations of the interaction region (Dolling, 2001). Numerous computational and numerical investigations have been conducted to determine the physical mechanisms at the origin of this unsteadiness and have led to a classification of the mechanisms into two main categories. On the one hand, Beresh *et al.* (2002), Ganapathisubramani *et al.* (2007), Ganapathisubramani *et al.* (2009) and Wu & Martín (2008) suggested that the SWBLI acts as an amplifier of upstream incoming disturbances that enter the shock-induced separated boundary layer. Recent studies have also demonstrated the importance of what is referred to as an upstream-influence shock (Tester *et al.*, 2018; Lash *et al.*, 2021; Nutter *et al.*, 2021; Sebastian & Lu, 2021), an oscillating shock that is located far upstream of the interaction and whose frequency content could be correlated with the unsteadiness of the shock-induced bubble. The related studies rely on the statistical correlation of the incoming perturbations and the low-frequency response of the interaction region. However, this approach does not seem applicable for all cases as, for example, Wu & Martín (2008) did not find a significant correlation in one of their configurations. On the other hand, Touber & Sandham (2008), Touber & Sandham (2009), Pirozzoli & Grasso (2006), Dussauge *et al.* (2006), Piponniau *et al.* (2009), Grilli *et al.* (2012), Sansica *et al.* (2016), Pasquariello *et al.* (2017), Adler & Gaitonde (2018) and Sasaki *et al.* (2021) showed evidence of mechanisms that have a more intrinsic character. In fact, this second theory propounds that a feedback mechanism can cause downstream disturbances, present in the aft-shock region, to be entrained and amplified within the recirculation bubble. In turbulent SWBLI, Clemens & Narayanaswamy (2014) have suggested that the two types of mechanisms are always present together, with the intrinsic one becoming more dominant as the separation region increases. In laminar/transitional SWBLI, according to Sansica *et al.* (2016), Dwivedi *et al.* (2020), Bonne *et al.* (2019) and Bugeat *et al.* (2022), the low-frequency unsteadiness is not a self-sustained mechanism and thus needs to be forced. However, since the interaction region acts as a low-pass spatial amplification filter (Sansica *et al.*, 2016; Bugeat *et al.*, 2022), the low-frequency oscillations do not need to be forced necessarily at a low frequency. Furthermore, Sansica *et al.* (2016) and Bonne *et al.* (2019) have argued that the low-frequency oscillations can originate from upstream traveling waves that are triggered by instability mechanisms or a laminar-turbulent transition process taking place in the downstream portion of the interaction region. Ultimately, al-

though remarkable progress has been made during the past decade, no consensus has been reached regarding the origin of this unsteadiness.

Several instability mechanisms in laminar and turbulent SWBLI have been investigated in past studies. Among all of them, global mechanisms are of particular interest because they represent localized modes that are intrinsic to the interaction region. Oscillatory global modes at the origin of the low-frequency breathing and the downstream vortex shedding were found by Nichols *et al.* (2017) and Pirozzoli *et al.* (2010) in turbulent SWBLI. However, in laminar (shock-induced) separation bubbles, only a global *stationary* mode has been found so far (Robinet, 2007; Hildebrand *et al.*, 2018; Rodríguez *et al.*, 2020), that is responsible for a two-to-three-dimensional topological change of the separation bubble. Although Robinet (2007) suggested that a three-dimensional bubble is a prerequisite for the low-frequency oscillations in laminar SWBLI, the non-oscillatory global instability mechanism cannot be held responsible for sustaining the unsteadiness. In this sense, Guiho *et al.* (2016) concluded that laminar SWBLIs in a broad range of conditions are globally stable and thus convective instability mechanisms should be considered.

Convective instabilities in laminar SWBLI were tackled by Yao *et al.* (2007) and Sansica *et al.* (2014) through the response of the flow to external forcing with Direct Numerical Simulations (DNS) and/or Large Eddy Simulations (LES). However, as mentioned in the introduction (Chapter 1), these methods require judicious initial conditions or forcing to perturb the (convectively unstable) flow and their relatively high computational cost restricts the study of the perturbation dynamics to a limited range of forcing configurations. To circumvent this limitation, Yao *et al.* (2007) and Sansica *et al.* (2016) relied on Linear Stability Theory (LST) and Parabolized Stability Equations (PSE) approaches to examine the growth of perturbations through convective instability mechanisms in laminar SWBLI. The stability results are in good agreement with DNS for weak oblique shocks. However, for strong interactions, the results are affected by the parallel or slow-evolution assumptions on which LST or PSE rely, respectively. Furthermore, although streamwise variations are better captured by PSE, the parabolized formulation of the equations in the streamwise direction prevents capturing the upstream response to downstream forcing. For these reasons, studying the stability of SWBLI requires considering fully-elliptic equations.

The streamwise BiGlobal stability problem is particularly suitable to identify instability mechanisms in SWBLI and has yielded different outcomes in the past. On the one hand, Robinet (2007), Pirozzoli *et al.* (2010) and Nichols *et al.* (2017) have highlighted the presence of the previously described *global* instability mechanisms that are localized in the shock-induced separation bubble. On the other hand, Guiho *et al.* (2016) have identified *convective* instability mechanisms that can be activated by external perturbations entering the bubble before being swept away by the flow. However, since the analyses are conducted in a stationary frame of reference, the results corresponding to convective instabilities are tainted by their sensitivity with respect to the truncation boundaries, i.e., domain length, boundary conditions, and streamwise discretization. Hence, because unstable global modes are not found, Guiho *et al.* (2016) could only conclude that their laminar SWBLIs are globally stable. The present work improves the characterization of the three-dimensional convective instability mechanisms in a two-dimensional laminar SWBLI flow with the moving-frame methodology.

5.2. Flow configuration and numerical setup

The flow considered in the present study consists of an incident shock that impinges on a laminar flat-plate boundary layer (figure 5.1). Experimental measurements of a similar flow

Table 5.1: Flow parameters for the laminar shock-wave/boundary-layer interaction.

M	u_e [m/s]	Ec	$T_{e,\text{total}}$ [K]	$p_{e,\text{static}}$ [Pa]	Re_e [1/m]	Re_{x_0}	$\text{Re}_{x_{\text{imping.}}}$	θ_{incident}
1.7	452.12	1.156	277.73	2.3×10^5	3.5×10^7	7×10^5	1.785×10^6	37.93°

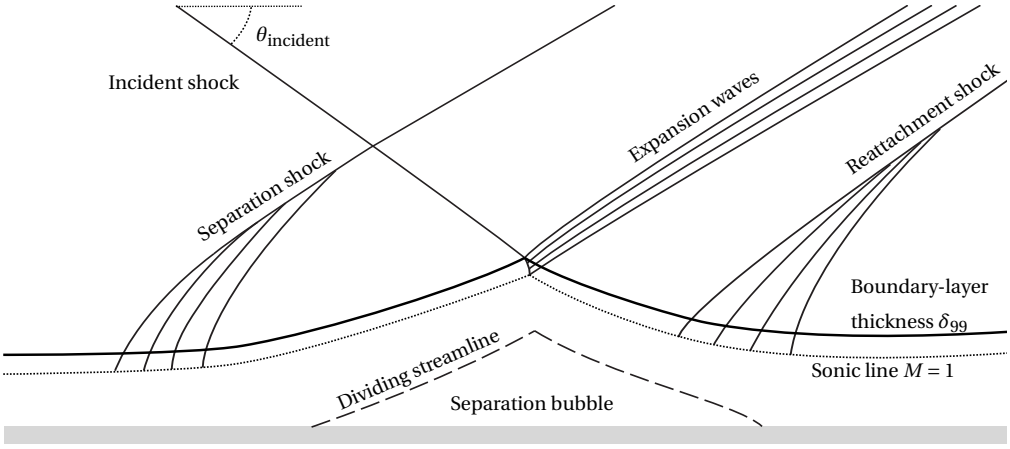

Figure 5.1: Schematic of a shock-wave/boundary-layer interaction with laminar separation bubble.

have been conducted by Giepman (2016) for various shock-wave angles, impinging locations and regimes of the incoming boundary layers. The present numerical analyses are conducted on one flow configuration for which the laminar-turbulent transition occurs downstream of the incident shock. The main setup parameters are summarized in table 5.1. The incoming laminar boundary layer enters the numerical domain at $x_{\text{f},0}/\ell = \text{Re}_{x_{\text{f},0}} = 7 \times 10^5$ with thickness $\delta_0/\ell = \text{Re}_{\delta_0} = 5073$. The freestream Mach and unit Reynolds numbers are M = 1.7 and $\text{Re}_e = 1/\ell = 3.5 \times 10^7$ [m^{-1}], respectively. The incident shock is generated in the freestream with a 2° wedge, has an angle $\theta_{\text{incident}} = 37.93°$, and impinges on the laminar boundary layer at $x_{\text{imping.}}/\ell = \text{Re}_{x_{\text{imping.}}} = 1.785 \times 10^6$. The measurements by Giepman (2016) indicate that the laminar-turbulent transition takes place as a consequence of the perturbation development in the SWBLI. When using a computational approach to simulate the flowfield without an artificial/numerical stabilization technique, this particular unsteadiness prevents the simulation from reaching a laminar steady state. Furthermore, the specific experimental conditions feature a wall-temperature distribution that varies in time and that would thus prevent finding a steady-state solution. To avoid complications introduced by such a boundary condition, and because no further information about perturbations is provided by the experiment anyway, a close but more canonical case is considered here, in which the wall is assumed to be adiabatic.

5.2.1. Numerical setup

The base flow is obtained by solving the compressible Navier-Stokes equations via finite-volume DNS (Hickel *et al.*, 2014). The time-integration is achieved with an explicit fourth-order Runge-Kutta scheme and the temporal resolution is fixed by a global time step such that the Courant-Friedrichs-Lewy condition CFL < 1 is satisfied for each grid point in the domain. The spatial discretization in the streamwise direction x relies on a uniform Carte-

sian structured grid with N_x points and the domain length for the base flow is $L/\ell = 2.5365 \times 10^6$. In the wall-normal direction y, the grid is stretched with a hyperbolic function in order to cluster grid points near the wall in the shear-layer region ($\Delta y^+ < 1$) and around the shock-impingement location. The domain height is $H/\ell = 0.76095 \times 10^6$, i.e., 150 times the boundary-layer height at the inlet. The convective fluxes are evaluated with a third-order weighted essentially non-oscillatory (WENO) scheme coupled with the Harten–Lax–van Leer contact (HLLC) approximate Riemann solver. The viscous fluxes are computed with a second-order central difference scheme. The effectiveness of the present flux-reconstruction method in obtaining non-oscillatory SWBLI flows has been previously assessed by Niessen (2017).

The boundary conditions are imposed as follows. A compressible flat-plate boundary-layer profile is prescribed at the inlet and the incident oblique shock, emanating from the upper boundary, is imposed by a Rankine-Hugoniot condition. The solid wall ($y = 0$) is an adiabatic surface on which the no-slip condition for the velocity is enforced (i.e., $u_i = 0$). At the outflow, a homogeneous Neumann condition in the streamwise direction governs all variables. To avoid shock-wave reflections on the domain borders, a Riemann-invariant-based non-reflective condition is imposed at all truncation boundaries.

5.2.2. Steady-state solution: Selective Frequency Damping method

Stability analysis relies on the evolution of perturbations around a base-flow solution $\overline{\boldsymbol{Q}}$, that is a laminar equilibrium solution of the governing equations (2.1). The base-flow solution must thus satisfy the steady Navier-Stokes equations

$$\frac{\partial \overline{\boldsymbol{Q}}}{\partial t_\mathrm{f}} = \mathcal{N}(\overline{\boldsymbol{Q}}) = 0\,. \tag{5.1}$$

Since the present flow naturally becomes unsteady, the Selective Frequency Damping (SFD) method (Åkervik *et al.*, 2006; Jordi *et al.*, 2014; Casacuberta *et al.*, 2018) is used in order to drive the unsteady flow field $\boldsymbol{q}_\mathrm{f}$ towards $\overline{\boldsymbol{Q}}$. The SFD approach contrasts with past stability analyses carried out on laminar SWBLI (Robinet, 2007; Yao *et al.*, 2007; Sansica *et al.*, 2014; Guiho *et al.*, 2016; Sansica *et al.*, 2016; Hildebrand *et al.*, 2018; Cerulus *et al.*, 2021), which used long-time nonlinear saturation of two-dimensional DNS to obtain stable steady-state base-flow solutions. This latter approach to obtain the laminar base flow is effective solely when the considered laminar flow is stable to all two-dimensional perturbations. For the present case, the flow configuration contains a strong shock-induced separation region with laminar-turbulent transition downstream of the separation-bubble apex, which thus prevents reaching a steady-state naturally. By considering the SFD approach, the instability mechanisms triggering the transition can be damped out and thus, upon achieving a negligible residual, an unstable steady-state base-flow solution can be accurately obtained.

In the SFD approach, a source term is introduced into the Navier-Stokes equations (2.1) that is proportional to the high-frequency content ($\boldsymbol{q}_\mathrm{f} - \boldsymbol{q}_\mathrm{lf}$) of the flow. The field $\boldsymbol{q}_\mathrm{lf}$ represents a low-pass filtered version of the flow field $\boldsymbol{q}_\mathrm{f}$ and serves as an approximation of the unknown base-flow solution $\overline{\boldsymbol{Q}}$. Following Åkervik *et al.* (2006), an exponential filter is chosen to calculate $\boldsymbol{q}_\mathrm{lf}$ and the modified Navier-Stokes equations are therefore given by

$$\frac{\partial \boldsymbol{q}_\mathrm{f}}{\partial t_\mathrm{f}} = \mathcal{N}(\boldsymbol{q}_\mathrm{f}) - \chi_s(\boldsymbol{q}_\mathrm{f} - \boldsymbol{q}_\mathrm{lf})\,, \tag{5.2a}$$

$$\frac{\partial \boldsymbol{q}_\mathrm{lf}}{\partial t_\mathrm{f}} = \frac{\boldsymbol{q}_\mathrm{f} - \boldsymbol{q}_\mathrm{lf}}{\Delta_s}\,, \tag{5.2b}$$

with the positive real-valued parameters Δ_s and χ_s representing the bandwidth of the filter and the feedback control parameter, respectively. In the present case, $\chi_s \delta_0 / u_e = 0.65$ and

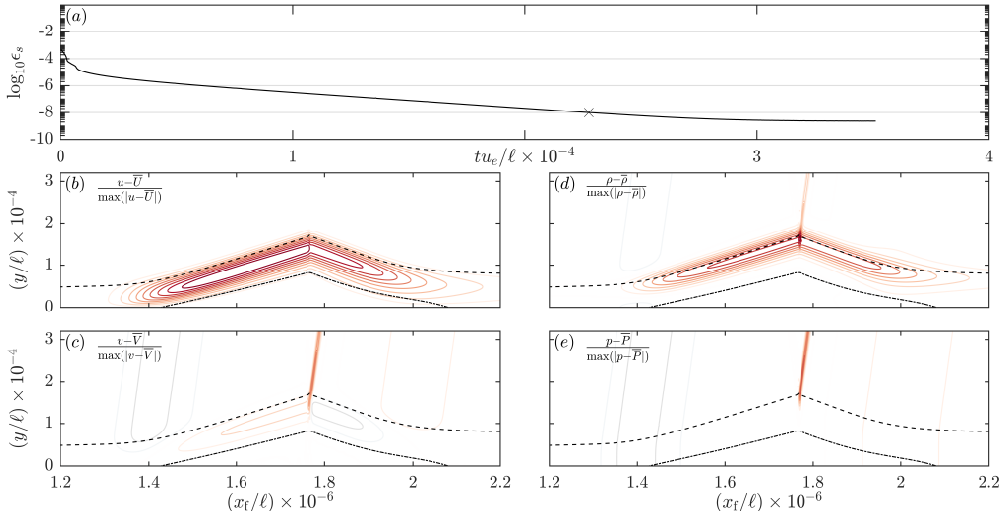

Figure 5.2: (*a*) SFD residual $\epsilon_s = ||\mathbf{q}_f - \mathbf{q}_{lf}||_{L_2} / \sqrt{\mathscr{S}_f}$ as a function of the physical time. Perturbation shape in space when $\epsilon_s = 10^{-8}$ (indicated by × in (*a*)): (*b*) $(u-\overline{U})/\max(|u-\overline{U}|)$; (*c*) $(v-\overline{V})/\max(|v-\overline{V}|)$; (*d*) $(\rho-\overline{\rho})/\max(|\rho-\overline{\rho}|)$; (*e*) $(p-\overline{P})/\max(|p-\overline{P}|)$ (colored lines, 20 contours from minimum (-1, gray) to maximum (1, red)). (*b–e*) Boundary-layer edge (δ_{90}, dashed); $\overline{U}=0$ (dash-dotted).

$\Delta_s u_e/\delta_0 = 1.64$ are used. The effectiveness of the SFD in driving $\boldsymbol{q}_f$ towards $\boldsymbol{q}_{lf}$ is assessed by monitoring the L_2-norm of the unsteady residual $\epsilon_s = ||\boldsymbol{q}_f - \boldsymbol{q}_{lf}||_{L_2} / \sqrt{\mathscr{S}_f}$, with $\mathscr{S}_f$ the surface area of the two-dimensional domain. Upon driving the residual to zero, the low-pass filtered variable $\boldsymbol{q}_{lf}$ satisfies the steady Navier-Stokes equations and the steady-state base-flow $\overline{\boldsymbol{Q}}$ is thus given by $\boldsymbol{q}_{lf}$. For the present case, the residual saturates at $\mathscr{O}(10^{-9})$ as depicted in figure 5.2(*a*).

As thoroughly demonstrated by Casacuberta *et al.* (2018), the SFD method relies on a strategical choice of the two parameters Δ_s and χ_s to effectively and efficiently converge to low residual levels. In particular, in the presence of an unsteady, two-dimensional global mode, Casacuberta *et al.* (2018) propose the unleash technique to determine optimal coefficients that maximize the convergence rate. First, the least stable steady mode that rules the convergence rate is evaluated when $\chi_s \neq 0$, i.e., when the time-integration is controlled with the SFD forcing term. In the present case, this steady mode corresponds to an expansion of the separation bubble (figure 5.2(*b–e*)) with a growth rate $\omega_i \ell / u_e = -2.434 \times 10^{-8}$. Since the growth rate is negative, the flow is effectively driven towards a steady-state solution for which the bubble expansion becomes less and less dominant. Second, a white-noise perturbation of magnitude ϵ_s is superimposed to the base flow $\overline{\boldsymbol{Q}} = \boldsymbol{q}_{lf}$, that has been obtained at a certain low residual ϵ_s. The time-integration is then pursued with $\chi_s = 0$, i.e., without the SFD forcing term. In this uncontrolled time-integration (with $\chi_s = 0$), the most unstable, two-dimensional global mode must establish with an exponential growth rate that corresponds to the slope of the temporal evolution of $||\boldsymbol{q}_f - \overline{\boldsymbol{Q}}||_{L_2}$. When using this technique, Casacuberta *et al.* (2018) indicate that the exponential growth could be preceded by an algebraic growth that rapidly becomes overwhelmed by the exponential growth of the most unstable global mode, if it exists. In the present case, the unleash technique, however, reveals only an algebraic growth that is not followed by any exponential growth. This thus indicates that the present SWBLI does not support any unstable, two-dimensional global mode. Accordingly, the SFD coefficients could not be optimized with the unleash technique. Despite

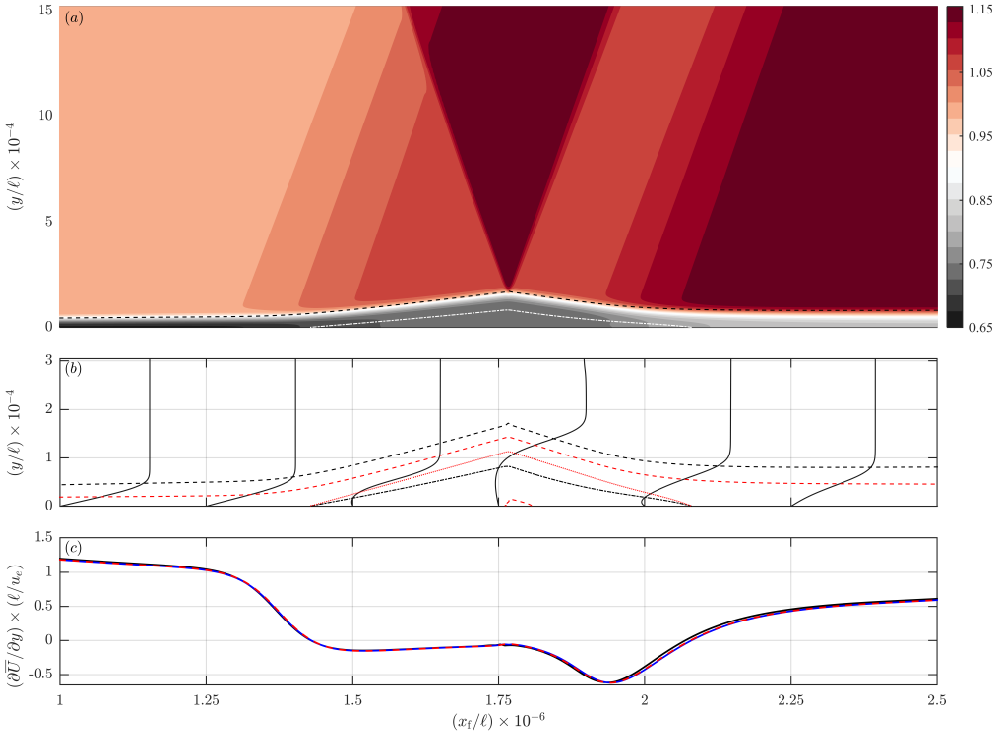

Figure 5.3: (*a*) Isocontours of $\overline{\rho}/\rho_e$. (*b*) $\overline{U}/u_e$-velocity profiles, magnified by a factor $30\mathrm{Re}_{\delta_0}$, at streamwise locations $x_f/\ell \times 10^{-6} = 1, 1.25, 1.5, 1.75, 2, 2.25$. Locus of generalized inflection points (dashed red line) and dividing streamline (dotted red line). (*a*, *b*) $\delta_{90} = \delta(\overline{U} = 0.90u_e)$ in dashed black line and $\overline{U} = 0$ in dash-dotted line. (*c*) $\partial\overline{U}/\partial y$ evaluated at the wall for grids $N_x \times N_y = 500 \times 250$ (solid black), 1000×500 (dashed red), and 2000×1000 (solid blue).

being not optimal, the aforementioned parameters did prove to be effective.

5.2.3. Base-flow results

The density field $\overline{\rho}$ of the base flow is presented in figure 5.3(*a*) in which the dashed black and dash-dotted white lines indicate the boundary-layer thickness ($\delta_{90} = \delta(\overline{U} = 0.9u_e)$) and the zero-velocity ($\overline{U} = 0$) isoline, respectively. A zoom-in representation of the separation bubble is shown in figure 5.3(*b*) along with the velocity profiles at several streamwise locations. The dividing streamline (dotted red line) and the zero-velocity isocontour (dash-dotted black line) show that the separation region is relatively long ($L_{\mathrm{sep}}/\ell \approx 6.50 \times 10^5$) compared to the boundary-layer thickness. The separation bubble has the typical triangular shape of laminar SWBLI and no secondary recirculation is found for the present case. Finally, for the same flow configuration, Niessen (2017) showed very good agreement with free-interaction theory (Chapman *et al.*, 1958).

A sensitivity analysis performed on the domain length confirms that the inflow and outflow boundaries do not interact with the long separation bubble and thus do not influence the results. The Riemann boundary conditions effectively avoid reflections that would impact the interior of the domain. Finally, grid convergence of the results is demonstrated in figure 5.3(*c*) by means of $\partial\overline{U}/\partial y$ evaluated at the wall for three different mesh sizes. The

coarsest grid consists of $N_x \times N_y = 500 \times 250$ points, with N_x and N_y the number of points in the streamwise and wall-normal directions, respectively. The intermediate grid is two times denser and the finest grid is four times denser than the coarsest grid in both directions. The length of the separation bubble, i.e., the distance between the two x-locations where $\partial\overline{U}/\partial y|_{y=0} = 0$, is $L_{\text{sep}}/\ell \times 10^{-5} = 6.36$, 6.48, and 6.50 from the least dense to the densest grid. This shows that the solution converges and that, with a further resolution increase, the difference in the separation length would be negligible. For the stability analyses, the base-flow solution on the densest grid is used.

Two-dimensional, unsteady global modes are found not to exist by using the unleash technique of the SFD method. Moreover, as later commented on in §5.3, three-dimensional, global modes, steady or unsteady, are neither expected nor recovered in the present computational effort. According to Robinet (2007), the three-dimensional steady global mode, associated with the spanwise modulation of the bubble, is unstable only if a secondary recirculation exists within the two-dimensional separation bubble. Since there is no secondary recirculation for the present configuration, the flow is expected to be globally stable. Furthermore, Avanci *et al.* (2019) proposed a geometrical criterion to determine whether the separation bubble is convectively or absolutely unstable. This criterion is based on the relative position between the dividing streamline (i.e., zero-mass flux isoline) and the locus of inflection points of the streamwise velocity profile in the wall-normal direction. In particular, they showed that, for incompressible flows, upstream propagation of disturbances is expected if the inflection points $y_{\mathscr{I}}$ lie below the zero-mass-flux isoline $y_{\mathscr{D}}$ (i.e., in the region where the streamwise mass flux is negative). If this is the case, an absolute instability mechanism is expected in the separation region. For compressible flows, these locations can be defined as

$$\frac{\partial}{\partial y}\left(\overline{\rho}\frac{\partial \overline{U}}{\partial y}\right)\bigg|_{y_{\mathscr{I}}} \overset{(a)}{=} 0, \qquad \int_0^{y_{\mathscr{D}}} \overline{\rho}\overline{U}\,\mathrm{d}y \overset{(b)}{=} 0 \tag{5.3}$$

As shown in figure 5.3(*b*), the wall-normal coordinate of the dividing streamline $y_{\mathscr{D}}$ (dotted red line) is located below the generalized inflection point $y_{\mathscr{I}}$ (dashed red line). Hence, upon extrapolating the criterion to the compressible regime, it is expected that the flow is not absolutely unstable but rather exhibits solely convective instability mechanisms.

5.3. Initial conditions: eigensolutions

In order to ensure the effectiveness of the present approach, it is key to consider eigensolutions that do not depend on the truncation boundaries, i.e., eigensolutions that have *both localized direct and adjoint eigenfunctions*. As for the incompressible boundary layer, an eigenfunction is deemed localized in the domain when (at least) an $\mathscr{O}(1)$-relative change in the domain length yields less than an $\mathscr{O}(10^{-4})$-relative change in both the real and imaginary parts of the eigenvalue. It is furthermore demanded that the eigenvalue converges when increasing the domain length. Based on these requirements, three different types of modes can be identified in the SWBLI. After presenting the numerical setup in §5.3.1, the spectra and eigenfunctions corresponding to these modes are discussed in §5.3.2. The underlying mechanisms of the eigengrowth are then analyzed in §5.3.3 and the influence of the frame speed on the solutions is discussed in §5.3.4 in order to identify the ideal initial conditions to disturb the flow.

Table 5.2: Stability-analysis reference parameters representative of the most unstable 2D and 3D cases.

	c_f/u_e	$\beta\ell$	N_x	x_{in}/ℓ	x_{out}/ℓ	N_y	$y_{i,1}/\ell$	$y_{i,2}/\ell$	y_{max}/ℓ
#1	0.628	0	1900	0.8×10^6	2.6×10^6	160	50×10^3	−−	3×10^5
#2	0.557	9.06×10^{-5}	2400	0.8×10^6	3.0×10^6	120	12×10^3	3×10^4	1×10^5
#3	0.587	9.06×10^{-5}	2400	0.8×10^6	3.0×10^6	120	12×10^3	3×10^4	1×10^5
#4	0.615	25.5×10^{-5}	2400	0.8×10^6	3.0×10^6	120	12×10^3	3×10^4	1×10^5

5.3.1. Numerical setup for the eigenvalue problem

The computational domain for the eigenvalue problem is truncated in the up- and downstream directions, at $x = x_{in}$ and $x = x_{out}$, and far from the flat plate at $y = y_{max}$ ($x = 0$ corresponds to the leading edge and $y = 0$ to the wall). The truncation boundaries at $x = x_{in}$ and $x = x_{out}$ are respectively referred to as the in- and outflow boundaries. The streamwise domain length is denoted by $L = x_{out} - x_{in}$. Homogeneous Neumann conditions are used at the in- and outflow boundaries for all perturbation variables in order to allow perturbations to be large at the boundaries if the dynamics in the interior of the domain demands it. At $y = y_{max}$, velocity and temperature perturbations are required to vanish. The direct and adjoint eigenvalue problems are discretized with a fourth-order central finite-difference scheme in x and Chebyshev collocation in y. The grid incorporates N_x and N_y discrete points in the streamwise and wall-normal directions, respectively. In the wall-normal direction y, the Malik mapping is used in order to place one-half of the collocation points in $[0, y_{i,1}]$ and the other in $[y_{i,1}, y_{max}]$ for the two-dimensional case. Since eigenfunctions have a slower decay and a smaller wavenumber in the wall-normal direction for two-dimensional cases than for three-dimensional cases, the Malik mapping is not suitable for solutions corresponding to non-zero β. Hence, for the three-dimensional ($\beta \neq 0$) cases, the collocation points in y-direction are instead mapped with the bi-quadratic mapping into three distinct regions $[0, y_{i,1}]$, $[y_{i,1}, y_{i,2}]$ and $[y_{i,2}, y_{max}]$, each having one-third of the collocation points. Furthermore, the domain height for non-zero β can also be reduced because of a much faster decay of the solutions of interest in the freestream compared to the two-dimensional case. Table 5.2 summarizes the parameters used for the selected reference cases. Since the base-flow and stability grids are different, the base-flow solution is spline interpolated onto the grids specifically designed for the stability analysis. Further details about the discretization and approach to numerically solve the problem can be found in Chapter 3.

5.3.2. Spectra and eigenfunctions

Solving the streamwise stability problem in the moving frame of reference implies finding eigensolutions in a large parameter space of a-priori prescribed (c_f, β)-combinations. Exploring this space from point to point reveals significant variations of the structure of the eigenvalue spectrum and this allows identifying various types of unstable modes. The different types of modes are classified according to their relative location with respect to the bubble apex when they achieve their maximum temporal growth rate. Hence, for any (c_f, β)-combination, upstream-type ('U') and downstream-type ('D') modes are found dominant upstream and downstream of the bubble apex, respectively. For large enough β, an additional mode that is dominant in the bubble apex can be found and is labeled as an apex-

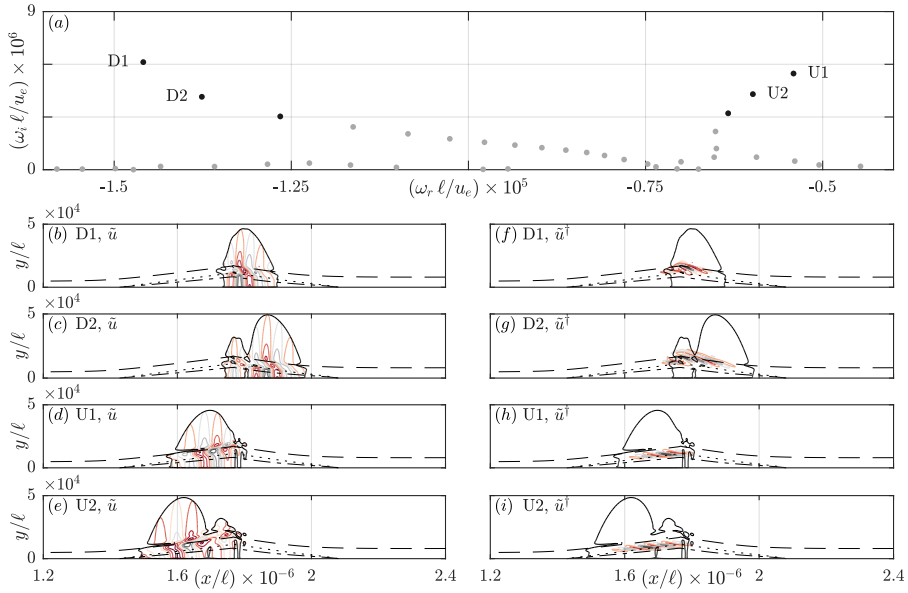

Figure 5.4: Most unstable modes for $c_f = 0.628u_e$ and $\beta = 0$. (*a*) ω-spectrum with eigenvalues corresponding to (non)localized eigenfunctions indicated by (gray) black dots, (*b–e*) direct and (*f–i*) adjoint eigenfunctions. (*b–c*,*f–g*) Downstream- and (*d–e*,*h–i*) upstream-type modes. (*b–i*) Isocontour of $|\tilde{u}|/|\tilde{u}|_{\max}$ (solid black, level: 1/9), (*b–e*) isocontours of $\mathscr{R}(\tilde{u})/|\tilde{u}|_{\max}$ (colored lines, from minimum (gray) to maximum (red) with $\Delta = 2/9$, with the phase set to zero where $|\tilde{u}|_{\max}$ is attained) and (*f–i*) isocontours of $\mathscr{R}(\tilde{u}^\dagger)/|\tilde{u}^\dagger|_{\max}$ (colored lines, from minimum (gray) to maximum (red) with $\Delta = 2/9$, with the phase set to zero where $|\tilde{u}^\dagger|_{\max}$ is attained) . (*b–i*) $\overline{U} = 0.9u_e$-isocontour (dashed black), dividing streamline (dotted black) and $\overline{U} = 0$-isocontour (dash-dotted).

type mode ('A'). In the following, an analysis of the two-dimensional solutions ($\beta = 0$) is first proposed before considering solutions related to $\beta > 0$. Although it is shown in §5.4 that the largest amplification of perturbation definitely stems from three-dimensional mechanisms, studying the two-dimensional case allows better understanding how the solutions vary in the (c_f, β)-space.

Two-dimensional eigensolutions ($\beta = 0$)

The region of the spectrum containing the most unstable eigenvalues for $\beta = 0$ is shown in figure 5.4(*a*). The eigenvalues corresponding to the upstream- and downstream-type modes align in two distinct branches, that together form a V in the unstable half-plane of the spectrum. The left branch (more negative ω_r) contains eigenvalues associated with downstream-type eigenfunctions (see figure 5.4(*b*,*c*)) while the right branch (less negative ω_r) represents eigensolutions that are here dominant upstream of the apex (figure 5.4(*d*,*e*)). The corresponding adjoint eigenfunctions are shown in figure 5.4(*f*,*g*) and (*h*,*i*) for the downstream- and upstream-type modes, respectively. The most unstable two-dimensional mode is reached by the downstream-type mode when prescribing $c_f/u_e = 0.628 \pm 0.001$. This frame speed is slightly greater than the sonic speed with respect to the freestream ($M_e c_f/u_e = 1.7 \times 0.628 = 1.068$).

Regarding the numerical sensitivity of the two-dimensional solutions, an $\mathscr{O}(10^{-4})$-relative change of the most unstable downstream-type eigenvalue is found when the domain in- and outlet are displaced by +20% and +10%, respectively. For the same variations of the domain length, the most unstable upstream-type eigenvalue experiences instead an $\mathscr{O}(10^{-5})$-relative

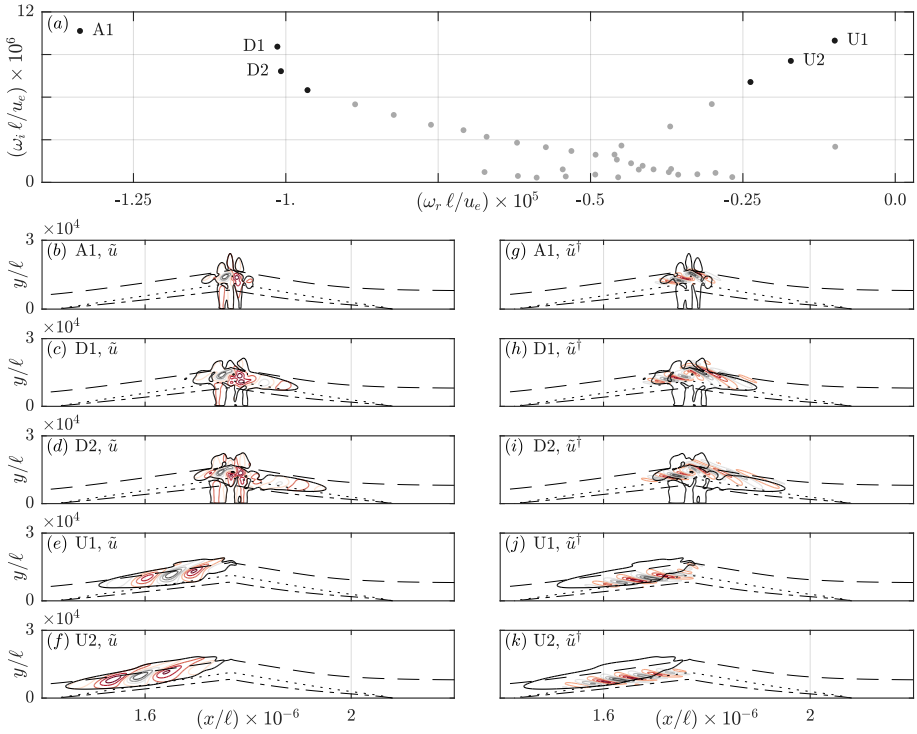

Figure 5.5: Most unstable modes at $c_f = 0.587 u_e$ and $\beta_{ud}\ell = 9.06 \times 10^{-5}$. (*a*) ω-spectrum with eigenvalues corresponding to (non)localized eigenfunctions indicated by (gray) black dots, (*b–f*) direct and (*g–k*) adjoint eigenfunctions. (*b,g*) Apex-type, (*c–d,h–i*) downstream-type and (*e–f*, *j–k*) upstream-type modes. (*b–k*) Isocontour of $|\tilde{u}|/|\tilde{u}|_{\max}$ (solid black, level: 1/9), (*b–f*) isocontours of $\mathscr{R}(\tilde{u})/|\tilde{u}|_{\max}$ (colored lines, from minimum (gray) to maximum (red) with $\Delta = 2/9$, with the phase set to zero where $|\tilde{u}|_{\max}$ is attained) and (*g–k*) isocontours of $\mathscr{R}(\tilde{u}^\dagger)/|\tilde{u}^\dagger|_{\max}$ (colored lines, from minimum (gray) to maximum (red) with $\Delta = 2/9$, with the phase set to zero where $|\tilde{u}^\dagger|_{\max}$ is attained) . (*b–k*) $\overline{U} = 0.9 u_e$-isocontour (dashed black), dividing streamline (dotted black) and $\overline{U} = 0$-isocontour (dash-dotted).

change. Finally, increasing the domain height by 25% yields a $\mathscr{O}(10^{-4})$-relative change in the most unstable eigenvalue of each mode type. Hence, two-dimensional eigensolutions with localized eigenfunctions, indicated by black dots in figure 5.4(*a*), are deemed independent of the numerical setup whereas solutions associated with non-localized eigenfunctions (gray dots in figure 5.4(*a*)) still depend on the truncation boundaries.

Three-dimensional eigensolutions ($\beta > 0$)

An exploration of the (c_f, β)-space reveals that the different types of modes reach their maximum growth rate for different combination of (c_f, β). Upstream- and downstream-type solutions reach their maximum growth rate for $\beta\ell \approx \beta_{ud}\ell = 9.06 \times 10^{-5}$ and $c_f/u_e = 0.557$ (upstream) and 0.587 (downstream). These solutions are shown in figure 5.5. As for the two-dimensional case, the adjoint eigenfunctions of all observed, localized, and unstable upstream-type modes are located downstream of the direct eigenfunctions and reach past the dividing streamline into the bubble. This represents an upstream-influence effect in the sense that the eigensolution is sensitive to the region occupied by the adjoint eigenfunctions, which for this case is located downstream of the direct eigenfunctions.

For large enough β, a third type of unstable mode is observed that is mostly dominant

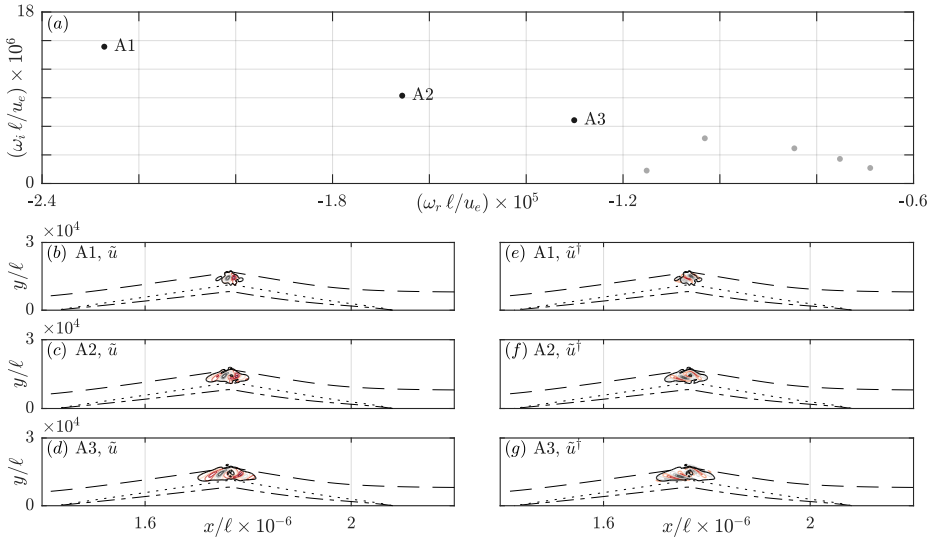

Figure 5.6: Most unstable apex modes at $c_f = 0.615 u_e$ and $\beta_a \ell = 25.5 \times 10^{-5}$. (*a*) ω-spectrum with eigenvalues corresponding to (non)localized eigenfunctions indicated by (gray) black dots, (*b–d*) direct and (*e–g*) adjoint eigenfunctions. (*b–g*) Isocontour of $|\tilde{u}|/|\tilde{u}|_{\max}$ (solid black, level: 1/9), (*b–d*) isocontours of $\mathscr{R}(\tilde{u})/|\tilde{u}|_{\max}$ (colored lines, from minimum (gray) to maximum (red) with $\Delta = 2/9$, with the phase set to zero where $|\tilde{u}|_{\max}$ is attained), (*e–g*) isocontours of $\mathscr{R}(\tilde{u}^\dagger)/|\tilde{u}^\dagger|_{\max}$ (colored lines, from minimum (gray) to maximum (red) with $\Delta = 2/9$, with the phase set to zero where $|\tilde{u}^\dagger|_{\max}$ is attained). (*b–g*) $\overline{U} = 0.9 u_e$-isocontour (dashed black), dividing streamline (dotted black) and $\overline{U} = 0$-isocontour (dash-dotted).

in the vicinity of the apex of the separation bubble. For the (c_f, β)-combination shown in figure 5.5, there are only localized apex modes (as it is observed to have branched off from the downstream-mode branch). The corresponding direct and adjoint eigenfunctions are shown in figure 5.5(*b*,*g*). Depending on the value of β, especially when it is large, multiple unstable apex-type modes can be found and the eigenvalues thus form a branch in the upper half-plane of the spectrum. The largest growth rate for the apex-mode, which also corresponds to the largest overall growth rate found for the present SWBLI in the (c_f, β)-parameter space, is attained when $c_f/u_e = 0.615$ and $\beta\ell = \beta_a \ell = 25.5 \times 10^{-5}$. The resulting spectrum is shown in figure 5.6(*a*). As shown in figure 5.6(*b*,*g*), the direct and adjoint eigenfunctions for β_a are all located close to the bubble apex and are very similar to the apex modes for the case $\beta = \beta_{ud}$. Although the apex-type mode at β_a reaches the largest eigengrowth of the entire (c_f, β)-parameter space, its very localized character in space implies that the mechanism only takes hold in a very limited spatial region around the bubble. In contrast, while the upstream- and downstream-type modes have a smaller temporal growth rate, their effect is distributed over a longer streamwise extent. It can thus be expected that these characteristics of the eigensolutions impact their time evolution in the shock-induced bubble. The effect of β is discussed in detail in section §5.4 by considering the initial-value problem.

All values of β and c_f for three-dimensional modes are used throughout the paper as reference cases in order to establish typical results obtained in the moving frame of reference. The spanwise wavenumbers are comparable to the findings in the literature (Robinet, 2007; Dwivedi *et al.*, 2020; Bugeat *et al.*, 2022) for laminar SWBLI. In particular, Dwivedi *et al.* (2020) found $\beta\ell = \beta\delta_0^*/\mathrm{Re}_{\delta_0^*} = 2.6/9660 = 26.9 \times 10^{-5}$, where δ_0^* is the inlet displacement thickness, with transient growth analysis of a hypersonic SWBLI. This β-value corresponds closely to $\beta_a \ell = 25.5 \times 10^{-5}$. The present frame speed also appears to be of a similar magnitude to the

group speeds that are found to be relevant by Dwivedi *et al.* (2020).

A careful verification shows that the most unstable eigensolutions are independent of the computational set-up, i.e., domain size and resolution. On the one hand, at $c_f/u_e = 0.58$ and $\beta_{ud}\ell = 9.06\times10^{-5}$, an $\mathcal{O}(10^{-5})$-relative change in the most unstable up- and downstream-type eigenvalue is observed when displacing the domain outlet by 20%, while maintaining the same streamwise grid density, and when decreasing the streamwise resolution by 25%, for the same domain. An $\mathcal{O}(10^{-4})$-change in the most unstable upstream and downstream-type eigenvalues is observed when increasing the domain height or decreasing the wall-normal resolution by 50%. The apex-type mode is less sensitive to the domain size, as a consequence of its smaller spatial support. A 50%-increase of the domain height or a 20%-change in the outlet locations yields at most an $\mathcal{O}(10^{-5})$-relative change in the most unstable apex-type eigenvalue. Having shorter wavelengths in both directions, the apex-type modes are more sensitive to the grid resolution than the other modes. This is demonstrated by decreasing either the streamwise or wall-normal resolution by 25%, which induces at most an $\mathcal{O}(10^{-4})$-relative variation in the most unstable apex-type eigenvalues. In conclusion, the convergence of the solutions is verified for all above parameters. In particular, it is observed that any $\mathcal{O}(1)$-relative change in the set-up parameters yields a negligible variation in the eigensolutions. This aspect significantly improves upon the $\mathcal{O}(1)$ variation of the eigenvalues with respect to the set-up parameters observed in past SWBLI studies based on a stationary-frame eigenvalue problem. It can thus be argued that the dependency of the eigensolutions with respect to the streamwise truncation boundaries that is usually observed in the stationary reference frame is effectively eliminated by solving the eigenvalue problem in the moving frame of reference. This setup-independence enables using the presently found solutions to identify physical instability mechanisms in SWBLI.

5.3.3. Instability mechanisms and in-depth eigengrowth analysis

In the following analysis, the mechanisms that contribute to the two- and three-dimensional instabilities are discussed. In particular, the growth rate associated with the eigensolutions is decomposed into its different contributions according to equation (2.76). Among all the terms of the perturbation/stability equations, only few have a significant contribution to the energy growth. A careful inspection that includes all terms shows that terms contributing more than 5% to the temporal growth rate dictate its overall trends across all considered cases. The present analyses focus only on those terms. By including all other terms in the remainder, the decomposition of the eigengrowth rate, i.e., equation (2.76) with $t_f = 0$ and $\check{q} = \tilde{q}$, reduces to

$$\omega_i = \underbrace{R_{\tilde{u}^*\tilde{v}} + R_{|\tilde{u}|^2}}_{\text{Reynolds stresses}} + \underbrace{R_{\tilde{s}^*\tilde{v}} + R_{\tilde{s}^*\tilde{u}}}_{\text{Reynolds heat fluxes}} + \underbrace{D_{\tilde{u},y} + D_{\tilde{w},y} + D_{\tilde{T},y}}_{\text{Dissipation}} + \underbrace{A_{\overline{U}} + A_{\overline{V}} + A_{c_f}}_{\text{Advection}} + \text{remainder}. \tag{5.4}$$

The contributions to the growth rate are presented in figure 5.7 for the most unstable two-dimensional (upper panels (*a*) and (*b*): $\beta = 0$) and three-dimensional (lower panels (*c*) through (*e*): $\beta > 0$) localized modes presented in §5.3.2. All upstream-type modes are shown in the left-most panels (*a*) and (*c*) and all downstream-type modes in the center panels (*b*) and (*d*). The apex-type modes for $\beta = \beta_a$ are shown in panel (*e*), while the apex-type mode found at $\beta = \beta_{ud}$ is presented with dashed lines among the downstream-type modes in panel (*d*). Note that some terms of equation (5.4) contribute less than 5% to the growth rate from case to case but are nevertheless included for cross-comparison purposes, whereas no term included in the remainder has an individual contribution larger than 5%.

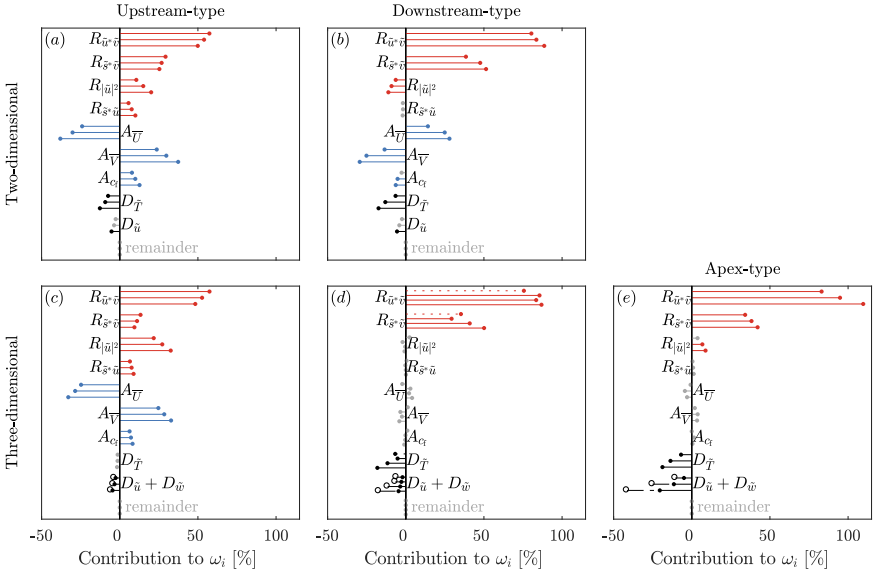

Figure 5.7: Relative contribution of the dominant terms to the ω_i-budget for the most unstable modes identified in §5.3. (*a–b*) $c_f = 0.628u_e$ and $\beta = 0$, (*c–d*) $c_f = 0.587u_e$ and $\beta_{ud}\ell = 9.06 \times 10^{-5}$ and (*e*) $c_f = 0.615u_e$ and $\beta_a\ell = 25.5 \times 10^{-5}$. (*a,c*) Upstream-type, (*b,d*) downstream-type (solid lines) and apex-type (dotted lines, (*d*)) and (*e*) β_a apex-type modes. Colors indicate the Reynolds-stress and heat-flux (red), advection (blue) and dissipation (black) terms. Terms in gray contribute to less than 5% to ω_i. For $\beta \neq 0$ (*c–e*), the dominant friction-induced dissipation terms are added up (open circles): solid black lines ended by closed circles for $D_{\tilde{u},y}$ contribution and dash-dotted black lines for $D_{\tilde{w},y}$ contribution.

Reynolds-stress and Reynolds-heat-flux terms $R_{\tilde{u}^*\tilde{v}}$ and $R_{\tilde{s}^*\tilde{v}}$

The largest contribution to the perturbation energy growth is the production term induced by the Reynolds stress $R_{\tilde{u}^*\tilde{v}}$, for all mode types. This is a consequence of both the large wall-normal gradient $\partial\overline{U}/\partial y > 0$ and the substantial region where $\mathscr{R}\{\tilde{u}^*\tilde{v}\} < 0$. More precisely, for all cases, the $\tilde{u}$ and $\tilde{v}$-eigenfunctions are mostly in anti-phase, i.e., $\mathscr{R}\{\tilde{u}^*\tilde{v}\} < 0$ (interpreting $\tilde{u}$ and $\tilde{v}$ as waves in the xy-plane), in the shear-layer where $\partial\overline{U}/\partial y > 0$ is large. The region where $\tilde{u}$ and $\tilde{v}$ are in-phase, i.e., $\mathscr{R}\{\tilde{u}^*\tilde{v}\} > 0$, is much smaller. This yields a significant imbalance between the productive and destructive regions leading to a largely positive $R_{\tilde{u}^*\tilde{v}}$-term. This mechanism is illustrated in figure 5.8(*b–c*) with the most unstable two-dimensional upstream-type mode. For the downstream- and apex-type modes, the anti-phase region is even more prevalent, such that $R_{\tilde{u}^*\tilde{v}}$ contributes to at least 75% of the energy growth of the downstream- and apex-type modes, while it does not exceed 55% for upstream-type modes. Furthermore, the relative contribution per mode type of the $R_{\tilde{u}^*\tilde{v}}$ Reynolds-stress to the growth rate is similar for both two- and three-dimensional cases. Only one significant difference in $R_{\tilde{u}^*\tilde{v}}$ is, however, observed between the most unstable two- and three-dimensional downstream-type modes. When considering more stable modes, the contributions of the wall-normal Reynolds stress $R_{\tilde{u}^*\tilde{v}}$ and heat-flux $R_{\tilde{s}^*\tilde{v}}$ decrease for upstream-type solutions while they both increase for downstream- and apex-type modes. However, at β_{ud}, it is found that $R_{\tilde{u}^*\tilde{v}}$ is larger for the most unstable downstream-type mode than for the second-most unstable downstream-type mode. In fact, comparing the energy budget of the two-dimensional downstream-type modes (figure 5.7(*b*)) and of the three-dimensional apex-, and downstream-type modes (figure 5.7(*d, e*)) suggests that the downstream-type and apex-type modes are closely related.

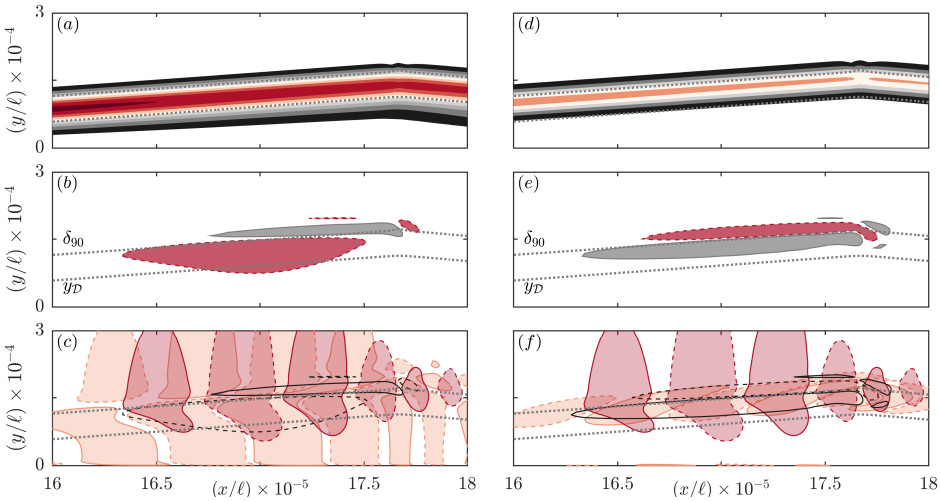

Figure 5.8: Decomposition of the $R_{\tilde{u}^*\tilde{v}}$ and $R_{\tilde{s}^*\tilde{v}}$ terms for the most unstable two-dimensional upstream-type mode at $c_f = 0.628u_e$. (*a*) Velocity gradient $\partial\overline{U}/\partial y$ and (*d*) temperature gradient $-\partial\overline{T}/\partial y$ (filled isocontours with levels from 0.05 (black) to 1.65 (red) with $\Delta = 0.2$). Regions where (*b*) $\tilde{u}$ and $\tilde{v}$ are locally in anti-phase (dark red, $\mathscr{R}\{\tilde{u}^*\,\tilde{v}\}\times\rho_e\ell^2 < -4\times10^{-11}\tilde{E} < 0$) and in phase (gray, $\mathscr{R}\{\tilde{u}^*\,\tilde{v}\}\times\rho_e\ell^2 > 4\times10^{-11}\tilde{E} > 0$), and (*e*) $\tilde{s}$ and $\tilde{v}$ are locally in anti-phase (dark red, $\mathscr{R}\{\tilde{s}^*\,\tilde{v}\}\times\rho_e\ell^2 < -4\times10^{-11}\tilde{E} < 0$) and in phase (gray, $\mathscr{R}\{\tilde{s}^*\,\tilde{v}\}\times\rho_e\ell^2 > 4\times10^{-11}\tilde{E} > 0$). (*c*,*f*) Positive (solid, $\mathscr{R}\{\tilde{q}\} \geq 2\times10^{-2}|\tilde{u}|_{\max}$) and negative (dashed, $\mathscr{R}\{\tilde{q}\} \leq 2\times10^{-2}|\tilde{u}|_{\max}$) regions for $\tilde{q} = \tilde{v}$ (red filled contour), (*c*) $\tilde{q} = \tilde{u}$ (orange filled contour), (*f*) $\tilde{q} = \tilde{s}$ (orange filled contour). (*c*,*f*) Black lines represent the limits of regions in (*b*,*e*), respectively: solid for positive and dashed for negative isocontours. (*a*–*f*) Dividing streamline (lower dotted line) and $\overline{U} = 0.90u_e$-isocontour (upper dotted line).

The production of entropy perturbation by the wall-normal base-flow heat flux, i.e., the $R_{\tilde{s}^*\tilde{v}}$-term, is the second-most destabilizing mechanism for all mode types, except for the three-dimensional upstream-type modes. Since the temperature gradient in the wall-normal direction is negative, regions that positively (negatively) contribute to the energy growth are the spatial regions where $\mathscr{R}\{\tilde{s}^*\,\tilde{v}\} > 0$ ($\mathscr{R}\{\tilde{s}^*\,\tilde{v}\} < 0$), i.e., regions where $\tilde{s}$ and $\tilde{v}$ are in-phase (out-of-phase). This behavior is illustrated in figure 5.8(*e*,*f*) and is the exact opposite of the $R_{\tilde{u}^*\tilde{v}}$ term. Furthermore, $R_{\tilde{s}^*\tilde{v}}$ is highly correlated with the wall-normal Reynolds stress $R_{\tilde{u}^*\tilde{v}}$ when moving along each branch. This is demonstrated by the Pearson correlation coefficient between $R_{\tilde{u}^*\tilde{v}}$ and $R_{\tilde{s}^*\tilde{v}}$ that is 1.000 and 0.994 for two-dimensional up- and downstream-type modes, respectively, 0.998 for three-dimensional upstream-type modes and 0.999 for β_a apex modes. Again, the behavior of the β_{ud} downstream- and apex-type modes (see figure 5.7(*d*)) does not follow the typical behavior observed for all other modes and no correlation was found.

For three-dimensional modes, the relation between $R_{\tilde{u}^*\tilde{v}}$ and $R_{\tilde{s}^*\tilde{v}}$ can differ since increasing the spanwise wavenumber tends to increase the ratio $|\tilde{u}|_{\max}/|\tilde{T}|_{\max}$, which, if this was the only variation, would automatically reduce the relative contribution of $R_{\tilde{s}^*\tilde{v}}$ with respect to $R_{\tilde{u}^*\tilde{v}}$. The variation of the ratio $|\tilde{u}|_{\max}/|\tilde{T}|_{\max}$, which increases by a factor 3 from $\beta = 0$ to $\beta = \beta_a$ for upstream-type three-dimensional eigenfunctions, significantly reduces the contribution $R_{\tilde{s}^*\tilde{v}}$ to the growth rate of the corresponding modes. In contrast, the velocity-temperature ratio of downstream-type modes is larger by a factor of about 1.5 only, at $\beta = \beta_a$, which is mostly balanced by a net productive region of $R_{\tilde{s}^*\tilde{v}}$ being twice smaller at $\beta = \beta_a$ than at $\beta = 0$. Hence, while the $R_{\tilde{s}^*\tilde{v}}$ term is much less dominant in three-dimensional versus two-dimensional upstream-type modes, its relative contribution to the growth rate remains

relatively constant in downstream- and apex-type modes.

Reynolds-stress and -heat-flux terms $R_{|\tilde{u}|^2}$ and $R_{\tilde{s}^*\tilde{u}}$

The different length scales in x and y imply that the Reynolds stress $R_{|\tilde{u}|^2}$ and heat-flux $R_{\tilde{s}^*\tilde{u}}$ terms, which involve the streamwise gradient of the base flow, contribute to a smaller extent to the growth rate than $R_{\tilde{u}^*\tilde{v}}$ and $R_{\tilde{s}^*\tilde{v}}$. The contribution of $R_{|\tilde{u}|^2}$ is governed by the size of the streamwise velocity perturbation and by the streamwise gradient $\partial\overline{U}/\partial x$, where the latter is the only factor that dictates the sign of $R_{|\tilde{u}|^2}$. Hence, the deceleration of the flow in the shear layer toward the bubble apex has a destabilizing effect through the $R_{|\tilde{u}|^2}$-term. This is especially observed for upstream- and apex-type modes, while the opposite effect occurs for the downstream-type modes that are subjected to $\partial\overline{U}/\partial x > 0$ behind the bubble apex. Note that the contribution of $R_{|\tilde{u}|^2}$ is relatively large in upstream-type modes, especially at β_{ud} for which it is the second largest contribution to the growth rate and thus prevails over $R_{\tilde{s}^*\tilde{v}}$. One reason for the significant contribution $R_{|\tilde{u}|^2}$ for larger β comes from the larger magnitude of $\tilde{u}$. The second reason is the reduction of the wall-normal extent of the eigenfunctions; for larger β, they are more confined in the shear layer (where $\partial\overline{U}/\partial x < 0$ has the largest magnitude) and thus have a much smaller wall-normal extent in the recirculation bubble (where $\partial\overline{U}/\partial x > 0$). For downstream modes, the reason for $R_{|\tilde{u}|^2}$ being much less negative when β increases is explained by the eigenfunctions being dominant close to the apex, where $\partial\overline{U}/\partial x$ is approximately anti-symmetric, i.e., it has the opposite sign on either side and equivalent magnitude in absolute value.

Finally, it can be observed that $R_{\tilde{s}^*\tilde{u}}$ is strongly destabilizing for all upstream modes, while barely contributing to the growth of other modes at all. The large productive contribution of $R_{\tilde{s}^*\tilde{u}}$ comes 1) from the positive temperature gradient in the streamwise direction upstream of the bubble apex and 2) from $\tilde{s}$ and $\tilde{u}$ being mostly out-of-phase in the separated shear layer. In contrast, either the similar size of the productive and destructive regions or the anti-symmetry of the streamwise temperature gradient with respect to the bubble apex strongly restrains the contribution of $R_{\tilde{s}^*\tilde{u}}$ in downstream or apex modes, respectively.

Advection terms

Advection terms quantify how much the perturbation structure stretches or shrinks in the x- and y- directions. This implies that, if the divergence of the in-plane base-flow velocity is zero, the contributions of the advection terms to the energy growth cancel out. Although the compressibility of the flow induces a non-zero velocity divergence, it is presently observed that the $\overline{U}$-advection approximately cancels the $\overline{V}$-advection (see figure 5.7). For this reason, advection terms are deemed conservative and are not considered as contributing to the growth rate.

For the solutions upstream of the bubble apex, the streamwise velocity of the base flow decreases in x and the perturbations are thus squeezed in this direction by a certain amount while being stretched in the wall-normal direction by approximately the same amount as the perturbations are carried upward by the separated shear-layer. The opposite behavior is observed for modes that are dominant downstream of the bubble apex. For three-dimensional downstream- and apex-type modes, the effect of advection is, however, mitigated by the fact that these modes are located close to the bubble apex, about which point the advection effects are approximately anti-symmetric and thus balanced. This results in an overall stretching/shrinking effect that is much smaller than for two-dimensional modes. However, the advection terms in the upstream-type modes are barely affected when considering non-zero β. It is evident that the most dominant instability mechanisms of upstream-type modes are highly similar in two- and three-dimensional cases, while two- and three-dimensional

downstream modes are noticeably different. A general observation is that the mechanisms in apex- and downstream-type modes are more prone to vary with respect to β than in the upstream-type modes. The latter are thus more easily identified among the other modes (of the entire spectrum). Nevertheless, the energy budget indicates mechanisms that are distinguishable from branch to branch and thus allows classifying the modes into different categories.

Artificially introduced by the use of a moving frame of reference, the term A_{c_f} is important to consider in the energy budget (see figure 5.7). It can be decomposed into two contributions: one from the streamwise boundaries and another one from the x-derivative of the $\mathscr{M}$-matrix (see equation (2.64)). Since the present eigensolutions have localized eigenfunctions, the contribution of the boundary integral is orders of magnitude smaller than the contribution from the $\mathscr{M}$-matrix. Furthermore, because the most common base-flow term in the $\mathscr{M}$-matrix is the density ρ, the derivative $\partial\overline{\rho}/\partial x$ has the greatest influence on the x-derivative of the $\mathscr{M}$-matrix. This implies that the sign of A_{c_f}, and so of the correction used in equation (2.64), can be related to the streamwise variation of the density, which depends on the relative position of the eigenfunctions with respect to the bubble apex. Hence, having $\partial\overline{\rho}/\partial x < 0$ upstream of the apex stretches the eigenfunction and thus produces perturbation energy. In other words, the upstream eigensolutions are rendered more unstable in the moving frame of reference than they should in an instantaneous sense in the stationary frame of reference. Although much smaller, the same effect is observed for apex modes. In contrast, (two-dimensional) downstream modes are subjected to a stabilizing effect induced by the moving frame of reference.

Dissipation terms

Since the net contribution of the advection terms to the growth rate is virtually zero, the dissipation terms are arguably the most stabilizing contributions of the energy growth rate. The only exception is the most unstable downstream mode that has a relatively large negative contribution from $R_{|\tilde{u}|^2}$. For all cases, moving downward along a branch in the eigenvalue spectrum is observed to be accompanied with more energy being dissipated through the dissipation terms (5.4). After integrating by parts these terms, it follows that their magnitude mostly depends on the absolute magnitude of the wall-normal derivatives of the eigenfunctions, i.e., the spatial structure of the perturbation in the wall-normal direction. On the one hand, this implies that highly oscillatory eigenfunctions in the wall-normal direction are much more prone to dissipating energy through the dissipation terms than eigenfunctions with a larger wavelength. On the other hand, eigenfunctions with a small wall-normal support dissipate more energy than eigenfunctions with a larger extent. Hence, in two-dimensional modes, the facts that the wall-normal extent of $|\tilde{T}|$ is shorter than that of $|\tilde{u}|$ and that $|\tilde{T}|_{\max}/|\tilde{u}|_{\max} \approx 2$ translates into a dissipation $D_{\tilde{u},y}$ that corresponds to only 35–40% of $D_{\tilde{T},y}$. In contrast, in three-dimensional modes, the larger ratio $|\tilde{u}|_{\max}/|\tilde{T}|_{\max}$ tends to increase the dissipation $D_{\tilde{u},y}$ with respect to $D_{\tilde{T},y}$. This is especially observable in upstream-type modes for which the ratio $|\tilde{u}|_{\max}/|\tilde{T}|_{\max}$ is three times larger at β_{ud} than at $\beta = 0$. Remarkably, the dissipation term $D_{\tilde{T},y}$ contributes to less than 2% of the growth rate, in absolute value, at β_{ud}, while it is as large as 12% for the least unstable two-dimensional upstream mode. Finally, when β departs from zero, the spanwise velocity perturbation component develops and the dissipation of energy through $D_{\tilde{w},y}$ increases. With the present β values, $D_{\tilde{w},y}$ varies from a relatively weak stabilizing effect in upstream-type modes to an important stabilizing effect that can be greater than or equal to $D_{\tilde{u},y}$ in downstream- and apex-type modes. Since the eigenfunctions of apex-type modes are highly confined in the bubble apex and thus have a similar wall-normal extent, the relative size of the dissipation

terms indicates how large the different components are with respect to each other.

As part of the first step of the moving-frame methodology, the above discussion allows gaining insight into the core mechanisms behind the eigengrowth. In particular, this helps understanding how the wave packets are amplified for small elapsed times. In order to study the complete behavior of convective mechanisms in SWBLI, the second stage of the present approach is to disturb the flow with eigenfunctions and then track the finite-time evolution of the wave-packet perturbation across the shock-induced bubble. To do this, the behavior of the eigensolutions with respect to the frame speed must be understood in order to select the ideal initial condition.

5.3.4. Dependency on the speed of the moving frame of reference

The characteristics of the eigensolutions, in particular the spatial extent and location of the eigenfunctions and their eigengrowth, depend on the prescribed frame speed. Understanding how exactly the solutions behave with respect to the frame speed is necessary for several reasons. First, an appropriate choice for the frame speed is required to obtain localized eigenfunctions in a given domain. Second, knowing the relation between the location of the eigenfunctions and the frame speed allows possibly adapting the domain to track instability mechanisms in the stationary frame. Note, however, that the results for the incompressible boundary layer suggest that it is not always possible to obtain accurate solutions for zero frame speed without having to simultaneously let both the streamwise domain size and resolution tend to infinity. Third, after establishing the relation between the position of the eigenfunction and the frame speed, the initial condition for the linearized Navier-Stokes equations can be appropriately chosen so as to yield stability information in a region of interest, e.g., to construct amplification curves with eigenfunctions that are upstream of a neutral-growth region. In the following, the overall dependency of the eigensolutions with respect to the frame speed is thus established for the present SWBLI configuration.

The variation of the eigensolutions with c_f yields several important insights. Figure 5.9 illustrates the frame-speed dependency of the instantaneous growth rate and the streamwise locations/extents of representative, *localized* direct and adjoint eigenfunctions for both β_ud and β_a. Outside the frame-speed range shown, the spectrum does not contain eigensolutions whose eigenfunctions are localized for the present domain length. Nevertheless, each mode type achieves a maximum growth rate within the considered range of frame speeds. The most unstable downstream- and upstream-type modes ($\beta_\mathrm{ud}\ell = 9.06\times10^{-5}$) attain their maximum at $c_\mathrm{f} = 0.587u_e$ and $0.56u_e$, respectively. For the apex modes, the maximum growth rate is reached at $c_\mathrm{f} = 0.615u_e$ and $0.63u_e$ for $\beta\ell = 25.5\times10^{-5}$ and 9.06×10^{-5}, respectively.

All eigenfunctions move in the x-direction when the frame speed varies and, in general, increasing c_f causes the direct and adjoint eigenfunctions to displace upstream and downstream, respectively. This is recorded in terms of the streamwise locations x_E, x_u and x_d of the eigenfunctions, as defined by equations (2.66) and (2.68) for $t = 0$. For the incompressible flat-plate boundary layer, the adjoint eigenfunctions move upstream when increasing the frame speed (Chapter 4). Note, however, that the presence of the shock in the flow likely prevents some of the eigenfunctions to displace freely along the shear layer. Hence, on the one hand, downstream-type modes at all considered β-values and apex-type modes for $\beta = \beta_\mathrm{a}$ barely move upstream of the shock-impinging location when the frame speed is increased. The eigenfunctions corresponding to these mode types at high frame speeds are mostly located in the vicinity of the bubble apex and have a relatively short streamwise extent. In contrast, upstream-type modes can move through the bubble apex and, when ap-

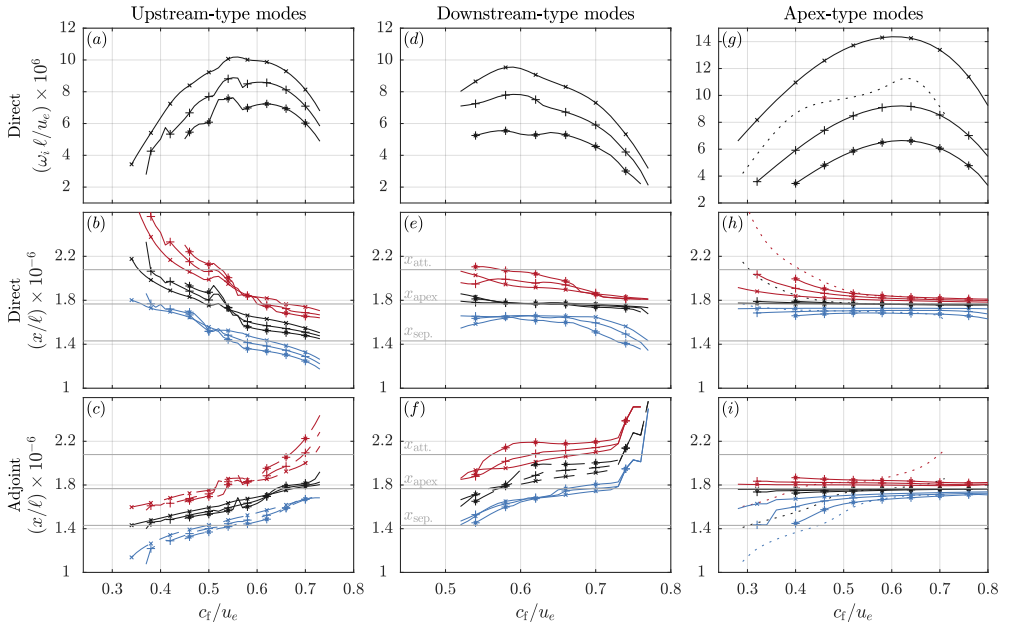

Figure 5.9: Variation of the initial-condition characteristics ($t = 0$ only) with respect to the frame speed c_f. (a–c) Upstream-, (d–f) downstream-, and (g–i) apex-type modes for (a–f) $\beta_{ud}\ell = 9.06 \times 10^{-5}$ and (g–i) $\beta_a\ell = 25.5 \times 10^{-5}$. Crosses, pluses and stars rank modes from most unstable to third-most unstable. Dotted line for unique apex-type mode at β_{ud}. (a,d,g) Temporal growth rate ω_i, (b–c,e–f,h–i) streamwise energy centroid x_E (black), upstream x_u (blue) and downstream x_d (red) extrema of the (b,e,h) direct and (c,f,i) adjoint eigenfunctions. (b–c,e–f,h–i) Gray lines indicate streamwise coordinates of separation ($x_{sep.}$), bubble apex (x_{apex}) and reattachment ($x_{att.}$).

proaching this particular location, the eigensolutions' characteristics are only slightly disrupted. In general, the solutions appear to be more unstable when they are located closer to the bubble apex in the streamwise direction as a consequence of the strong velocity gradients involved. For all cases, a mode achieves its maximum growth rate at the frame speed for which the energy centroids of the direct and adjoint eigenfunctions are the closest; the overlap of the direct and adjoint eigenfunctions is likely maximized. Finally, it is important to notice that the solutions belonging to different branches can, for some (c_f, β)-combinations, feature similar characteristics. Hence, in some cases, it can be more difficult to distinguish and track mode types in the eigenvalue spectrum.

Since eigenfunctions move and their extent increases/decreases when changing the frame speed, extreme values of the frame speed inevitably lead to eigenfunctions that interact with the truncation boundaries. Hence, because localized eigenfunctions are sought to ensure the effectiveness of the present method, it is required to understand the process that leads an eigenfunction to interact with the truncation boundaries. The most frequent type of interaction, that was discussed in Chapter 4, is caused by the displacement of the eigenfunction toward the inlet or outlet truncation boundary. A large amplitude at the streamwise boundaries, which is quantified by equation (2.68a) evaluated at the boundary, implies that the eigensolutions highly depend on the boundary conditions and domain length. As mentioned previously, a high numerical dependency is here defined as when an $\mathcal{O}(1)$-change in the domain length induces at least an $\mathcal{O}(10^{-4})$-change in the eigenvalue. For the present outlet location, the most unstable eigensolution for the up-/downstream and apex modes

at $\beta\ell = 9.06 \times 10^{-5}$ becomes domain-dependent for $c_f < 0.38u_e$, $0.5u_e$ and $0.3u_e$, respectively. The onset of the interaction with the domain limit can be observed in figure 5.9(*b*) with the downstream extent of the upstream-type eigenfunctions reaching the location of the outlet boundary ($x_f/\ell = 3.0 \times 10^6$) as the frame speed decreases. For the same mode type, an increase of the frame speed causes the eigenfunctions to move toward the inlet boundary before interacting with it when $c_f > 0.73u_e$. In contrast, downstream-type modes are observed to reach only the outlet boundary (at low frame speeds) because their upstream propagation (as the frame speed is increased) is strongly slowed down by the shock. Furthermore, close to the bubble apex, the downstream-type eigenfunctions feature a much higher streamwise wavenumber and, although the reference cases are converged with respect to the streamwise resolutions, a denser grid would be required to resolve downstream modes at $c_f > 0.73u_e$. A very similar observation is made for the apex-type modes at β_a, that can be resolved with the present discretization up to $c_f = 0.75u_e$. As a final remark, it is important to emphasize that the tendency of the eigenfunctions to interact with the truncation boundaries is not an issue per se. This tendency must be understood, however, in order to find the most upstream, domain-independent localized eigenfunctions, for example.

For the present flow case, no two- or three-dimensional localized eigensolutions were found when decreasing the frame speed to zero, i.e., when the eigenvalue problem is solved in the stationary frame of reference. This situation is similar to that of the incompressible boundary layer and this suggests that the present SWBLI case does not support a globally unstable mechanism. Hence, it is necessary to consider eigensolutions for a non-zero frame speed in order to describe the pertinent instability mechanisms. More specifically, from now on, frame speeds that yield sufficiently upstream and setup-independent eigenfunctions are selected as initial conditions to solve the initial-value problem (2.13) and to obtain converged Fourier coefficients (2.69) for streamwise locations of interest.

5.4. Finite-time evolution of perturbations

In the following, the most amplified perturbation content, i.e., spanwise wavelength and frequency, is determined. The eigensolutions only provide the largest instantaneous growth rate; their relation to the most amplified disturbance is yet to be identified. Hence, to characterize the spatial evolution of the convective instabilities, the SWBLI flow is disturbed with eigensolutions. The finite-time evolution of wave-packet perturbations can thus be assessed by solving the initial-value problem (2.13) in the *stationary* frame of reference. In order to represent the perturbation evolution as individual-frequency amplification curves, as traditionally provided by the LST and PSE approaches, the wave-*packet* signal is converted into the monochromatic, wave-*train* representation using the Fourier-transform approach detailed in §2.7.3.

First, the flow is disturbed with the apex- and upstream-type eigenfunctions at β_a and β_{ud}, respectively. The particular initial conditions are chosen based on the β-values maximizing the instantaneous growth rate (for all β- and c_f-values). Later, the effect of varying β is studied while using both initial conditions. Since amplification curves over the largest streamwise extent of the shock-induced bubble are sought, the most upstream initial condition, per mode type, is considered in order to obtain converged Fourier coefficients in the region of interest. The highest frame speed for which localized solutions are found is $c_f = 0.73u_e$. Note that the initial condition must be localized in space to ensure that the resulting temporal solution is not a boundary-dependent wave-train solution but is instead a wave packet containing a broad range of frequencies. All the solutions considered to initialize the temporal problem are independent of the numerical setup. Using these ini-

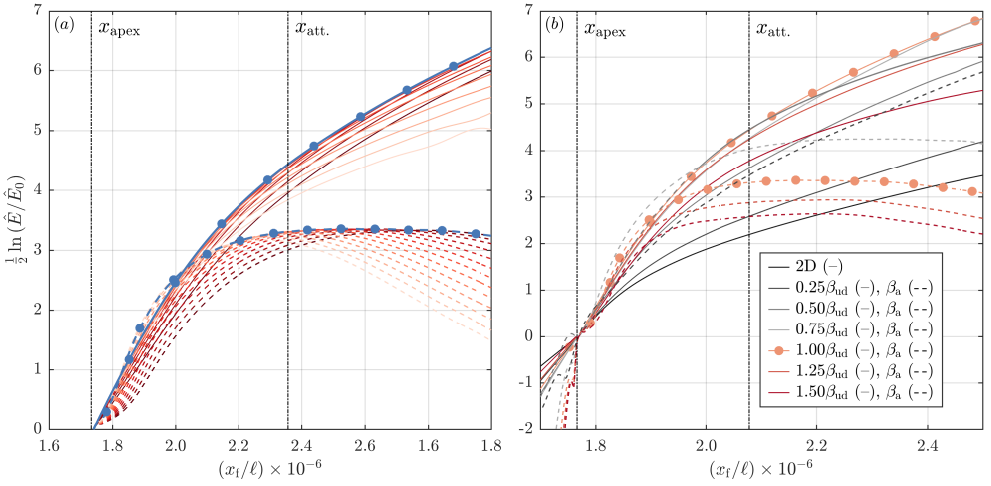

Figure 5.10: (*a*) Amplification curves and (*b*) envelope of amplification factor curves normalized at $x_{\text{f},0}/\ell = 1.77\times 10^6$. (*a*) Apex mode at β_{a} (dashed) and upstream mode at β_{ud} (solid) for frequencies $\Omega_r\ell/u_e\times 10^5$ ranging from 2.077 (light red) to 4.845 (dark red) with step 0.23. Envelopes of individual amplification curves indicated by blue lines and filled circles. (*b*) Envelope for upstream- (solid) and apex-type (dashed) modes at different β (colored lines). Filled circles for envelopes at β_{ud} and β_{a} of panel (*a*). Vertical dash-dotted lines: streamwise location of the bubble apex and reattachment.

tial conditions, the instantaneous validity of the eigensolutions, that can be assessed with equation (2.64), is verified for small elapsed times. Note that, in compressible flows, the corrected eigengrowth $\omega_{i,c}$ (equation (2.65)) accounts for the non-constant $\mathscr{M}$ matrix and thus $\omega_{i,c}\neq\omega_i$. In contrast, for incompressible flows, the definition of the energy norm leads to $\omega_{i,c}=\omega_i$ (see Chapter 4). For the present SWBLI case, the corrected eigengrowth rate $\omega_{i,c}$ and the instantaneous energy growth rate $\sigma(t_{\text{f}})$ are equal up to $O(10^{-6})$ and $O(10^{-5})$ relative errors for upstream- and apex-type modes, respectively. A similar result holds when comparing the instantaneous group speed $c_{\text{g}}(t_{\text{f}})$ (equation (2.67)) against the frame speed c_{f}. In this framework, eigensolutions are thus demonstrated to be representative of the instantaneous perturbation dynamics. For longer-time dynamics, the Fourier coefficients of the time-evolved wave packets are computed and are presented in figure 5.10(*a*). All curves are normalized at $x_{\text{f},0}/\ell = x_{\text{apex}}/\ell = 1.77\times 10^6$, which corresponds to the most upstream location where converged Fourier coefficients can be found for the *apex*-type modes since no eigenfunction of this mode type can be found far upstream of the bubble apex.

The Fourier coefficients in figure 5.10(*a*) show that, although the apex-type modes have the largest growth rate around the incident shock, they do not yield the largest amplification-factor envelope over the extent of the bubble. This behavior was expected from the apex-type eigensolutions shown in figure 5.9: the large growth rate is achieved only over a very small streamwise extent of the bubble. In contrast, the upstream-type wave packet at β_{ud} covers a much longer extent of the shock-induced bubble in the streamwise direction, and despite a relatively smaller growth rate as suggested by the eigensolutions, yields the largest spatial amplification in the SWBLI. Following this reasoning, downstream-type modes can only cover a shorter streamwise extent of the bubble than that of upstream modes. Since their corresponding temporal growth rate is smaller than or equal to that of upstream-type modes, downstream-type modes yield only a smaller overall amplification and thus are omitted for sake of conciseness.

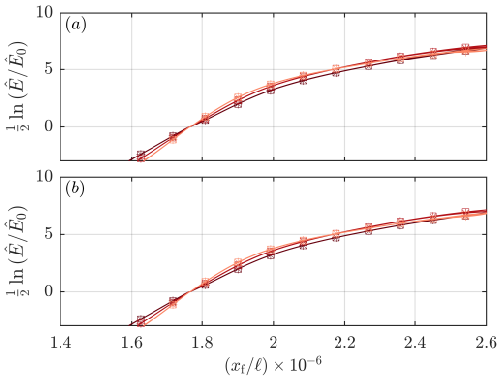

Figure 5.11: Spatial amplification of upstream-type wave packets for $\beta = \beta_{ud}$. Individual-frequency amplification curves obtained from initialization with (*a*) the three most unstable eigenfunctions of the upstream-type family (from most unstable to least unstable: squares, crosses and pluses) at $c_f/u_e = 0.73$ and (*b*) the most unstable eigenfunction at $c_f/u_e = 0.67$ (pluses), 0.70 (crosses) and 0.73 (squares). Colored lines for frequencies $\Omega_f \ell/u_e \times 10^5 = 0.2307$, 0.3461, and 0.3922 (light to dark red).

A parametric study on the spanwise wavenumber is performed in order to identify the critical β-values yielding the largest perturbation amplification. To do this, a range of β/β_{ud}-values from 0 to 1.5 is considered for the upstream-type mode. For the apex-type mode, β/β_a-values ranging from 0.25 to 1.5 are considered. Both cases have uniform steps of 0.25. The frame speed used to obtain the initial conditions is kept at $c_f = 0.73u_e$ for all cases. The resulting amplification envelopes are given in figure 5.10(*b*) for upstream-type (solid) and apex-type (dashed) modes. These results indicate that, for the present SWBLI conditions, the most critical three-dimensional convective instabilities are characterized by a spanwise wavelength $\lambda_z/\ell \approx 2\pi/(\beta_{ud}\ell) = 6.9\times10^4$, which is approximately 10.7 times smaller than the length of the bubble ($L_{sep}/\ell \approx 6.5\times10^5$), and a frequency of about $f = 9.3(\pm0.58)$ kHz at the reattachment point. With the present selection of discrete β-values used for the parametric study, the uncertainty on the most-amplified spanwise wavelength reasonably scales to about ±2.7% of the bubble length.

Considering the bubble length as a reference length, the characteristic frequency of the present convective mechanisms corresponds to a Strouhal number $St = fL_{sep}/u_e = 0.38$ that is in the medium-frequency range ($St = 0.3-0.5$) of the frequencies that can be found in SWBLIs (Guiho *et al.*, 2016; Larchevêque, 2016; Sansica *et al.*, 2016; Bonne *et al.*, 2019; Pasquariello *et al.*, 2017; Nichols *et al.*, 2017; Bugeat *et al.*, 2022). While Bonne *et al.* (2019) associated these medium frequencies with large-scale breathing motions of the bubble in transitional SWBLIs, Nichols *et al.* (2017), Sasaki *et al.* (2021) (turbulent) and Bugeat *et al.* (2022) (laminar) suggest instead that medium frequencies represent convective instability mechanisms of the shear-layer and that the bubble breathing occurs in the low-frequency range ($St < 0.1$). In this range, the breathing motion would be associated with a low-frequency global mode encompassing the entire recirculation region (Robinet, 2007; Nichols *et al.*, 2017; Bugeat *et al.*, 2022). Since the wave packets observed in the present flow configuration are dominant in the shear-layer, the present linear convective mechanisms are arguably not representative of a self-sustained large-scale breathing of the bubble.

The β-parameter study suggests that the spanwise wavenumber $\beta = \beta_{ud}$ yields the largest amplification when using the upstream-type initial condition. Remarkably, it also maximizes the amplification of the apex-type initial condition, as observed for the case with the

β-value closest to β_{ud}, that is $\beta = 0.5\beta_a \approx \beta_{ud}$. Hence, although β_a yields the maximum growth rate of the apex-type mode, it does not lead to the maximum amplification. The solutions initialized with the upstream- and apex-type modes with $\beta \approx \beta_{ud}$ are found to display similar characteristics. For example, the most amplified frequency at the reattachment point is similar (9.3 ± 0.58 kHz) and, as quantified later in figure 5.12, the mechanisms underlying the growth are very similar. This shows that the most amplified disturbance can be identified with more than one type of initial condition and thus that β_{ud} effectively yields the largest amplification. Note that disturbing the flow with the upstream-type solutions is preferred over downstream- or apex-type modes in the sense that the region of converged Fourier coefficients reaches farther upstream of the shock-induced bubble and spans a much larger streamwise extent of the perturbation growth in the flow.

To further ensure that the most critical dynamics are effectively captured by one initial condition, a sensitivity study is conducted by disturbing the flow with, on the one hand, the three most unstable solutions of the upstream-type family at $c_f/u_e = 0.73$ and, on the other hand, the most unstable upstream-type eigenfunctions obtained at $c_f/u_e = 0.67$, 0.70, and 0.73. The amplification curves are shown in figure 5.11 at three different frequencies and are indistinguishable from one initial condition to another. As for the incompressible flat-plate boundary layer, the only difference is observed in the spatial extent of the region within which converged Fourier coefficients could be obtained; the more upstream the initial condition, the longer the spatial extent. Hence, when using the present methodology, it is strongly advised to consider the most upstream and localized initial condition. This can be done by changing (usually increasing) the frame speed. Since amplification curves are independent of the frame speed and eigenfunctions, a single localized initial condition is sufficient to identify the most-amplified perturbation dynamics.

5.5. Physical mechanisms of the most amplified three-dimensional perturbations

The most amplified perturbations across the shock-induced bubble have been identified, the present section discusses the mechanisms that contribute to the three-dimensional instabilities responsible for this growth. To characterize these mechanisms, the upcoming analyses rely on the energy-budget methodology (Chapter 2) where only the terms that contribute more than 5% to the temporal growth rate are considered. The decomposition of the growth rate (equation (2.76)) is thus reduced to

$$\sigma(t_f) = \underbrace{R_{\check{u}^*\check{v}} + R_{|\check{u}|^2}}_{\text{Reynolds stresses}} + \underbrace{R_{\check{s}^*\check{v}} + R_{\check{s}^*\check{u}}}_{\text{Reynolds heat fluxes}} + \underbrace{D_{\check{u},y} + D_{\check{w},y} + D_{\check{T},y}}_{\text{Dissipation}} + \text{remainder}, \tag{5.5}$$

where all other terms individually contributing less than 5% to the energy growth and the terms related to the advection of perturbations are included in a remainder that itself, i.e., the sum of the neglected terms, represents less than 10% of the growth rate. To track the evolution of the contributions, the different terms are computed along $x_E(t_f)$ of the temporally-evolving wave packets and are shown in figure 5.12; panels 5.12(*a–d*) show the results for the upstream-type mode and 5.12(*e–h*) for the apex-type mode.

As a consequence of the large wall-normal gradient $\partial\overline{U}/\partial y > 0$ and the substantial region where $\check{u}$ and $\check{v}$ are out-of-phase (i.e., $\mathscr{R}\{\check{u}^*\check{v}\} < 0$), the Reynolds stress $R_{\check{u}^*\check{v}}$ is the largest contribution to the growth rate, for both the upstream- and apex-type wave packets. Furthermore, $R_{\check{u}^*\check{v}}$ is strongly activated in the region of the bubble apex as the wave packets move downstream such that it reaches its largest destabilizing contribution downstream of

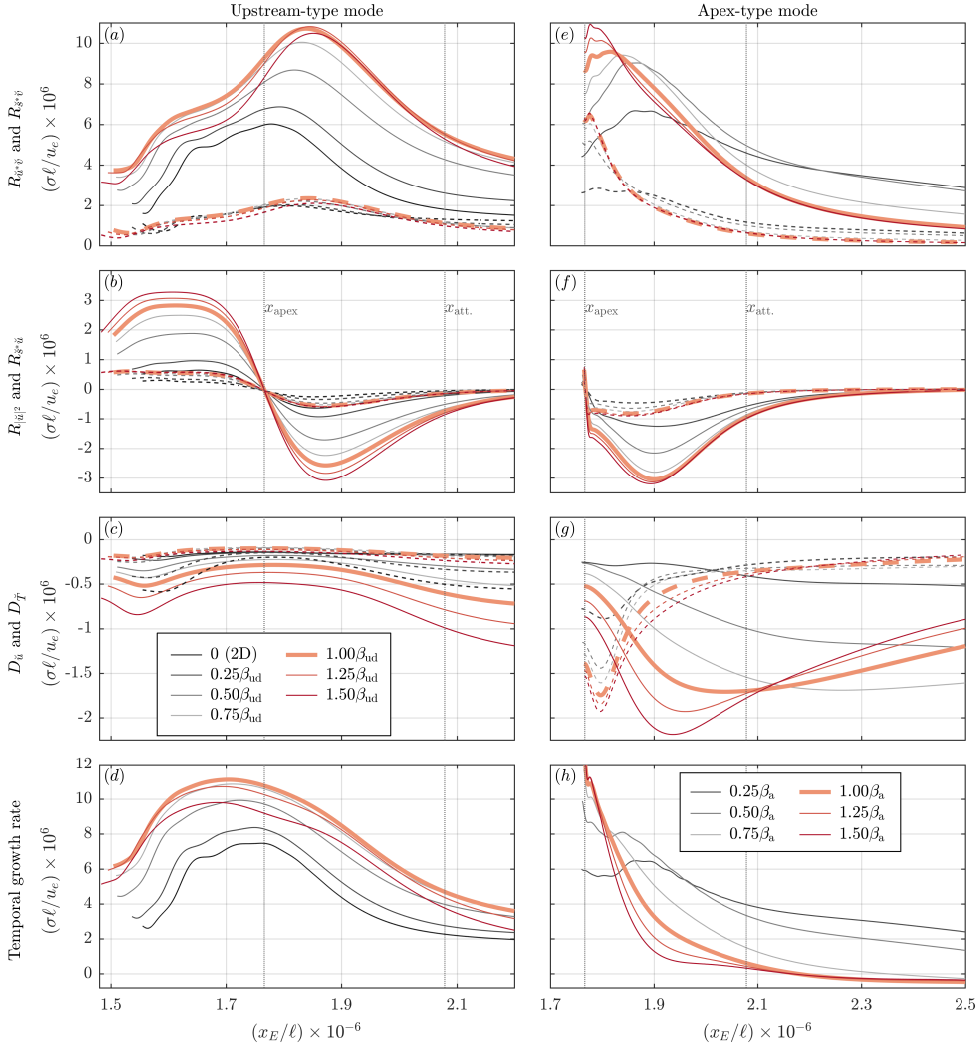

Figure 5.12: Streamwise variation of the dominant contributions to the temporal growth rate (equation (5.5)) of the temporal wave packets: (a,e) $R_{\tilde{u}^*\tilde{v}}$ (solid) and $R_{\tilde{s}^*\tilde{v}}$ (dashed), (b,f) $R_{|\tilde{u}|^2}$ (solid) and $R_{\tilde{s}^*\tilde{u}}$ (dashed), (c,g) $D_{\tilde{u},y}$ (solid) and $D_{\tilde{T},y}$ (dashed), (d,h) temporal growth rate $\sigma(t)$. $(a–d)$ Upstream- and $(e–h)$ apex-type modes for relevant β-values with contributions at β_{ud} and β_{a} highlighted by thicker line. $(a–h)$ Vertical lines: streamwise location of the bubble apex and reattachment.

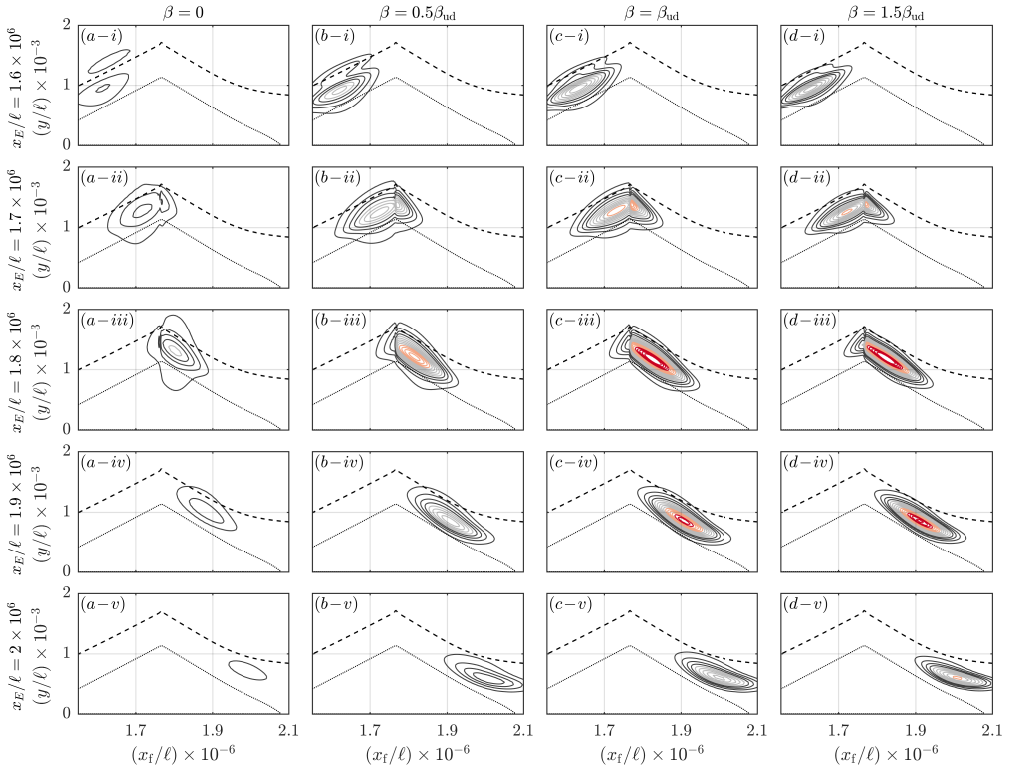

Figure 5.13: Wall-normal Reynolds stress for different β (columns (*a*–*d*)) at several locations of the x-centroid (rows (*i*–*v*)) of the upstream-type wave packet. Isocontours of $\mathscr{R}\{\check{u}^*\,\check{v}/\check{E}\} \times \rho_e \ell^2$ indicated by colored lines from -9×10^{-10} (red) to -0.5×10^{-10} (gray) with $\Delta = 0.5 \times 10^{-10}$. Boundary-layer edge ($\delta_{90}$, dashed) and dividing streamline (dotted).

the bubble apex, in close vicinity of the incident shock. In this region, the factor $\overline{\rho}\partial\overline{U}/\partial y > 0$ is relatively constant in the streamwise direction. Consequently, as shown in figure 5.13, the large size of $R_{\check{u}^*\check{v}}$ in the apex region is caused by a significant growth of $\mathscr{R}\{\check{u}^*\,\check{v}/\check{E}\}$ downstream of the shock.

A similar behavior is observed for the Reynolds heat-flux $R_{\check{s}^*\check{v}}$. For the upstream-type wave packets, however, the contribution of $R_{\check{s}^*\check{v}}$ is an order of magnitude smaller than that of $R_{\check{u}^*\check{v}}$. This follows from: 1) the smaller wall-normal gradient $\partial\overline{T}/\partial y$, 2) the reduced unbalance between the out-of-phase and in-phase regions of $\check{s}$ and $\check{v}$, and 3) the smaller relative magnitude of $\check{T}$ compared to $\check{u}$. These last two effects are, nonetheless, mitigated for apex-type wave packets such that $R_{\check{s}^*\check{v}}$ and $R_{\check{u}^*\check{v}}$ together produce most of the perturbation energy, especially in the immediate vicinity of the bubble apex.

The Reynolds stress $R_{\check{u}^*\check{v}}$ and heat-flux $R_{\check{s}^*\check{v}}$ are both maximized over the span of the shock-induced bubble at β_{ud}, which also maximizes the amplification envelope. This can be explained by considering the evolution of $\mathscr{R}\{\check{u}^*\,\check{v}/\check{E}\}$ as depicted in figure 5.13. For an increasing spanwise wavenumber, $\mathscr{R}\{\check{u}^*\,\check{v}/\check{E}\}$ increases in magnitude and, simultaneously, covers a smaller area in space. These two variations have an antagonistic effect on the integral value $R_{\check{u}^*\check{v}}$ that thus attains a maximum for $\beta = \beta_{\mathrm{ud}}$. The Reynolds heat-flux $R_{\check{s}^*\check{v}}$ features a similar behavior, but to a lesser extent following both its smaller magnitude and weaker dependency on β than those of $R_{\check{u}^*\check{v}}$. Hence, the wall-normal Reynolds stress $R_{\check{u}^*\check{v}}$

arguably governs the amplification of convective perturbations across the SWBLI.

Depending on the wave-packet location in the bubble, the streamwise Reynolds-stress $R_{|\check{u}|^2}$ and Reynolds-heat-flux $R_{\check{s}^*\check{u}}$ terms contribute to producing or destroying perturbation energy. The positive or negative contribution of these terms depends on the streamwise gradient of the streamwise base-flow velocity, $\partial\overline{U}/\partial x$, that has opposite signs on the two sides of the bubble. Hence, when the incoming perturbation crosses the bubble apex, $R_{|\check{u}|^2}$ and $R_{\check{s}^*\check{u}}$ rapidly become stabilizing as the flow accelerates and eventually reach their maximum stabilizing contribution in the aft-bubble region. $R_{|\check{u}|^2}$ becomes as large as 30% of $R_{\check{u}^*\check{v}}$ in absolute value. Thereby, $R_{|\check{u}|^2}$ prevents the maximum temporal growth to occur in the post-shock region (see figure 5.12(*d*)). Instead, the temporal growth rate is maximum upstream of the apex when $R_{|\check{u}|^2}$ produces perturbation energy along $R_{\check{u}^*\check{v}}$. Hence, while the Reynolds stress $R_{\check{u}^*\check{v}}$ term is usually the largest contribution to the growth rate in wall-bounded flows, the contribution $R_{|\check{u}|^2}$ plays a significant role in the present flow configuration in which the streamwise velocity rapidly varies in the streamwise direction.

The contribution of the streamwise Reynolds-stress $R_{|\check{u}|^2}$ to the perturbation energy becomes more significant as β increases. This is further supported by the Pearson-correlation coefficient, when comparing the streamwise variation of $R_{\check{u}^*\check{v}}$ with the temporal growth rate. This coefficient decreases from 0.99 ($\beta = 0$) to 0.82 ($\beta = 1.5\beta_{\mathrm{ud}}$), for the upstream-type wave packet, while the correlation between $R_{\check{u}^*\check{v}}+R_{|\check{u}|^2}$ and the temporal growth rate remains constant. For the apex-type wave packet, slightly weaker correlations are found, except when additionally including the wall-normal Reynolds-heat-flux term that produces significant perturbation energy alongside $R_{\check{u}^*\check{v}}$.

The dissipation terms for the upstream- and apex-type modes are given in figure 5.12(*c*,*g*), respectively. These terms present one of the main differences between the aforementioned mode types, which is explained by their high correlation with both the spatial extent and wavenumber of the wave packet. Hence, the dissipation terms of the apex-type wave packets, that have a short streamwise extent and wavelength, are much stronger than those of upstream-type wave packets. Furthermore, since the amplitude of $\check{T}$ and $\check{u}$ are similar for the apex-type mode, $D_{\check{T},y}$ and $D_{\check{u},y}$ dissipate a similar amount of perturbation energy. In contrast, upstream-type wave packets have a much larger ratio $|\check{u}|/|\check{T}|$, especially for increasing β, and are thus mostly stabilized by $D_{\check{u},y}$.

5.6. Temporal wave packets and eigenfunctions

It has been demonstrated that the eigensolutions are instantaneously valid. An eigenfunction used as an initial condition of the temporal perturbation problem renders an instantaneous growth rate at $t = 0$ that deviates gradually from the eigengrowth rate for $t > 0$. In this section, the comparison is extended for non-zero elapsed times. In particular, the perturbation wave packets at different time instants are compared against eigensolutions for different frame speeds. First, a qualitative comparison of the eigenfunctions and wave packets is proposed. Second, the temporal instantaneous growth and eigengrowth rates are decomposed into their individual contributions to the perturbation energy equation and are then compared for different time instants and frame speeds.

Once initialized from a moving-frame eigenfunction, the wave packet naturally evolves in time and moves from one spatial location to another. For this initial-value problem, time is the governing parameter. In contrast, obtaining moving-frame eigenfunctions at different locations relies on solving the stability eigenvalue problem for various frame speeds. For both initial-value and eigenvalue problems, the spatial location of the solutions is unknown. Furthermore, the relationship between space, time and frame speed is a-priori unknown. In

order to compare the behavior of the instability mechanisms as predicted by the initial-value and eigenvalue problems, the eigenfunctions and temporal wave packets are compared at identical locations of their energy centroids. To do this, the frame speeds of the eigensolution are identified such that the streamwise energy centroid of the corresponding eigenfunction matches against the streamwise centroid of the temporal wave packet obtained at different time instants. The results for $\beta = \beta_{\mathrm{ud}}$ are shown in figure 5.14 for all three types of eigenfunctions and the most amplified wave packet as found in §5.4. These results show that the finite-time response is remarkably well represented by the eigensolutions. In particular, the upstream-type eigenfunction at different frame speeds is a good representation of the evolution of the temporal wave packet in the upstream region of the bubble apex. As depicted in figure 5.15(*a*), this similarity likely stems from the correlation between the streamwise evolution of the wave-packet group speed and the eigensolution frame speeds. Figure 5.15(*b*) also shows good agreement between the temporal and eigengrowth rates. Nevertheless, the characteristics of the upstream-type eigensolutions start deviating from the temporal evolution for locations downstream of the bubble apex. At these locations, the two other mode types emerge with equally large growth rates and thus likely influence the temporal evolution (see figure 5.15(*b*)). In order to clarify this behavior, the physical underlying mechanisms of the eigenfunctions and the wave packets are investigated.

The perturbation energy equations, that are given in reduced forms by equations (5.4) and (5.5) for the eigengrowth and wave-packet growth rates, respectively, are considered. The results are shown in figure 5.15 for the wave packets at different time instants (black lines and symbols) and the eigenfunctions at different frame speeds. For the following analyses, the advection terms are taken out from the remainder of equation (5.5). Although the sum of these terms cancels out, they vary rapidly in space and are thus relevant to compare the evolution of the solutions across the bubble. Figure 5.15(*f*) shows that the spatial variation of the advection terms is remarkably similar between wave packets and eigenfunctions. In particular, the evolution of $A_{\overline{U}}$ and $A_{\overline{V}}$ for upstream-type eigensolutions over the streamwise extent of the bubble gives a very good representation of the advection mechanisms taking place in the temporal wave packet. When the wave packet and eigenfunction move through the bubble apex, the transition of the advection term $A_{\overline{V}}$ from a productive to a destructive contribution, and, vice versa for $A_{\overline{U}}$, is similar for both solutions. Note that this transition was also observed between upstream and downstream-type eigensolutions in §5.3.3. Although the other mode types cannot estimate the contribution of the advection terms in the entire shock-induced bubble, they still give a good representation of these contributions downstream of the bubble apex. In fact, the advection terms have similar behavior and amplitude for all mode types downstream of the incident shock. As a final remark, figure 5.15(*f*) clearly demonstrates that the $A_{\overline{U}}$ and $A_{\overline{V}}$ terms have antagonistic contributions at any location in the flow for all cases. Hence, as mentioned previously, the overall contribution of the advection terms to the growth rate is several orders of magnitude lower than the contribution of the Reynolds-stress, Reynolds-heat-flux and dissipation terms; advection terms neither significantly produce nor destroy perturbation energy in the present case.

As indicated by figure 5.15, all dominant contributions to the upstream-type eigengrowth rate are in good agreement with the contributions to the wave-packet growth rate. The main discrepancies are observed in close proximity to the bubble and are mostly noticeable on the Reynolds stress $R_{|\tilde{u}|^2}$ and dissipation $D_{\tilde{T},y}$. For $R_{|\tilde{u}|^2}$, the difference between the eigensolutions and the wave packet stems from the eigenfunctions being spread over two distinct parts located upstream and downstream of the apex (see figure 5.14(*b*) at $c_{\mathrm{f}} = 0.53u_e$). Since the streamwise gradient $\partial\overline{U}/\partial x$ in the shear layer has an opposite sign on either side of the

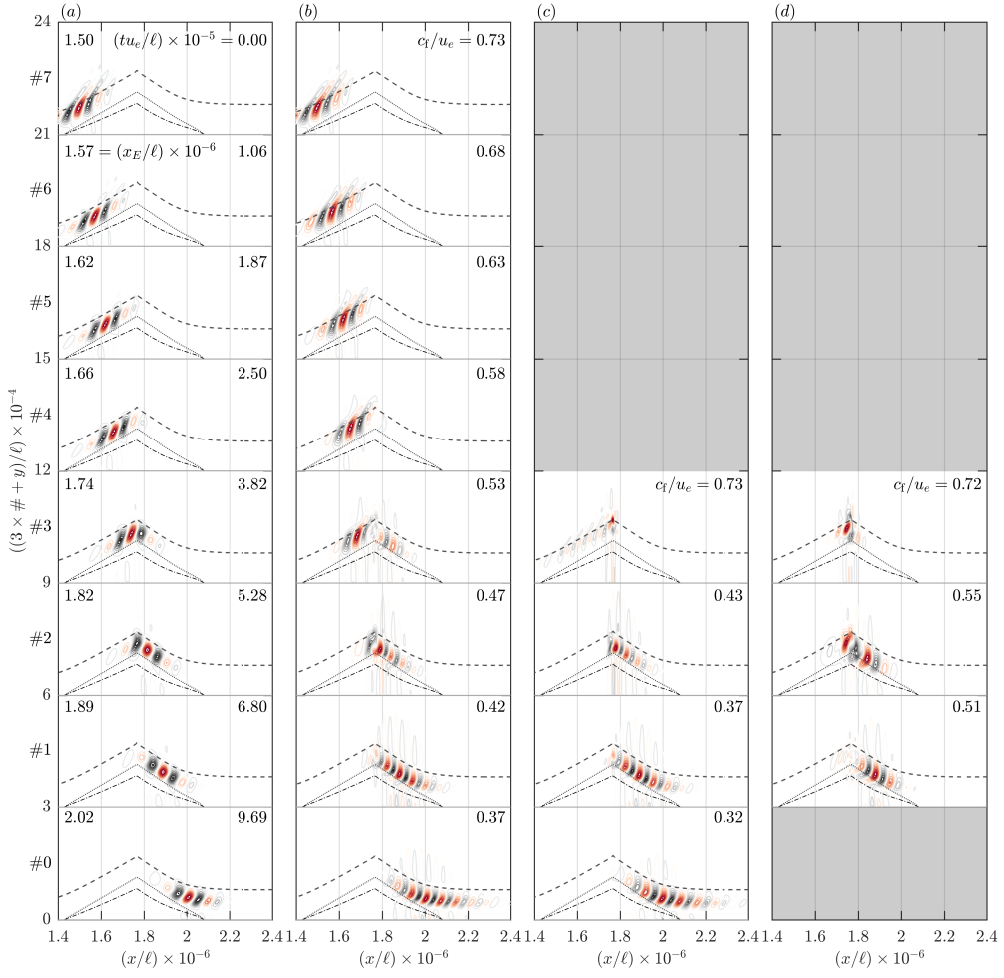

Figure 5.14: Evolution at β_{ud} of (*a*) the temporal wave packet initialized from the most unstable upstream eigenfunction at $c_f = 0.73u_e$, (*b–d*) the most unstable (*b*) upstream-, (*c*) apex- and (*d*) downstream-type eigenfunctions at different frame speeds. (*a–d*) Isocontours of $\mathscr{R}(\tilde{u}')/|\tilde{u}'|_{max}$ (colored lines, from minimum (gray) to maximum (red) with $\Delta = 2/9$, with the phase set to zero where $|\tilde{u}'|_{max}$ is attained). $\overline{U} = 0.9u_e$-isocontour (dashed black), dividing streamline (dotted black) and $\overline{U} = 0$-isocontour (dash-dotted). The eigenfunctions and wavepackets are labeled from #0 to #7 (bottom to top) and the y-axis is scaled accordingly. (*c,d*) Gray patches if no localized eigenfunction found at the location of the wave packet.

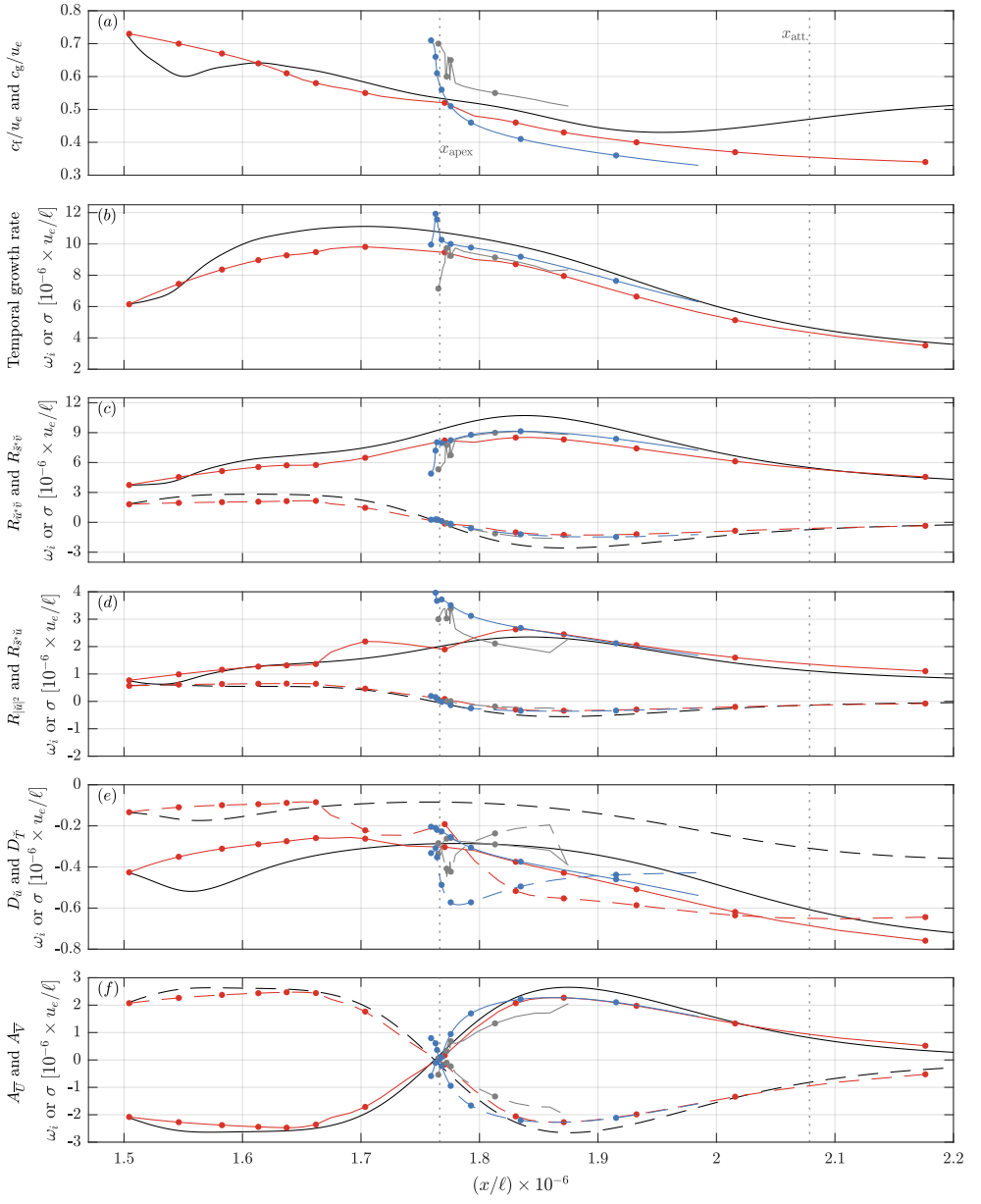

Figure 5.15: Spatial evolution of (*a*) the frame (colored lines) and group (black line) speeds and (*b–f*) the dominant contributions to the energy growth for the three-dimensional eigenfunctions and wave packets at β_{low}: (*b*) growth rate $(\omega_i \ell/u_e) \times 10^6$, (*c*) Reynolds stresses $R_{\tilde{u}^*\tilde{v}}$ (solid) and Reynolds heat-fluxes $R_{\tilde{s}^*\tilde{v}}$ (dashed), (*d*) $R_{|\tilde{u}|^2}$ (solid) and $R_{\tilde{s}^*\tilde{u}}$ (dashed), (*e*) dissipation terms $D_{\tilde{u}}$ (solid) and $D_{\tilde{T}}$ (dashed) and (*f*) $\overline{U}$-advection (solid) and $\overline{V}$-advection (dashed) for upstream- (red), apex- (blue) and downstream-type (gray) modes at the frame speeds indicated in panel (*a*). (*a–f*) The group speed and the terms contributing to temporal growth rate $(\sigma\ell/u_e) \times 10^6$ of the wave packet are in black. Streamwise location of bubble apex indicated by vertical dotted gray line.

bubble apex, the productive contribution of $R_{|\tilde{u}|^2}$ significantly increases when a structure rapidly emerges in the downstream part of the bubble. The wave-packet evolution across the incident shock does not experience this relatively complex behavior of the eigenfunctions but, instead, evolves smoothly from the upstream to the downstream region of the bubble. Nevertheless, once the wave packet and eigenfunctions are fully supported in the downstream part of the bubble, the Reynolds stresses $R_{|\tilde{u}|^2}$ and $R_{|\tilde{u}|^2}$ are again similar. The temperature dissipation term $D_{\tilde{T},y}$ of the upstream-type eigensolutions also features a sudden variation near the bubble apex. In this case, it is due to a rapid decrease of the ratio $|\tilde{u}|_{\max}/|\tilde{T}|_{\max}$. In §5.3.3, it was found that this ratio is relatively large for upstream-type eigenfunctions whereas it is much smaller for downstream- and apex-type modes. However, the magnitude of the variation of $D_{\tilde{T},y}$ and $R_{|\tilde{u}|^2}$ does not strongly impact the overall growth rate of the eigensolutions that, as shown in figure 5.15(*b*), follows relatively well the evolution of temporal growth rate of the perturbation wave packet.

The fact that the eigengrowth and wave-packet growth rates are in good agreement stems from the two most dominant contributions, i.e., the wall-normal Reynolds stress and heat flux, that are very similar for the temporal wave packet and upstream-type eigensolutions. Again, the largest differences are observed near the apex but are much less significant and rapid than for $R_{|\tilde{u}|^2}$ and $D_{\tilde{T},y}$. For the present case, the difference only translates into a mild underestimation of $R_{\tilde{u}^*\tilde{v}}$ and $R_{\tilde{s}^*\tilde{v}}$, in absolute value, by the upstream-type eigenfunctions. Near the apex, figure 5.15 shows that the apex- (blue) and downstream-type (gray) modes emerge with dominant contributions. They are as large as in the upstream modes (red symbols) and thus approach the evolution of the temporal wave packet in the region downstream of the shock. In fact, the apex-type eigenfunctions offer a slightly better estimation of the time-dependent mechanisms for locations downstream of the bubble apex.

Further characterization of the eigenfunction switch at the shock location is beyond the present scope, but this particular aspect deserves clarification in future work. A possible approach to assess these effects in the temporal evolution is to project a wave packet used as an initial condition onto an eigenbasis and track the evolution of the projection coefficients as the wave packet evolves in time. In this way, the weights of the different modes contributing to the temporal wave packet can be determined and, accordingly, the contribution of each mode to the wave-packet evolution throughout the shock could be quantified. Although the described analysis is insightful to fully characterize how each component participates in the perturbation evolution, it can be concluded that, except around the apex, the mechanisms yielding the largest amplification in the bubble can essentially be characterized by eigenfunctions. Hence, the wave-packet dynamics in the present flow case are deemed well represented by eigensolutions even if the most representative eigensolution likely switches from an upstream-type to an apex-type mode as time advances.

5.7. Intermediate conclusion

In this chapter, linear stability analyses of a laminar SWBLI were performed to, first, assess the effectiveness of the moving-frame approach and, second, determine the most amplified convective disturbance mechanisms. The laminar SWBLI base-flow field was obtained by using the selective frequency damping approach, which, prior to linear stability analyses, indicates that the flow does not support the temporal growth of a disturbance in a fixed region of space. This means that no two-dimensional global instabilities exist in the present configuration and, thus, at least all two-dimensional instability mechanisms should be convective. Furthermore, as part of the linear stability analyses, no three-dimensional global modes were found. Hence, because 1) the flow supports large gradients and 2) no localized

eigensolutions could be found in the *stationary* frame of reference, studying the stability of the present SWBLI arguably requires solving the two-dimensional stability problem using the moving-frame approach.

As demonstrated for the incompressible boundary layer, the moving frame allows capturing convective mechanisms as eigensolutions with eigenfunctions that are localized in the streamwise direction. Hence, the solutions can be made independent of the computational setup (truncation-boundary positions and conditions and grid resolution) and this allowed identifying three types of unstable, localized modes (upstream-, downstream- and apex-type modes) for a wide range of spanwise wavenumbers and frame speeds. The characteristic frequency of these instability mechanisms is at least one order of magnitude larger than what is usually observed for the low-frequency breathing of the bubble and none of the linear mechanisms found could be related to any low-frequency unsteadiness of the SWBLI. Instead, the medium-frequency mechanisms that are presently found represent convective instability mechanisms of the separated shear layer and can enter the reverse-flow region.

By considering the finite-time evolution of the wave-packet perturbations obtained from the initial-value problem using the moving-frame eigenfunctions as initial condition, the spatial evolution of the convective instabilities has been assessed. First, the perturbation amplification is quantified by reconstructing the individual-frequency amplification curves by Fourier-transforming the signal. To the greatest extent, this allows determining the most amplified perturbation content of the SWBLI, in particular in terms of the most amplified spanwise wavenumber, which is found to be as large as about 10% of the bubble length, and frequency, which is about 9 kHz at the streamwise location of the reattachment. Second, the perturbation wave packet is decomposed into the individual components that contribute to its growth. It is observed that the wall-normal Reynolds stress produces most of the disturbance energy over the whole extent of the SWBLI. Nevertheless, although the streamwise Reynolds stress has a smaller magnitude, it can interfere either productively or destructively with the wall-normal Reynolds stress depending on whether the wave-packet is located upstream or downstream of the bubble apex. This contribution of the streamwise Reynolds-stress results in an overall upstream shift of the maximum temporal growth and intensifies when increasing the spanwise wavenumber β. At a particular spanwise wavenumber $\beta = \beta_{\mathrm{ud}}$, the (integral) wall-normal Reynolds-stress and Reynolds-heat flux of the temporal wave-packet are maximized along the complete spatial extent of the shock-induced bubble. By analyzing the variation of the spatial organization of the dominant factors that appear in the integrand of the wall-normal Reynolds-stress term as β increases, it is found that its maximum magnitude increases, while the area over which it is active shrinks so that it leads the integral value to reach a maximum for $\beta = \beta_{\mathrm{ud}}$. In turn, the largest amplification in the present flow configuration is achieved for this wavenumber, which also corresponds to the spanwise wavenumber that displays the maximum growth rate of the moving-frame initial condition.

A major finding is that the moving-frame eigensolutions provide a remarkably good estimation of the evolution of the time-dependent wave packet. Although a switch from one eigensolution to another near the apex likely occurs, the largest amplification of the wave packet and its underlying mechanisms are mostly represented by one type of eigensolution at a time. Hence, this allows concluding that the moving-frame eigensolutions provide a very reasonable expectation for the spatio-temporal evolution of the wave-packet perturbations. This is very useful, because this means that the eigensolutions can be used to guide the more expensive wave-packet calculations in determining the most-amplified perturbation content.

Without having applied the moving-frame methodology to other flow configurations,

the present results suggest that this approach opens the way for the structured characterization of the laminar-turbulent transition of separation bubbles in general (including the incompressible, transonic, and hypersonic regimes), starting from the homogeneous, linear, convectively unstable disturbance mechanisms. It is likely that separation bubbles show similar, more, or fewer mode types and that modes other than the upstream-type mode can dominate in particular conditions. Future research efforts should be invested in thoroughly exploring the behavior of the newly found mechanisms for other flow configurations (varying Mach number, Reynolds number, shock strength, etc.).

As a final remark, it important to emphasize that only an insight into primary convective instabilities in SWBLI is presently proposed and nonlinear effects, that take place when the perturbation amplitude becomes significantly large, are not considered. Assessing nonlinear mechanisms, however, requires a judicious choice of initial conditions. By using the moving-frame solutions, a careful control of these initial conditions is possible and this thus provides a structured strategy that can be applied to study the route from linear perturbation growth to laminar-turbulent transition in SWBLI.

References

ACKERET, J., FELDMANN, F. & ROTT, N. 1947 Investigations of compression shocks and boundary layers in gases moving at high speed. *Tech. Rep.* NACA-TM-1113. National Advisory Committee for Aeronautics.

ADLER, M. C. & GAITONDE, D. V. 2018 Dynamic linear response of a shock/turbulent-boundary-layer interaction using constrained perturbations. *Journal of Fluid Mechanics* **840**, 291–341.

ÅKERVIK, E., BRANDT, L., HENNINGSON, D. S., HŒPFFNER, J., MARXEN, O. & SCHLATTER, P. 2006 Steady solutions of the Navier-Stokes equations by selective frequency damping. *Physics of Fluids* **18** (6), 068102.

AVANCI, M. P., RODRÍGUEZ, D. & ALVES, L. S. D. B. 2019 A geometrical criterion for absolute instability in separated boundary layers. *Physics of Fluids* **31** (1), 014103.

BABINSKY, H. & HARVEY, J. 2011 *Shock wave–boundary-layer interactions*. Cambridge: Cambridge University Press.

BERESH, S. J., CLEMENS, N. T. & DOLLING, D. S. 2002 Relationship between upstream turbulent boundary-layer velocity fluctuations and separation shock unsteadiness. *AIAA Journal* **40** (12), 2412–2422.

BONNE, N., BRION, V., GARNIER, E., BUR, R., MOLTON, P., SIPP, D. & JACQUIN, L. 2019 Analysis of the two-dimensional dynamics of a Mach 1.6 shock wave/transitional boundary layer interaction using a RANS based resolvent approach. *Journal of Fluid Mechanics* **862**, 1166–1202.

BUGEAT, B., ROBINET, J.-C., CHASSAING, J.-C. & SAGAUT, P. 2022 Low-frequency resolvent analysis of the laminar oblique shock wave/boundary layer interaction. *Journal of Fluid Mechanics* **942**.

CASACUBERTA, J., GROOT, K. J., TOL, H. J. & HICKEL, S. 2018 Effectivity and efficiency of selective frequency damping for the computation of unstable steady-state solutions. *Journal of Computational Physics* **375**, 481–497.

CERULUS, N., QUINTANILHA, H. & THEOFILIS, V. 2021 Global linear stability analysis of the supersonic flows over a hollow cylinder flare model. In *AIAA Scitech 2021 Forum*.

CHAPMAN, D., KUEHN, D. & LARSON, H. 1958 Investigation of separated flow in supersonic and subsonic streams with emphasis of the effect of transition . *Tech. Rep.* 1356. National Advisory Committee for Aeronautics. Ames Aeronautical Lab, Moffett Field, CA, United States.

CLEMENS, N. T. & NARAYANASWAMY, V. 2014 Low-frequency unsteadiness of shock wave/turbulent boundary layer interactions. *Annual Review of Fluid Mechanics* **46** (1), 469–492.

DÉLERY, J. & DUSSAUGE, J.-P. 2009 Some physical aspects of shock wave/boundary layer interactions. *Shock Waves* **19** (6), 453–468.

DÉLERY, J., MARVIN, J. G. & RESHOTKO, E. 1986 Shock-wave boundary layer interactions. *Tech. Rep.* ADA171302. Advisory Group for Aerospace Research and Development.

DOLLING, D. S. 2001 Fifty years of shock-wave/boundary-layer interaction research: what next? *AIAA Journal* **39** (8), 1517–1531.

DONALDSON, C. D. 1944 Effects of interaction between normal shock and boundary layer. *Tech. Rep.* NACA-CB-4A27. National Advisory Committee for Aeronautics.

DUSSAUGE, J.-P., DUPONT, P. & DEBIÈVE, J. F. 2006 Unsteadiness in shock wave boundary layer interactions with separation. *Aerospace Science and Technology* **10** (2), 85–91.

DWIVEDI, A., HILDEBRAND, N., NICHOLS, J. W., CANDLER, G. V. & JOVANOVIĆ, M. R. 2020 Transient growth analysis of oblique shock-wave/boundary-layer interactions at Mach 5.92. *Physical Review Fluids* **5** (1), 063904.

FAGE, A. & SARGENT, R. F. 1947 Shock-wave and boundary-layer phenomena near a flat surface. *Proceedings of the Royal Society of London. Series A. Mathematical and Physical Sciences* **190**, 1–20.

FERRI, A. 1939 Experimental results with airfoils tested in the high-speed tunnel at Guidonia. *Tech. Rep.* NACA-TM-946. National Advisory Committee for Aeronautics.

GAITONDE, D. V. 2015 Progress in shock wave/boundary layer interactions. *Progress in Aerospace Sciences* **72**, 80–99.

GAITONDE, D. V. & ADLER, M. C. 2023 Dynamics of three-dimensional shock-wave/boundary-layer interactions. *Annual Review of Fluid Mechanics* **55** (1), 291–321.

GANAPATHISUBRAMANI, B., CLEMENS, N. T. & DOLLING, D. S. 2007 Effects of upstream boundary layer on the unsteadiness of shock-induced separation. *Journal of Fluid Mechanics* **585**, 369–394.

GANAPATHISUBRAMANI, B., CLEMENS, N. T. & DOLLING, D. S. 2009 Low-frequency dynamics of shock-induced separation in a compression ramp interaction. *Journal of Fluid Mechanics* **636**, 397–425.

GIEPMAN, R. H. M. 2016 Flow control for oblique shock wave reflections. PhD thesis, Delft University of Technology.

GRILLI, M., SCHMID, P. J., HICKEL, S. & ADAMS, N. A. 2012 Analysis of unsteady behaviour in shockwave turbulent boundary layer interaction. *Journal of Fluid Mechanics* **700**, 16–28.

GUIHO, F., ALIZARD, F. & ROBINET, J. C. 2016 Instabilities in oblique shock wave/laminar boundary-layer interactions . *Journal of Fluid Mechanics* **789**, 1–35.

HICKEL, S., EGERER, C. P. & LARSSON, J. 2014 Subgrid-scale modeling for implicit large eddy simulation of compressible flows and shock-turbulence interaction. *Physics of Fluids* **26** (10), 106101.

HILDEBRAND, N. J., DWIVEDI, A., NICHOLS, J. W., JOVANOVIĆ, M. R. & CANDLER, G. V. 2018 Simulation and stability analysis of oblique shock-wave/boundary-layer interactions at Mach 5.92. *Physical Review Fluids* **3** (1), 013906.

JORDI, B. E., COTTER, C. J. & SHERWIN, S. J. 2014 Encapsulated formulation of the selective frequency damping method. *Physics of Fluids* **26** (3), 034101.

LARCHEVÊQUE, L. 2016 Low- and Medium-Frequency Unsteadinesses in a Transitional Shock–Boundary Reflection with Separation. In *54th AIAA Aerospace Sciences Meeting*.

LASH, L. E., GRAGSTON, M., KRETH, P. A., MCDANIEL, Z., CODER, J. G. & SCHMISSEUR, J. D. 2021 Upstream influence in shock wave/transitional boundary layer interactions at mach 1.8. *AIAA Journal* **59** (12), 4842–4857.

LIEPMANN, H. W. 1946 The interaction between boundary layer and shock waves in transonic flow. *Journal of the Aeronautical Sciences* **13** (12), 623–637.

NICHOLS, J. W., LARSSON, J., BERNARDINI, M. & PIROZZOLI, S. 2017 Stability and modal analysis of shock/boundary layer interactions. *Theoretical and Computational Fluid Dynamics* **31** (1), 33–50.

NIESSEN, S. E. M. 2017 BiGlobal stability analysis: laminar shock-wave/boundary-layer interactions. Master's thesis, University of Liège, Faculty of Applied Sciences.

NUTTER, N. F., COBOURN, J. W., BOND, R. B., KRETH, P. A., SCHMISSEUR, J. D., GLASBY, R. S., STEFANSKI, D. L., HERETH, E. & CODER, J. G. 2021 Simulations of dynamic shock wave/boundary layer interactions using hpcmp create^{TM}-av kestrel coffe. In *AIAA Scitech 2021 Forum*.

PASQUARIELLO, V., HICKEL, S. & ADAMS, N. A. 2017 Unsteady effects of strong shock-wave/boundary-layer interaction at high Reynolds number. *Journal of Fluid Mechanics* **823**, 617–657.

PIPONNIAU, S., DUSSAUGE, J. P., DEBIÈVE, J. F. & DUPONT, P. 2009 A simple model for low-frequency unsteadiness in shock-induced separation. *Journal of Fluid Mechanics* **629**, 87–108.

PIROZZOLI, S. & GRASSO, F. 2006 Direct numerical simulation of impinging shock wave/turbulent boundary layer interaction at M=2.25. *Physics of Fluids* **18** (6), 065113.

PIROZZOLI, S., LARSSON, J., NICHOLS, J., BERNARDINI, M., MORGAN, B. & LELE, S. 2010 Analysis of unsteady effects in shock/boundary layer interactions. In *Proceedings of the Summer Program*, pp. 153–164. Center for Turbulence Research.

ROBINET, J. C. 2007 Bifurcations in shock-wave/laminar-boundary-layer interaction: global instability approach. *Journal of Fluid Mechanics* **579**, 85–112.

RODRÍGUEZ, D., GENNARO, E. M. & SOUZA, L. F. 2020 Self-excited primary and secondary instability of laminar separation bubbles. *Journal of Fluid Mechanics* **906**, A13.

SANSICA, A., SANDHAM, N. D. & HU, Z. 2014 Forced response of a laminar shock-induced separation bubble. *Physics of Fluids* **26** (9), 093601.

SANSICA, A., SANDHAM, N. D. & HU, Z. 2016 Instability and low-frequency unsteadiness in a shock-induced laminar separation bubble. *Journal of Fluid Mechanics* **798**, 5–26.

SASAKI, K., BARROS, D. C., CAVALIERI, A. V. G. & LARCHEVÊQUE, L. 2021 Causality in the shock wave/turbulent boundary layer interaction. *Physical Review Fluid* **6**, 064609.

SEBASTIAN, J. J. & LU, F. K. 2021 Upstream-influence scaling of fin-induced laminar shockwave/boundary-layer interactions. *AIAA Journal* **59** (5), 1861–1864.

TESTER, B. W., CODER, J. G., COMBS, C. S. & SCHMISSEUR, J. D. 2018 Hybrid rans/les simulation of transitional shockwave/boundary-layer interaction. In *2018 Fluid Dynamics Conference*.

TOUBER, E. & SANDHAM, N. D. 2008 Oblique shock impinging on a turbulent boundary layer: Low-frequency mechanisms. In *38th AIAA Fluid Dynamics Conference and Exhibit*. University of Southampton, Southampton, United Kingdom.

TOUBER, E. & SANDHAM, N. D. 2009 Large-eddy simulation of low-Frequency unsteadiness in a turbulent shock-induced separation bubble . *Theoretical and Computational Fluid Dynamics* **23** (2), 79–107.

WU, M. & MARTÍN, M. P. 2008 Analysis of shock motion in shockwave and turbulent boundary layer interaction using direct numerical simulation data. *Journal of Fluid Mechanics* **594**, 71–83.

YAO, Y., KRISHNAN, L., SANDHAM, N. D. & ROBERTS, G. T. 2007 The effect of Mach number on unstable disturbances in shock/boundary-layer interactions. *Physics of Fluids* **19** (5), 054104.

6

Conclusion

In the context of laminar-turbulent transition and flow stability analyses, the present thesis focused on studying linear convective instability mechanisms in fluid flows with rapid variations in both wall-normal and streamwise directions. Since gradients in a flow field are at the core of the instability mechanisms, all gradients must be accounted for in stability analyses in order to accurately describe the perturbation dynamics. However, the traditional formulations of the stability equations either neglect the spatial variation of the flow or faces a major numerical issue.

Nowadays, the aforementioned limitations still prevent capturing the general perturbation dynamics of convective instabilities in (at least) two-dimensional flows. This aspect has motivated the present work that targets an accurate, fully-elliptic representation of this particular type of instabilities without restriction on the in-plane gradients. The objectives of this thesis were two-fold. First, a novel approach for stability analysis of convective instabilities was proposed with all the elements necessary for the interpretation of the solutions. Second, the convective instability mechanisms in a laminar shock-wave/boundary-layer interaction were studied with the proposed methodology.

6.1. Representation of convective instabilities in two-dimensional flows

The literature presents many attempts to describe convective instability mechanisms in two-dimensional flows, especially in flows that develop in the streamwise direction. On the one hand, the traditional Linear Stability Theory (LST) and Parabolized Stability Equations (PSE) methods do not account for large gradients in the streamwise direction. On the other hand, the fully-elliptic two-dimensional stability problem, i.e., the so-called BiGlobal stability problem, provides solutions that are tainted by a notorious sensitivity of the solutions to the truncation boundaries (domain length, boundary conditions and discretization). In fact, when aiming to represent two-dimensional convective instabilities in a stationary frame of reference, the corresponding solutions are characterized by eigenfunctions that grow exponentially from the inlet to the outlet of the domain. Hence, on the one hand, the solutions are rapidly conditioned by numerical overflow issues taking place within the domain limits; an eigenfunction reaches from very low amplitude at the inlet to very high amplitude at the outlet. Accordingly, increasing the domain length makes the conditioning of the problem

worse since more exponential growth must be contained in the domain. On the other hand, this implies that the eigenfunctions have a non-zero amplitude at the truncation boundaries; the eigensolutions thus depend on the boundary locations and conditions. If two-dimensional convective instabilities are sought, it is thus essential to tackle the mechanisms at the origin of this unbounded growth that prevents obtaining an accurate numerical representation of the solutions.

In the linear system that governs the perturbation evolution, the advection component inherently translates into an exponential growth that allows the transport of perturbations in a particular direction. Hence, since a convective instability mechanism continuously sweeps a disturbance introduced in the flow, the effect of the advection translates into a spatial exponential growth in the direction of the propagation. However, since the BiGlobal stability problem in the stationary frame of reference inherently targets the long-time evolution of perturbations, the eigenfunctions representing convective instabilities must include the advection-induced growth in the streamwise direction. Because convective disturbances leave the flow undisturbed in the long-time horizon, the BiGlobal framework is arguably not reasonable to describe convective instability mechanisms. Hence, the literature proposes other methods that instead focus on the finite-time representation of this type of instabilities.

The finite-time response of a two-dimensional flow field can be studied with the optimal-perturbation method, resolvent analysis or the Harmonic Linearized Navier-Stokes (HLNS) approach. While the first two rely on solving an optimization problem, the HLNS method solves the linearized perturbation problem with a temporal forcing usually imposed at the domain inlet. Because the optimal-perturbation and resolvent analysis methods seek initial conditions or forcing that maximize the amplification of the perturbation in the flow, they constrain the study of the flow stability to very specific scenarios that are physically not realizable; the optimal perturbation growth is likely not reproducible in an experimental context. Although the HLNS approach does not constrain the perturbation dynamics to an optimal scenario only, forcing a flow with an arbitrary function can condition the flow response to the specific forcing and thus occult the inherent perturbation dynamics. Therefore, because all three aforementioned approaches provide particular results, it is questionable whether they can unambiguously represent convective instabilities in two-dimensional flows.

All the above considerations pose a fundamental problem regarding the ambiguity behind the representation of two-dimensional convective instabilities. On the one hand, the BiGlobal stability problem inherently focuses on the long-time horizon that is conflicting with the representation of convective instabilities that are continuously transported by the flow. Hence, looking for perturbations for an indefinitely long time translates into seeking solutions that have likely left the region of interest. Although the eigensolutions form together a basis that is valid for all times and that can be used to project arbitrary disturbances onto, there is still the question about the validity of the projection coefficients that are sensitive to the numerical setup. On the other hand, although seeking a finite-time solution is much more reasonable for this type of instabilities, having to resort to a particular scenario is too restrictive. Hence, there is a need to find a compromise between the two approaches; the long-time dynamics must be abandoned for the finite-time dynamics and, in turn, no particular growth scenario must be favored such that the general perturbations dynamics of convective instabilities can be obtained. In this context, this thesis proposed a novel approach for the representation of convective instabilities in two-dimensional flows by considering a moving frame of reference.

6.2. A novel perspective with the moving-frame methodology

The present framework developed for the representation of convective instabilities with the two-dimensional stability problem is built on the BiGlobal eigenvalue problem formulated in a moving frame of reference. In this frame of reference, the advection-induced growth is reduced and thus the eigensolutions feature localized eigenfunctions that do not reach from the inlet to the outlet of the domain. Hence, the notorious numerical dependence of the two-dimensional streamwise eigensolutions on the truncation boundaries can be effectively removed.

In the moving frame of reference, the base flow is time dependent. This must be neglected upon casting the perturbation problem in an eigenvalue problem. Nevertheless, the eigensolutions solve the stationary-frame linearized Navier-Stokes equations in an instantaneous sense only; the moving-frame eigensolutions do not solve the linearized Navier-Stokes equations for all times. This property of the eigensolutions was sacrificed in order to obtain a setup-independent basis for the general dynamics that is not restricted to the optimal-growth scenario. Losing this property moreover implied that the time-asymptotic interpretation that usually accompanies eigenvalue analyses is lost as well. Nevertheless, this interpretation was anyway arguably unsuitable in the context of convective perturbations, because they are swept out of the region of interest after a finite time.

The other usual properties of an eigenvalue problem formulated in the stationary frame of reference are preserved in the sense that there is no restriction to a particular frequency, any perturbation can be reconstructed by a superposition of the eigenmodes, and the scope of the eigenfunction expansion can be reduced to the dominant eigenmodes. Furthermore, the selection of the dominant eigenmodes can be based on the imaginary part of the eigenvalues obtained in the moving frame of reference; it is a non-trivial result that these values represent the instantaneous perturbation growth only if the moving-frame eigenfunctions are localized. Because the moving-frame eigenfunctions are instantaneously-valid solutions satisfying the stationary-frame equations for zero elapsed time, they are ideal candidate to initialize the integration of the perturbation equations. Hence, in order to obtain the finite-time evolution of the perturbations, the present approach proposes to integrate in time the moving-frame eigensolutions introduced in the stationary-frame equations. It is equivalent to the spatial marching technique on which the PSE method relies, except that the present approach has no model error because all base-flow gradients are accounted for.

The eigenfunctions obtained in the moving frame of reference take the form of spatially distributed wave packets that contain a band of frequencies. After disturbing the flow in the stationary-frame problem with these two-dimensional eigenfunctions, the finite-time dynamics of temporal *wave packets* are thus recovered. However, in the context of stability analysis, the interpretation of wave-packet instabilities is less usual than single-frequency *wave trains*. Hence, in order to recover more traditional results, but with all in-plane gradients being now accounted for, the present approach relies on decomposing the wave packets into their individual-frequency components with Fourier transforms. This allows obtaining neutral and amplification curves of the perturbations in a given flow field. Ultimately, the amplification curves can be used to reconstruct the traditional N-curves on which the e^N-method relies to predict the laminar-turbulent transition in a flow.

6.3. Key results and discussions

In the present work, the moving-frame method was applied to two flow configurations. First, the incompressible flat-plate boundary layer was considered because it is the archetype of non-parallel flows that support only convective instabilities and its base flow is repro-

ducible up to arbitrary precision. Since this flow is only slowly evolving in the streamwise direction, the LST and PSE methods can be used without introducing large model errors. The traditional stationary-frame BiGlobal framework, however, fails in providing an accurate representation of the convective instability solutions that do not depend on the truncation boundaries. The flat-plate boundary layer is thus a judicious choice to validate the present methodology while also highlighting the superiority of the proposed moving-frame approach over the traditional stationary-frame BiGlobal method.

Secondly, the moving-frame method was applied to a laminar shock-wave/boundary-layer interaction (SWBLI). The first motivation for considering the SWBLI was to demonstrate the effectiveness of the method for highly two-dimensional flows. The second motivation was to contribute to a better understanding of the convective instability mechanisms in SWBLI. It was made possible with the moving-frame approach that improves the representation of the linear perturbation dynamics by avoiding both optimal scenarios and assumptions on the spatial variation of the flow. The key results obtained in both the flat-plate boundary layer and the SWBLI are discussed in the following.

6.3.1. The moving-frame methodology

A first key result is that the dependency of the eigenvalue problem with respect to the truncation boundaries can be effectively eliminated by using a moving frame of reference. By formulating the eigenvalue problem this way, the eigenfunctions describing convective mechanisms become localized in the streamwise direction. As a consequence, converged solutions can be obtained that are independent of the imposed truncation boundary conditions. For the two base-flow configurations considered in the present thesis, sensitivity analyses performed on the spatial discretization, domain length and boundary conditions demonstrated that, for a given frame speed, the sensitivity of the eigensolutions to the numerical configuration in the streamwise direction can be made as small as in the wall-normal direction. According to the inherent decay of shear-layer instabilities in the freestream, the literature usually reports that the numerical sensitivity to wall-normal boundary conditions is reasonably low. Hence, placing both wall-normal and streamwise truncation boundaries sufficiently far from the region of interest allows obtaining results that are arguably independent of the numerical setup.

Obtaining setup-independent eigensolutions relies on obtaining direct and adjoint eigenfunctions that are both localized. This result is not surprising in the sense that the overlap of the direct and adjoint eigenfunctions describes where the solutions are the most sensitive to any physical or numerical variation of the base flow or setup. In the eigenvalue spectrum of the boundary layer, it was found that converged eigenvalues form a main branch that is distinguishable from unconverged eigenvalues, which instead lie on side and downward branches. Only the main branch contains eigensolutions associated with direct and adjoint eigenfunctions that are both localized. Hence, the amplitude of both direct and adjoint eigenfunctions at the truncation boundary can be correlated with the numerical dependency of the solutions with respect to the numerical setup. In practice, for a given numerical setup, determining the amplitude at the truncation boundaries allows a rapid identification of converged solutions in an eigenvalue spectrum, especially when the spectrum is much more convoluted than that of the boundary layer. This approach was used to highlight relevant solutions for the SWBLI. Nevertheless, finding these solutions still relies on an appropriate choice of frame speed.

The frame speed is the key parameter of the method since, for a given numerical setup, it allows recovering eigensolutions with localized eigenfunctions. It is thus essential to un-

derstand how eigensolutions behave with respect to the frame speed. A general observation is that, for a given type of mode, a high-frame-speed eigenfunction has a shorter spatial extent, a smaller wavelength and is located more upstream than an eigenfunction obtained at a lower frame speed. Hence, the numerical requirement to resolve an eigensolution with a localized eigenfunctions depends on the frame speed. A thorough analysis of the boundary-layer eigensolutions with respect to the frame speed showed that the variation of the spatial extent and wavelength with respect to the frame speed does not occur at the same rate. In particular, it was shown that the grid density must be continuously increased when lowering the frame speed. That is, finding converged solutions in the stationary frame of reference is likely impossible for the flat-plate boundary layer. This finding is in agreement with the fact that the boundary layer is globally stable for all Reynolds numbers. These results emphasize the need for using the moving-frame approach with a frame speed chosen such that the spatial extent and wavelength of the eigenfunctions are supported by the numerical setup. In other words, from a numerical point of view only, the frame speed is a tool to find localized solutions for a given setup.

Once the moving-frame eigensolutions are identified, the proposed methodology relies on disturbing the flow with the corresponding eigenfunctions in order to study the finite-time perturbation dynamics of the convective instabilities. A major finding is that the solutions of the eigenvalue problem solved in a moving frame of reference are remarkably convenient to initialize the perturbation problem for two main reasons. The first reason is that the moving-frame eigensolutions satisfy the temporal perturbation equations and are thus instantaneously valid for zero elapsed time. For both flow cases, it was verified that the eigengrowth rate and frame speed of the moving-frame eigensolutions are the same as the temporal growth rate and group speed of the wave packets, respectively; the initial short-time perturbation dynamics coincide with the dynamics predicted by the moving-frame eigensolutions. Hence, the moving-frame eigensolutions indicate the main features of the instability mechanisms in an instantaneous sense, ahead of solving the (initial-value) perturbation problem. Furthermore, this brings an additional interpretation of the frame speed that is not only a numerical tool to find localized eigensolutions but also represents the physical group speed at which the wave packet moves in the flow field. Finally, having moving-frame eigensolutions that satisty the perturbation equations for zero elapsed time also implies that the time response of the flow to these initial conditions is not polluted by any inadvertent transients. This improves upon the PSE method for which the spatial integration is initialized with LST solutions that do not exactly satisfy the PSE .

The second motivation for using moving-frame eigenfunctions as initial conditions is that the amplification curves are independent of the frame speed and the mode chosen to initialize the problem. For the incompressible boundary layer, this was demonstrated by considering modes along the main branch that were obtained at different frame speeds or were different from the most unstable one. After Fourier transforming the temporal wave packets, the N-factor and neutral curves were reconstructed for the different modes and frame speeds. In regions of converged Fourier coefficients, no difference were found for the curves obtained with the different initial conditions. Note that obtaining converged Fourier coefficient is guaranteed if the amplitude of the signal, i.e., the temporal wave packet, vanishes at the initial and final times, up to numerical precision. Hence, more upstream eigenfunctions can resolved more upstream locations with converged Fourier coefficients. The exact same conclusion was found for the SWBLI. The only difference that is observed when disturbing a flow with different moving-frame eigenfunctions comes from not recovering information for streamwise stations located upstream of the initial condition. Hence, a key requirement of the present method is to use initial conditions that are located upstream

of the region where perturbation growth is expected. Although meeting this requirement can be difficult for some flow configurations, this is arguably the main limitation of the moving-frame approach. In both the incompressible flat-plate boundary layer and the laminar SWBLI, it was possible to find such upstream solutions, but it may be more difficult in other cases (SWBLIs or much broader classes of flows). A solution to this would be to rely on a wave packet tracking strategy to increase the flexibility in tracking the eigenfunctions as β and c_f, or other parameters, are varied.

All aforementioned results demonstrate the effectiveness of the present methodology in providing practical stability information without assumption on the flow field evolution. Hence, the fully-elliptic representation of the general perturbation dynamics of convective instabilities is arguably made possible with the moving-frame method. Besides the above general observations made on the two considered flow configurations, specific results associated with the SWBLI deserve some more attention.

6.3.2. Convective instabilities in a shock-wave/boundary-layer interaction

The SWBLI was obtained with direct numerical simulations that indicated that the laminar-turbulent transition takes place downstream of the shock-induced bubble apex. Because the flow is inherently unsteady, the selective frequency damping method was used to drive the flow toward a steady state that is key for linear stability analyses. This allowed obtaining an unstable laminar SWBLI base flow, up to numerical precision. Prior to using the base flow in actual stability analyses, continuing the simulations without the selective-frequency-damping forcing term, i.e., using the so-called unleash technique, suggested that the present SWBLI does not support two-dimensional global modes and is rather convectively unstable. This conclusion was strengthened by the fact that the dividing streamline is located beneath the generalized inflection point line and thus that no absolute instability exists in the separation bubble. Finally, the linear stability analyses conducted in the moving frame of reference with the frame speed decreased to zero, i.e., toward the stationary frame of reference, indicated again that the present SWBLI does not support unstable two- and three-dimensional global eigenmodes. From these observations, the flow was deemed convectively unstable only.

After solving the eigenvalue problem in the moving frame of reference, three types of localized modes were found in the present laminar SWBLI. The associated eigenvalues arrange themselves into distinct branches in the spectrum that were traced in the frame-speed and spanwise-wavenumber parameter space, abbreviated (c_f,β)-parameter space in the following. The three different modes were labeled as upstream, downstream and apex-type modes depending on the location of the eigenfunctions associated with the most unstable eigensolutions with respect to the bubble apex. This classification of modes is thus strictly valid for the (c_f,β)-combinations yielding the largest growth per mode type and the fact that the frame speed strongly influences the location of the eigenfunctions in the domain can question the present choice of classification. This is especially the case for upstream-type modes that can actually be found downstream of the bubble apex for small frame speeds; they are, however, more stable than the ones located upstream of the apex. Furthermore, an in-depth analysis of the individual contributions of the eigengrowth rate indicated that the apex and downstream-type modes can share very similar characteristics for some (c_f,β)-combinations. This thus suggested that apex and downstream-type modes are likely related to each other and that considering the main components of the eigengrowth rate would possibly be a better approach to classify the different mode types.

In contrast to the other mode types that cannot move upstream of the incident shock,

the upstream-type eigenfunctions can likely be moved toward the flat-plate leading edge for high frame speeds. This suggests that they could possibly be associated with boundary-layer modes. Figuring this out would require solving the moving-frame eigenvalue problem for a base flow with a more upstream inlet location. If more upstream inlet locations are considered, two scenarios can be expected from the observations made in this work. Assuming a fixed frame speed, these two scenarios likely depend on the location of the separation bubble with respect to the actual location of a mode of the undisturbed boundary-layer, i.e., the compressible boundary layer without shock wave. If a mode of the undisturbed boundary layer is supposed to be located at the same Reynolds number as a SWBLI (upstream) mode, the mode found in the eigenvalue spectrum for the SWBLI would most likely be an actual boundary-layer mode altered by the local dynamics of the separation bubble. Instead, if a boundary-layer mode exists outside of the separation bubble region, then two distinct eigenvalues would be found in the spectrum: one for the SWBLI, another one for the undisturbed boundary layer. If these two scenarios can actually be observed, it would then suggest that modes can 'interact' with each other. Hence, decomposing the eigengrowth rates into their individual contribution would again be essential to unequivocally classify the mode types.

Since all mode types were found localized in the domain and independent of the numerical setup, it could be verified that, once introduced into the stationary-frame perturbation equations, the eigensolutions represent the instantaneous characteristics of the temporal wave packet for zero elapsed time. The only slight difference compared to the flat-plate boundary layer is in the choice of the energy norm. In fact, in contrast to the incompressible case, the energy-norm matrix is not constant in space and a base-flow-dependent correction term must thus be added to the eigengrowth to obtain the instantaneous temporal growth rate. Nevertheless, because this correction is time-independent, it does not prevent interpreting the eigensolutions as instantaneous solutions of the stationary-frame equations.

After the temporal integration of the moving-frame eigenfunctions in the stationary frame of reference, the frequency-wise amplifications curve were obtained for the shock-induced separation bubble. This allowed determining the most amplified frequency and spanwise wavenumber of three-dimensional perturbations in SWBLI. However, no neutral point could be recovered, and thus no N-factor curve, per se, could be fully reconstructed. The curves obtained in the SWBLI are rather ΔN-factor curves that depend on the arbitrarily chosen location for the normalization. Determining neutral points would require initializing the initial-value problem with more upstream eigenfunctions, that, given the inlet location of the present base flow, could not be found. Obtaining these eigenfunctions would require computing another base flow with an inlet that reaches further upstream toward the leading edge of the flat plate. In this way, a longer portion of the boundary layer ahead of the incident shock would be captured and actual N-factor curves, i.e., amplification curves defined from the neutral points onward, could be recovered. The present results, however, already indicated the most amplified frequencies and spanwise wavenumbers in the region of the shock-induced bubble and that neutral-growth locations do not exist in this region of the flow.

The spanwise wavenumbers are an input of the system that require a parameter analysis to determine the largest amplification of perturbations across the shock-induced bubble. This parameter analysis has first been performed for the moving-frame eigensolutions for all mode types and indicated which spanwise wavenumbers yield the largest *eigengrowth* rate. Then, the moving-frame eigenfunctions were used as initial condition to integrate the perturbation equations in time and a sensitivity analysis performed on the spanwise wavenumbers allowed identifying the ones associated with the largest *perturbation growth*. A ma-

jor finding is that the wavenumbers corresponding to the largest wave-packet amplification are the same as the wavenumbers associated with the largest eigengrowth rate. Hence, although it was demonstrated that the moving-frame eigensolutions are only strictly valid for zero elapsed time, the present results showed that they likely give a good estimation of the temporal evolution of the wave packets. A particular emphasis was thus put on comparing the temporal evolution of the wave-packet perturbations with the moving-frame eigensolutions obtained at different frame speeds. Remarkably good agreements were found between the two types of solutions regarding the perturbation structure and growth rates. Furthermore, it was observed that the underlying instability mechanisms were well estimated by the eigensolutions. In this regard, the present results are a first indication that the eigensolutions can be used to guide more expensive simulations involving the temporal integration of the (linearized) governing equations.

The fact that the temporal wave packet and the eigensolutions are, however, not exactly the same likely lies in the governing equations that allow or not for the non-modal evolution of the perturbation, respectively. This is especially observed for the different moving-frame mode types that are dominant on either side of the shock-induced bubble. The temporal evolution of the wave packets suggests that a weak non-modal growth takes place up- and downstream of the shock while a strong and brief non-modal effect arises around the bubble apex and induces a switch between two mode types. Furthermore, it is suspected that a similar mechanism can take place when a boundary-layer mode enters the separated shear layer. Assessing this effect would help determining whether the upstream-type mode is a boundary-layer mode or not. This, however, requires a more upstream domain inlet than presently used. In the end, non-modal growth was not analyzed in the present work but it is deemed relevant to further investigate how non-modal solutions are related to moving-frame modal solutions.

On the one hand, the observations made in the SWBLI are comforting in the sense that the moving-frame method can effectively address the fully-elliptic representation of convective instabilities in highly two-dimensional flows. On the other hand, some results suggest that the moving-frame eigensolutions could be interpreted beyond the zero-elapsed-time constraint and this would require further investigation.

6.4. Outlook

General perspectives regarding the moving-frame methodology are discussed in what follows. On the one hand, the results obtained in the incompressible flat-plate boundary layer and SWBLI cases illustrate how the moving-frame method works and how it can be leveraged to determine the stability of flows supporting convective instability mechanisms. The present results show that the moving-frame method improves upon existing methodologies such as LST or PSE by extending stability analyses to two-/three-dimensional flows, and optimal-growth or HLNS methods by avoiding specific scenarios of perturbation growth. On the other hand, the present observations also highlight the limitations and the main requirements of the moving-frame approach. Further theoretical investigations are also required to better assess how the moving-frame eigensolutions can be used to predict the finite-time evolution of perturbations or to tackle disturbance receptivity in a flow field. All these aspects are discussed in the following.

The main difficulty encountered when using the moving-frame method is to find solutions that can be used to identify neutral points, especially in flows with a region of interest, e.g., a shock-induced bubble, that is located far away from the neutral-growth locations. In fact, this requires using a long numerical domain such that moving-frame and tempo-

ral solutions can be captured upstream of the regions where the spatial growth is neutral. However, obtaining these solutions usually requires increasing the frame speed and thus increasing the need in spatial resolution because the wavelength decreases with larger frame speed. Hence, requiring both a long numerical domain that contains all regions of interest and a dense numerical discretization to capture small wavelengths can yield unreasonable computational costs. In order to minimize this computational requirement, a numerical methodology that tracks the temporal wave packets would be a very effective approach to complement the present moving-frame approach. This type of numerical procedure has recently been devised in direct numerical simulations by Browne *et al.* (2019) [An efficient linear wavepacket tracking method for hypersonic boundary-layer stability prediction. *J. Comput. Phys* 380] and is a promising tool to extend the field of application of the present methodology.

When solving an eigenvalue problem to study the linear stability of complex flow fields, the resulting spectra of eigenvalues can be difficult to interpret, especially if the solutions are tainted by numerical artifacts. A typical example of complicated spectrum can be found when solving the two-dimensional stability problem in the stationary frame of reference to find convective modes. In this case, the very wide arc-shaped branch containing the eigenvalues associated with the modes of interest can lie in the stable or unstable plane of the spectrum depending on the domain length. Hence, isolating modes can be a tedious task, especially if they are in the stable plane of the spectrum where most of the other eigensolutions lie. In the present work, it was found that using the moving frame of reference often simplifies the eigenvalue spectrum. Since the contribution of the streamwise advection is mitigated, the width of many arc-shaped branches is reduced. More importantly, solutions that are truly unstable are moved towards the unstable plane, because the solutions are independent of the numerical setup. Nevertheless, the SWBLI case indicated that, in the presence of several unstable modes, tracking one given mode type in the spectrum in a large parameter space is not trivial. Although restricting the tracking to localized eigenfunctions helps identifying relevant modes, the classification of the different modes used in this work could be improved. In future work, it is recommended to decompose the eigengrowth into their individual contribution with the perturbation energy equation and then classify the eigensolutions according to the actual physical properties of the instability mechanisms.

The flow configurations and, in particular the geometries, considered in the present work were relatively simple in the sense that the only solid wall is a flat plate. While considering these flows was ideal to develop the method and validate the results, actual real flow configurations can be much more complex and future work should focus on applying the moving-frame method to flows with geometries that depart from the flat plate. Typical canonical cases supporting convective instabilities that could be considered in the first place are back-/forward facing steps, airfoil or bluff-body wakes or even micro-ramps. Note that Mittal *et al.* (2008) [Onset of shear layer instability in flow past a cylinder. *Phys. Fluids* 20 (5)] showed that convective instabilities behind a cylinder can be captured in the moving frame of reference. This can be explained by the fact that the geometry is actually discarded from the perturbation problem and only the flow field resulting from the presence of the geometry is necessary to support perturbations. In order to confirm this argument, future investigations should consider other non-flat-plate cases with the complete moving-frame framework, and related analyses, proposed in the present work. This would validate the fact that the role of the moving-frame speed is to mitigate the advection of perturbation by the base flow.

An important finding of the present work is that the moving-frame eigensolutions obtained at different frame speeds give a good approximation of the temporal wave packets

for non-zero elapsed times. Nevertheless, eigensolutions and temporal wave packets are not the same. In particular, the former assume a modal evolution of the perturbations that, as demonstrated, is strictly valid for zero elapsed time whereas the temporal wave packets evolve without particular constraint. In order to shed light on the differences between eigensolutions and wave packets, a better quantification of the non-modal effects is required. In particular, superimposing a wave packet onto the moving-frame basis could indicate whether the temporal evolution of perturbations relies on one mode or a combination of modes. Such analysis would need to assess the weight of the projection coefficients for each mode. This investigation can indicate, on the one hand, the contribution of non-modal effects to the evolution of a perturbation and, on the other hand, how the transition from one type of instability mechanism to another takes place. From a different perspective, the contribution of convective- and component-type non-normalities to the overall non-modal evolution of a perturbation could also be assessed. Furthermore, an in-depth analysis of the variation of the non-modal effects when departing from stationary-frame to moving-frame eigensolutions would shed light on the remaining non-modal content in the latter.

A key process in the evolution of perturbations in fluid flows is related to the mechanisms that transfer external disturbances into the shear layer. As mentioned in the introduction, this process is called receptivity and determines the initial condition of the perturbation evolution. Usually, receptivity analysis relies on finding the initial condition or forcing yielding the largest perturbation growth in the flow, but these scenarios are physically unrealizable. Using the moving-frame methodology, receptivity analysis could be extended to sub-optimal scenarios. The moving-frame adjoint eigensolutions and adjoint initial-value problem could be used to study how the disturbances that are inherent to a region of interest, e.g., the separation bubble, are effectively forced elsewhere. For instance, an adjoint solution moving out of the boundary layer and toward the freestream would indicate that the inherent disturbances are sensitive to freestream turbulence and insensitive to forcing at the wall. Hence, in addition to study how a perturbation evolves in a flow, the present method would also be capable to determine how a disturbance initially enters a flow.

Finally, the ultimate perspective of the present methodology is to give the opportunity to study the evolution of convective instabilities toward their nonlinear breakdown by disturbing the (nonlinear) Navier Stokes equations with the moving-frame eigensolutions. Approaching this problem is, however, not trivial. For instance, the entire SWBLI flow, and in particular the region around the incident shock, acts as an amplifier of external (numerical) disturbances. These disturbances can be difficult to control in direct numerical simulations and can overwhelm the actual perturbation evolution. Hence, extreme care should be taken to ignore/control the low-level numerical noise and thus fully benefit from the sharpness of the eigensolution used as an initial condition. Analyzing the nonlinear evolution of wave packets in such complicated flow fields can improve the understanding of the mechanisms behind the route to turbulence. Accordingly, this can provide novel perspectives to advance in the modeling of the laminar-turbulent transition and to support the development of control strategies for a greener aviation industry.

A

Perturbation and stability equations

In this appendix, the perturbation equations in the stationary frame of reference are given for two-dimensional streamwise base flows, i.e., base flows without spatial variation in the z-direction, in §A.1. The continuous direct and adjoint BiGlobal stability equations in the stationary frame of reference are then introduced in §A.2 and §A.3, respectively. Finally, the equivalence between the (ρ', T') and (p', T')-based energy matrices is demonstrated in §A.4.

A.1. Perturbation equations in the stationary frame of reference

The perturbation equations are formulated for the vector $\boldsymbol{q}'_{\mathrm{f}} = [u'_{\mathrm{f}}, v'_{\mathrm{f}}, w'_{\mathrm{f}}, T'_{\mathrm{f}}, \rho'_{\mathrm{f}}]^T$ and are the (x,y)-plane equivalent of the equations derived by Padilla Montero & Pinna (2021) [Analysis of the instabilities induced by an isolated roughness element in a laminar high-speed boundary layer. Journal of Fluid Mechanics 915]. As mentioned in Chapter 2, the combination of the (ρ', T')-formulation with the internal energy equation (2.1c) is preferred in order to have diagonal matrices that multiply the temporal derivative terms. This avoids any convoluted energy transfer between the continuity and energy equations caused by the pressure-temperature coupling through the temporal derivative terms. Since these equations are used for the finite-time dynamics of the perturbations, they are formulated in the stationary frame of reference.

Continuity perturbation equation

$$\frac{\partial \rho'_{\mathrm{f}}}{\partial t} + \overline{\rho}\left(\frac{\partial u'_{\mathrm{f}}}{\partial x_{\mathrm{f}}} + \frac{\partial v'_{\mathrm{f}}}{\partial y} + \frac{\partial w'_{\mathrm{f}}}{\partial z}\right) + \rho'_{\mathrm{f}}\left(\frac{\partial \overline{U}}{\partial x_{\mathrm{f}}} + \frac{\partial \overline{V}}{\partial y}\right) + \overline{U}\frac{\partial \rho'_{\mathrm{f}}}{\partial x_{\mathrm{f}}} + \overline{V}\frac{\partial \rho'_{\mathrm{f}}}{\partial y} + \overline{W}\frac{\partial \rho'_{\mathrm{f}}}{\partial z} + u'_{\mathrm{f}}\frac{\partial \overline{\rho}}{\partial x_{\mathrm{f}}} + v'_{\mathrm{f}}\frac{\partial \overline{\rho}}{\partial y} = 0 \quad \text{(A.1a)}$$

x-momentum perturbation equation

$$
\begin{aligned}
&\overline{\rho}\frac{\partial u_\mathrm{f}'}{\partial t}+\overline{\rho}\left(\overline{U}\frac{\partial u_\mathrm{f}'}{\partial x_\mathrm{f}}+\overline{V}\frac{\partial u_\mathrm{f}'}{\partial y}+\overline{W}\frac{\partial u_\mathrm{f}'}{\partial z}+u_\mathrm{f}'\frac{\partial \overline{U}}{\partial x_\mathrm{f}}+v_\mathrm{f}'\frac{\partial \overline{U}}{\partial y}\right)+\rho_\mathrm{f}'\left(\overline{U}\frac{\partial \overline{U}}{\partial x_\mathrm{f}}+\overline{V}\frac{\partial \overline{U}}{\partial y}\right)\\
&\quad=-\frac{1}{\gamma M^2}\left(\overline{T}\frac{\partial \rho_\mathrm{f}'}{\partial x_\mathrm{f}}+\overline{\rho}\frac{\partial T_\mathrm{f}'}{\partial x_\mathrm{f}}+T_\mathrm{f}'\frac{\partial \overline{\rho}}{\partial x_\mathrm{f}}+\rho_\mathrm{f}'\frac{\partial \overline{T}}{\partial x_\mathrm{f}}\right)+\frac{\overline{\lambda}}{\mathrm{Re}}\left(\frac{\partial^2 u_\mathrm{f}'}{\partial x_\mathrm{f}^2}+\frac{\partial^2 v_\mathrm{f}'}{\partial x_\mathrm{f}\partial y}+\frac{\partial^2 w_\mathrm{f}'}{\partial x_\mathrm{f}\partial z}\right)\\
&\qquad+\frac{\overline{\mu}}{\mathrm{Re}}\left(2\frac{\partial^2 u_\mathrm{f}'}{\partial x_\mathrm{f}^2}+\frac{\partial^2 u_\mathrm{f}'}{\partial y^2}+\frac{\partial^2 u_\mathrm{f}'}{\partial z^2}+\frac{\partial^2 v_\mathrm{f}'}{\partial x_\mathrm{f}\partial y}+\frac{\partial^2 w_\mathrm{f}'}{\partial x_\mathrm{f}\partial z}\right)\\
&\qquad+\frac{1}{\mathrm{Re}}\frac{\mathrm{d}\overline{\lambda}}{\mathrm{d}\overline{T}}\left[\frac{\partial \overline{T}}{\partial x_\mathrm{f}}\left(\frac{\partial u_\mathrm{f}'}{\partial x_\mathrm{f}}+\frac{\partial v_\mathrm{f}'}{\partial y}+\frac{\partial w_\mathrm{f}'}{\partial z}\right)+\frac{\partial T_\mathrm{f}'}{\partial x_\mathrm{f}}\left(\frac{\partial \overline{U}}{\partial x_\mathrm{f}}+\frac{\partial \overline{V}}{\partial y}\right)+T_\mathrm{f}'\left(\frac{\partial^2 \overline{U}}{\partial x_\mathrm{f}^2}+\frac{\partial^2 \overline{V}}{\partial x_\mathrm{f}\partial y}\right)\right]\\
&\qquad+\frac{1}{\mathrm{Re}}\frac{\mathrm{d}\overline{\mu}}{\mathrm{d}\overline{T}}\left[2\frac{\partial \overline{T}}{\partial x_\mathrm{f}}\frac{\partial u_\mathrm{f}'}{\partial x_\mathrm{f}}+\frac{\partial \overline{T}}{\partial y}\frac{\partial u_\mathrm{f}'}{\partial y}+\frac{\partial \overline{T}}{\partial y}\frac{\partial v_\mathrm{f}'}{\partial x_\mathrm{f}}+2\frac{\partial T_\mathrm{f}'}{\partial x_\mathrm{f}}\frac{\partial \overline{U}}{\partial x_\mathrm{f}}+\frac{\partial T_\mathrm{f}'}{\partial y}\left(\frac{\partial \overline{U}}{\partial y}+\frac{\partial \overline{V}}{\partial x_\mathrm{f}}\right)\right.\\
&\qquad\left.+\frac{\partial T_\mathrm{f}'}{\partial z}\frac{\partial \overline{W}}{\partial x_\mathrm{f}}+T_\mathrm{f}'\left(2\frac{\partial^2 \overline{U}}{\partial x_\mathrm{f}^2}+\frac{\partial^2 \overline{U}}{\partial y^2}+\frac{\partial^2 \overline{V}}{\partial x_\mathrm{f}\partial y}\right)\right]\\
&\qquad+\frac{1}{\mathrm{Re}}\frac{\mathrm{d}^2\overline{\lambda}}{\mathrm{d}\overline{T}^2}\frac{\partial \overline{T}}{\partial x_\mathrm{f}}T_\mathrm{f}'\left(\frac{\partial \overline{U}}{\partial x_\mathrm{f}}+\frac{\partial \overline{V}}{\partial y}\right)+\frac{1}{\mathrm{Re}}\frac{\mathrm{d}^2\overline{\mu}}{\mathrm{d}\overline{T}^2}T_\mathrm{f}'\left[2\frac{\partial \overline{T}}{\partial x_\mathrm{f}}\frac{\partial \overline{U}}{\partial x_\mathrm{f}}+\frac{\partial \overline{T}}{\partial y}\left(\frac{\partial \overline{U}}{\partial y}+\frac{\partial \overline{V}}{\partial x_\mathrm{f}}\right)\right]
\end{aligned}
\tag{A.1b}
$$

y-momentum perturbation equation

$$
\begin{aligned}
&\overline{\rho}\frac{\partial v_\mathrm{f}'}{\partial t}+\overline{\rho}\left(\overline{U}\frac{\partial v_\mathrm{f}'}{\partial x_\mathrm{f}}+\overline{V}\frac{\partial v_\mathrm{f}'}{\partial y}+\overline{W}\frac{\partial v_\mathrm{f}'}{\partial z}+u_\mathrm{f}'\frac{\partial \overline{V}}{\partial x_\mathrm{f}}+v_\mathrm{f}'\frac{\partial \overline{V}}{\partial y}\right)+\rho_\mathrm{f}'\left(\overline{U}\frac{\partial \overline{V}}{\partial x_\mathrm{f}}+\overline{V}\frac{\partial \overline{V}}{\partial y}\right)\\
&\quad=-\frac{1}{\gamma M^2}\left(\overline{T}\frac{\partial \rho_\mathrm{f}'}{\partial y}+\overline{\rho}\frac{\partial T_\mathrm{f}'}{\partial y}+T_\mathrm{f}'\frac{\partial \overline{\rho}}{\partial y}+\rho_\mathrm{f}'\frac{\partial \overline{T}}{\partial y}\right)+\frac{\overline{\lambda}}{\mathrm{Re}}\left(\frac{\partial^2 u_\mathrm{f}'}{\partial x_\mathrm{f}\partial y}+\frac{\partial^2 v_\mathrm{f}'}{\partial y^2}+\frac{\partial^2 w_\mathrm{f}'}{\partial y\partial z}\right)\\
&\qquad+\frac{\overline{\mu}}{\mathrm{Re}}\left(\frac{\partial^2 u_\mathrm{f}'}{\partial x_\mathrm{f}\partial y}+\frac{\partial^2 v_\mathrm{f}'}{\partial x_\mathrm{f}^2}+2\frac{\partial^2 v_\mathrm{f}'}{\partial y^2}+\frac{\partial^2 v_\mathrm{f}'}{\partial z^2}+\frac{\partial^2 w_\mathrm{f}'}{\partial y\partial z}\right)\\
&\qquad+\frac{1}{\mathrm{Re}}\frac{\mathrm{d}\overline{\lambda}}{\mathrm{d}\overline{T}}\left[\frac{\partial \overline{T}}{\partial y}\left(\frac{\partial u_\mathrm{f}'}{\partial x_\mathrm{f}}+\frac{\partial v_\mathrm{f}'}{\partial y}+\frac{\partial w_\mathrm{f}'}{\partial z}\right)+\frac{\partial T_\mathrm{f}'}{\partial y}\left(\frac{\partial \overline{U}}{\partial x_\mathrm{f}}+\frac{\partial \overline{V}}{\partial y}\right)+T_\mathrm{f}'\left(\frac{\partial^2 \overline{U}}{\partial x_\mathrm{f}\partial y}+\frac{\partial^2 \overline{V}}{\partial y^2}\right)\right]\\
&\qquad+\frac{1}{\mathrm{Re}}\frac{\mathrm{d}\overline{\mu}}{\mathrm{d}\overline{T}}\left[\frac{\partial \overline{T}}{\partial x_\mathrm{f}}\frac{\partial u_\mathrm{f}'}{\partial y}+2\frac{\partial \overline{T}}{\partial y}\frac{\partial v_\mathrm{f}'}{\partial y}+\frac{\partial \overline{T}}{\partial x_\mathrm{f}}\frac{\partial v_\mathrm{f}'}{\partial x_\mathrm{f}}+2\frac{\partial T_\mathrm{f}'}{\partial y}\frac{\partial \overline{V}}{\partial y}+\frac{\partial T_\mathrm{f}'}{\partial x_\mathrm{f}}\left(\frac{\partial \overline{U}}{\partial y}+\frac{\partial \overline{V}}{\partial x_\mathrm{f}}\right)\right.\\
&\qquad\left.+\frac{\partial T_\mathrm{f}'}{\partial z}\frac{\partial \overline{W}}{\partial y}+T_\mathrm{f}'\left(\frac{\partial^2 \overline{U}}{\partial x_\mathrm{f}\partial y}+\frac{\partial^2 \overline{V}}{\partial x_\mathrm{f}^2}+2\frac{\partial^2 \overline{V}}{\partial y^2}\right)\right]\\
&\qquad+\frac{1}{\mathrm{Re}}\frac{\mathrm{d}^2\overline{\lambda}}{\mathrm{d}\overline{T}^2}\frac{\partial \overline{T}}{\partial y}T_\mathrm{f}'\left(\frac{\partial \overline{U}}{\partial x_\mathrm{f}}+\frac{\partial \overline{V}}{\partial y}\right)+\frac{1}{\mathrm{Re}}\frac{\mathrm{d}^2\overline{\mu}}{\mathrm{d}\overline{T}^2}T_\mathrm{f}'\left[\frac{\partial \overline{T}}{\partial x_\mathrm{f}}\left(\frac{\partial \overline{U}}{\partial y}+\frac{\partial \overline{V}}{\partial x_\mathrm{f}}\right)+2\frac{\partial \overline{T}}{\partial y}\frac{\partial \overline{V}}{\partial y}\right]
\end{aligned}
\tag{A.1c}
$$

z-momentum perturbation equation

$$
\begin{aligned}
&\overline{\rho}\frac{\partial w_\mathrm{f}'}{\partial t}+\overline{\rho}\left(\overline{U}\frac{\partial w_\mathrm{f}'}{\partial x_\mathrm{f}}+\overline{V}\frac{\partial w_\mathrm{f}'}{\partial y}+\overline{W}\frac{\partial w_\mathrm{f}'}{\partial z}+u_\mathrm{f}'\frac{\partial \overline{W}}{\partial x_\mathrm{f}}+v_\mathrm{f}'\frac{\partial \overline{W}}{\partial y}\right)+\rho_\mathrm{f}'\left(\overline{U}\frac{\partial \overline{W}}{\partial x_\mathrm{f}}+\overline{V}\frac{\partial \overline{W}}{\partial y}\right)\\
&\quad=-\frac{1}{\gamma M^2}\left(\overline{T}\frac{\partial \rho_\mathrm{f}'}{\partial z}+\overline{\rho}\frac{\partial T_\mathrm{f}'}{\partial z}\right)+\frac{\overline{\lambda}}{\mathrm{Re}}\left(\frac{\partial^2 u_\mathrm{f}'}{\partial x_\mathrm{f}\partial z}+\frac{\partial^2 v_\mathrm{f}'}{\partial y\partial z}+\frac{\partial^2 w_\mathrm{f}'}{\partial z^2}\right)\\
&\qquad+\frac{\overline{\mu}}{\mathrm{Re}}\left(\frac{\partial^2 u_\mathrm{f}'}{\partial x_\mathrm{f}\partial z}+\frac{\partial^2 v_\mathrm{f}'}{\partial y\partial z}+\frac{\partial^2 w_\mathrm{f}'}{\partial x_\mathrm{f}^2}+\frac{\partial^2 w_\mathrm{f}'}{\partial y^2}+2\frac{\partial^2 w_\mathrm{f}'}{\partial z^2}\right)\\
&\qquad+\frac{1}{\mathrm{Re}}\frac{\mathrm{d}\overline{\lambda}}{\mathrm{d}\overline{T}}\frac{\partial T_\mathrm{f}'}{\partial z}\left(\frac{\partial \overline{U}}{\partial x_\mathrm{f}}+\frac{\partial \overline{V}}{\partial y}\right)\\
&\qquad+\frac{1}{\mathrm{Re}}\frac{\mathrm{d}\overline{\mu}}{\mathrm{d}\overline{T}}\left[\frac{\partial \overline{T}}{\partial x_\mathrm{f}}\frac{\partial u_\mathrm{f}'}{\partial z}+\frac{\partial \overline{T}}{\partial y}\frac{\partial v_\mathrm{f}'}{\partial z}+\frac{\partial \overline{T}}{\partial x_\mathrm{f}}\frac{\partial w_\mathrm{f}'}{\partial x_\mathrm{f}}+\frac{\partial \overline{T}}{\partial y}\frac{\partial w_\mathrm{f}'}{\partial y}+\frac{\partial T_\mathrm{f}'}{\partial x_\mathrm{f}}\frac{\partial \overline{W}}{\partial x_\mathrm{f}}+\frac{\partial T_\mathrm{f}'}{\partial y}\frac{\partial \overline{W}}{\partial y}\right.\\
&\qquad\left.+T_\mathrm{f}'\left(\frac{\partial^2 \overline{W}}{\partial x_\mathrm{f}^2}+\frac{\partial^2 \overline{W}}{\partial y^2}\right)\right]+\frac{1}{\mathrm{Re}}\frac{\mathrm{d}^2\overline{\mu}}{\mathrm{d}\overline{T}^2}T_\mathrm{f}'\left[\frac{\partial \overline{T}}{\partial x_\mathrm{f}}\frac{\partial \overline{W}}{\partial x_\mathrm{f}}+\frac{\partial \overline{T}}{\partial y}\frac{\partial \overline{W}}{\partial y}\right]
\end{aligned}
\tag{A.1d}
$$

Internal energy perturbation equation

$$
\begin{aligned}
&\overline{\rho}\frac{\partial T_\mathrm{f}'}{\partial t}+\overline{\rho}\left(\overline{U}\frac{\partial T_\mathrm{f}'}{\partial x_\mathrm{f}}+\overline{V}\frac{\partial T_\mathrm{f}'}{\partial y}+\overline{W}\frac{\partial T_\mathrm{f}'}{\partial z}+u_\mathrm{f}'\frac{\partial \overline{T}}{\partial x_\mathrm{f}}+v_\mathrm{f}'\frac{\partial \overline{T}}{\partial y}\right)+\rho_\mathrm{f}'\left(\overline{U}\frac{\partial \overline{T}}{\partial x_\mathrm{f}}+\overline{V}\frac{\partial \overline{T}}{\partial y}\right)\\
&\quad=(1-\gamma)\left[\overline{\rho}\,\overline{T}\left(\frac{\partial u_\mathrm{f}'}{\partial x_\mathrm{f}}+\frac{\partial v_\mathrm{f}'}{\partial y}+\frac{\partial w_\mathrm{f}'}{\partial z}\right)+\left(\rho_\mathrm{f}'\overline{T}+\overline{\rho}T_\mathrm{f}'\right)\left(\frac{\partial \overline{U}}{\partial x_\mathrm{f}}+\frac{\partial \overline{V}}{\partial y}\right)\right]\\
&\qquad+\frac{\gamma\mathrm{Ec}}{\mathrm{Re}}\left\{2\overline{\lambda}\left(\frac{\partial u_\mathrm{f}'}{\partial x_\mathrm{f}}+\frac{\partial v_\mathrm{f}'}{\partial y}+\frac{\partial w_\mathrm{f}'}{\partial z}\right)\left(\frac{\partial \overline{U}}{\partial x_\mathrm{f}}+\frac{\partial \overline{V}}{\partial y}\right)+\frac{\mathrm{d}\overline{\lambda}}{\mathrm{d}\overline{T}}T_\mathrm{f}'\left[\left(\frac{\partial \overline{U}}{\partial x_\mathrm{f}}\right)^2+2\frac{\partial \overline{U}}{\partial x_\mathrm{f}}\frac{\partial \overline{V}}{\partial y}+\left(\frac{\partial \overline{V}}{\partial y}\right)^2\right]\right\}\\
&\qquad+\frac{\gamma\mathrm{Ec}}{\mathrm{Re}}\left\{2\overline{\mu}\left[2\frac{\partial u_\mathrm{f}'}{\partial x_\mathrm{f}}\frac{\partial \overline{U}}{\partial x_\mathrm{f}}+\frac{\partial u_\mathrm{f}'}{\partial z}\frac{\partial \overline{W}}{\partial x_\mathrm{f}}+2\frac{\partial v_\mathrm{f}'}{\partial y}\frac{\partial \overline{V}}{\partial y}+\frac{\partial v_\mathrm{f}'}{\partial z}\frac{\partial \overline{W}}{\partial y}+\left(\frac{\partial u_\mathrm{f}'}{\partial y}+\frac{\partial v_\mathrm{f}'}{\partial x_\mathrm{f}}\right)\left(\frac{\partial \overline{U}}{\partial y}+\frac{\partial \overline{V}}{\partial x_\mathrm{f}}\right)\right.\right.\\
&\qquad\left.+\frac{\partial w_\mathrm{f}'}{\partial x_\mathrm{f}}\frac{\partial \overline{W}}{\partial x_\mathrm{f}}+\frac{\partial w_\mathrm{f}'}{\partial y}\frac{\partial \overline{W}}{\partial y}\right]+\frac{\mathrm{d}\overline{\mu}}{\mathrm{d}\overline{T}}T_\mathrm{f}'\left[2\left(\frac{\partial \overline{U}}{\partial x_\mathrm{f}}\right)^2+\left(\frac{\partial \overline{U}}{\partial y}\right)^2+2\left(\frac{\partial \overline{U}}{\partial y}\right)\left(\frac{\partial \overline{V}}{\partial x_\mathrm{f}}\right)\right.\\
&\qquad\left.\left.+\left(\frac{\partial \overline{V}}{\partial x_\mathrm{f}}\right)^2+2\left(\frac{\partial \overline{V}}{\partial y}\right)^2+\left(\frac{\partial \overline{W}}{\partial x_\mathrm{f}}\right)^2+\left(\frac{\partial \overline{W}}{\partial y}\right)^2\right]\right\}\\
&\qquad+\frac{\gamma}{\mathrm{RePr}}\left\{\overline{k}\left(\frac{\partial^2 T_\mathrm{f}'}{\partial x_\mathrm{f}^2}+\frac{\partial^2 T_\mathrm{f}'}{\partial y^2}+\frac{\partial^2 T_\mathrm{f}'}{\partial z^2}\right)+\frac{\mathrm{d}\overline{k}}{\mathrm{d}\overline{T}}\left[2\frac{\partial T_\mathrm{f}'}{\partial x_\mathrm{f}}\frac{\partial \overline{T}}{\partial x_\mathrm{f}}+2\frac{\partial T_\mathrm{f}'}{\partial y}\frac{\partial \overline{T}}{\partial y}+T_\mathrm{f}'\left(\frac{\partial^2 \overline{T}}{\partial x_\mathrm{f}^2}+\frac{\partial^2 \overline{T}}{\partial y^2}\right)\right]\right.\\
&\qquad\left.+\frac{\mathrm{d}^2\overline{k}}{\mathrm{d}\overline{T}^2}T_\mathrm{f}'\left[\left(\frac{\partial \overline{T}}{\partial x_\mathrm{f}}\right)^2+\left(\frac{\partial \overline{T}}{\partial y}\right)^2\right]\right\}
\end{aligned}
\tag{A.1e}
$$

A.2. Direct stability equations in a moving frame of reference

Continuity stability equation

$$-\mathrm{i}\omega\tilde{\rho}+\overline{\rho}\left(\frac{\partial\tilde{u}}{\partial x}+\frac{\partial\tilde{v}}{\partial y}+\mathrm{i}\beta\tilde{w}\right)+\tilde{\rho}\left(\frac{\partial\overline{U}}{\partial x}+\frac{\partial\overline{V}}{\partial y}\right)+\left(\overline{U}-c_\mathrm{f}\right)\frac{\partial\tilde{\rho}}{\partial x}+\overline{V}\frac{\partial\tilde{\rho}}{\partial y}+\mathrm{i}\beta\overline{W}\tilde{\rho}+\tilde{u}\frac{\partial\overline{\rho}}{\partial x}+\tilde{v}\frac{\partial\overline{\rho}}{\partial y}=0 \tag{A.2a}$$

x-momentum stability equation

$$\begin{aligned}
&-\mathrm{i}\omega\overline{\rho}\tilde{u}+\overline{\rho}\left(\left(\overline{U}-c_\mathrm{f}\right)\frac{\partial\tilde{u}}{\partial x}+\overline{V}\frac{\partial\tilde{u}}{\partial y}+\mathrm{i}\beta\overline{W}\tilde{u}+\tilde{u}\frac{\partial\overline{U}}{\partial x}+\tilde{v}\frac{\partial\overline{U}}{\partial y}\right)+\tilde{\rho}\left(\overline{U}\frac{\partial\overline{U}}{\partial x}+\overline{V}\frac{\partial\overline{U}}{\partial y}\right)\\
&\quad=-\frac{1}{\gamma M^2}\left(\overline{T}\frac{\partial\tilde{\rho}}{\partial x}+\overline{\rho}\frac{\partial\tilde{T}}{\partial x}+\tilde{T}\frac{\partial\overline{\rho}}{\partial x}+\tilde{\rho}\frac{\partial\overline{T}}{\partial x}\right)+\frac{\overline{\lambda}}{\mathrm{Re}}\left(\frac{\partial^2\tilde{u}}{\partial x^2}+\frac{\partial^2\tilde{v}}{\partial x\partial y}+\mathrm{i}\beta\frac{\partial\tilde{w}}{\partial x}\right)\\
&\qquad+\frac{\overline{\mu}}{\mathrm{Re}}\left(2\frac{\partial^2\tilde{u}}{\partial x^2}+\frac{\partial^2\tilde{u}}{\partial y^2}-\beta^2\tilde{u}+\frac{\partial^2\tilde{v}}{\partial x\partial y}+\mathrm{i}\beta\frac{\partial\tilde{w}}{\partial x}\right)\\
&\qquad+\frac{1}{\mathrm{Re}}\frac{\mathrm{d}\overline{\lambda}}{\mathrm{d}\overline{T}}\left[\frac{\partial\overline{T}}{\partial x}\left(\frac{\partial\tilde{u}}{\partial x}+\frac{\partial\tilde{v}}{\partial y}+\mathrm{i}\beta\tilde{w}\right)+\frac{\partial\tilde{T}}{\partial x}\left(\frac{\partial\overline{U}}{\partial x}+\frac{\partial\overline{V}}{\partial y}\right)+\tilde{T}\left(\frac{\partial^2\overline{U}}{\partial x^2}+\frac{\partial^2\overline{V}}{\partial x\partial y}\right)\right]\\
&\qquad+\frac{1}{\mathrm{Re}}\frac{\mathrm{d}\overline{\mu}}{\mathrm{d}\overline{T}}\left[2\frac{\partial\overline{T}}{\partial x}\frac{\partial\tilde{u}}{\partial x}+\frac{\partial\overline{T}}{\partial y}\frac{\partial\tilde{u}}{\partial y}+\frac{\partial\overline{T}}{\partial y}\frac{\partial\tilde{v}}{\partial x}+2\frac{\partial\tilde{T}}{\partial x}\frac{\partial\overline{U}}{\partial x}+\frac{\partial\tilde{T}}{\partial y}\left(\frac{\partial\overline{U}}{\partial y}+\frac{\partial\overline{V}}{\partial x}\right)\right.\\
&\qquad\left.+\mathrm{i}\beta\tilde{T}\frac{\partial\overline{W}}{\partial x}+\tilde{T}\left(2\frac{\partial^2\overline{U}}{\partial x^2}+\frac{\partial^2\overline{U}}{\partial y^2}+\frac{\partial^2\overline{V}}{\partial x\partial y}\right)\right]\\
&\qquad+\frac{1}{\mathrm{Re}}\frac{\mathrm{d}^2\overline{\lambda}}{\mathrm{d}\overline{T}^2}\frac{\partial\overline{T}}{\partial x}\tilde{T}\left(\frac{\partial\overline{U}}{\partial x}+\frac{\partial\overline{V}}{\partial y}\right)+\frac{1}{\mathrm{Re}}\frac{\mathrm{d}^2\overline{\mu}}{\mathrm{d}\overline{T}^2}\tilde{T}\left[2\frac{\partial\overline{T}}{\partial x}\frac{\partial\overline{U}}{\partial x}+\frac{\partial\overline{T}}{\partial y}\left(\frac{\partial\overline{U}}{\partial y}+\frac{\partial\overline{V}}{\partial x}\right)\right]
\end{aligned} \tag{A.2b}$$

y-momentum stability equation

$$\begin{aligned}
&-\mathrm{i}\omega\overline{\rho}\tilde{v}+\overline{\rho}\left(\left(\overline{U}-c_\mathrm{f}\right)\frac{\partial\tilde{v}}{\partial x}+\overline{V}\frac{\partial\tilde{v}}{\partial y}+\overline{W}\frac{\partial\tilde{v}}{\partial z}+\tilde{u}\frac{\partial\overline{V}}{\partial x}+\tilde{v}\frac{\partial\overline{V}}{\partial y}\right)+\tilde{\rho}\left(\overline{U}\frac{\partial\overline{V}}{\partial x}+\overline{V}\frac{\partial\overline{V}}{\partial y}\right)\\
&\quad=-\frac{1}{\gamma M^2}\left(\overline{T}\frac{\partial\tilde{\rho}}{\partial y}+\overline{\rho}\frac{\partial\tilde{T}}{\partial y}+\tilde{T}\frac{\partial\overline{\rho}}{\partial y}+\tilde{\rho}\frac{\partial\overline{T}}{\partial y}\right)+\frac{\overline{\lambda}}{\mathrm{Re}}\left(\frac{\partial^2\tilde{u}}{\partial x\partial y}+\frac{\partial^2\tilde{v}}{\partial y^2}+\mathrm{i}\beta\frac{\partial\tilde{w}}{\partial y}\right)\\
&\qquad+\frac{\overline{\mu}}{\mathrm{Re}}\left(\frac{\partial^2\tilde{u}}{\partial x\partial y}+\frac{\partial^2\tilde{v}}{\partial x^2}+2\frac{\partial^2\tilde{v}}{\partial y^2}-\beta^2\tilde{v}+\mathrm{i}\beta\frac{\partial\tilde{w}}{\partial y}\right)\\
&\qquad+\frac{1}{\mathrm{Re}}\frac{\mathrm{d}\overline{\lambda}}{\mathrm{d}\overline{T}}\left[\frac{\partial\overline{T}}{\partial y}\left(\frac{\partial\tilde{u}}{\partial x}+\frac{\partial\tilde{v}}{\partial y}+\mathrm{i}\beta\tilde{w}\right)+\frac{\partial\tilde{T}}{\partial y}\left(\frac{\partial\overline{U}}{\partial x}+\frac{\partial\overline{V}}{\partial y}\right)+\tilde{T}\left(\frac{\partial^2\overline{U}}{\partial x\partial y}+\frac{\partial^2\overline{V}}{\partial y^2}\right)\right]\\
&\qquad+\frac{1}{\mathrm{Re}}\frac{\mathrm{d}\overline{\mu}}{\mathrm{d}\overline{T}}\left[\frac{\partial\overline{T}}{\partial x}\frac{\partial\tilde{u}}{\partial y}+2\frac{\partial\overline{T}}{\partial y}\frac{\partial\tilde{v}}{\partial y}+\frac{\partial\overline{T}}{\partial x}\frac{\partial\tilde{v}}{\partial x}+2\frac{\partial\tilde{T}}{\partial y}\frac{\partial\overline{V}}{\partial y}+\frac{\partial\tilde{T}}{\partial x}\left(\frac{\partial\overline{U}}{\partial y}+\frac{\partial\overline{V}}{\partial x}\right)\right.\\
&\qquad\left.+\mathrm{i}\beta\tilde{T}\frac{\partial\overline{W}}{\partial y}+\tilde{T}\left(\frac{\partial^2\overline{U}}{\partial x\partial y}+\frac{\partial^2\overline{V}}{\partial x^2}+2\frac{\partial^2\overline{V}}{\partial y^2}\right)\right]\\
&\qquad+\frac{1}{\mathrm{Re}}\frac{\mathrm{d}^2\overline{\lambda}}{\mathrm{d}\overline{T}^2}\frac{\partial\overline{T}}{\partial y}\tilde{T}\left(\frac{\partial\overline{U}}{\partial x}+\frac{\partial\overline{V}}{\partial y}\right)+\frac{1}{\mathrm{Re}}\frac{\mathrm{d}^2\overline{\mu}}{\mathrm{d}\overline{T}^2}\tilde{T}\left[\frac{\partial\overline{T}}{\partial x}\left(\frac{\partial\overline{U}}{\partial y}+\frac{\partial\overline{V}}{\partial x}\right)+2\frac{\partial\overline{T}}{\partial y}\frac{\partial\overline{V}}{\partial y}\right]
\end{aligned} \tag{A.2c}$$

z-momentum stability equation

$$
\begin{aligned}
&-\mathrm{i}\omega\overline{\rho}\tilde{w}+\overline{\rho}\left(\left(\overline{U}-c_\mathrm{f}\right)\frac{\partial\tilde{w}}{\partial x}+\overline{V}\frac{\partial\tilde{w}}{\partial y}+\mathrm{i}\beta\overline{W}\tilde{w}+\tilde{u}\frac{\partial\overline{W}}{\partial x}+\tilde{v}\frac{\partial\overline{W}}{\partial y}\right)+\tilde{\rho}\left(\overline{U}\frac{\partial\overline{W}}{\partial x}+\overline{V}\frac{\partial\overline{W}}{\partial y}\right)\\
&\quad=-\frac{\mathrm{i}\beta}{\gamma M^2}\left(\overline{T}\tilde{\rho}+\overline{\rho}\tilde{T}\right)+\frac{\overline{\lambda}}{\mathrm{Re}}\left(\mathrm{i}\beta\frac{\partial\tilde{u}}{\partial x}+\mathrm{i}\beta\frac{\partial\tilde{v}}{\partial y}-\beta^2\tilde{w}\right)\\
&\qquad+\frac{\overline{\mu}}{\mathrm{Re}}\left(\mathrm{i}\beta\frac{\partial\tilde{u}}{\partial x}+\mathrm{i}\beta\frac{\partial\tilde{v}}{\partial y}+\frac{\partial^2\tilde{w}}{\partial x^2}+\frac{\partial^2\tilde{w}}{\partial y^2}-2\beta^2\tilde{w}\right)+\frac{\mathrm{i}\beta}{\mathrm{Re}}\frac{\mathrm{d}\overline{\lambda}}{\mathrm{d}\overline{T}}\tilde{T}\left(\frac{\partial\overline{U}}{\partial x}+\frac{\partial\overline{V}}{\partial y}\right)\\
&\qquad+\frac{1}{\mathrm{Re}}\frac{\mathrm{d}\overline{\mu}}{\mathrm{d}\overline{T}}\left[\mathrm{i}\beta\frac{\partial\overline{T}}{\partial x}\tilde{u}+\mathrm{i}\beta\frac{\partial\overline{T}}{\partial y}\tilde{v}+\frac{\partial\overline{T}}{\partial x}\frac{\partial\tilde{w}}{\partial x}+\frac{\partial\overline{T}}{\partial y}\frac{\partial\tilde{w}}{\partial y}+\frac{\partial\tilde{T}}{\partial x}\frac{\partial\overline{W}}{\partial x}+\frac{\partial\tilde{T}}{\partial y}\frac{\partial\overline{W}}{\partial y}\right.\\
&\qquad\left.+\tilde{T}\left(\frac{\partial^2\overline{W}}{\partial x^2}+\frac{\partial^2\overline{W}}{\partial y^2}\right)\right]+\frac{1}{\mathrm{Re}}\frac{\mathrm{d}^2\overline{\mu}}{\mathrm{d}\overline{T}^2}\tilde{T}\left[\frac{\partial\overline{T}}{\partial x}\frac{\partial\overline{W}}{\partial x}+\frac{\partial\overline{T}}{\partial y}\frac{\partial\overline{W}}{\partial y}\right]
\end{aligned}
\tag{A.2d}
$$

Internal energy stability equation

$$
\begin{aligned}
&-\mathrm{i}\omega\overline{\rho}\tilde{T}+\overline{\rho}\left(\left(\overline{U}-c_\mathrm{f}\right)\frac{\partial\tilde{T}}{\partial x}+\overline{V}\frac{\partial\tilde{T}}{\partial y}+\mathrm{i}\beta\overline{W}\tilde{T}+\tilde{u}\frac{\partial\overline{T}}{\partial x}+\tilde{v}\frac{\partial\overline{T}}{\partial y}\right)+\tilde{\rho}\left(\overline{U}\frac{\partial\overline{T}}{\partial x}+\overline{V}\frac{\partial\overline{T}}{\partial y}\right)\\
&\quad=(1-\gamma)\left[\overline{\rho}\,\overline{T}\left(\frac{\partial\tilde{u}}{\partial x}+\frac{\partial\tilde{v}}{\partial y}+\mathrm{i}\beta\tilde{w}\right)+\left(\tilde{\rho}\,\overline{T}+\overline{\rho}\tilde{T}\right)\left(\frac{\partial\overline{U}}{\partial x}+\frac{\partial\overline{V}}{\partial y}\right)\right]\\
&\qquad+\frac{\gamma\mathrm{Ec}}{\mathrm{Re}}\left\{2\overline{\lambda}\left(\frac{\partial\tilde{u}}{\partial x}+\frac{\partial\tilde{v}}{\partial y}+\mathrm{i}\beta\tilde{w}\right)\left(\frac{\partial\overline{U}}{\partial x}+\frac{\partial\overline{V}}{\partial y}\right)+\frac{\mathrm{d}\overline{\lambda}}{\mathrm{d}\overline{T}}\tilde{T}\left[\left(\frac{\partial\overline{U}}{\partial x}\right)^2+2\frac{\partial\overline{U}}{\partial x}\frac{\partial\overline{V}}{\partial x}+\left(\frac{\partial\overline{V}}{\partial y}\right)^2\right]\right\}\\
&\qquad+\frac{\gamma\mathrm{Ec}}{\mathrm{Re}}\left\{2\overline{\mu}\left[2\frac{\partial\tilde{u}}{\partial x}\frac{\partial\overline{U}}{\partial x}+\mathrm{i}\beta\tilde{u}\frac{\partial\overline{W}}{\partial x}+2\frac{\partial\tilde{v}}{\partial y}\frac{\partial\overline{V}}{\partial y}+\mathrm{i}\beta\tilde{v}\frac{\partial\overline{W}}{\partial y}+\left(\frac{\partial\tilde{u}}{\partial y}+\frac{\partial\tilde{v}}{\partial x}\right)\left(\frac{\partial\overline{U}}{\partial y}+\frac{\partial\overline{V}}{\partial x}\right)\right.\right.\\
&\qquad\left.+\frac{\partial\tilde{w}}{\partial x}\frac{\partial\overline{W}}{\partial x}+\frac{\partial\tilde{w}}{\partial y}\frac{\partial\overline{W}}{\partial y}\right]+\frac{\mathrm{d}\overline{\mu}}{\mathrm{d}\overline{T}}\tilde{T}\left[2\left(\frac{\partial\overline{U}}{\partial x}\right)^2+\left(\frac{\partial\overline{U}}{\partial y}\right)^2+2\left(\frac{\partial\overline{U}}{\partial y}\right)\left(\frac{\partial\overline{V}}{\partial x}\right)+\left(\frac{\partial\overline{V}}{\partial x}\right)^2\right.\\
&\qquad\left.\left.+2\left(\frac{\partial\overline{V}}{\partial y}\right)^2+\left(\frac{\partial\overline{W}}{\partial x}\right)^2+\left(\frac{\partial\overline{W}}{\partial y}\right)^2\right]\right\}\\
&\qquad+\frac{\gamma}{\mathrm{RePr}}\left\{\overline{k}\left(\frac{\partial^2\tilde{T}}{\partial x^2}+\frac{\partial^2\tilde{T}}{\partial y^2}-\beta^2\tilde{T}\right)+\frac{\mathrm{d}\overline{k}}{\mathrm{d}\overline{T}}\left[2\frac{\partial\tilde{T}}{\partial x}\frac{\partial\overline{T}}{\partial x}+2\frac{\partial\tilde{T}}{\partial y}\frac{\partial\overline{T}}{\partial y}+\tilde{T}\left(\frac{\partial^2\overline{T}}{\partial x^2}+\frac{\partial^2\overline{T}}{\partial y^2}\right)\right]\right.\\
&\qquad\left.+\frac{\mathrm{d}^2\overline{k}}{\mathrm{d}\overline{T}^2}\tilde{T}\left[\left(\frac{\partial\overline{T}}{\partial x}\right)^2+\left(\frac{\partial\overline{T}}{\partial y}\right)^2\right]\right\}
\end{aligned}
\tag{A.2e}
$$

A.3. Continuous adjoint stability equations in a moving frame of reference

Continuity adjoint stability equation

$$
\begin{aligned}
&\mathrm{i}\omega\tilde{\rho}^\dagger + \overline{\rho}\left(\frac{\partial\tilde{u}^\dagger}{\partial x} + \frac{\partial\tilde{v}^\dagger}{\partial y} + \mathrm{i}\beta\tilde{w}^\dagger\right) + \tilde{\rho}^\dagger\left(\frac{\partial\overline{U}}{\partial x} + \frac{\partial\overline{V}}{\partial y}\right) - \left(\overline{U} - c_\mathrm{f}\right)\frac{\partial\tilde{\rho}^\dagger}{\partial x} - \overline{V}\frac{\partial\tilde{\rho}^\dagger}{\partial y} + \mathrm{i}\beta\overline{W}\tilde{\rho}^\dagger \\
&\quad + \frac{\overline{\rho}^2}{\overline{P}}\tilde{u}^\dagger\left(\overline{U}\frac{\partial\overline{U}}{\partial x} + \overline{V}\frac{\partial\overline{U}}{\partial y}\right) + \frac{\overline{\rho}^2}{\overline{P}}\tilde{v}^\dagger\left(\overline{U}\frac{\partial\overline{V}}{\partial x} + \overline{V}\frac{\partial\overline{V}}{\partial y}\right) \\
&\quad + \frac{\overline{\rho}\tilde{T}^\dagger}{(\gamma-1)\overline{T}^2}\left(\overline{U}\frac{\partial\overline{T}}{\partial x} + \overline{V}\frac{\partial\overline{T}}{\partial y}\right) + \frac{\overline{\rho}\tilde{T}^\dagger}{\overline{T}}\left(\frac{\partial\overline{U}}{\partial x} + \frac{\partial\overline{V}}{\partial y}\right) = 0
\end{aligned}
\tag{A.3a}
$$

x-momentum adjoint stability equation

$$
\begin{aligned}
&\mathrm{i}\omega\overline{\rho}\tilde{u}^\dagger + \overline{\rho}\left(\left(c_\mathrm{f} - \overline{U}\right)\frac{\partial\tilde{u}^\dagger}{\partial x} - \overline{V}\frac{\partial\tilde{u}^\dagger}{\partial y} + \mathrm{i}\beta\overline{W}\tilde{u}^\dagger + \tilde{u}^\dagger\frac{\partial\overline{U}}{\partial x} + \tilde{v}^\dagger\frac{\partial\overline{V}}{\partial x} + \tilde{w}^\dagger\frac{\partial\overline{W}}{\partial x} + \frac{\tilde{T}^\dagger}{\gamma\mathrm{Ec}\overline{T}}\frac{\partial\overline{T}}{\partial x}\right) + \frac{\overline{P}}{\overline{\rho}}\tilde{\rho}^\dagger\frac{\partial\overline{\rho}}{\partial x} \\
&\quad = -\frac{1}{\gamma M^2}\left(\overline{T}\frac{\partial\tilde{\rho}^\dagger}{\partial x} + \overline{\rho}\frac{\partial\tilde{T}^\dagger}{\partial x} + \tilde{T}^\dagger\frac{\partial\overline{\rho}}{\partial x} + \tilde{\rho}^\dagger\frac{\partial\overline{T}}{\partial x}\right) \\
&\qquad + \frac{\overline{\lambda}}{\mathrm{Re}}\left[\frac{\partial^2\tilde{u}^\dagger}{\partial x^2} + \frac{\partial^2\tilde{v}^\dagger}{\partial x\partial y} - \mathrm{i}\beta\frac{\partial\tilde{w}^\dagger}{\partial x} - \frac{2}{\overline{T}}\frac{\partial\tilde{T}^\dagger}{\partial x}\left(\frac{\partial\overline{U}}{\partial x} + \frac{\partial\overline{V}}{\partial y}\right) - 2\frac{\tilde{T}^\dagger}{\overline{T}}\left(\frac{\partial^2\overline{U}}{\partial x^2} + \frac{\partial^2\overline{V}}{\partial x\partial y}\right)\right] \\
&\qquad + \frac{\overline{\mu}}{\mathrm{Re}}\left[2\frac{\partial^2\tilde{u}^\dagger}{\partial x^2} + \frac{\partial^2\tilde{u}^\dagger}{\partial y^2} - \beta^2\tilde{u}^\dagger + \frac{\partial^2\tilde{v}^\dagger}{\partial x\partial y} - \mathrm{i}\beta\frac{\partial\tilde{w}^\dagger}{\partial x} - \frac{4}{\overline{T}}\frac{\partial\tilde{T}^\dagger}{\partial x}\frac{\partial\overline{U}}{\partial x}\right. \\
&\qquad\quad \left. - \frac{2}{\overline{T}}\frac{\partial\tilde{T}^\dagger}{\partial y}\left(\frac{\partial\overline{U}}{\partial y} + \frac{\partial\overline{V}}{\partial x}\right) + 2\mathrm{i}\beta\frac{\tilde{T}^\dagger}{\overline{T}}\frac{\partial\overline{W}}{\partial x} - 2\frac{\tilde{T}^\dagger}{\overline{T}}\left(2\frac{\partial^2\overline{U}}{\partial x^2} + \frac{\partial^2\overline{U}}{\partial y^2} + \frac{\partial^2\overline{V}}{\partial x\partial y}\right)\right] \\
&\qquad + \frac{1}{\mathrm{Re}}\frac{\mathrm{d}\overline{\lambda}}{\mathrm{d}\overline{T}}\left[\frac{\partial\overline{T}}{\partial x}\left(\frac{\partial\tilde{u}^\dagger}{\partial x} + \frac{\partial\tilde{v}^\dagger}{\partial y} - \mathrm{i}\beta\tilde{w}^\dagger\right) - 2\frac{\partial\overline{T}}{\partial x}\frac{\tilde{T}^\dagger}{\overline{T}}\left(\frac{\partial\overline{U}}{\partial x} + \frac{\partial\overline{V}}{\partial y}\right)\right] \\
&\qquad + \frac{1}{\mathrm{Re}}\frac{\mathrm{d}\overline{\mu}}{\mathrm{d}\overline{T}}\left[2\frac{\partial\overline{T}}{\partial x}\frac{\partial\tilde{u}^\dagger}{\partial x} + \frac{\partial\overline{T}}{\partial y}\frac{\partial\tilde{u}^\dagger}{\partial y} + \frac{\partial\overline{T}}{\partial y}\frac{\partial\tilde{v}^\dagger}{\partial x} - 4\frac{\partial\overline{T}}{\partial x}\frac{\tilde{T}^\dagger}{\overline{T}}\frac{\partial\overline{U}}{\partial x} - 2\frac{\partial\overline{T}}{\partial y}\frac{\tilde{T}^\dagger}{\overline{T}}\left(\frac{\partial\overline{U}}{\partial y} + \frac{\partial\overline{V}}{\partial x}\right)\right]
\end{aligned}
\tag{A.3b}
$$

y-momentum adjoint stability equation

$$
\begin{aligned}
&\mathrm{i}\omega\overline{\rho}\tilde{v}^\dagger + \overline{\rho}\left(\left(c_\mathrm{f}-\overline{U}\right)\frac{\partial\tilde{v}^\dagger}{\partial x} - \overline{V}\frac{\partial\tilde{v}^\dagger}{\partial y} + \mathrm{i}\beta\overline{W}\tilde{v}^\dagger + \tilde{u}^\dagger\frac{\partial\overline{U}}{\partial y} + \tilde{v}^\dagger\frac{\partial\overline{V}}{\partial y} + \tilde{w}^\dagger\frac{\partial\overline{W}}{\partial y} + \frac{\tilde{T}^\dagger}{\gamma\mathrm{Ec}\overline{T}}\frac{\partial\overline{T}}{\partial y}\right) + \frac{\overline{P}}{\overline{\rho}}\tilde{\rho}^\dagger\frac{\partial\overline{\rho}}{\partial y} \\
&\quad = -\frac{1}{\gamma M^2}\left(\overline{T}\frac{\partial\tilde{\rho}^\dagger}{\partial x} + \overline{\rho}\frac{\partial\tilde{T}^\dagger}{\partial x} + \tilde{T}^\dagger\frac{\partial\overline{\rho}}{\partial x} + \tilde{\rho}^\dagger\frac{\partial\overline{T}}{\partial x}\right) \\
&\qquad + \frac{\overline{\lambda}}{\mathrm{Re}}\left[\frac{\partial^2\tilde{u}^\dagger}{\partial x\partial y} + \frac{\partial^2\tilde{v}^\dagger}{\partial y^2} - \mathrm{i}\beta\frac{\partial\tilde{w}^\dagger}{\partial y} - \frac{2}{\overline{T}}\frac{\partial\tilde{T}^\dagger}{\partial y}\left(\frac{\partial\overline{U}}{\partial x} + \frac{\partial\overline{V}}{\partial y}\right) - 2\frac{\tilde{T}^\dagger}{\overline{T}}\left(\frac{\partial^2\overline{U}}{\partial x\partial y} + \frac{\partial^2\overline{V}}{\partial y^2}\right)\right] \\
&\qquad + \frac{\overline{\mu}}{\mathrm{Re}}\left[\frac{\partial^2\tilde{u}^\dagger}{\partial x\partial y} + \frac{\partial^2\tilde{v}^\dagger}{\partial x^2} + 2\frac{\partial^2\tilde{v}^\dagger}{\partial y^2} - \beta^2\tilde{v}^\dagger - \mathrm{i}\beta\frac{\partial\tilde{w}^\dagger}{\partial y} - \frac{4}{\overline{T}}\frac{\partial\tilde{T}^\dagger}{\partial y}\frac{\partial\overline{V}}{\partial y}\right. \\
&\qquad\quad \left. - \frac{2}{\overline{T}}\frac{\partial\tilde{T}^\dagger}{\partial x}\left(\frac{\partial\overline{U}}{\partial y} + \frac{\partial\overline{V}}{\partial x}\right) + 2\mathrm{i}\beta\frac{\tilde{T}^\dagger}{\overline{T}}\frac{\partial\overline{W}}{\partial y} - 2\frac{\tilde{T}^\dagger}{\overline{T}}\left(\frac{\partial^2\overline{U}}{\partial x\partial y} + \frac{\partial^2\overline{V}}{\partial x^2} + 2\frac{\partial^2\overline{V}}{\partial y^2}\right)\right] \\
&\qquad + \frac{1}{\mathrm{Re}}\frac{\mathrm{d}\overline{\lambda}}{\mathrm{d}\overline{T}}\left[\frac{\partial\overline{T}}{\partial y}\left(\frac{\partial\tilde{u}^\dagger}{\partial x} + \frac{\partial\tilde{v}^\dagger}{\partial y} - \mathrm{i}\beta\tilde{w}^\dagger\right) - 2\frac{\partial\overline{T}}{\partial y}\frac{\tilde{T}^\dagger}{\overline{T}}\left(\frac{\partial\overline{U}}{\partial x} + \frac{\partial\overline{V}}{\partial y}\right)\right] \\
&\qquad + \frac{1}{\mathrm{Re}}\frac{\mathrm{d}\overline{\mu}}{\mathrm{d}\overline{T}}\left[\frac{\partial\overline{T}}{\partial x}\frac{\partial\tilde{u}^\dagger}{\partial y} + \frac{\partial\overline{T}}{\partial x}\frac{\partial\tilde{v}^\dagger}{\partial x} + 2\frac{\partial\overline{T}}{\partial y}\frac{\partial\tilde{v}^\dagger}{\partial y} - 4\frac{\partial\overline{T}}{\partial y}\frac{\tilde{T}^\dagger}{\overline{T}}\frac{\partial\overline{V}}{\partial y} - 2\frac{\partial\overline{T}}{\partial x}\frac{\tilde{T}^\dagger}{\overline{T}}\left(\frac{\partial\overline{U}}{\partial y} + \frac{\partial\overline{V}}{\partial x}\right)\right]
\end{aligned}
\tag{A.3c}
$$

z-momentum adjoint stability equation

$$
\begin{aligned}
&\mathrm{i}\omega\overline{\rho}\tilde{w}^\dagger + \overline{\rho}\left(\left(c_\mathrm{f}-\overline{U}\right)\frac{\partial\tilde{w}^\dagger}{\partial x} - \overline{V}\frac{\partial\tilde{w}^\dagger}{\partial y} + \mathrm{i}\beta\overline{W}\tilde{w}^\dagger\right) \\
&\quad = -\frac{\mathrm{i}\beta}{\gamma M^2}\left(\overline{T}\tilde{\rho}^\dagger + \overline{\rho}\tilde{T}^\dagger\right) + \frac{\overline{\lambda}}{\mathrm{Re}}\left[-\mathrm{i}\beta\frac{\partial\tilde{u}^\dagger}{\partial x} - \mathrm{i}\beta\frac{\partial\tilde{v}^\dagger}{\partial y} - 2\beta^2\tilde{w}^\dagger + 2\mathrm{i}\beta\frac{\tilde{T}^\dagger}{\overline{T}}\left(\frac{\partial\overline{U}}{\partial x} + \frac{\partial\overline{V}}{\partial y}\right)\right] \\
&\qquad + \frac{\overline{\mu}}{\mathrm{Re}}\left[-\mathrm{i}\beta\frac{\partial\tilde{u}^\dagger}{\partial x} - \mathrm{i}\beta\frac{\partial\tilde{v}^\dagger}{\partial y} + \frac{\partial^2\tilde{w}^\dagger}{\partial x^2} + \frac{\partial^2\tilde{w}^\dagger}{\partial y^2} - 2\beta^2\tilde{w}^\dagger\right. \\
&\qquad\quad \left. + \frac{2}{\overline{T}}\frac{\partial\tilde{T}^\dagger}{\partial x}\frac{\partial\overline{W}}{\partial x} + \frac{2}{\overline{T}}\frac{\partial\tilde{T}^\dagger}{\partial y}\frac{\partial\overline{W}}{\partial y} + 2\frac{\tilde{T}^\dagger}{\overline{T}}\left(\frac{\partial^2\overline{W}}{\partial x^2} + \frac{\partial^2\overline{W}}{\partial y^2}\right)\right] \\
&\qquad + \frac{1}{\mathrm{Re}}\frac{\mathrm{d}\overline{\mu}}{\mathrm{d}\overline{T}}\left(-\mathrm{i}\beta\frac{\partial\overline{T}}{\partial x}\tilde{u}^\dagger - \mathrm{i}\beta\frac{\partial\overline{T}}{\partial y}\tilde{v}^\dagger + \frac{\partial\overline{T}}{\partial x}\frac{\partial\tilde{w}^\dagger}{\partial x} + \frac{\partial\overline{T}}{\partial y}\frac{\partial\tilde{w}^\dagger}{\partial y} + 2\frac{\partial\overline{T}}{\partial x}\frac{\tilde{T}^\dagger}{\overline{T}}\frac{\partial\overline{W}}{\partial x} + 2\frac{\partial\overline{T}}{\partial y}\frac{\tilde{T}^\dagger}{\overline{T}}\frac{\partial\overline{W}}{\partial y}\right)
\end{aligned}
\tag{A.3d}
$$

Internal energy adjoint stability equation

$$
\begin{aligned}
&\mathrm{i}\omega\overline{\rho}\tilde{T}^{\dagger}+\overline{\rho}\left(\left(c_{\mathrm{f}}-\overline{U}\right)\frac{\partial\tilde{T}^{\dagger}}{\partial x}-\overline{V}\frac{\partial\tilde{T}^{\dagger}}{\partial y}+\mathrm{i}\beta\overline{W}\tilde{T}^{\dagger}\right)\\
&\quad=(\gamma-1)\left[\overline{\rho}\,\overline{T}\left(\frac{\partial\tilde{u}^{\dagger}}{\partial x}+\frac{\partial\tilde{v}^{\dagger}}{\partial y}+\mathrm{i}\beta\tilde{w}^{\dagger}\right)+\overline{\rho}\tilde{T}^{\dagger}\left(\frac{\partial\overline{U}}{\partial x}+\frac{\partial\overline{V}}{\partial y}\right)\right]\\
&\quad+\frac{\gamma\mathrm{Ec}\,\overline{T}}{\mathrm{Re}}\frac{\mathrm{d}\overline{\lambda}}{\mathrm{d}\overline{T}}\left\{\left(-\frac{\partial\tilde{u}^{\dagger}}{\partial x_{\mathrm{f}}}-\frac{\partial\tilde{v}^{\dagger}}{\partial y}+\mathrm{i}\,\beta\,\tilde{w}^{\dagger}\right)\left(\frac{\partial\overline{U}}{\partial x_{\mathrm{f}}}+\frac{\partial\overline{V}}{\partial y}\right)+\frac{\tilde{T}^{\dagger}}{\overline{T}}\left[\left(\frac{\partial\overline{U}}{\partial x}\right)^{2}+2\frac{\partial\overline{U}}{\partial x}\frac{\partial\overline{V}}{\partial y}+\left(\frac{\partial\overline{V}}{\partial y}\right)^{2}\right]\right\}\\
&\quad+\frac{\gamma\mathrm{Ec}\,\overline{T}}{\mathrm{Re}}\frac{\mathrm{d}\overline{\mu}}{\mathrm{d}\overline{T}}\left\{-2\frac{\partial\overline{U}}{\partial x_{\mathrm{f}}}\frac{\partial\tilde{u}^{\dagger}}{\partial x_{\mathrm{f}}}-\frac{\partial\overline{U}}{\partial y}\left(\frac{\partial\tilde{u}^{\dagger}}{\partial y}+\frac{\partial\tilde{v}^{\dagger}}{\partial x_{\mathrm{f}}}\right)-\frac{\partial\overline{V}}{\partial x_{\mathrm{f}}}\left(\frac{\partial\tilde{u}^{\dagger}}{\partial y}+\frac{\partial\tilde{v}^{\dagger}}{\partial x_{\mathrm{f}}}\right)-2\frac{\partial\tilde{v}^{\dagger}}{\partial y}\frac{\partial\overline{V}}{\partial y}\right.\\
&\qquad+\frac{\partial\overline{W}}{\partial x_{\mathrm{f}}}\left(\mathrm{i}\,\beta\,\tilde{u}^{\dagger}-\frac{\partial\tilde{w}^{\dagger}}{\partial x_{\mathrm{f}}}\right)+\frac{\partial\overline{W}}{\partial y}\left(\mathrm{i}\,\beta\,\tilde{v}^{\dagger}-\frac{\partial\tilde{w}^{\dagger}}{\partial y}\right)+\frac{\tilde{T}^{\dagger}}{\overline{T}}\left[2\left(\frac{\partial\overline{U}}{\partial x}\right)^{2}+\left(\frac{\partial\overline{U}}{\partial y}\right)^{2}\right.\\
&\qquad\left.\left.+2\left(\frac{\partial\overline{U}}{\partial y}\right)\left(\frac{\partial\overline{V}}{\partial x}\right)+\left(\frac{\partial\overline{V}}{\partial x}\right)^{2}+2\left(\frac{\partial\overline{V}}{\partial y}\right)^{2}+\left(\frac{\partial\overline{W}}{\partial x}\right)^{2}+\left(\frac{\partial\overline{W}}{\partial y}\right)^{2}\right]\right\}\\
&\quad+\frac{\gamma\overline{k}}{\mathrm{RePr}}\left(\frac{\partial^{2}\tilde{T}^{\dagger}}{\partial x^{2}}+\frac{\partial^{2}\tilde{T}^{\dagger}}{\partial y^{2}}-\beta^{2}\tilde{T}^{\dagger}\right)
\end{aligned}
\tag{A.3e}
$$

A.4. Energy weight matrices

This section aims to show the equivalence between the two energy weight matrices presented in Chapter 2. Since the derivation apply to both moving and stationary frame of reference, all subscripts 'f' are dropped in what follows for sake of clarity. These matrices are given by

$$
\mathscr{M}=\mathrm{diag}\left(\overline{\rho},\overline{\rho},\overline{\rho},\frac{\overline{\rho}}{\gamma\mathrm{Ec}\,\overline{T}},\frac{\overline{T}}{\gamma M^{2}\overline{\rho}}\right),
\tag{A.4}
$$

for the density formulation of the perturbations equations, i.e., for $\boldsymbol{q}'=[u',v',w',T',\rho']^{\mathrm{T}}$, and

$$
\mathscr{M}=\begin{bmatrix}
\overline{\rho} & 0 & 0 & 0 & 0\\
0 & \overline{\rho} & 0 & 0 & 0\\
0 & 0 & \overline{\rho} & 0 & 0\\
0 & 0 & 0 & \frac{\overline{\rho}}{\mathrm{Ec}\,\overline{T}} & -\frac{1}{\overline{T}}\\
0 & 0 & 0 & -\frac{1}{\overline{T}} & \frac{1}{\overline{P}}
\end{bmatrix},
\tag{A.5}
$$

for the pressure formulation, i.e., for $\boldsymbol{q}'=[u',v',w',T',p']^{\mathrm{T}}$. The equivalence between these two weight matrices can be shown by considering first the matrix (A.5) in the energy integral given by equation (2.56) such that

$$
E=\int_{\mathcal{V}}\overline{\rho}\left(|u'|^{2}+|v'|^{2}+|w'|^{2}\right)\mathrm{d}\mathcal{V}+T'^{*}\left(\frac{\overline{\rho}}{\mathrm{Ec}\,\overline{T}}T'-\frac{1}{\overline{T}}p'\right)+p'^{*}\left(-\frac{1}{\overline{T}}T'+\frac{1}{\overline{P}}p'\right)\mathrm{d}\mathcal{V}
\tag{A.6}
$$

$$
=\underbrace{\int_{\mathcal{V}}\overline{\rho}\left(|u'|^{2}+|v'|^{2}+|w'|^{2}\right)\mathrm{d}\mathcal{V}}_{E_k}+\underbrace{\int_{\mathcal{V}}\frac{\overline{\rho}}{\mathrm{Ec}\,\overline{T}}|T'|^{2}+\frac{1}{\overline{P}}|p'|^{2}-\frac{1}{\overline{T}}T'^{*}p'-\frac{1}{\overline{T}}p'^{*}T'\,\mathrm{d}\mathcal{V}}_{E_p},
\tag{A.7}
$$

with E_k and E_p the kinetic energy and generalized potential energy terms, respectively. Using the ideal-gas law for perturbations (2.15b) to replace the pressure perturbation by the density perturbation allows rearranging the potential-energy term as

$$\begin{aligned} E_p &= \int_{\mathcal{V}} \frac{\overline{\rho}}{\mathrm{Ec}\,\overline{T}}|T'|^2 + \frac{\overline{P}}{\overline{T}^2}|T'|^2 + \frac{\overline{P}}{\overline{\rho}^2}|\rho'|^2 + \frac{\overline{P}}{\overline{\rho}\,\overline{T}}\left(\rho'^* T' + T'^* \rho'\right) - \frac{\overline{P}}{\overline{\rho}\,\overline{T}}\left(T'^* \rho' + \rho'^* T'\right) - 2\frac{\overline{P}}{\overline{T}^2}|T'|^2 \,\mathrm{d}\mathcal{V} \\ &= \int_{\mathcal{V}} \frac{\overline{\rho}}{\mathrm{Ec}\,\overline{T}}|T'|^2 - \frac{\overline{P}}{\overline{T}^2}|T'|^2 + \frac{\overline{P}}{\overline{\rho}^2}|\rho'|^2 \,\mathrm{d}\mathcal{V}\,. \end{aligned} \tag{A.8}$$

Furthermore, considering the ideal-gas law for the base-flow variables to eliminate the pressure $\overline{P}$ and using the Eckert number $\mathrm{Ec} = (\gamma-1)M^2$, the potential energy becomes

$$\begin{aligned} E_p &= \int_{\mathcal{V}} \frac{\overline{\rho}}{\overline{T}}\left(\frac{1}{\mathrm{Ec}} - \frac{1}{\gamma M^2}\right)|T'|^2 + \frac{\overline{T}}{\gamma M^2 \overline{\rho}}|\rho'|^2 \,\mathrm{d}\mathcal{V} \\ &= \int_{\mathcal{V}} \frac{\overline{\rho}}{\overline{T}}\left(\frac{\gamma}{\gamma\,\mathrm{Ec}} - \frac{\gamma-1}{\gamma\,\mathrm{Ec}}\right)|T'|^2 + \frac{\overline{T}}{\gamma M^2 \overline{\rho}}|\rho'|^2 \,\mathrm{d}\mathcal{V} \\ &= \int_{\mathcal{V}} \frac{\overline{\rho}}{\gamma\,\mathrm{Ec}\,\overline{T}}|T'|^2 + \frac{\overline{T}}{\gamma M^2 \overline{\rho}}|\rho'|^2 \,\mathrm{d}\mathcal{V} \\ &= \int_{\mathcal{V}_\mathrm{f}} \frac{\overline{\rho}}{\gamma\,\mathrm{Ec}\,\overline{T}}|T'|^2 + \frac{\overline{T}}{\gamma M^2 \overline{\rho}}|\rho'|^2 \,\mathrm{d}\mathcal{V}\,, \end{aligned} \tag{A.9}$$

such that the perturbation energy is finally given by

$$E = E_k + E_p = \int_{\mathcal{V}} \overline{\rho}\left(|u'|^2 + |v'|^2 + |w'|^2\right) + \frac{\overline{\rho}}{\gamma\,\mathrm{Ec}\,\overline{T}}|T'|^2 + \frac{\overline{T}}{\gamma M^2 \overline{\rho}}|\rho'|^2 \,\mathrm{d}\mathcal{V}\,, \tag{A.10}$$

which is equivalent to considering the matrix (2.57) that followed the definition of the perturbation energy as originally proposed by Chu (1965) [On the energy transfer to small disturbances in fluid flow (Part I), *Acta Mechanica*, vol. 1, no. 3, pp. 215–234].